

CENTRAL LIBRARY

**SCHOLARLY ARTICLES**

*A CURRENT AWARENESS BULLETIN  
OF ARTICLES BY  
FACULTY, STUDENTS AND ALUMNI*

~ **MARCH 2013** ~

DELHI TECHNOLOGICAL UNIVERSITY

(FORMERLY *DELHI COLLEGE OF ENGINEERING*)

GOVT. OF N.C.T. OF DELHI

SHAHBAD DAULATPUR, MAIN BAWANA ROAD

DELHI 110042

# PREFACE

This is the Third Issue of Current Awareness Bulletin for the year 2013, started by **Delhi Technological University Library**. The aim of the bulletin is to compile, preserve and disseminate information published by the Faculty, Students and Alumni for mutual benefits. The bulletin also aims to propagate the intellectual contribution of DTU as a whole to the academia. It contains information resources available in the internet in the form of articles, reports, presentation published in international journals, websites, etc. by the faculty and students of Delhi Technological University in the field of science and technology. The publication of Faculty and Students, which are not covered in this bulletin, may be because of the reason that the full text either was not accessible or could not be searched by the search engine used by the library for this purpose. To make the bulletin more comprehensive, the learned faculty and Students may provide their uncovered publication to the library either through email or in CD, etc.

This issue contains the information published during March 2013. The arrangement of the contents is alphabetical wise starting from A-Z. The Full text of the article, which is either subscribed by the University or available in the web, is provided in this Bulletin.

## CONTENTS

1. A Research Review of Power Quality Problems in Electrical Power System, Anurag Agarwal, **\*Sanjiv Kumar**, Sajid Ali
2. Current Controlled Differential Difference Current Conveyor Transconductance Amplifier and Its Application, **\*Neeta Pandey**, Praveen Kumar and **\*Jaya Choudhary**
3. Distributed Drives Monitoring and Control: A Laboratory Setup, **\*Mini Sreejeth**, **\*Parmod Kumar**, and **\*Madhusudan Singh**
4. Effect of different metallic nano – inclusions (Ag,Al,AuandCu) and gain assistance for isotropic left – handed photonic material in blue light region, M. Rajput, **\*R.K.Sinha**, S.K.Varshney
5. Genetically Modified Plants: Public and Scientific Perceptions, **\*Smita Rastogi Verma**
6. Optical Absorption and Luminescent Characteristics of Dy<sup>3+</sup> doped Zinc Alumino Bismuth Borate Glasses for Lasing materials and White LEDs, K.Swapna, Sk.Mahamuda, **\*A. Srinivasa Rao**, **\*M.Jayasimhadri**, T.Sasikala<sup>3</sup> and L. Rama Moorthy
7. Performance Analysis of MIMO Network Coding with SISO Physical-Layer Network, Alpana Sahu, **#Rajveer Mittal**
8. PROTECTION OF FLOOD EMBANKMENTS BY SPURS WITH REFERENCE TO KOSI RIVER, **#S.K. MAZUMDER**
9. Realization of AND gate in Y shaped photonic crystal wave guide, Preeti Rani,**\*Yogita Kalra** and **\*R.K.Sinha**
10. Synthesis and Luminescent Features of NaCaPO<sub>4</sub>: Tb<sup>3+</sup> Green Phosphor for near UV-based LEDs, B. V. Ratnam, **\*M. Jayasimhadri**, G. Bhaskar Kumar, Kiwan Jang, S. S. Kim, Y. I. Lee, J. M. Lim, D. S. Shin and T. K. Song

**\* Faculty**

**# Alumni**

# A Research Review of Power Quality Problems in Electrical Power System

**Anurag Agarwal**

Electrical & Electronics and  
Instrumentation Department  
MIT, Moradabad (UP), INDIA

**Sanjiv Kumar**

Delhi Technological University  
Delhi, INDIA  
Email: activesanjiv007@rediffmail.com

**Sajid Ali**

Electrical Department  
MIT, Meerut (UP), INDIA  
Email: sajidali.ali01@gmail.com

## ABSTRACT

Power quality issues have become important to electricity consumers at all levels of usage. Sensitive equipment and non-linear loads are now more commonplace in both the industrial commercial sectors and the domestic environment. The dominant application of electronics today is to process information. The computer industry is the biggest user of semiconductor devices, and consumer electronics. Due to the successful development of semiconductors, electronic system and controls have gained wide acceptance in power, information and computing technology and due to the continuous use of drive systems (rotating machines, controlling thyristor and associated electronic components) in industry and in power stations, and the need to keep such systems running reliably, electronic equipment are becoming an integral part of today's industrial, institutional, and commercial facilities. Unfortunately, the same type of equipment often generates power supply disturbances, which in turns affect other items of equipment, and are more likely to generate the distorting harmonics. These harmonics can cause power to be used inefficiently and can be a source of premature equipment failure that will halt production in industrial processing, will result in loss of life in hospitals, data processing activities in real time such as banking transaction processing may be lost, etc. The principal aim of this paper is to investigate the most common power quality problems, the effect of the harmonics on the power quality, the ways of evaluating the amount of harmonic distortion present in a power system which lead to isolate the cause of the problem and finally device a solution for a good power quality.

**Keywords:** Power quality, monitoring equipments, mitigation techniques.

## I. INTRODUCTION

Power quality problem in the power system has gained importance since the late 1980s. The interest in Power Quality (PQ) is related to all three parties concerned with the power i.e. utility companies, equipment manufacturers and electric power consumers. Problems affecting the electricity supply that were once considered tolerable by the electric utilities and users are now often taken as a problem to the users of everyday equipment. Understanding power quality can be confusing at best. There have been numerous articles and books concerning power quality[10]. There are two terms known in power systems about the quality of power: Good power quality and poor power quality. Good power quality can be used to describe a power supply that is always available, always within the voltage and frequency tolerances and has a pure noise-free sinusoidal wave shape to all equipment, because most equipment was designed on that basis[13]. Unfortunately, most of the equipment that is manufactured also distorts the voltage[12] on the distribution system, leading to what is known as poor power quality. And thus affecting other

equipment that was designed with the expectation of consistent undistorted voltage, and are thus sensitive[11] to power disturbances resulting in reduced performance and will cause equipment miss operation or premature failure. The cost of power quality problems can be very high and include the cost of downtimes, loss of customer confidence and, in some cases, equipment damage. Indeed, power quality is an important point in the relationship between suppliers and consumers[12] but might become a contractual obligation that stress on improving voltage quality, availability, performance[8] and efficiency and these improvements will have: Benefits for industrial customers (customized and flexible availability) and for suppliers utilities.

## II. CLASSIFICATION AND IMPACT OF PQ PROBLEMS

To make the study of Power Quality problems useful, the various types of disturbances need to be classified by magnitude and duration.

## 2.1 Undervoltages

Short duration under-voltages are called “Voltage Sags” or “Voltage Dips [IEC]”. Voltage sag [17, 18] is a reduction in the supply voltage magnitude followed by a voltage recovery after a short period of time. Excessive network loading, loss of generation, incorrectly set transformer taps and voltage regulator malfunctions, causes under voltage. Loads with a poor power factor or a general lack of reactive power support on a network also contribute. Under voltage can also indirectly lead to overloading problems as equipment takes an increased current to maintain power output (e.g. motor loads).

## 2.2 Voltage Dips

The major cause of voltage dips on a supply system is a fault on the system, i.e. sufficiently remote electrically that a voltage interruption does not occur. Other sources are the starting of large loads and, occasionally, the supply of large inductive loads [18]. The impact on consumers may range from the annoying (non-periodic light flicker) to the serious (tripping of sensitive loads and stalling of motors).

## 2.3 Voltage Surges/Spikes

Voltage surges/spikes are the opposite of dips – a rise that may be nearly instantaneous (spike) or takes place over a longer duration (surge). These are most often caused by lightning strikes and arcing during switching operations on circuit breakers/contactors (fault clearance, circuit switching, especially switch off of inductive loads).

## III. FREQUENCY VARIATIONS

Frequency variations that are large enough to cause problems are most often encountered in small isolated networks, due to faulty or maladjusted governors. Other causes are serious overloads on a network, or governor failures, though on an interconnected network, a single governor failure will not cause widespread disturbances of this nature.

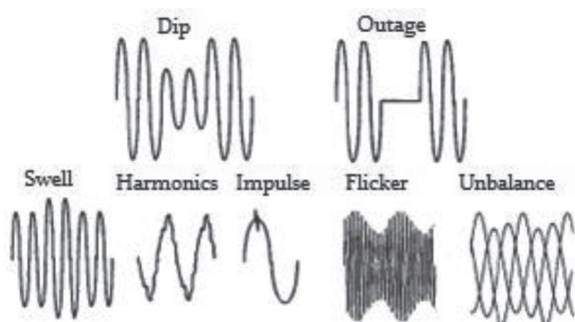


Figure 1: Different Problems encountered with PQ

## 3.1 Causes of Power Quality Problems

In today's fast-paced environments, a huge amount of money is spent on state of the art computer controlled equipment and systems. These systems are often installed in “unfriendly”

electrical environments, which cause owners, industrial companies and investors a great deal of frustration and disappointment and in many cases, result in a great loss of time and money, and that lead us to ask a valuable question “What is the problem?” The answer to this question could have one or more of the following points:

- Computer malfunctions
- Interrupted manufacturing sequences
- Catastrophic failures
- Erratic equipment behaviour
- High electrical maintenance cost.

But whatever the answer is, Chapman [7] has classified them as a power quality problems and the latter is subdivided into two categories:

- Supply system quality problems.
- Installation and load related problems.

## 3.2 Supply System Quality Problems

- Supply interruption
- Transient interruption
- Transients
- Undervoltage/over voltage
- Voltage dip/voltage surge
- Voltage imbalance
- Flicker
- Harmonic distortion

According to Douglas et al. [6] the above problems can be classified into one of three disturbance categories based upon duration: Transient disturbances include unipolar Transients, oscillatory transients (such as Capacitor switching), localized milliseconds. Transients can originate internally within the building or externally on utility power lines. They represent about 12 to 15% of all power line problems. These Disturbances can cause:

- Damage to electronic lighting systems
- Shutdown to sensitive equipment
- Immediate or latent damage to digital
- Microprocessor controlled equipment.

Monetary disturbances are voltages increases or decreases (sags, swells, and interruptions) lasting more than 10 milliseconds but less than three seconds. The majority of voltage sags result on utility lines from faults on the Distribution or transmission lines and they represent about 60% of all power problems. Voltage swells are the least frequent of the Power line problems representing about 2 to 3% of all power problems occurring to industry studies [10].

These momentary disturbances can cause:

- Sudden decrease in line loads
- losing wiring
- Re-energizing of power after a utility power

Interruption, when power comes back in. Steady-state disturbances are voltage increases or decreases (under voltages, over voltages, and interruptions). Interruptions and power outages can originate from electrical short circuits in Building wiring or on utility power lines. These interruptions will cause electrical, computer and electronic equipments shut down and losses in operations and revenues.

### 3.3 Installation and Load Related Problems

The major problems in this category can be classified [5] in one of the three following groups:

- Harmonic currents
- Earth (Ground) leakage currents
- Voltage dips and transients

#### 3.3.1 Harmonic Currents

These currents will cause wiring, motors and transformers to overheat. The result may be a breakdown of insulation and a significant reduction of equipment lifespan. Some of the adverse effects of concentrated nonlinear loads upon a facility are:

- Nuisance tripping of circuit breakers
- Overvoltage problems
- Metering problems
- Overheating of transformers and induction motors'
- Computer malfunctions
- Metering problems
- High levels of neutral-to-ground voltage
- Power factor rate penalties

All non-linear loads generate harmonics. This includes all loads, which use switching to control or convert power, for example:

- Switched mode power supplies— computers, office equipment, domestic equipment:
- Variable speed motor drives
- Thyristor controlled heating elements
- Dimmer switches
- Solid state fluorescent lamp ballasts
- Over loading magnetic devices such as motors, lamp ballast and transformers as a result of saturation of the magnetic core material.

#### 3.3.2 Earth Leakage Currents

The principal design consideration for an earthing system is that it must protect people and animals from receiving potentially fatal electric shocks in the event of a fault condition. Now, earth conductors are carrying large leakage current permanently as well as serving as a sink for high frequency noise currents. If for any reason the connection to earth is poor, then the impedance of the primary earth route will be high and

earth Leakage currents will seek alternative routes to earth. This may result in current flowing in unexpected places with consequent risk should the system be disconnected.

#### 3.3.3 Voltage Dips, Flat Topping and Transients

Heavy loads such as air conditioning systems, large motors during the starting process, principally cause Dips. However, flat topping is caused by electronic equipment such as the start -up of printers. The combination of surges and dips in the voltage lead to what is known as voltage Flicker and this latter is caused by the operation of large cyclic loads and can reduce the life of motors drives and electrical contacts.

## IV. OBJECTIVE OF A POWER QUALITY SURVEY

The power quality survey is the first, and perhaps most important, step in identifying and solving power problems cited previously. In other words it is thus designed to locate, identify and eliminate the electrical disturbances which disrupt data collection networks, PLCs, variable speed motor drives thyristor controlled heating elements and other sensitive electronic equipment that contain some 162 form of microchip or "logic circuits". There are two types of power quality surveys: The first type is a preventative survey, uses a Number of tests and inspections to locate potential Problems before they cause a production outage. The second type is, a troubleshooting survey, it is used to locate and eliminate problems as quickly as possible after a production outage. Whether the investigation involves a simple piece of equipment or the facility's entire electrical system, the survey process typically requires the following steps [6].

- Planning and preparing the survey
- Inspecting the site
- Monitoring the power
- Analysing the monitoring and inspection data
- Applying corrective solutions.

From the above steps, the survey should provide the background information and basic methodology and tools required to benchmark the power quality performance and improve the reliability with respect to interruptions. Thus, the process basically involves finding out the What, Where, When, How and Why of the power related Problems at hand. Monitor requirements[3,4]: what are the requirements or what are the specific equipment resources needed, to get the job done. Where to monitor: depends on where the Problems are observed or suspected. When to monitor: The time when the problem occurs can also provide important clues about the nature of the power problem. If the problem occurs at a certain time of day, the equipment switched on at that time should be suspect. The monitoring period should last at least as long as one "business Cycle," which is how long it takes for the process in the facility to repeat itself.

- How long to monitor.
- Data collection and analysis systems.
- Indices for describing performance.
- Results of other benchmarking efforts from around the world.
- Other benefits of the bench marking effort. As part of the planning and preparation process it is necessary to obtain a site history for the facility of equipment being investigated. Asking questions of equipment operators or others familiar with operations is an important part of a site history.

#### 4.1 Inspecting the Site

The site examination begins by visually inspecting outside the facility and around the immediate vicinity in order to gain a better perspective of the utility service area. Inspecting the facility helps to identify equipment that might cause interference. It will also surface electrical distribution system problems such as broken or corroded conduits, hot or noisy transformers, poorly fitted electrical panel covers and more. Any inspection should include a physical review of the wiring from the critical load to the electrical service entrance and any loads, which might cause power problems, will be identified.

#### 4.2 Monitoring the Power

To solve a power problem for a single unit of equipment, the monitor should be placed as close to the load as possible. Looking for a power quality problem, need that voltage signal is monitored and finally to find the cause, accurate measurement of power quality issues requires that the monitor accurately [4] measure the voltage and current waveforms.

#### 4.3 Analyzing the Monitoring and Inspection Data

To identify equipment problems, it is key to analyse data in a systematic manner. First, look for power events that occurred during intervals of equipment malfunction. Second, identify power events that exceed performance parameters for the affected equipment. Third, review power monitor data to identify unusual or severe events. Finally, correlate problems found during the Physical inspection with equipment symptoms.

### V. SOLUTIONS

#### 5.1 Solutions to Supply System Quality Problems

The potential solutions for such problems are dependent on the type of disturbance. However, for the voltage disturbances, such as momentary outage, sags and swells and transient voltages, the most convenient solutions to improve the performance of a sensitive equipment is to install a protective device between the power source and sensitive equipment. There is a wide variety of protective devices [1,2], each device

has a different problem solving function and can be used in a variety of applications. Voltage regulators are installed between the power source and sensitive equipment to control the incoming voltage in order to sustain a constant output voltage, it protects the equipment against overvoltage's and under voltages. However, Transient Voltage Surge Suppressors (TVSS) cuts noise and voltage transients only, and it does not regulate voltage to limit surges and sags.

#### 5.2 Solution of Harmonic Problems

With current technology, virtually all of today's high performance electronic equipment uses static power rectifiers, which convert alternating current to direct current, and the reverse. It pulls a non-linear current and the latter induces voltage distortion and when 163 distorted voltage is delivered to equipment designed to expect a sinusoidal voltage, the result is overheating or malfunctions. Harmonic currents are a fact of life and cannot be eliminated unless nonlinear loads are avoided, all industry is increasingly exposed. Although future developments may provide improved electronic systems producing lower levels of harmonics, the problem must be addressed in current and future installations. Since harmonic currents cannot be prevented, installations must be designed to cope with them. Utility companies impose limits on the Harmonic voltage distortion, which a customer's site can impose on the system. Where the utility limits are exceeded, special additional steps must be taken to filter the harmonic content. Active harmonic filters] are now becoming available which inject an exactly complimentary harmonic current into the supply to cancel that produced by the non-linear loads. Harmonic filters will provide a solution, although all ramifications of their use may not be anticipated in advance. Filters types include line-reactors, passive harmonic filters, active harmonic filters, electronic feedback filters and special transformers that use out of phase windings to accomplish harmonic reduction] While these units are effective at reducing the harmonic current as seen by the utility, they do not reduce the harmonic current flowing in the cables of the installation. According to Martin[5] practicing the following measures minimizes the effect of harmonics: Take account of harmonic generating loads when planning the installation.

- Reduce the number of socket outlets on each circuit and increase the number of circuits.
- Carefully distribute these circuits among the phases to reduce out of balance currents.
- Increase the cross sectional area (CSA) of feeders.
- Two sizes up is a good rule of thumb with a sound technical justification— and it saves energy too!
- Increase the CSA of neutral feeders and distribution panels - twice the phase CSA is recommended. The old practice of using half sized neutrals is definitely no longer satisfactory!
- Uses 5 core copper cable—one core for each phase and two for the neutral. Keep circuits, which supply harmonic generators- such as office equipment and variable speed

drives separate from those supplying harmonic hating Loads such as induction motors:

- Maintain records of cable layout and usage.
- Maintain and upgrade the system carefully.
- Consult the relevant records before making changes.
- Routinely monitor neutral and phase currents.
- Check for excessive heating in transformers, motors and distribution boards.

### 5.3 Solution of Earth Leakage Problems

The primary purpose of grounding electrical systems is to protect personnel and property if a fault (short circuit) were to occur. The second purpose of a grounding system is to provide a controlled, low impedance path for lightning induced currents to flow to the earth harmlessly. Problems can be avoided if it is recognized that the grounding system in electrical installations is no longer designed solely for fault conditions. Wherever modern electronic equipment is used, the earth acts as a key working component of the electrical installation. As such, it must be given equal consideration in terms of:

- Impedances
- Connections
- Documentation
- Working practices

## VI. MITIGATION EQUIPMENTS

Mitigation equipment exists for each of the above power-quality problems. Some of this equipment are listed below:

### 6.1 Thyristor-Based Static Switch

The static switch is a versatile device for switching a new element into the circuit when voltage support is needed. To correct quickly for voltage spikes, sags, or interruptions, the static switch can be used to switch in one of the following:

- Capacitor
- Filter
- Alternate power line
- Energy storage system.

The static switch can be used in the alternate power line application. This scheme requires two independent power lines from the utility. It protects against 85% of the interruptions and voltage sags.

### 6.2 Energy Storage Systems

Storage systems can be used to protect sensitive production equipment from shutdowns caused by voltage sags or momentary interruptions. These are usually dc storage systems, such as UPS, batteries, superconducting magnet energy storage (SMES) [23], storage capacitors etc. The output of

these devices is supplied to the system through an inverter on a momentary basis by a fast acting electronic switch. Enough energy is fed to the system to replace the energy that would be lost by the voltage sag or interruption.

### 6.3 Filters

Initially, lossless passive filters (LC) have been used to reduce harmonics, and capacitors have been chosen for power-factor correction of nonlinear loads. Active filters (AFs) [24, 25] have been explored in shunt and series configurations to compensate for different types of non-linear loads. These are shunt-connected devices used to eliminate harmonics. Either passive (LC or RLC) networks or active (voltage source converter) technologies are possible.

### 6.4 Static Var Compensators (SVCS)

This is a shunt-connected assembly of capacitors, and possibly reactors, which provides reactive power to a network during disturbances to minimize them. It is normally applied to transmission networks to counter voltage dips/surges during faults and enhance power transmission capacity on long transmission circuits.

## VII. CONCLUSIONS

The present paper gives an assessment of power quality. Various issues concerning PQ have been highlighted and discussed. The paper also discusses about various issues related to power quality classification and characterization of disturbances, propagation of disturbances, and measurement strategies being used to monitor the power quality. Semiconductors are the heart of computer industry; unfortunately these electronic components are non-linear and thus may affect the safe or reliable operation of computers and computer-based equipment. Often more important than the physical effect on the equipment is the loss of productivity resulting from computer equipment failure, miscalculations and downtime. And thus changes in the equipment on site will change the harmonic Profile, so rendering the filters ineffective. Thus due to the technology and software now available, monitoring is highly-effective means to detect, solve, and even prevent problems on both utility and customer, it can detect problem conditions throughout the system before they cause equipment malfunctions, and even equipment damage or failure. However, before monitoring a design step is needed and should take into account the electrical environment and define how the electrical installation must meet the needs of the business.

## REFERENCES

- [1] M.B. Brennen and B. Banerjee, "Low cost, high performance active power line conditioners". *Proc. Conf. PQA 94*, Part 2, Amsterdam, The Netherlands, Oct. 24- 27, 1994.
- [2] J.M. Powell, "Power conditioning system and apparatus" U.S. Patent 4, 544, 877, Oct.1, 1985.

- [3] "Comprehensive monitoring—covering all aspects" <http://www.powerquality.com/art0031/art1.htm>
- [4] Dennis Stewart, "Cover Story: Power monitoring technology-Dispelling—metering myths" <http://www.powerquality.com/articles.html>
- [5] Marty Martin, "Common power quality problems and best practice solutions," Shangri-la Kuala Lumpur, Malaysia 14. August 1997.
- [6] Douglas S. Dorr, Thomas M. Gruz and James J. Stanislawski. "Interpreting recent power quality surveys to define the electrical environment", <http://www.powerquality.com/art0021/art1.htm>
- [7] David Chapman, "Electrical design—A good practice guide", CDA Publication 123, Dec. 1997.
- [8] D.D. Sabin and A. Sundaram, "Quality enhances reliability". IEEE Spectrum, Feb. 1996. 34-41.
- [9] N.G. Hingorani, "Introducing custom power," *IEEE Spectrum*, Jun. 1995, 41-48.
- [10] "Details of equipment sensitivity," <http://www.powerquality.com/pqpark/pqpk1052.htm>
- [11] A. Rash, "Power quality and harmonics in the supply network: a look at common practices and standards," in Proc. on MELECON' 98, Vol.2, pp.1219-1223, May1998.
- [12] R.C. Sermon, "An overview of power quality standards and guidelines from the end-user's point-of-view," in *Proc. Rural Electric Power Conf.*, pp. 1-15, May 2005.
- [13] IEC 61000-4-30, "Testing and measurement techniques—Power quality measurement methods," pp. 19, 78, 81, 2003.
- [14] EN 50160, "Voltage characteristics of electricity supplied by public distribution systems," 1999.
- [15] D.L. Brooks, R.C. Dugan, M. Wacziarg, A. Sundaram, "Indices for Assessing Utility Distribution System RMS Variation Performance," *IEEE Transactions on Power Delivery*, Vol.13, No. 1, Jan. 1998.
- [16] M.H.J. Bollen, *Understanding Power Quality Problems: Voltage Sags and Interruptions*, New York, IEEE Press, 1999.
- [17] E. Styvaktakis, M.H.J. Bollen, I.Y.H. Gu, "Classification of power system events: Voltage dips," 9th International IEEE Conference on Harmonics and Quality of Power, Orlando, Florida USA, Vol. 2, pp. 745- 750, October 1-4, 2000.
- [18] A. Domijan, G.T. Heydt, A.P.S. Meliopoulos, S.S. Venkata, S. West, "Directions of research on electric power quality," *IEEE Transactions on Power Delivery*, Vol. 8, pp. 429-436, 1993.
- [19] R.C. Dugan, M.F. McGranaghan, and H.W. Beaty, *Electric Power Systems Quality*, New York, McGraw-Hill, 1996.
- [20] J. Arrillaga, N.R. Watson and S. Chen, *Power system quality assessment*, John Wiley and Sons, 2000.
- [21] IEEE Working Group on Voltage Flicker and Service to Critical Loads, "Power Quality—Two Different Perspectives," presented at IEEE/PES 1900 Winter Meeting, Atlanta, GA, Feb. 1990.
- [22] IEEE Recommended Practice for Monitoring Electric Power Quality, IEEE Standard 1159– 1995.
- [23] H.J. Kim, K.C. Seong, J.W. Cho, J.H. Bae, K.D. Sim, S. Kim, E.Y. Lee, K. Ryu and S.H. Kim, "3 MJ/750 kVA SMES System for Improving Power Quality," *IEEE Trans. on Superconductivity*, Vol. 16, issue 2, pp. 574- 577, June, 2006.
- [24] W.M Grady, M.J. Samotyj, and A.H. Noyola, "Survey of active power line conditioning methodologies," *IEEE Trans. Power Delivery*, Vol. 5, pp. 1536–1542, 1990.
- [25] B. Singh, K. AL Haddad and A. Chandra, "A review of active filters for power quality improvement," *IEEE Trans. Ind. Electron.*, Vol. 46, pp. 960–970, 1999.

## Research Article

# Current Controlled Differential Difference Current Conveyor Transconductance Amplifier and Its Application as Wave Active Filter

Neeta Pandey,<sup>1</sup> Praveen Kumar,<sup>2</sup> and Jaya Choudhary<sup>1</sup>

<sup>1</sup> Department of Electronics and Communications, Delhi Technological University, Bawana Road, Delhi 110042, India

<sup>2</sup> Department of Electronics and Communications, IMS Engineering College, Ghaziabad, Uttar Pradesh-201009, India

Correspondence should be addressed to Neeta Pandey; [n66pandey@rediffmail.com](mailto:n66pandey@rediffmail.com)

Received 17 November 2012; Accepted 10 December 2012

Academic Editors: H. A. Alzahr and H.-C. Chien

Copyright © 2013 Neeta Pandey et al. This is an open access article distributed under the Creative Commons Attribution License, which permits unrestricted use, distribution, and reproduction in any medium, provided the original work is properly cited.

This paper proposes current controlled differential difference current conveyor transconductance amplifier (CCDDCCTA), a new active building block for analog signal processing. The functionality of the proposed block is verified via SPICE simulations using 0.25  $\mu\text{m}$  TSMC CMOS technology parameters. The usefulness of the proposed element is demonstrated through an application, namely, wave filter. The CCDDCCTA-based wave equivalents are developed which use grounded capacitors and do not employ any resistors. The flexibility of terminal characteristics is utilized to suggest an alternate wave equivalents realization scheme which results in compact realization of wave filter. The feasibility of CCDDCCTA-based wave active filter is confirmed through simulation of a third-order Butterworth filter. The filter cutoff frequency can be tuned electronically via bias current.

## 1. Introduction

The current mode approach for analog signal processing circuits and systems has received considerable attention and emerged as an alternate method besides the traditional voltage mode circuits [1] due to its potential performance features like wide bandwidth, less circuit complexity, wide dynamic range, low power consumption, and high operating speed. The current mode active elements are appropriate to operate with signals in current, voltage, or mixed mode and are gaining acceptance as building blocks in high performance circuit designs which is clear from the availability of wide variety of current mode active elements [2–10]. Recently some analog building blocks [11–16] based on current conveyor variants and transconductance amplifier (TA) cascades in monolithic chip are proposed in open literature which gives compact implementation of signal processing circuits and systems. The examples of such blocks are current conveyor transconductance amplifier (CCTA) [11, 12], current controlled current conveyor transconductance amplifier (CCCCTA) [13], differential voltage current

conveyor transconductance amplifier (DVCCCTA) [14], differential voltage current controlled conveyor transconductance amplifier DVCCCTA [15], and differential difference current conveyor transconductance amplifier (DDCCTA) [16].

A new active building block, namely, current controlled differential difference current conveyor transconductance amplifier (CCDDCCTA) which has current controlled differential difference current conveyor (CCDDCC) [10] as input block followed by a TA. The CCDDCCTA possesses all the good properties of CCCCTA and DVCCCTA including the possibility of inbuilt tuning of the parameters of the signal processing circuits to be implemented and also all the versatile and special properties of DDCC such as easy implementation of differential and floating input circuits [9, 17, 18]. The CCDDCCTA can be implemented using separate CCDDCC and OTA analog building blocks, but it will be more convenient and useful if CCDDCCTA is implemented in monolithic chip which will result in compact implementation of signal processing circuits and systems. The analytical formulations for port relationship of the proposed

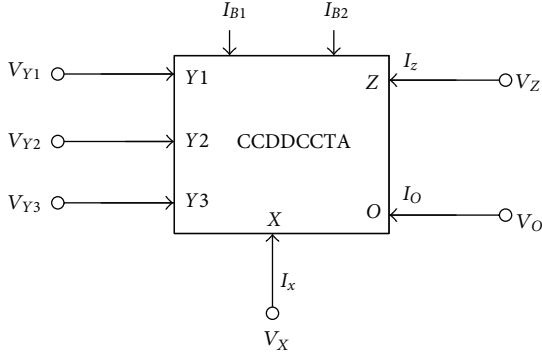


FIGURE 1: Schematic symbol of CCDDCCTA.

CCDDCCTA circuit are presented in Section 2. Section 3 elaborates the concept of wave filter followed by derivation of CCDDCCTA-based wave equivalent of series inductor. The methodology for obtaining wave equivalent of other passive elements is outlined. An alternate scheme for wave equivalents of shunt capacitor and inductor is also presented. A third order Butterworth filter has been designed using the outlined approach and is presented in Section 4 followed by conclusion. The functionality has been verified through SPICE simulation using 0.25  $\mu\text{m}$  TSMC CMOS technology parameters.

## 2. Proposed CCDDCCTA

The CCDDCCTA is an extension of CCDDCC [10] and consists of differential amplifier, translinear loop, and transconductance amplifier. The port relationships of the CCDDCCTA as shown in Figure 1 can be characterized by the following matrix:

$$\begin{bmatrix} I_{Y1} \\ I_{Y2} \\ I_{Y3} \\ V_X \\ I_Z \\ I_O \end{bmatrix} = \begin{bmatrix} 0 & 0 & 0 & 0 & 0 & 0 \\ 0 & 0 & 0 & 0 & 0 & 0 \\ 0 & 0 & 0 & 0 & 0 & 0 \\ 1 & -1 & 1 & R_x & 0 & 0 \\ 0 & 0 & 0 & 1 & 0 & 0 \\ 0 & 0 & 0 & 0 & -g_m & 0 \end{bmatrix} \begin{bmatrix} V_{Y1} \\ V_{Y2} \\ V_{Y3} \\ V_X \\ V_Z \\ V_O \end{bmatrix}, \quad (1)$$

where  $R_x$  is the intrinsic resistance at  $X$  terminal, and  $g_m$  is the transconductance from  $Z$  terminal to  $O$  terminal of the CCDDCCTA.

The CMOS-based internal circuit of CCDDCCTA in CMOS is depicted in Figure 2. The transistors  $M_1$  to  $M_{10}$  present differential difference voltage ( $V_{Y1} - V_{Y2} + V_{Y3}$ ) at gate terminal of  $M_6$ , and transistors  $M_{11}$  to  $M_{23}$  form translinear loop and transistors  $M_{24}$  to  $M_{31}$  are connected as transconductance amplifier. The analytical expressions for port relationships are obtained in the following sub sections.

**2.1. Relationship between Voltages of  $X$  Port and  $Y1$ ,  $Y2$ , and  $Y3$  Ports.** The analysis of the differential difference part and

translinear loop (comprising of transistors from  $M_1$  to  $M_{21}$ ) of the circuit of Figure 2 gives the voltage at  $X$  port as

$$V_X = \beta_1 V_{Y1} - \beta_2 V_{Y2} + \beta_3 V_{Y3} + \varepsilon_V + I_X R_X, \quad (2)$$

where  $R_X = 1/(g_{m16} + g_{m18})$

$$\begin{aligned} \beta_1 &= \frac{1}{P_1} \left( g_{m5} g_{m8} + \frac{g_{m5} (g_{m6} g_{m7} - g_{m5} g_{m8})}{g_{m5} + g_{m6}} \right), \\ \beta_2 &= \frac{1}{P_1} \left( g_{m2} g_{m7} + \frac{g_{m2} (g_{m2} g_{m7} - g_{m3} g_{m8})}{g_{m2} + g_{m3}} \right), \\ \beta_3 &= \frac{1}{P_1} \left( g_{m3} g_{m8} + \frac{g_{m3} (g_{m2} g_{m7} - g_{m3} g_{m8})}{g_{m2} + g_{m3}} \right), \\ \varepsilon_V &= \frac{I_B}{P_1} \left( \frac{g_{m2} g_{m7} - g_{m3} g_{m8}}{g_{m2} + g_{m3}} + \frac{g_{m6} g_{m7} - g_{m5} g_{m8}}{g_{m5} + g_{m6}} \right) \\ &\quad + \frac{I_{B1}}{g_{m16} + g_{m18}} \left( \frac{g_{m20} g_{m12} g_{m18}}{g_{m11} g_{m17} g_{m19}} - \frac{g_{m13} g_{m16}}{g_{m11} g_{m15}} \right), \\ P_1 &= g_{m6} g_{m7} - \frac{g_{m6} (g_{m6} g_{m7} - g_{m5} g_{m8})}{g_{m5} + g_{m6}}, \end{aligned} \quad (3)$$

where  $I_B$  represents the current flowing through transistor  $M_1$ ,  $M_4$ , and  $M_9$ . With matched transconductances  $g_{m2} = g_{m3} = g_{m5} = g_{m6}$  and  $g_{m7} = g_{m8}$ ,  $V_X$  is obtained as

$$V_X = V_{Y1} - V_{Y2} + V_{Y3} + I_X R_X. \quad (4)$$

**2.2. Relationship between Currents at  $Z$  and  $X$  Ports.** The analysis of the portion of the circuit comprising of transistors from  $M_{11}$  to  $M_{23}$  of the circuit of Figure 2 gives

$$I_Z = \alpha I_X + \varepsilon_1, \quad (5)$$

where

$$\begin{aligned} \alpha &= \frac{1}{g_{m16} + g_{m18}} \left( \frac{g_{m18} g_{m22}}{g_{m21}} + \frac{g_{m23} g_{m16}}{g_{m14}} \right), \\ \varepsilon_1 &= \left( \frac{g_{m12} g_{m20} g_{m18} g_{m22}}{g_{m11} g_{m17} g_{m19} g_{m21}} - \frac{g_{m13} g_{m16} g_{m23}}{g_{m11} g_{m14} g_{m15}} \right) \\ &\quad + \frac{1}{g_{m16} + g_{m18}} \left( \frac{g_{m18} g_{m22}}{g_{m21}} + \frac{g_{m23} g_{m16}}{g_{m14}} \right) \\ &\quad \times \left( \frac{-g_{m12} g_{m18} g_{m20}}{g_{m11} g_{m17} g_{m19}} + \frac{g_{m13} g_{m16}}{g_{m11} g_{m15}} \right) I_{B1}. \end{aligned} \quad (6)$$

For matched transistors, (6) reduced to

$$I_Z = I_X. \quad (7)$$

**2.3. Relation for Currents at  $O$  Port.** The transistor comprising from  $M_{24}$  to  $M_{31}$  forms transconductance amplifier (TA). Assuming gate voltages of transistors  $M_{24}$  and  $M_{25}$  as  $V_{T1}$  and  $V_{T2}$ , respectively, the output currents  $I_O$  may be found as

$$I_O = \gamma_1 V_{T1} - \gamma_2 V_{T2} + \varepsilon_2, \quad (8)$$

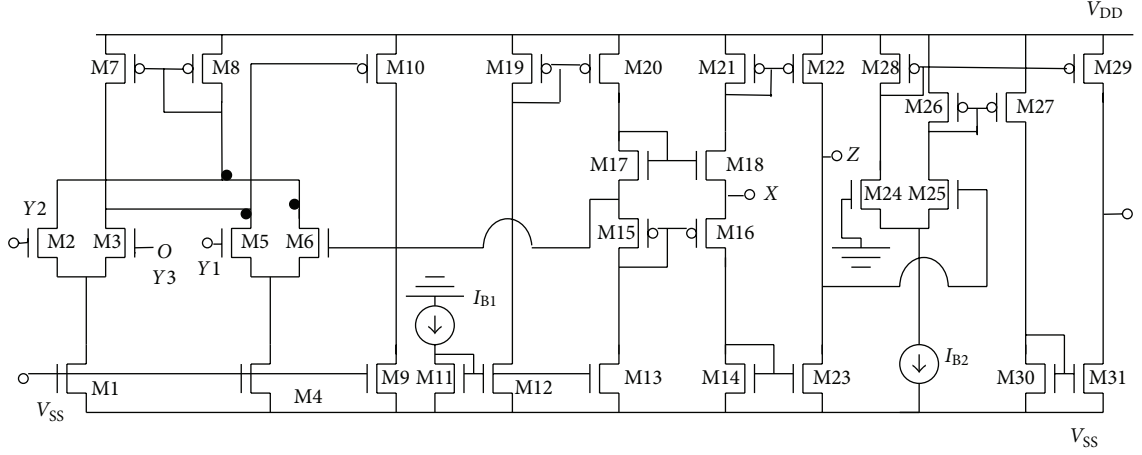


FIGURE 2: CMOS implementation of CCDDCCTA.

where

$$\gamma_1 = \frac{-1}{g_{m24} + g_{m25}} \left( \frac{g_{m24}g_{m25}g_{m29}}{g_{m28}} + \frac{g_{m24}g_{m25}g_{m27}g_{m31}}{g_{m26}g_{m30}} \right),$$

$$\gamma_2 = \frac{-1}{g_{m24} + g_{m25}} \left( \frac{g_{m24}g_{m25}g_{m29}}{g_{m28}} + \frac{g_{m24}g_{m25}g_{m27}g_{m31}}{g_{m26}g_{m30}} \right),$$

$$\varepsilon_2 = \frac{I_{B2}}{g_{m24} + g_{m25}} \left( \frac{-g_{m24}g_{m29}}{g_{m28}} + \frac{g_{m25}g_{m27}g_{m31}}{g_{m26}g_{m30}} \right). \quad (9)$$

With  $g_{m24} = g_{m25} = g_m$ ,  $g_{m26} = g_{m27}$ ,  $g_{m28} = g_{m29}$ , and  $g_{m30} = g_{m31}$ , (8) reduced to

$$I_O = g_m V_{T1} - g_m V_{T2}, \quad (10)$$

as  $V_{T1} = 0$  and  $V_{T2} = V_Z$

$$I_O = -g_m V_Z, \quad (11)$$

where

$$g_m = \sqrt{2\mu C_{OX} \left( \frac{W}{L} \right)_{24,25} I_{B2}}. \quad (12)$$

**2.4. Simulation.** To verify the port relationship of proposed CCDDCCTA, PSPICE simulations have been carried out using TSMC 0.25  $\mu\text{m}$  CMOS process model parameters. The aspect ratio of various transistors for CCDDCCTA is given in Table 1. The supply voltages of  $V_{DD} = -V_{SS} = 1.25\text{ V}$  and  $V_{BB} = -0.8\text{ V}$  are used. The DC transfer characteristics of the proposed CCDDCCTA from Y1, Y2, and Y3 terminals to X terminal are shown in Figure 3. The variation of current at Z terminal with X terminal current is shown in Figure 4. Figures 3 and 4 verify the port relationships. The variation of resistance,  $R_X$  with respect to bias current  $I_{B1}$ , is shown in Figure 5. The transconductance of CCDDCCTA is bias current controllable which is depicted in Figure 6 by varying  $I_{B2}$  from 0 to 800  $\mu\text{A}$ . There is decrease in transconductance for bias currents larger than 400  $\mu\text{A}$ . This is due to transistors  $M_{24}$ ,  $M_{25}$  entering in linear region of operation from saturation region.

TABLE 1: Aspect ratio of various transistors.

Transistors	$W (\mu\text{m})/L (\mu\text{m})$ ratio
$M_1, M_4, M_9, M_{11}-M_{14}, M_{23}$ , and $M_{30}-M_{31}$	3.0/0.25
$M_2-M_3, M_5-M_6$	1.0/0.25
$M_7-M_8$	5.0/0.25
$M_{10}$	12.5/0.25
$M_{15}$	8.0/0.25
$M_{16}$	9.0/0.25
$M_{18}$	4.5/0.25
$M_{27}$	4.35/0.25
$M_{17}, M_{19}-M_{22}, M_{24}-M_{25}, M_{26}$ , and $M_{28}-M_{29}$	5.0/0.25

### 3. CCDDCCTA's Application as Wave Active Filter

In this section the proposed CCDDCCTA has been used to develop higher-order filter. There are many schemes for simulating higher order filters using doubly terminated lossless ladders available in the literature. The element replacement, operational simulation, and impedance scaling schemes employ mostly lossless integrator which is not easy to implement in integrated circuits due to active and passive element imperfections. Recently, wave approach based ladder filter realization has received attention which relies on modelling incident and reflected voltage waves. It utilizes only lossy integrators for passive component representation and results in a very modular structure. Considering this, some wave active filters have been reported in the literature [19–22]. The wave active filter realization using proposed CCDDCCTA is presented in this section which has the following advantageous features.

- (i) It does not use any resistor in contrast to those proposed in [19–21].
- (ii) It uses only active elements and capacitors similar to [22].

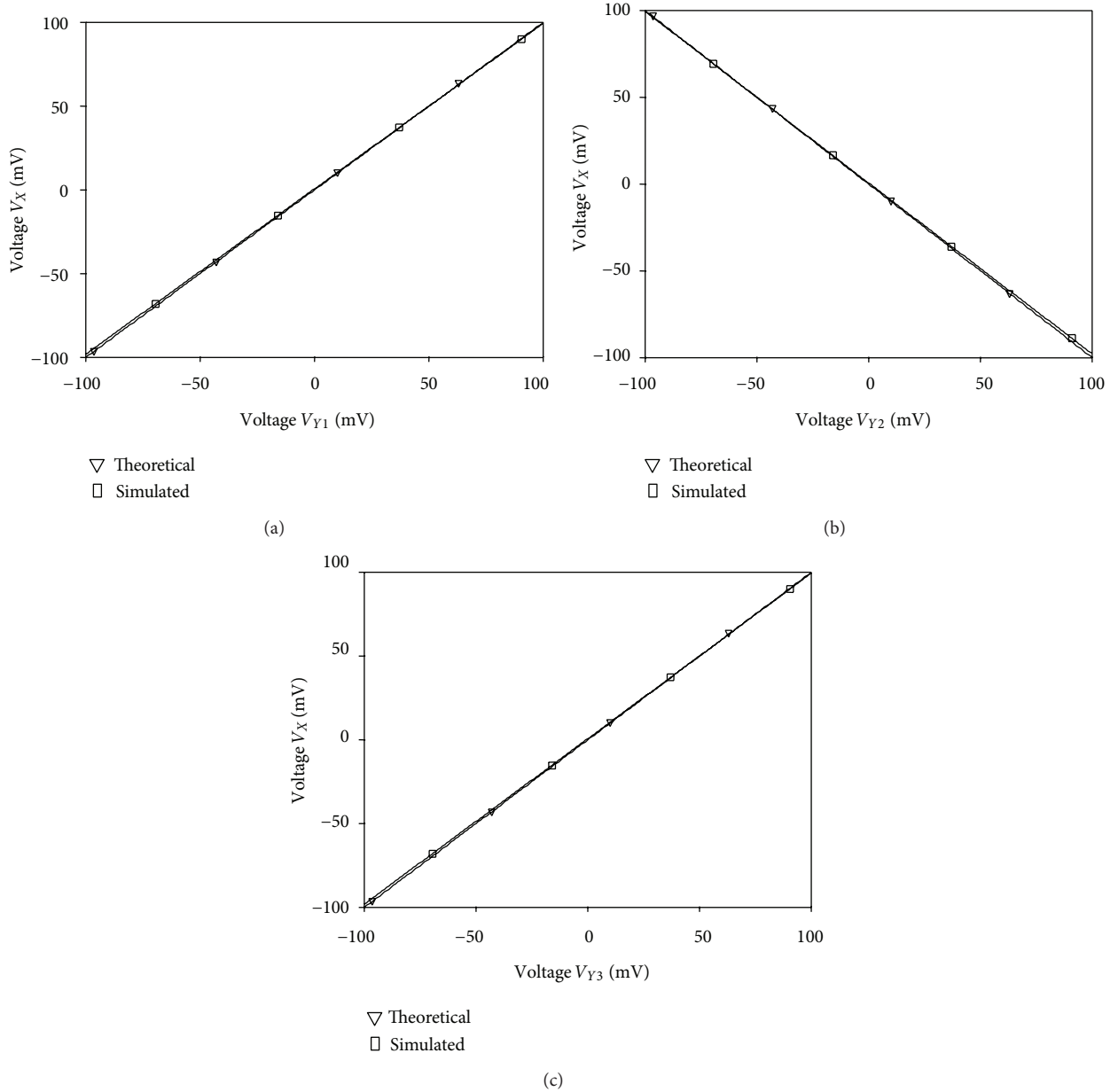


FIGURE 3: DC transfer characteristic for voltage transfer from (a) Y1 port to X port, (b) Y2 port to X port, and (c) Y3 port to X port.

- (iii) It possesses an attractive feature of electronic tunability via bias currents of CCDDCCTA similar to the reported in [22].
- (iv) The availability of an additional voltage input terminal in CCDDCCTA as compared to DVCCCTA, the active elements required for wave equivalent can be reduced. Thus, the proposed element gives a compact resistorless realization of wave filter than the one reported in [22].

**3.1. Derived Basic Wave Equivalent.** According to wave method, the corresponding LC ladder filter is split into two-port subnetworks which are fully described using the

wave variables, defined as incident and reflected waves. By choosing an inductor in a series branch as the elementary building block, its wave equivalent includes an appropriately configured lossy integrator. The wave equivalents of the other passive elements are derived by interchanging the terminals of the appropriate wave signals and signal inversion. Then each element of the passive prototype filter is substituted by its wave equivalent.

The development of the filter using wave method is based on modeling incident and reflected voltage waves. For a two-port network of Figure 7, the voltage wave is defined as

$$A_j = V_j + I_j R_j, \quad B_j = V_j - I_j R_j, \quad (13)$$

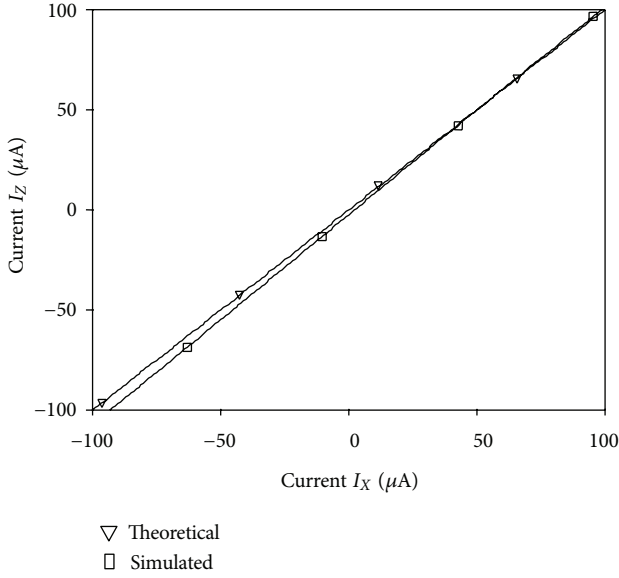


FIGURE 4: DC transfer characteristic for current transfer from X port to Z port.

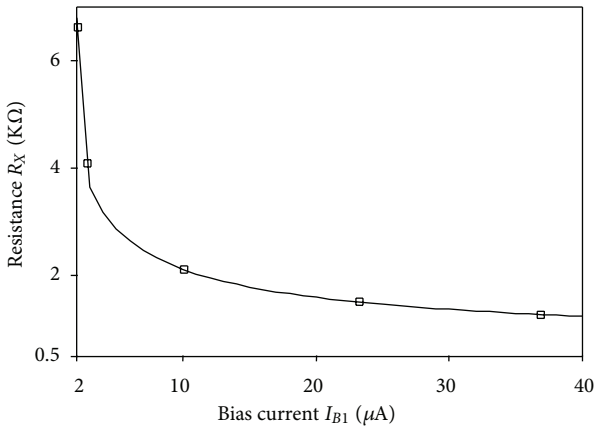


FIGURE 5: Variation of resistance with bias current  $I_{B1}$ .

where  $A_j$ ,  $B_j$ , and  $R_j$  ( $j = 1, 2$ ) represent incident and reflected voltage waves and port normalization resistance of port  $j$ , respectively.

Equation (13) can be expressed in terms of scattering matrix  $S$  as

$$\begin{bmatrix} B_1 \\ B_2 \end{bmatrix} = S \begin{bmatrix} A_1 \\ A_2 \end{bmatrix}. \quad (14)$$

The ladder network may be viewed in terms of its constituent series-arm impedance elements and shunt-arm admittance elements [19, 20], and the scattering matrices

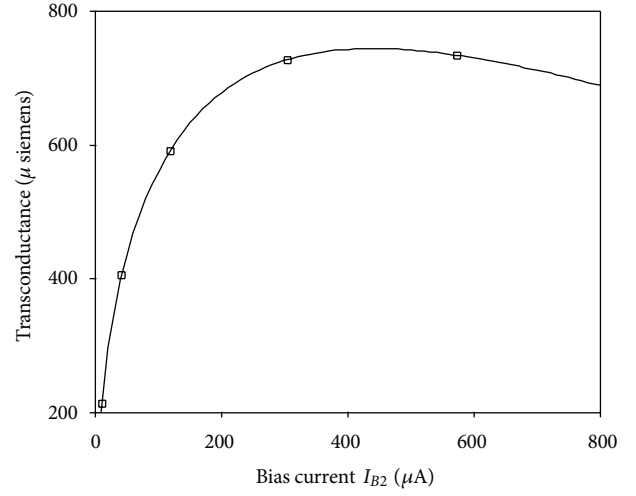


FIGURE 6: Variation of transconductance with bias current  $I_{B2}$ .

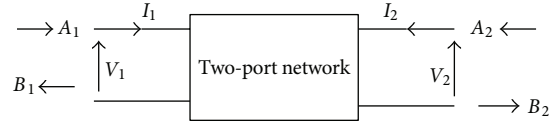


FIGURE 7: Two-port network with wave variables.

( $S_Z$  and  $S_Y$ ) [20] for series-arm impedance ( $Z$ ) and shunt-arm admittance ( $Y$ ) are represented as

$$S_Z = \begin{bmatrix} \frac{Z}{2R + Z} & \frac{2R}{2R + Z} \\ \frac{2R}{2R + Z} & \frac{Z}{2R + Z} \end{bmatrix}, \quad (15)$$

$$S_Y = \begin{bmatrix} \frac{-Y}{2G + Y} & \frac{2G}{2G + Y} \\ \frac{2G}{2G + Y} & \frac{-Y}{2G + Y} \end{bmatrix}, \quad (16)$$

where  $R$  is port normalization resistance, and  $G$  is its reciprocal.

The series inductor  $L$  is considered as a basic element for the wave active filter realization. Its scattering matrix ( $S_{Z,L}$ ) may be obtained from

$$S_{Z,L} = \frac{1}{1 + s\tau} \begin{bmatrix} s\tau & 1 \\ 1 & s\tau \end{bmatrix}, \quad (17)$$

where  $\tau = L/2R$  represents time constant.

Using (14) and (17), the reflected wave ( $B_j$ ,  $j = 1, 2$ ) for a series inductor can be expressed in terms of its incident wave ( $A_j$ ,  $j = 1, 2$ ) as

$$B_1 = A_1 - \frac{1}{1 + s\tau} (A_1 - A_2), \quad (18)$$

$$B_2 = A_2 + \frac{1}{1 + s\tau} (A_1 - A_2). \quad (19)$$

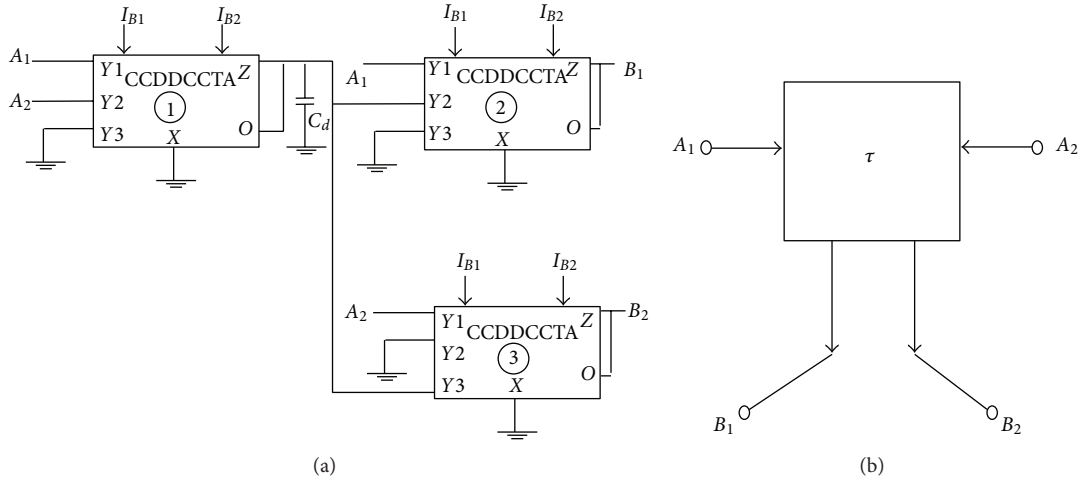


FIGURE 8: (a) Complete schematic of CCDDCCTA-based wave equivalent of series inductor and (b) its symbolic representation.

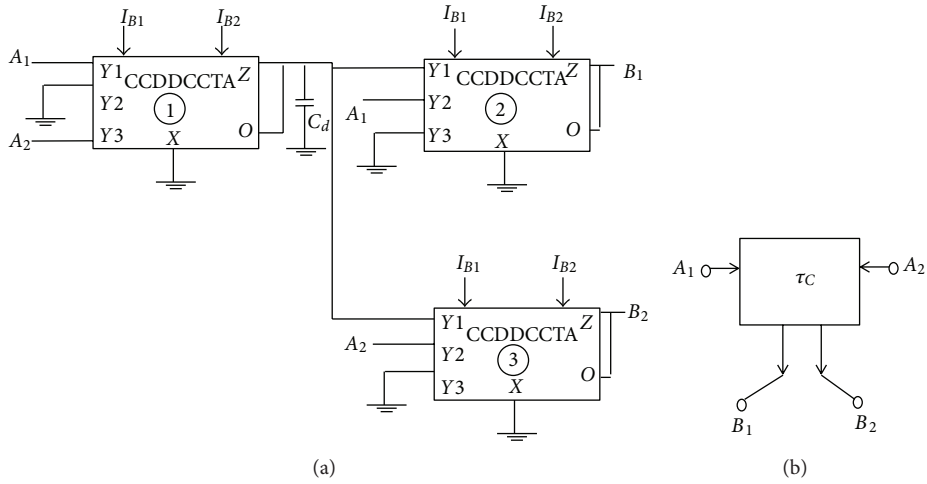


FIGURE 9: (a) Complete schematic of CCDDCCTA-based wave equivalent of shunt capacitor and (b) its symbolic representation.

The circuit implementation of (18) is derived by cascading lossy integration subtraction with subtraction, whereas (19) requires a lossy integration subtraction followed by an adder. The complete realization is depicted in Figure 8. The CCDDCCTA marked as “1” in Figure 8(a) performs lossy integration subtraction and provides output voltages  $V_1$  as

$$V_1 = (A_1 - A_2) \frac{1}{1 + s\tau}, \quad (20)$$

where  $\tau = R_X C_d$  is time constant and  $g_m R_X = 1$ . Using (18), (19), and (20), the value of  $C_d$  may be computed as

$$R_X C_d = \frac{L}{2R}. \quad (21)$$

With  $R = R_X$ , the value of capacitor  $C_d$  may be expressed as

$$C_d = \frac{L}{2R^2}. \quad (22)$$

The CCDDCCTAs marked as “2” and “3” in Figure 8(a) perform subtraction and addition operations and provide the output voltages as

$$B_1 = A_1 - V_1 = A_1 - \frac{1}{1 + s\tau} (A_1 - A_2) \text{ with } g_m R_X = 1,$$

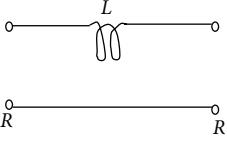
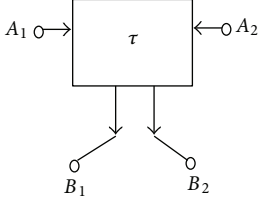
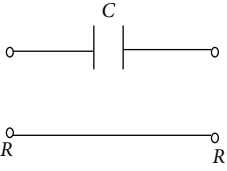
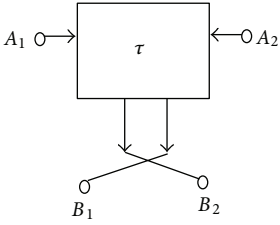
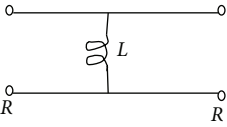
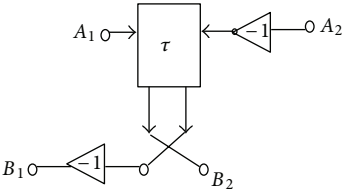
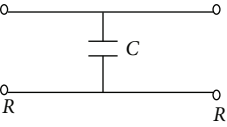
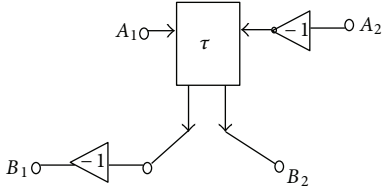
$$B_2 = A_2 + V_1 = A_2 + \frac{1}{1 + s\tau} (A_1 - A_2) \text{ with } g_m R_X = 1. \quad (23)$$

The symbolic representation of the wave element is shown in Figure 8(b) [19–22].

The wave equivalent of other reactive elements can be obtained using the basic wave equivalent of Figure 8. The wave equivalent for inductor and capacitor in series and shunt branches is given in Table 2 which can be obtained by swapping outputs and signal inversion.

**3.2. Alternate Scheme for Shunt Impedance Realization.** An alternate scheme for wave equivalent realization of shunt

TABLE 2: Wave equivalent of elementary two-port network consisting of single element in series and shunt branch.

Elementary two-port network	Port connection	Realized time constant; capacitor value for CCDDCCTA-based wave equivalent
		$\tau = L/2R$ $C_d = L/2R^2$
		$\tau = 2RC$ $C_d = 2C$
		$\tau = 2L/R$ $C_d = 2L/R^2$
		$\tau = RC/2$ $C_d = C/2$

impedances is suggested in this section. This scheme is based on direct realization of port relation of shunt capacitor wave equivalent. It may be noted from Table 2 that shunt capacitor requires two inverters with a basic wave equivalent of Figure 8 amounting to a total of five CCDDCCTAs. Using (16), the incident ( $A_j, j = 1, 2$ ) and the reflected wave ( $B_j, j = 1, 2$ ) for a shunt capacitor are related through the following scattering matrix:

$$S_{Y.C} = \frac{1}{1 + s\tau_C} \begin{bmatrix} -s\tau_C & 1 \\ 1 & -s\tau_C \end{bmatrix}, \quad (24)$$

where  $\tau_C = RC/2$  is time constant. The expressions for reflected waves  $B_1$  and  $B_2$  become

$$\begin{aligned} B_1 &= -A_1 + \frac{1}{1 + s\tau_C} (A_1 + A_2), \\ B_2 &= -A_2 + \frac{1}{1 + s\tau_C} (A_1 + A_2). \end{aligned} \quad (25)$$

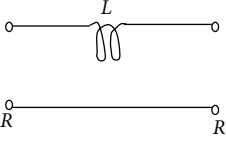
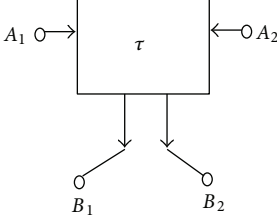
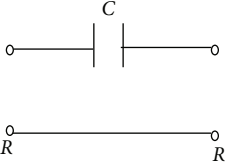
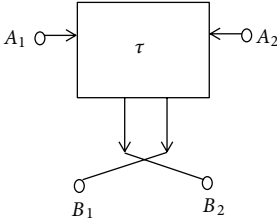
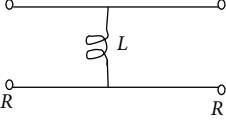
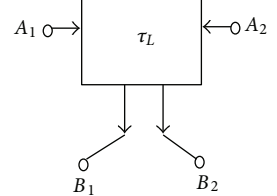
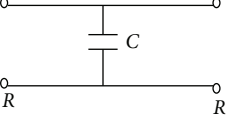
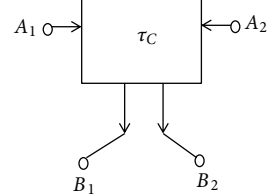
The implementation of (25) and (33) requires two operations-lossy integration addition and subtraction. The high impedance input terminal Y3 of CCDDCCTA can be used for lossy integration addition, and proper outputs are

obtained by feeding  $A_1$  and  $A_2$  to Y2 terminals of second and third CCDDCCTAs as shown in Figure 9(a). This realization may be represented by a symbol of Figure 9(b) for clarity. This slight modification in implementation method results in the saving of two CCDDCCTAs. Similar reduction of active element may be achieved for a shunt inductor as shown in Figure 10. The complete set of wave equivalents is summarized in Table 3. It may be noted that all the wave equivalents in Table 3 use only three active blocks. Thus, this method leads to a compact realization of wave active filter as compared to the one proposed in [22].

The design of wave active filter [19–22] starts with the selection of prototype filter based on specifications. The individual inductors or capacitors are replaced by their wave equivalents resulting in a modular realization. The complete filter schematic is then implemented by cascading the wave equivalents of the passive elements of prototype ladder.

**3.3. Simulation of Third-Order Butterworth Filter.** The theoretical proposition is verified using SPICE simulations using 0.25  $\mu\text{m}$  TSMC CMOS technology parameters and power supply of  $\pm 1.25$  V. The usefulness of the proposed CCDDCCTA is shown by implementing wave active filter based on

TABLE 3: Elementary two-port network consisting of single element in series and shunt branch using alternate scheme.

Elementary two-port network	Port connection	Realized time constant; capacitor value for CCDDCCTA-based wave equivalent
		$\tau = L/2R$ $C_d = L/2R^2$
		$\tau = 2RC$ $C_d = 2C$
		$\tau = 2L/R$ $C_d = 2L/R^2$
		$\tau = RC/2$ $C_d = C/2$

the method outlined in Sections 3.1 and 3.2. A third-order low-pass filter of Figure 11 has been taken as prototype. The normalized component values are  $R_s = 1$ ,  $L_1 = 1$ ,  $L_2 = 1$ ,  $C_1 = 2$ , and  $R_L = 1$  for maximally flat response.

The wave equivalent topology of Figure 11 may be constructed by replacing series inductor and shunt capacitor by wave equivalent of Table 3 and is shown in Figure 12. For cutoff frequency  $f_o = 10$  MHz, the bias currents  $I_{B1}$  and  $I_{B2}$  are taken as  $25 \mu\text{A}$  and  $200 \mu\text{A}$ , respectively. The capacitor values for wave equivalent of series inductors ( $L_1$ ,  $L_2$ ) and shunt capacitors ( $C_1$ ) are  $5.4 \text{ pF}$ ,  $5.4 \text{ pF}$ , and  $10.8 \text{ pF}$ , respectively. The topology of Figure 12 has been simulated using CCDDCCTA-based wave equivalent discussed in Section 3. Figures 13 and 14 show the simulated low pass responses ( $V_{\text{out}}$ ) and its complementary high-pass response ( $V_{\text{out},c}$ ), respectively. The tunability of the filter response by varying bias current  $I_{B1}$  from  $10 \mu\text{A}$  to  $50 \mu\text{A}$  and  $I_{B2}$  from  $50 \mu\text{A}$  to  $400 \mu\text{A}$  ( $I_{B2} = 8I_{B1}$  for  $g_m R_x = 1$ ) is also studied through simulations, and the results are shown in Figure 15. The power dissipation of the CCDDCCTA-based filter is simulated to be  $13.7 \text{ mW}$ , whereas TA-based wave filter power dissipation is found to be  $25.6 \text{ mW}$ .

To study the time domain behavior, input signal comprised of two frequencies of  $5 \text{ MHz}$  and  $20 \text{ MHz}$  is applied. Signal amplitude was  $50 \text{ mV}$  each. The transient response with its spectrum for input and output is shown in Figure 16, which clearly shows that the  $20 \text{ MHz}$  signal is significantly attenuated. The proposed circuit is also tested to judge the level of harmonic distortion at the output of the signal. The %THD result is shown in Figure 17 which shows that the output distortion is low and within acceptable limit of  $6\%$  up to about  $300 \text{ mV}$ .

#### 4. Conclusion

In this paper current controlled differential difference current conveyor transconductance amplifier (CCDDCCTA), a new active building block for analog signal processing, is presented. The expressions for port characteristics are derived and verified through SPICE. The wave filter based on CCDDCCTA is included to show the usefulness of the element. The CCDDCCTA-based wave equivalent of series inductor is introduced which is applied for other passive element realization by making suitable connections. The

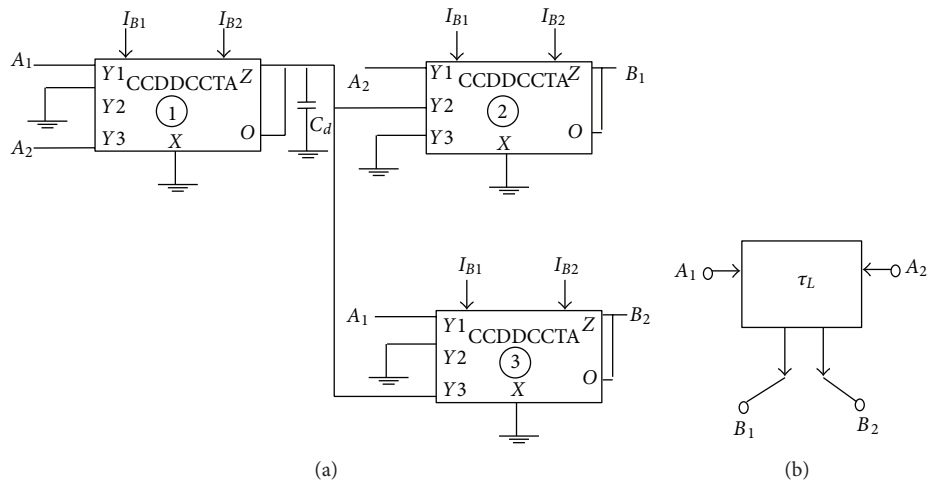


FIGURE 10: (a) Complete schematic of CCDDCCTA-based wave equivalent of shunt inductor and (b) its symbolic representation.

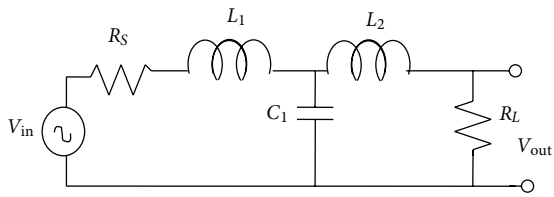


FIGURE 11: Third order low-pass Butterworth Filter.

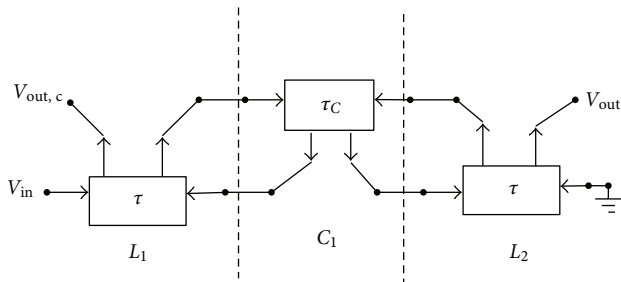


FIGURE 12: Wave equivalent of prototype filter.

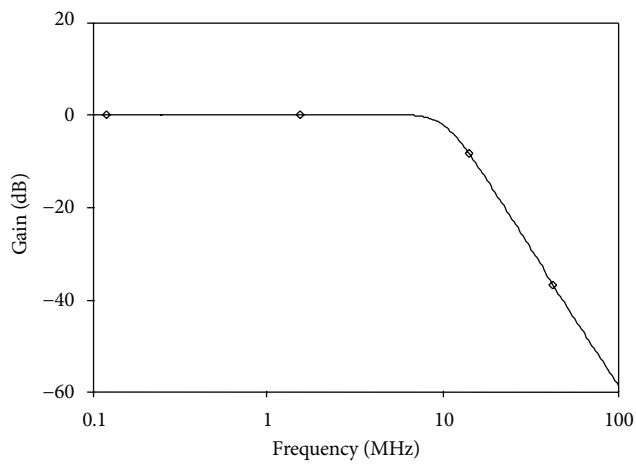


FIGURE 13: Frequency response of third order low-pass filter.

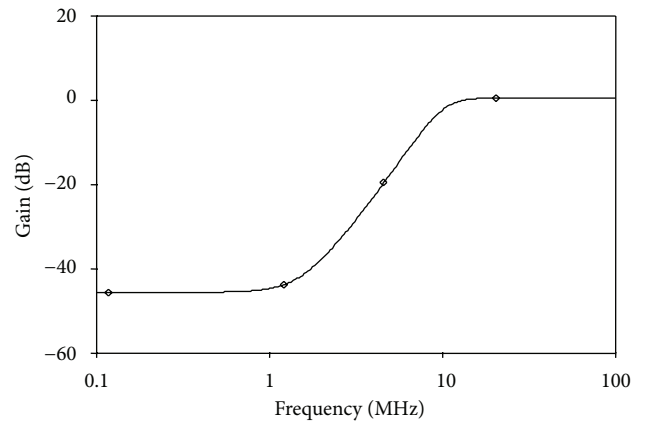


FIGURE 14: Frequency response of complementary high-pass filter.

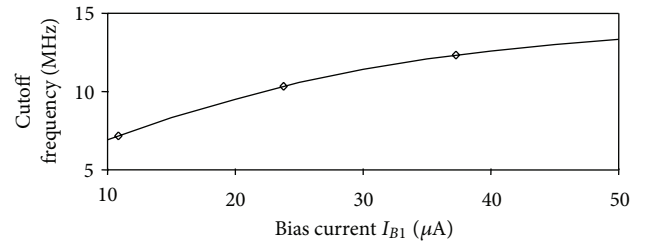


FIGURE 15: Demonstration of electronic tunability.

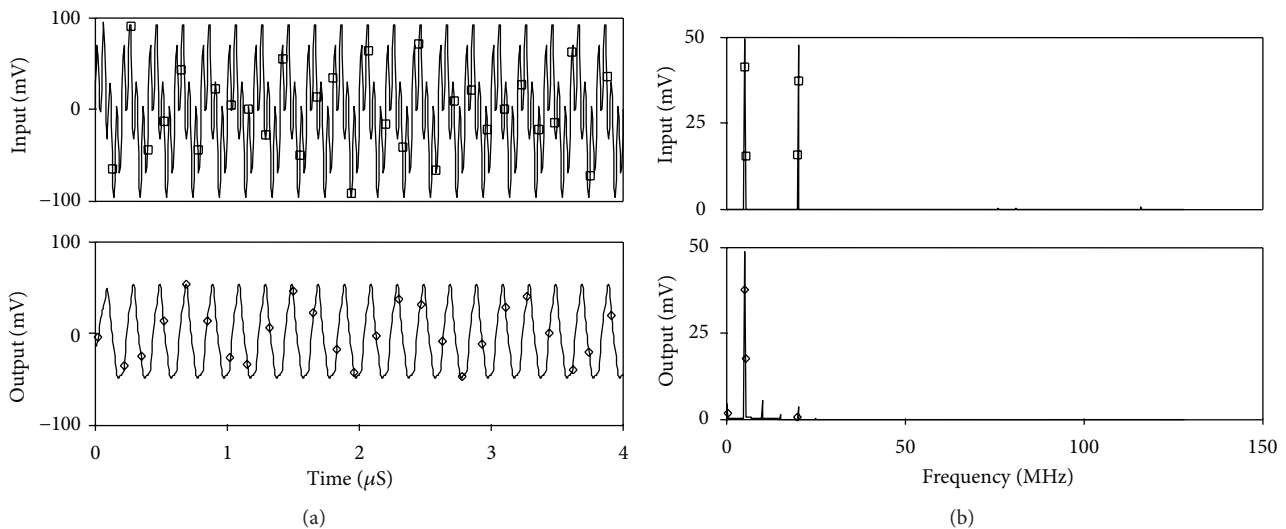


FIGURE 16: Transient response with (a) input and output signals and (b) spectrum of input and output signals.

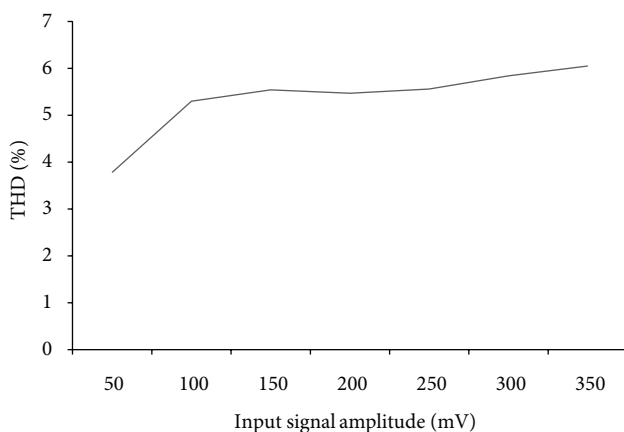


FIGURE 17: Variation of %THD with input signal amplitude.

availability of additional input terminals in CCDDCCTA is gainfully used for obtaining a compact realization of shunt impedance wave equivalents. The structure is resistorless, employs grounded capacitors, possesses electronic tunability of cutoff frequency, and is modular.

## References

- [1] G. FerriI and N. C. Guerrini, *Low-Voltage Low-Power CMOS Current Conveyors*, Kluwer Academic, London, UK.
- [2] R. L. Geiger and E. Sanchez-Sinencio, "Active filter design using operational transconductance amplifiers: a tutorial," *IEEE Circuits and Devices Magazine*, vol. 1, no. 2, pp. 20–32, 1985.
- [3] C. Toumazou, "Pynea, current feedback opamp: a blessing in disguise?" *IEEE Circuits and Devices Magazine*, vol. 10, pp. 43–47, 1994.
- [4] A. S. Sedra and K. C. Smith, "A second generation current conveyor its application," *IEEE Transactions on Circuit Theory*, vol. 17, no. 1, pp. 132–134, 1970.
- [5] I. A. Awad and A. M. Soliman, "Inverting second generation current conveyors: the missing building blocks, CMOS realizations and applications," *International Journal of Electronics*, vol. 86, no. 4, pp. 413–432, 1999.
- [6] A. Fahre, "High frequency applications based on a new current controlled conveyor," *IEEE Transactions on Circuits and Systems I*, vol. 43, no. 2, pp. 82–91, 1996.
- [7] H. O. Elwan and A. M. Soliman, "Novel CMOS differential voltage current conveyor and its applications," *IEE Proceedings Circuits Devices Systems*, vol. 144, pp. 195–200, 1997.
- [8] F. Kafe and C. Psychalinos, "Differential voltage class-AB current controlled current conveyor," in *Proceedings of the IEEE International Conference on Electronics, Circuits, and Systems (ICECS '10)*, pp. 458–461, December 2010.
- [9] W. Chiu, S. I. Liu, H. W. Tsao, and J. J. Chen, "CMOS differential difference current conveyors and their applications," *IEE Proceedings on Circuits Devices Systems*, vol. 143, pp. 91–96, 1996.
- [10] P. Prommee and M. Somdunyanok, "CMOS-based current-controlled DDCC and its applications to capacitance multiplier and universal filter," *International Journal of Electronics and Communications*, vol. 65, no. 1, pp. 1–8, 2011.
- [11] R. Prokop and V. Musil, "CCTA-a new modern circuit block and its internal realization," in *Proceedings of International Conference on Electronic Devices and Systems (IMAPSCZ '05)*, pp. 89–93.
- [12] W. Jaikla, P. Silapan, C. Chanapromma, and M. Siripruchyanun, "Practical implementation of CCTA based on commercial CCII and OTA," in *Proceedings of the International Symposium on Intelligent Signal Processing and Communication Systems (ISPACS '08)*, 2008.
- [13] M. Siripruchyanun and W. Jaikla, "Current controlled current conveyor transconductance amplifier (CCCCTA): a building block for analog signal processing," *Electrical Engineering*, vol. 90, no. 6, pp. 443–453, 2008.
- [14] A. Jantakun, N. Pisutthipong, and M. Siripruchyanun, "A synthesis of temperature insensitive/electronically controllable floating simulators based on DV-CCTAs," in *Proceedings*

of the 6th International Conference on Electrical Engineering/Electronics, Computer, Telecommunications and Information Technology (ECTI-CON '09), pp. 560–563, May 2009.

- [15] W. Jaikla, M. Siripruchyanun, and A. Lahiri, “Resistorless dual-mode quadrature sinusoidal oscillator using a single active building block,” *Microelectronics Journal*, vol. 42, no. 1, pp. 135–140, 2011.
- [16] N. Pandey and S. K. Paul, “Differential difference current conveyor transconductance amplifier (DDCCTA): a new analog building block for signal processing,” *Journal of Electrical and Computer Engineering*, vol. 2011, Article ID 361384, 10 pages, 2011.
- [17] E. A. Soliman and S. A. Mahmoud, “New CMOS fully differential current conveyor and its application in realizing sixth order complex filter,” in *Proceedings of the IEEE International Symposium on Circuits and Systems (ISCAS '09)*, pp. 57–60, May 2009.
- [18] M. A. Ibrahim and H. Kuntman, “A novel high CMRR high input impedance differential voltage-mode KHN-biquad employing DO-DDCCs,” *International Journal of Electronics and Communications*, vol. 58, no. 6, pp. 429–433, 2004.
- [19] H. Wupper and K. Meerkoetter, “New active filter synthesis based on scattering parameters,” *IEEE Transactions on Circuits and Systems*, vol. 22, no. 7, pp. 594–602, 1975.
- [20] I. Haritantis, A. G. Constantinides, and T. Deliyannis, “Wave active filters,” *Proceedings of the IEE*, vol. 123, no. 7, pp. 676–682, 1976.
- [21] G. Koukiou and C. Psychalinos, “Modular filter structures using current feedback operational amplifiers,” *Radioengineering*, vol. 19, no. 4, pp. 662–666, 2010.
- [22] N. Pandey and P. Kumar, “Realization of resistorless wave active filter using differential voltage current controlled conveyor transconductance amplifier,” *Radioengineering*, vol. 20, pp. 911–916, 2011.

## Research Article

# Distributed Drives Monitoring and Control: A Laboratory Setup

**Mini Sreejeth, Parmod Kumar, and Madhusudan Singh**

*Department of Electrical Engineering, Delhi Technological University, Bawana Road, New Delhi 110042, India*

Correspondence should be addressed to Mini Sreejeth; [minisreejeth@dce.ac.in](mailto:minisreejeth@dce.ac.in)

Received 21 November 2012; Revised 24 December 2012; Accepted 30 December 2012

Academic Editor: Paolo Colantonio

Copyright © 2013 Mini Sreejeth et al. This is an open access article distributed under the Creative Commons Attribution License, which permits unrestricted use, distribution, and reproduction in any medium, provided the original work is properly cited.

A laboratory setup of distributed drives system comprising a three-phase induction motor (IM) drive and a permanent magnet synchronous motor (PMSM) drive is modeled, designed, and developed for the monitoring and control of the individual drives. The integrated operation of IM and PMSM drives system has been analyzed under different operating conditions, and their performance has been monitored through supervisory control and data acquisition (SCADA) system. The necessary SCADA graphical user interface (GUI) has also been created for the display of drive parameters. The performances of IM and PMSM under parametric variations are predicted through sensitivity analysis. An integrated operation of the drives is demonstrated through experimental and simulation results.

## 1. Introduction

Monitoring and control of drives is a necessary prerequisite for quality control of a product as well as for energy conservation in automated process plants. Electrical energy is supplied to the motors through power electronic converter to get the desired torque/speed characteristics of the motors for motion control in industrial processes. This is achieved through modern motor drives, advance control algorithms, and intelligent devices such as programmable logic controller (PLC), digital signal processor (DSP), and microcontroller. This makes the operation of drives complex, sophisticated, and expensive [1]. Further, in production plant, the process is distributed at shop level based on functional requirements, which results in distribution of the various drives for different process operations. In distributed drives system, the processing tasks are physically distributed among the various drives, which requires placement of the necessary computing, with optimal volume of data, close to the process. Such system also provides fault tolerant and self-diagnostic capability and enhances the reliability of overall system. Thus, a distributed drives system has partially autonomous local computing devices with input, output, and storage capability, interconnected through a digital communication link coordinated by a supervisory control and data acquisition system. The distributed system has the advantages of local

as well as centralized control. In such cases, the SCADA and programmable logic controller coordinate the local controllers through a communication link [2].

In the past few decades, limited literatures are available on distributed drives control using PLC. Applications of PLC have been reported for monitoring control system of an induction motor [3, 4]. PLC has been also used as a power factor controller for power factor improvement and to keep the voltage to frequency ratio of a three-phase IM, constant under all control conditions [5]. Also, a vector-oriented control scheme, for the regulation of voltage and current of three-phase pulse width modulation inverter, which uses a complex programmable logic device (CPLD) [6], has been reported. Remote control and operation of electric drive need a large amount of data to be acquired, processed, and presented by the SCADA system [7, 8]. In this paper, distributed control for a three-phase IM drive and a three-phase PMSM drive is configured, designed, and developed for experimental work, and integrated control operation is demonstrated through experimental and simulation results. The application of adjustable speed drives (ASDs) for fans, pumps, blowers, and compressors do not require very precise speed control. Speed sensor in a drive adds cost and reduces the reliability of the drive. Therefore, for applications requiring moderate performance, sensorless drive is a better option, and, hence, sensorless vector control is used for IM control [9–14]. On the

other hand, PMSMs are generally used for low-power servo applications where very precise position control is required. A PID controller is applied [15] to the position control, and a model reference adaptive control has been implemented for the PMSM [16]. As speed estimators and observers rely on the knowledge of motor parameters, they are inadequate for accurate position estimation. In the present work, a position feedback encoder is used for PMSM, and an indirect field-oriented control is employed for its control [17–19].

A detailed study on distributed drives including design, development, and testing of prototype distributed drives is demonstrated. The monitoring and supervisory control of IM and PMSM drives, thereby validating the concept of distributed drives, is also described. Further, the developed experimental setup enables and facilitates imparting training and providing the facilities with hands of experimentation, research, and practical training. The necessary SCADA GUI has also been created for the display of drive parameters such as speed. The performances of IM and PMSM are predicted by sensitivity analysis.

## 2. Control Algorithm

Sensorless control for IM and indirect field-oriented control for the PMSM have been used in distributed control of the drives.

### 2.1. Sensorless Control of Three-Phase IM Drive

**2.1.1. Flux Estimator.** The direct and quadrature rotor flux components ( $\psi_{dr}^s$  and  $\psi_{qr}^s$ ) are estimated from the IM terminal voltages ( $v_a$ ,  $v_b$ , and  $v_c$ ), currents ( $i_a$ ,  $i_b$ , and  $i_c$ ), stator resistance of the motor,  $R_s$ , the stator and rotor self-inductances  $L_s$  and  $L_r$ , respectively, and their mutual inductance  $L_m$ , which are described in (1) to (3); [20], consider

$$\psi_{ds}^s = \int (v_{ds}^s - R_s i_{ds}^s) dt, \quad (1)$$

$$\psi_{qs}^s = \int (v_{qs}^s - R_s i_{qs}^s) dt,$$

where

$$\begin{aligned} v_{qs}^s &= \frac{2}{3}v_a - \frac{1}{3}v_b - \frac{1}{3}v_c, \\ v_{ds}^s &= -\frac{1}{\sqrt{3}}v_b + \frac{1}{\sqrt{3}}v_c, \\ i_{qs}^s &= \frac{2}{3}i_a - \frac{1}{3}i_b - \frac{1}{3}i_c, \\ i_{ds}^s &= -\frac{1}{\sqrt{3}}i_b + \frac{1}{\sqrt{3}}i_c, \end{aligned} \quad (2)$$

$$\psi_{dr}^s = \frac{L_r}{L_m} (\psi_{ds}^s - \sigma L_s i_{ds}^s),$$

$$\psi_{qr}^s = \frac{L_r}{L_m} (\psi_{qs}^s - \sigma L_s i_{qs}^s),$$

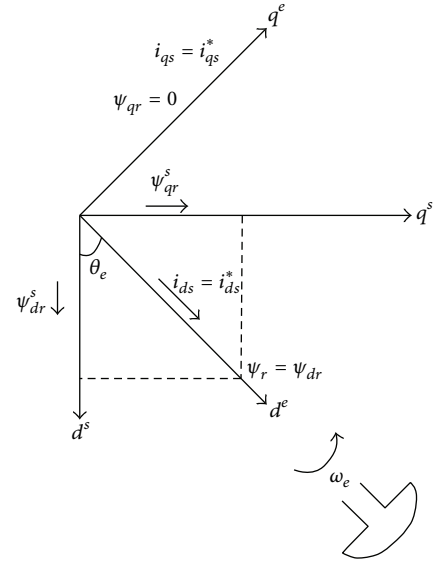


FIGURE 1: Phasors showing rotor flux orientation.

where

$$\sigma = 1 - \frac{L_m^2}{L_r L_s} \quad (3)$$

and  $i_{ds}^s$ ,  $i_{qs}^s$ ,  $\psi_{ds}^s$ , and  $\psi_{qs}^s$  are stator direct and quadrature axis currents and fluxes, respectively.

Also,

$$\psi_r = \sqrt{(\psi_{qr}^s)^2 + (\psi_{dr}^s)^2}. \quad (4)$$

The correct alignment of current,  $i_{ds}$ , in the direction of flux,  $\psi_r$ , and the current,  $i_{qs}$ , perpendicular to it are needful requirements in vector control. This alignment is depicted in Figure 1 using rotor flux vectors  $\psi_{dr}^s$  and  $\psi_{qr}^s$ , where  $d^e$ - $q^e$  frame is rotating at synchronous speed with respect to stationary frame  $d^s$ - $q^s$ , and at any instance, the angular position of  $d^e$  axis with respect to the  $d^s$  axis is  $\theta_e$ , where

$$\begin{aligned} \theta_e &= \omega_e t, \quad \cos \theta_e = \frac{\psi_{dr}^s}{\psi_r}, \\ \sin \theta_e &= \frac{\psi_{qr}^s}{\psi_r}. \end{aligned} \quad (5)$$

**2.1.2. Speed Estimator.** The speed is estimated by using the data of the rotor flux vector ( $\psi_r$ ), obtained in a flux estimator as follows.

The rotor circuit equations [20] of  $d^s$ - $q^s$  frame are written as

$$\begin{aligned} \frac{d\psi_{dr}^s}{dt} + R_r i_{dr}^s + \omega_r \psi_{qr}^s &= 0, \\ \frac{d\psi_{qr}^s}{dt} + R_r i_{qr}^s - \omega_r \psi_{dr}^s &= 0. \end{aligned} \quad (6)$$

Adding terms  $(L_m R_r / L_r) i_{ds}^s$  and  $(L_m R_r / L_r) i_{qs}^s$ , respectively, on both sides of the previous equation, we get

$$\frac{d\psi_{dr}^s}{dt} + \frac{R_r}{L_r} (L_m i_{ds}^s + L_r i_{dr}^s) + \omega_r \psi_{qr}^s = \left( \frac{L_m R_r}{L_r} \right) i_{ds}^s, \quad (7)$$

$$\frac{d\psi_{qr}^s}{dt} + \frac{R_r}{L_r} (L_m i_{qs}^s + L_r i_{qr}^s) - \omega_r \psi_{dr}^s = \left( \frac{L_m R_r}{L_r} \right) i_{qs}^s, \quad (8)$$

$$\frac{d\psi_{dr}^s}{dt} = \frac{L_m}{\tau_r} i_{ds}^s - \omega_r \psi_{qr}^s - \frac{1}{\tau_r} \psi_{dr}^s, \quad (9)$$

$$\frac{d\psi_{qr}^s}{dt} = \frac{L_m}{\tau_r} i_{qs}^s + \omega_r \psi_{dr}^s - \frac{1}{\tau_r} \psi_{qr}^s, \quad (10)$$

where

$$\begin{aligned} L_m i_{ds}^s + L_r i_{dr}^s &= \psi_{dr}^s, \\ L_m i_{qs}^s + L_r i_{qr}^s &= \psi_{qr}^s, \end{aligned} \quad (11)$$

and  $\tau_r$  (i.e.,  $L_r / R_r$ ) is the rotor time response. Also, from (5),

$$\theta_e = \tan^{-1} \frac{\psi_{qr}^s}{\psi_{dr}^s}. \quad (12)$$

Differentiating the aforementioned, we get

$$\frac{d\theta_e}{dt} = \frac{\psi_{dr}^s \psi_{qr}^s - \psi_{qr}^s \psi_{dr}^s}{\psi_r^2}. \quad (13)$$

Combining (7), (8), and (13) and simplifying, one yields

$$\begin{aligned} \omega_r &= \frac{d\theta_e}{dt} - \frac{L_m}{\tau_r} \left[ \frac{\psi_{dr}^s i_{qs}^s - \psi_{qr}^s i_{ds}^s}{\psi_r^2} \right], \\ \omega_r &= \frac{1}{\psi_r^2} \left( [\psi_{dr}^s \psi_{qr}^s - \psi_{qr}^s \psi_{dr}^s] - \frac{L_m}{\tau_r} [\psi_{dr}^s i_{qs}^s - \psi_{qr}^s i_{ds}^s] \right), \end{aligned} \quad (14)$$

where  $\psi_{qr}^s$  and  $\psi_{dr}^s$  are first derivatives of  $\psi_{qr}^s$  and  $\psi_{dr}^s$ , respectively.

The torque component of current  $i_{qs}^*$  and the flux component of current  $i_{ds}^*$  are evaluated from the speed control loop and the flux control loop, respectively, as follows:

$$\begin{aligned} i_{qs}^* &= (\omega_r - \omega_r^*) G_1, \\ i_{ds}^* &= (\Psi_r - \Psi_r^*) G_2, \end{aligned} \quad (15)$$

where  $\omega_r^*$  and  $\Psi_r^*$  are the reference speed and flux;  $G_1$  and  $G_2$  are the gain of speed loop and flux loop;  $\psi_r$  and  $\omega_r$  are computed using the flux and speed estimators, respectively, as explained earlier.

The principal vector control parameters,  $i_{ds}^*$  and  $i_{qs}^*$ , which are DC values in synchronously rotating frame, are converted to stationary frame with the help of unit vectors ( $\sin \theta$  and  $\cos \theta$ ) generated from flux vectors  $\psi_{dr}^s$  and  $\psi_{qr}^s$  as given by (5).

The resulting stationary frame signals are then converted to phase current commands for the inverter [20]. The torque is estimated using (16) as

$$T_e = \frac{3}{2} \left( \frac{P}{2} \right) \frac{L_m}{L_r} (\psi_{dr}^s i_{qs}^s - \psi_{qr}^s i_{ds}^s). \quad (16)$$

The block diagram of the sensorless vector control for the IM drive is shown in Figure 2.

**2.2. Control Scheme for Three-Phase PMSM Drive.** The rotor of PMSM is made up of permanent magnet of Neodymium-iron-boron, which offers high energy density. Based on the assumptions that (i) the rotor copper losses are negligible, (ii) there is no saturation, (iii) there are no field current dynamics, and (iv) no cage windings are on the rotor, the stator  $d$ - $q$  equations of the PMSM in the rotor reference frame are as follows [17, 21]:

$$v_{qs} = R_s i_{qs} + \frac{d}{dt} \lambda_{qs} + \omega_s \lambda_{ds}, \quad (17)$$

$$v_{ds} = R_s i_{ds} + \frac{d}{dt} \lambda_{ds} - \omega_s \lambda_{qs},$$

where

$$\begin{aligned} \lambda_{qs} &= L_{qs} i_{qs}, \\ \lambda_{ds} &= L_{ds} i_{ds} + \lambda_f. \end{aligned} \quad (18)$$

$v_{ds}$  and  $v_{qs}$  are the  $d$ ,  $q$  axis voltages,  $i_{ds}$  and  $i_{qs}$  are the  $d$ ,  $q$  axis stator currents,  $L_{ds}$  and  $L_{qs}$  are the  $d$ ,  $q$  axis inductance,  $\lambda_{ds}$  and  $\lambda_{qs}$  are the  $d$ ,  $q$  axis stator flux linkages,  $\lambda_f$  is the flux linkage due to the rotor magnets linking the stator, while  $R_s$  and  $\omega_s$  are the stator resistance and inverter frequency, respectively. The inverter frequency  $\omega_s$  is related to the rotor speed  $\omega_r$  as follows:

$$\omega_s = \frac{P}{2} \omega_r, \quad (19)$$

where  $P$  is the number of poles, and the electromagnetic torque  $T_e$  is

$$T_e = \frac{3}{2} \left( \frac{P}{2} \right) [\lambda_f i_{qs} + (L_{ds} - L_{qs}) i_{ds} i_{qs}]. \quad (20)$$

This torque,  $T_e$ , encounters load torque, moment of inertia of drive, and its damping constant. Thus, the equation for the motion is given by

$$T_e = T_L + B \omega_r + J \frac{d}{dt} \omega_r, \quad (21)$$

where  $T_L$  is the load torque,  $J$  moment of inertia, and  $B$  damping coefficient.

Figure 3 shows the typical block diagram of a PMSM drive. The system consists of a PMSM, speed/position feedback, an inverter, and a controller (constant torque and flux weakening operation, generation of reference currents, and PI controller). The error between the commanded and actual

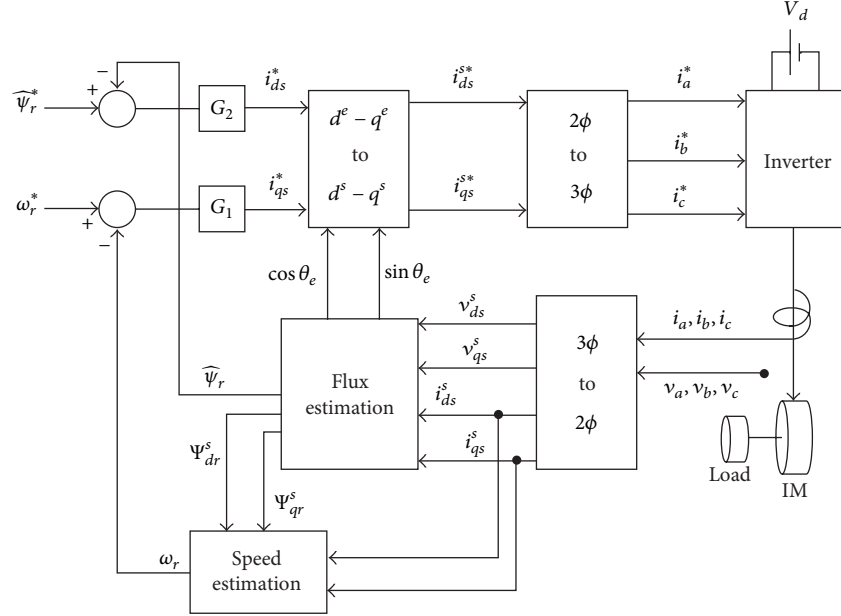


FIGURE 2: Block diagram of sensor less vector control for three-phase IM drive.

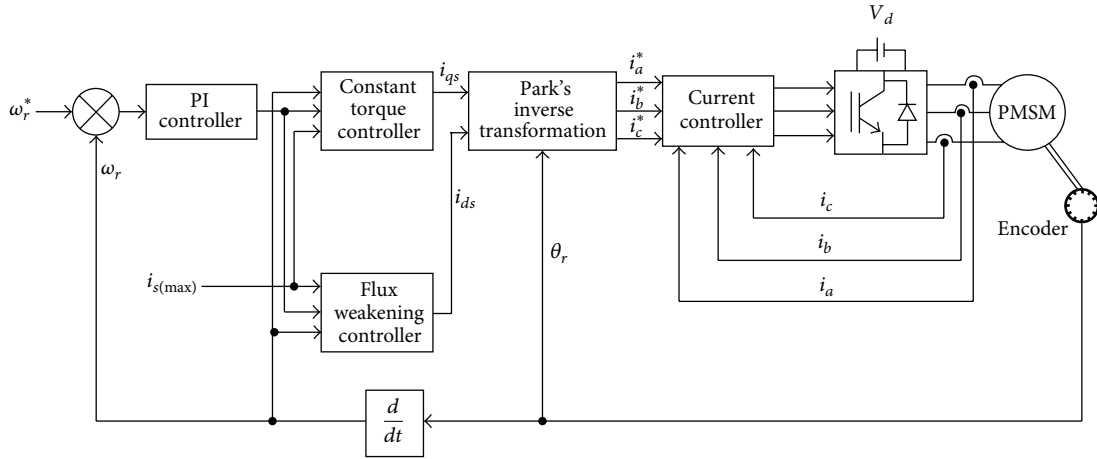


FIGURE 3: Block diagram of three-phase PMSM drive.

speed is operated upon by the PI controller to generate the reference torque.

The ratio of torque reference and motor torque constant is used during constant torque operation to compute the reference quadrature axis current,  $i_{qs}^*$ . For operation up to rated speed, the direct axis current is made equal to zero. From these  $d$ - $q$  axes currents and the rotor position/speed feedback, the reference stator phase currents are obtained using Park's inverse transformation as given in (22)

$$\begin{bmatrix} i_a \\ i_b \\ i_c \end{bmatrix} = \begin{bmatrix} \cos \theta_r & \sin \theta_r & 1 \\ \cos \left( \theta_r - \frac{2\pi}{3} \right) & \sin \left( \theta_r - \frac{2\pi}{3} \right) & 1 \\ \cos \left( \theta_r + \frac{2\pi}{3} \right) & \sin \left( \theta_r + \frac{2\pi}{3} \right) & 1 \end{bmatrix} \begin{bmatrix} i_{qs}^* \\ i_{ds}^* \\ i_{0s} \end{bmatrix}, \quad (22)$$

where  $i_{0s}$  is the zero sequence current, which is zero for a balanced system.

The hysteresis PWM current controller attempts to force the actual motor currents to reference current values using stator current feedback. The error between these currents is used to switch the PWM inverter. The output of the PWM is supplied to the stator of the PMSM, which yields the commanded speed. The position feedback is obtained by an optical encoder mounted on the machine shaft.

In order to operate the drive in the flux weakening mode, it is essential to find the maximum speed. The maximum operating speed with zero torque can be obtained from the steady state stator voltage equations. The flux weakening controller computes the demagnetizing component of stator current,  $i_{ds}^*$ , satisfying the maximum current and voltage limits. For this direct axis current and the rated stator current, the quadrature axis current can be obtained from (23)

$$I_s = \sqrt{i_{ds}^{*2} + i_{qs}^{*2}}. \quad (23)$$

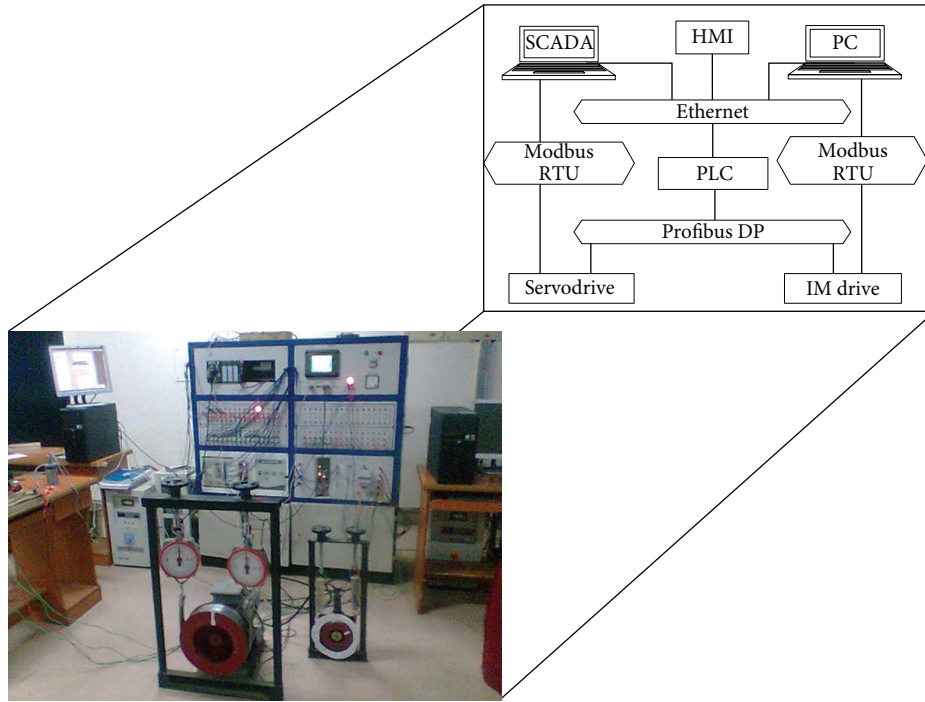


FIGURE 4: Schematic layout of distributed drives laboratory setup.

These  $d$ - $q$  axes currents and the rotor position/speed can be utilized to obtain the commanded speed.

### 3. Sensitivity Analysis of IM and PMSM

Sensitivity analysis is used by designers of machines for the prediction of the effect of parameter of interest on the performance variables of the motor. In the present study, sensitivity values of the performance variables like power input, power output, efficiency, power factor, stator current, starting current, magnetizing current, developed torque, and starting torque, with respect to the equivalent circuit parameters, are obtained for the IM. The sensitivity is computed by (24), as sensitivity of a variable  $N$  with respect to a parameter  $\alpha$  can be represented as

$$S_{\alpha}^N = 100 \cdot \frac{(N_c - N_n)}{N_n}, \quad (24)$$

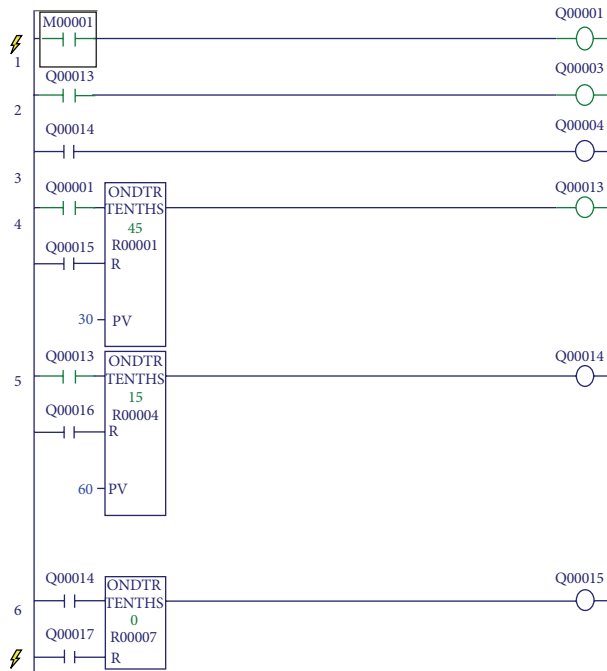
where  $N_n$  is the performance variable with nominal parameters, and  $N_c$  is the value of the performance variable when the value of the parameter  $\alpha$  is increased by defined deviation value. A similar analysis is also carried out for PMSM.

### 4. Laboratory Setup of the Distributed Drives System

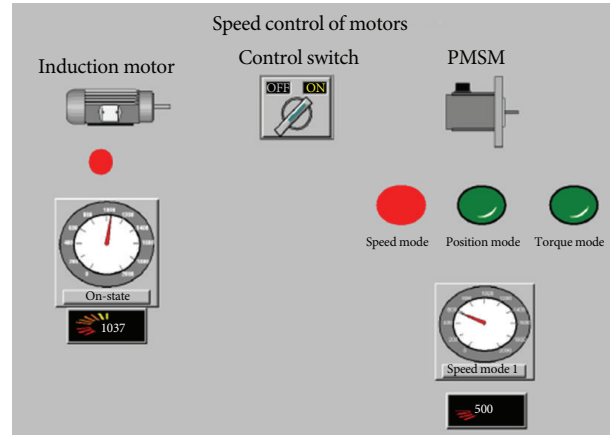
To analyse the utility of distributed drive system, a laboratory setup has been designed and developed for research and development activities. Figure 4 shows laboratory setup which incorporates industry standard networking. It has an IEEE 802.3 compliant Ethernet data highway and is currently

supporting a network of two-operator consoles, a PLC, and two drives (IM drive and PMSM drive) all connected in star topology. The PLC (GE Fanuc 90-30) coordinates the operation of these drives. The PLC passes real-time data to the operator console via Ethernet interface using customized software, namely, VersaMotion, for PMSM drive and DCT software for the IM drive. The input/output (I/O) units of PLC and drives communicate using Profibus-DP [22, 23]. The communication between individual drives and PCs, SCADA, is through Modbus protocol.

**4.1. PLC in Distributed Drive System.** The PLC used in the laboratory setup consists of several modules, namely, Power Supply, CPU, Digital Input, Digital Output, and Network Modules. The digital input module is a 0–30 V DC, 7 mA with positive/negative logic and 16 input points. This module is used to read ON/OFF position of different contacts used to control the drives. There are two output modules with 32 points operating at 24 V DC, which are used to output the status of the individual drive, alarm signal, and so forth based on the decision made by the control strategy that is written as ladder logic program in the PLC. The power supply of PLC is capable of supporting 100–240 V AC or 125 V DC. The CPU has a user logic memory of 240 Kbytes. The communication module includes Profibus module operating at baud rate of 1.5 Mbps with a power requirement of 5 V DC. Proficy Machine Edition 5.9 provides software utilities for PLC programming. The PLC is programmed in ladder diagrams, and program is downloaded in the PLC from a personal computer through RS 232C serial interface. A ladder diagram consists of graphic symbols like contacts, coils, timers, counters, and so forth which are laid out in networks



(a)



(b)

FIGURE 5: (a) Ladder logic for integrated operation of IM and PMSM drives. (b) SCADA GUI developed for the speed control of the distributed drives.

similar to a rung of a relay logic diagram. The PLC stores the inputs (ON/OFF status of coils), execute, the user program cyclically, and finally writes the outputs (energizing a coil for actual opening/closing of contacts) to the output status table. This read-execute-write cycle is called a scan cycle. The ladder logic diagram for the integrated operation of the IM and PMSM drives is shown in Figure 5(a).

**4.2. SCADA.** For the remote monitoring and control of the drives, GE Fanuc SCADA Cimplicity 7.5 software is used. The SCADA software is loaded on the server PC which provides supervision in the form of graphical animation and data trends of the processes on the window of PC or screen of HMI. The Cimplicity project wizard window is used to configure various communication ports and the controller type and also to create new points corresponding to addresses used in the controller. This graphical interactive window is used to animate the drive system. At present, controls like start, stop, speed control, and so forth are developed on the software window to control the drives remotely. Each drive can be controlled locally at the field level, through the PLC, or through the SCADA interface. The SCADA GUI developed for the speed control of the distributed drives is shown in Figure 5(b). The control algorithm has been implemented and tested for a three-phase squirrel cage induction motor and three-phase PMSM drive. The technical specifications for these drives are presented in Tables 1 and 2.

## 5. Results and Discussions

A three-phase sensorless induction drive and a three-phase PMSM drive are configured in the SCADA system. The

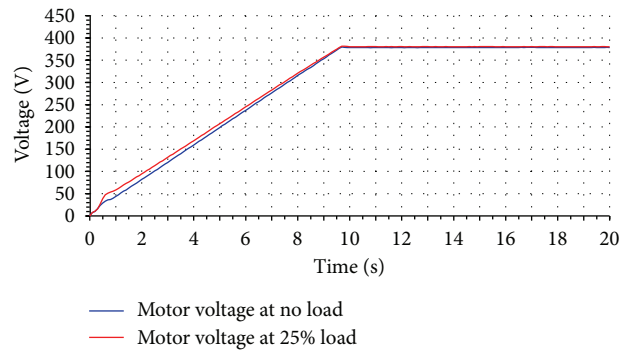


FIGURE 6: Voltage variation of IM drive during starting at different loads and 1440 rpm speed.

operation and performance characteristics of the drives are monitored and studied under varying torque and speed conditions. Simulation results are also described. In order to study the effect of parametric variation on the motor performance variable, sensitivity analysis is carried out for both IM and PMSM with respect to their respective equivalent circuits.

**5.1. Performance of Three-Phase IM Drive under Different Load Conditions.** Figure 6 to Figure 11 show the variation of various parameters of sensorless control induction motor drive during starting at no load and 25% load conditions. Figures 6 and 7 show the variation of voltage and frequency. Both the voltage and frequency increase linearly till they attain a value of 385 V and 48 Hz, respectively, at rated speed

TABLE 1: Technical specifications of three-phase induction motor.

Connection type	$\Delta$
Input voltage	415 V $\pm$ 10%
Input current	7 A
Rated power	3.7 kW
Input frequency	50 Hz
Pole number	4
Rated speed	1440 rpm

TABLE 2: Technical specifications of three-phase PMSM.

Parameter	Value
Rated output	1.0 kW
Rated torque	3.18 Nm
Motor voltage	110 V
Rated current	7.3 A
Maximum current	21.9 A
Encoder position feedback	2500 ppr
Peak torque	9.54 Nm
Rated speed	3000 rpm
Moment of inertia	0.000265 kg·m <sup>2</sup>
Armature resistance	0.2 $\Omega$
Armature inductance	2 mH

under no load starting condition. While the machine is started with a load of 25%, the variations in voltage and frequency are almost similar to that of the previous case.

Figure 8 shows the variation of current during starting under no load and 25% load conditions. The starting current was 4.38 A during starting which is settled down to a steady state value of 3.1 A in 2 s under no load case. While with 25% load, the starting current was 5.7 A which is settled down to steady state value of 3.25 A in about 10 s.

Figure 9 shows the variation of torque during starting with no load and 25% load. At no load starting, it is observed that the negative peak torque value is 5.9 Nm at the first instance, and then it reaches a positive peak value of 10.3 Nm and finally settles down to a steady state value of 0.7 Nm in about 10 s. While with 25% load starting, the negative peak torque value at the first instance is 6 Nm, and the positive peak value is 20.1 Nm which finally settles down to a steady value of 4.5 Nm in 12 s. Figure 10 shows the power variation at starting with no load and 25% load. The power drawn during transient period is 0.18 kW, which decreases to a value of 0.1 kW, then it increases linearly to a value of 0.3 kW and finally settles down to a value of 0.14 kW in 11 s. When the machine is started with 25% load, the initial power drawn is 0.42 kW, which then increases to a value of 1.3 kW and finally settles down to a value of 0.8 kW in 13 s.

Figure 11 shows the speed response of IM during starting at no load and 25% load. It is observed that the motor reaches its rated speed that is, 1440 rpm in about 9 s under no load starting and in about 10 s under 25% load at starting. Figure 12 shows simulated dynamic performance of IM drive under no

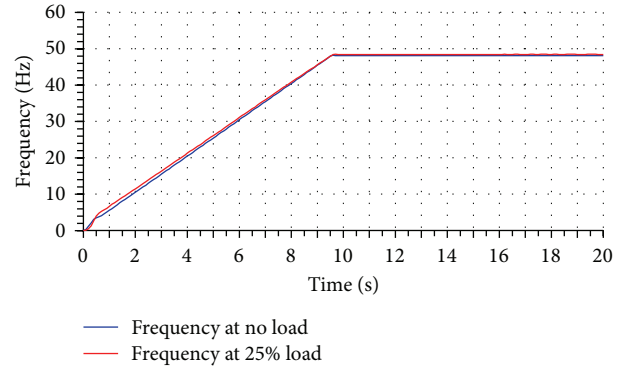


FIGURE 7: Frequency variation of IM drive during starting at different loads and 1440 rpm speed.

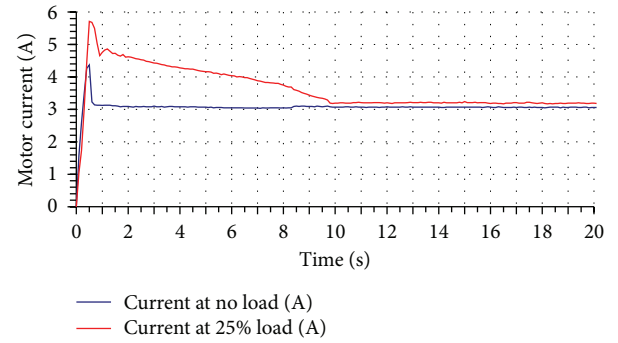


FIGURE 8: Current variation of IM drive during starting at different loads and 1440 rpm speed.

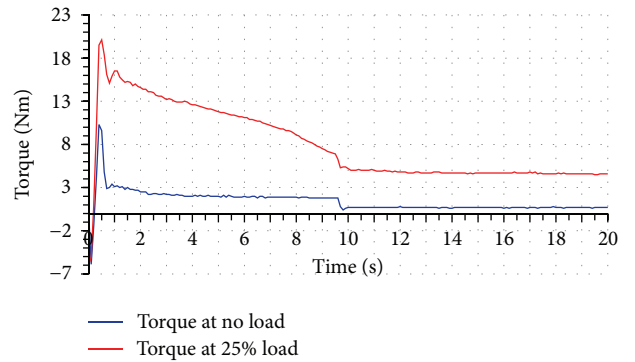


FIGURE 9: Torque variation of IM drive during starting at different loads and 1440 rpm speed.

load and at rated speed of 1440 rpm. The motor attains the desired speed of 1440 rpm in about 5.5 s.

**5.2. Starting Performance of Three-Phase PMSM Drive under No Load Condition.** Figure 13 shows the dynamic performance of PMSM under no load with a reference speed of 3000 rpm. The motor attains the set synchronous speed of 3000 rpm in about 300 ms. Figure 14 shows simulated dynamic performance of PMSM at no load with a reference

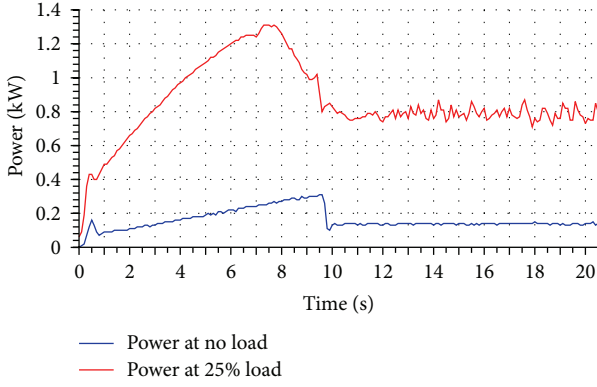


FIGURE 10: Power variation of IM drive during starting at different loads and 1440 rpm speed.

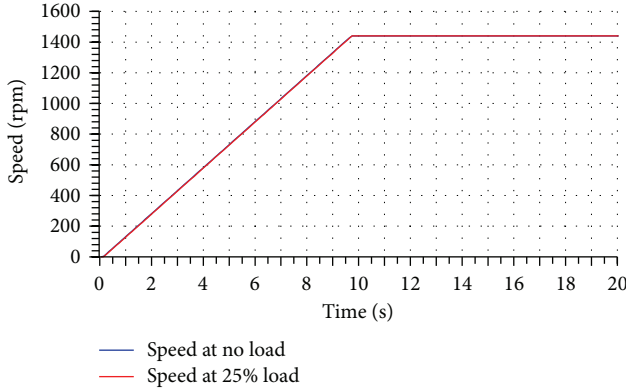


FIGURE 11: Speed variation of IM drive during starting at different loads and 1440 rpm speed.

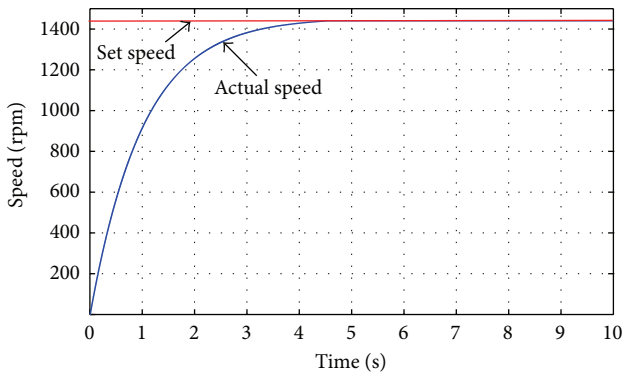


FIGURE 12: Simulated speed response of three-phase IM drive at no load and rated speed.

speed of 3000 rpm. The motor attains the set synchronous speed of 3000 rpm in about 280 ms.

**5.3. Sensitivity Analysis for Performance Variables of PMSM.** Motor parameters like stator resistance and inductance vary depending on operating conditions, mainly motor duty cycle, effect of magnetic saturation, and so forth. The effect of

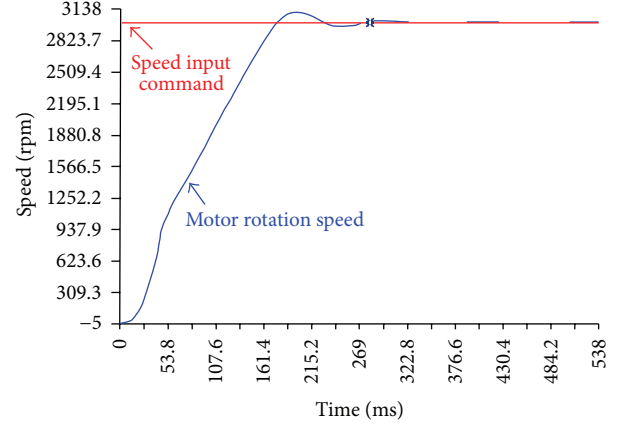


FIGURE 13: Experimental starting response of three-phase PMSM at no load and rated speed.

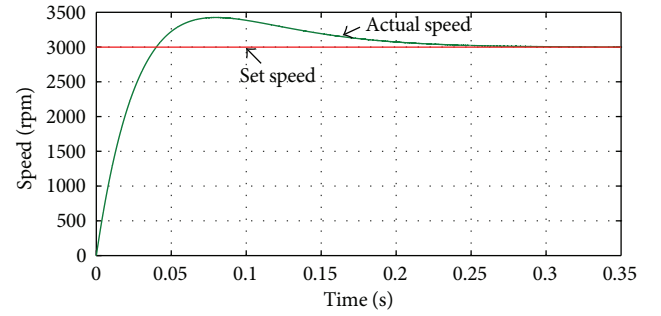


FIGURE 14: Simulated starting response of three-phase PMSM at no load and rated speed.

parametric variations on the efficiency of PMSM has been analyzed and is shown in Figure 15 for rated speed and rated torque conditions, where  $\delta$  represents the parameter variation coefficient and is defined as the ratio of new parameter value to the actual parameter value. That is,

$$\delta = \frac{R'_s}{R_s} = \frac{L'_s}{L_s}, \quad (25)$$

where  $R'_s$  and  $L'_s$  are the new stator resistance and stator inductance, respectively. In the present analysis,  $\delta$  is determined for 1% deviation in motor parameters.

It is observed from Figure 15 that the variation in the efficiency is negligibly small with variation in  $R_s$  and  $L_s$ , and it follows a Gaussian distribution. The variation in efficiency due to change in  $R_s$  and  $L_s$  is expressed as a fourth order polynomial using best fit curve in Figure 15, where

$$\begin{aligned} \Delta\eta|_{R_s} &= 0.38\delta^4 - 1.58\delta^3 + 2.07\delta^2 - 0.91\delta + 0.04, \\ \Delta\eta|_{L_s} &= 0.16\delta^4 - 0.59\delta^3 + 0.55\delta^2 + 0.01\delta - 0.13. \end{aligned} \quad (26)$$

**5.4. Sensitivity Analysis for Performance Variables of IM.** Table 3 shows the sensitivity of different performance variables of three-phase IM with respect to its equivalent circuit

TABLE 3: Sensitivity of performance variables of three-phase IM.

Parameters	(Output power = full load = 3.7 kW. $s = 0.043$ )						
	$R_s$	$R_r$	$X_s$	$X_r$	$X_m$	$V$	$f$
Power input	-0.022	-0.891	-0.099	-0.014	0.035	2.010	-0.078
Power output	-0.107	-0.888	-0.103	-0.021	0.085	2.090	-0.037
Efficiency	-0.085	0.003	-0.004	-0.006	0.051	0.078	0.041
Power factor	0.029	-0.235	-0.050	-0.038	0.289	0.000	0.202
Stator current	-0.052	-0.658	-0.050	0.023	-0.254	1.000	-0.280
Starting current	-0.184	-0.131	-0.352	-0.309	-0.022	1.000	-0.681
Magnetizing current	-0.052	0.063	-0.050	-0.004	-0.950	1.000	-1.003
Torque	-0.103	-0.854	-0.099	-0.020	0.082	2.010	-0.036
Starting torque	-0.367	0.734	-0.702	-0.707	0.047	2.010	-1.357

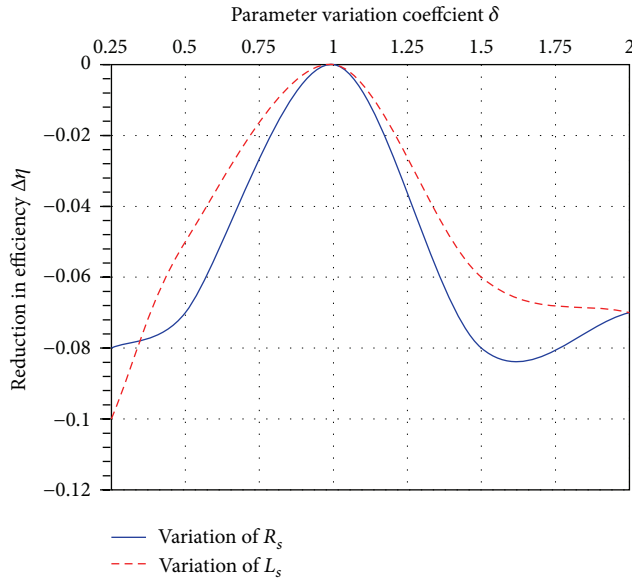


FIGURE 15: Effect of parametric variations on the efficiency of PMSM for rated speed and rated torque.

parameters. The sensitivity of the power input and power output with respect to  $R_r$  is the highest and is the lowest with respect to  $X_r$ . Motor efficiency is less sensitive to all the equivalent circuit parameters, with variation in  $R_s$  and  $X_m$  affecting it more compared to other parameters. The power factor is more affected by variation in  $X_m$  and  $R_r$ , while variations in other parameters have less effect on it. The stator current is more affected by variation in  $R_r$  and least by variation in  $X_r$ . The sensitivity of starting current with respect to  $X_s$  and  $X_r$  is the highest while with respect to  $X_m$  is the lowest. Magnetizing current is more sensitive to changes in  $X_m$  and less sensitive to changes in  $X_r$ . The developed torque and starting torque are mainly affected by variations in  $R_r$ . The sensitivity of developed torque is the least with respect to  $X_r$  and  $X_m$ , respectively.

The sensitivity of the performance variables with respect to frequency and supply voltage is also obtained. It is observed

that the frequency variation has maximum effect on starting torque and magnetizing current followed by starting current. The sensitivity of developed torque with respect to frequency is the least. The sensitivity of power input, power output, developed torque, and starting torque with respect to supply voltage is 2% each. Similarly, the stator current, starting current, magnetizing current, and so forth change by 1% with respect to variation in supply voltage. The supply voltage variation has negligible effect on efficiency, while power factor is not affected by supply voltage variation.

## 6. Conclusion

A prototype of distributed drives system, consisting of a three-phase IM drive and a PMSM drive, is designed, developed, and implemented as a laboratory setup. This prototype system demonstrates the operation and control of distributed drives through PLC and SCADA. The operation, control, and monitoring of various performance parameters of PMSM and IM under different operating conditions are carried out in detail. A detailed sensitivity analysis is also carried out to observe the effect of parametric variations on performance of the motors.

## Conflict of Interests

In this research work, GE Fanuc 90-30 Series PLC has been used for creation of the laboratory setup. The said PLC uses Profibus DP protocol for communication between the input/output modules and the drives. The selection of the PLC is intended solely to facilitate research and development work and is not based on any commercial interest.

## Acknowledgments

This work was supported in part by the MODROB Scheme of AICTE, India. The authors gratefully acknowledge the support provided by AICTE, India, and GE Fanuc in setting up the laboratory infrastructure in the Electrical Engineering Department at Delhi Technological University, New Delhi, India.

## References

- [1] J. Chang, "High-frequency and precision three-phase sine/ PWM controller with near-zero frequency of MPU intervention-novel design supporting distributed AC drive systems," *IEEE Transactions on Industrial Electronics*, vol. 52, no. 5, pp. 1286–1296, 2005.
- [2] J. M. Liptak, H. R. Orndorff, and E. M. Innes, "A programmable local controller for AC adjustable frequency drive controllers," in *Proceedings of the IEEE Industry Applications Society Annual Meeting*, vol. 1, pp. 572–577, October 1988.
- [3] M. G. Ioannides, "Design and implementation of PLC-based monitoring control system for induction motor," *IEEE Transactions on Energy Conversion*, vol. 19, no. 3, pp. 469–476, 2004.
- [4] Y. Birbir and H. S. Nogay, "Design and implementation of PLC-based monitoring control system for three phase induction motors fed by PWM inverter," *International Journal of Systems Applications, Engineering and Development*, vol. 2, no. 3, pp. 128–135, 2008.
- [5] A. R. Al-Ali, M. M. Negm, and M. Kassas, "A PLC based power factor controller for a 3-phase induction motor," in *Proceedings of the IEEE Industry Applications Society Annual Meeting (IAS '00)*, vol. 2, pp. 1065–1072, October 2000.
- [6] J. Y. Jyang and Y. Y. Tzou, "A CPLD based voltage/current vector controller for 3- phase PWM inverters," in *Proceedings of the 29th Annual IEEE Power Electronics Specialists Conference*, vol. 1, pp. 262–268.
- [7] M. S. Thomas, P. Kumar, and V. K. Chandna, "Design, development, and commissioning of a supervisory control and data acquisition (SCADA) laboratory for research and training," *IEEE Transactions on Power Systems*, vol. 19, no. 3, pp. 1582–1588, 2004.
- [8] R. D. Pedroza, Internet based FLARE and LFGTE facilities Remote Monitoring and Control, [http://www.scsengineers.com/Papers/Pedroza\\_Internet\\_Based\\_Flare\\_and\\_LFGTE.SWANA\\_2007.pdf](http://www.scsengineers.com/Papers/Pedroza_Internet_Based_Flare_and_LFGTE.SWANA_2007.pdf).
- [9] R. Krishnan and F. C. Doran, "Study of parameter sensitivity in high performance inverter fed Induction motor Drive systems," *IEEE Transactions on Industry Applications*, vol. 23, no. 4, pp. 623–635, 1987.
- [10] S. B. Bodkhe and M. V. Aware, "Speed-sensorless, adjustable-speed induction motor drive based on dc link measurement," *International Journal of Physical Sciences*, vol. 4, no. 4, pp. 221–232, 2009.
- [11] J. Holtz, "Sensorless control of induction motor drives," *Proceedings of the IEEE*, vol. 90, no. 8, pp. 1359–1394, 2002.
- [12] K. Rajashekara, A. Kawamura, and K. Matsuse, Eds., *Sensorless Control of AC Drives*, IEEE Press, New York, NY, USA, 1996.
- [13] B. K. Bose and N. R. Patel, "Sensorless stator flux oriented vector controlled induction motor drive with neuro-fuzzy based performance enhancement," in *Proceedings of the 32nd IEEE Industry Applications Conference IAS Annual Meeting*, pp. 393–400, October 1997.
- [14] C. Schauder, "Adaptive speed identification for vector control of induction motors without rotational transducers," *IEEE Transactions on Industry Applications*, vol. 28, no. 5, pp. 1054–1061, 1992.
- [15] R. C. Garcia, W. I. Suemitsu, and J. O. P. Pinto, "Precise position control of a PMSM based on new adaptive PID controllers," in *Proceedings of Annual Conference of the IEEE Industrial Electronics Society*, pp. 1912–1917, November 2011.
- [16] M. Tárník and J. Murgaš, "Model reference Adaptive control of permanent magnet synchronous motor," *Journal of Electrical Engineering*, vol. 62, no. 3, pp. 117–125, 2011.
- [17] P. Pillay and R. Krishnan, "Modeling, simulation, and analysis of permanent-magnet motor drives. I. The permanent-magnet synchronous motor drive," *IEEE Transactions on Industry Applications*, vol. v, pp. 265–273, 1989.
- [18] S. Vaez-Zadeh, "Variable flux control of permanent magnet synchronous motor drives for constant torque operation," *IEEE Transactions on Power Electronics*, vol. 16, no. 4, pp. 527–534, 2001.
- [19] Z. Haigang, Q. Weiguo, W. Yanxiang, G. Shihong, and Y. Yuan, "Modeling and simulation of the permanent magnet synchronous motor drive," in *Proceedings of the International Conference on Uncertainty Reasoning and Knowledge Engineering Energy*, pp. 256–260, 2011.
- [20] B. K. Bose, *Modern Power Electronics and AC Drives*, Pearson Education, Upper Saddle River, NJ, USA, 1st edition, 2003.
- [21] R. Krishnan, *Electric Motor Drives- Modeling Analysis and Control*, Pearson Prentice Hall, Upper Saddle River, NJ, USA, 1st edition, 2007.
- [22] *Proficy Machine Edition 5. 90 User's Manual*, GE Fanuc, Yamanashi, Japan, 2007.
- [23] "Versa Motion Servo Motors and Amplifiers User's Manual," Tech. Rep. GFK-2480, GE Fanuc, Yamanashi, Japan, 2007.



# Effect of different metallic nano-inclusions (Ag, Al, Au and Cu) and gain assistance for isotropic left-handed photonic material in blue light region

M. Rajput<sup>a</sup>, R.K. Sinha<sup>a,\*</sup>, S.K. Varshney<sup>b,2</sup>

<sup>a</sup> TIFAC-Centre of Relevance and Excellence in Fiber Optics and Optical Communication, Department of Applied Physics, Delhi Technological University (Formerly Delhi College of Engineering, Faculty of Technology, University of Delhi), Bawana Road, Delhi-110042, India

<sup>b</sup> Department of Electronics & Electrical Communication Engineering, Indian Institute Technology Kharagpur, 721302, West Bengal, India

## ARTICLE INFO

### Article history:

Received 22 March 2011

Received in revised form

16 October 2012

Accepted 19 October 2012

### Keywords:

Negative index materials

Left-handed materials

Photonic crystals

## ABSTRACT

A gain assisted Double Negative-Metallo-Semiconductor Photonic Crystal (DN-MSPC) for blue light with effect of different plasmonic (Al, Ag, Au, Cu) nanorod inclusions is presented. Effect of different metal nanocomposites and inverted host matrix, on dispersion and transmission properties of the designed DN-MSPC is demonstrated. Negative real values of both permeability ( $\mu$ ) and permittivity ( $\epsilon$ ) with extremely low imaginary values in the visible region are obtained by applying coupled dipole approximation for different nanocomposites. It is shown that index matching to the incident medium and compensated losses due to the gain assistance lead to the light amplification in the designed structure. A comparison of dispersion properties and left-handed resonance for different plasmonic nanocomposites of a similar shape and geometry shows permittivity-dependent dispersion and resonant properties. Fabrication tolerance with effect of change in plasmonic nanorod radius by  $\pm 10\%$  is also analyzed. Furthermore, the sensitivity of the left-handed transmission to index changes of the host material (i.e., refractive index sensitivity) and highest left-handed transmission efficiency ( $> 99\%$ ) is also investigated for biosensing application.

© 2012 Elsevier Ltd. All rights reserved.

## 1. Introduction

In 1968, Veselago predicted negative index materials (NIMs) with simultaneously negative permittivity  $\epsilon$  and permeability  $\mu$  forming a left-handed triplet of wave vector  $\mathbf{k}$ , the electric field vector  $\mathbf{E}$  and the magnetic field vector  $\mathbf{H}$  for an isotropic medium, called left-handed materials (LHMs) or “double-negative material (DNM)” [1]. According to his analysis, in such a DNM, the poynting vector of a plane wave is anti-parallel to its phase velocity. In LHMs light is allowed to bend in a direction opposite to that of ordinary material. This phenomenon is called negative refraction (NR) (Fig. 1). It is noticed that in such a material the wave vector  $\mathbf{k}$  is anti-parallel to the poynting vector. Hence, energy propagates against the wave vector and phase lies in the propagation direction.

After more than 30 years, in 1999 Pendry demonstrated a design of NIM with composite structure consisting of rows of split ring resonators and wire strips [2,3]. Negative refraction in microwave region is also observed in the NIMs, where both

electric permittivity and magnetic permeability are negative [4–6]. In 2000, Notomi proposed a pioneering theory of electromagnetic propagation in strongly modulated photonic crystal and the refraction in the vicinity of photonic band gap [7]. However, the remarkable phenomenon of all angle negative refraction (AANR) in infrared region from 2-D and 3-D photonic crystals was well explained by Luo et al. in 2002 [8]. In the same year Baba and Mastumoto analyzed the photonic crystal superprism wavelengths around  $1.5 \mu\text{m}$  [9]. Researchers have also explored similar light behavior i.e. phenomenon of NR, by engineering the dispersion properties of dielectric and metallic Photonic crystals (PhC) in IR and microwave region [7–16] with and without negative refractive index. However, in recent past, there has been explosive interest in negative refraction and NIM in visible region with a view of their application in the design and development of photonic devices at nanoscale. Split ring resonator (SRR) structures at nanoscale have been designed to achieve NIM in the infrared region and suffer with saturation limit of resonant magnetic response with a negative effective permeability at optical frequencies [17,18]. Following these issues, alternative approaches to design and develop new materials exhibiting negative refraction have attracted attention of researchers [19–26,28].

In our previous paper, we have achieved AANR in visible region with only aluminum nanorod inclusion in lossless semiconductor host material [26]. There was no amplification in

\* Corresponding author. Tel.: +91 11 27871017; fax: +91 11 27871023.

E-mail addresses: monika\_scholar@yahoo.com (M. Rajput),

dr\_rk\_sinha@yahoo.com (R.K. Sinha),

skvarshney@ece.iitkgp.ernet.in (S.K. Varshney).

<sup>1</sup> Tel.: +91 11 27871017, fax: +91 11 27871023.

<sup>2</sup> Tel.: +91 3222 283504 (O), fax: +91 3222 282264.

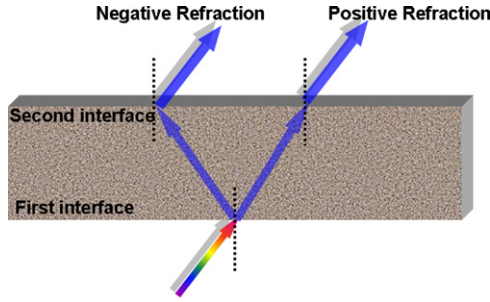


Fig. 1. Schematic exhibiting negative and positive refraction.

output signal because host material used for the designing LHM was considered to be lossless.

In present paper, we present the study and effect of different metal nanocomposites on dispersion and transmission properties of the designed left-handed photonic crystal structure with an inverted or host material in gain state. Aluminum (Al), Silver (Ag), Gold (Au) and Copper (Cu) are used in order to study the effect of different metal nanocomposites. Dispersion properties of designed DN-MSPC with different metallic nanorod inclusion are presented. All angle negative refraction for transverse magnetic<sup>TM</sup> polarization of blue light with different metallic nanoinclusion is observed, however, dispersion properties of the designed DN-MSPC changed dramatically for different metallic nanorod inclusion. The  $\epsilon$  and  $\mu$  values of the medium also define the state of any material i.e. gain state or loss state, which can be determined by the sign of  $[\epsilon]\text{Im}\mu + |\mu|\text{Im}\epsilon$ . The expression with positive sign i.e.,  $[\epsilon]\text{Im}\mu + |\mu|\text{Im}\epsilon > 0$ , represents the loss state of a medium and with the negative sign i.e.,  $[\epsilon]\text{Im}\mu + |\mu|\text{Im}\epsilon < 0$ , represents the gain state of a medium. The gain state in the designed DN-MSPC is achieved for the blue light; however, wavelength bandwidth region for gain assistance varies with different plasmonic nanocomposites. Coupling and resonant excitation between plane and polariton wave also contribute in the light amplification. Therefore, the blue light grows exponentially inside the structure due to gain state of the medium and amplification of the light is achieved. Gain assisted isotropic MSPC yielding real part of electric permittivity and magnetic permeability negative ( $\epsilon < 0$  and  $\mu < 0$ ) with low values of their imaginary parts forming DNM. Hence, a NIM having negative values of  $\epsilon$  and  $\mu$  is obtained, which yields a shrinking dispersion relation with increasing frequency in an isotropic medium.

In order to confirm the validity of the proposed structure as an efficient LHM, a high (99%) left-handed transmission efficiency (LHTE) of the designed DN-MSPC is also achieved. This value of LHTE is highest to the best our knowledge. The calculated LHTE has different value with different plasmonic nanoinclusions and decreases from Al to Cu as; Al (99%) > Ag (89%) > Au (78%) > Cu (71%). Fabrication tolerance analysis was further performed by varying the plasmonic nanorod radius for  $\pm 10\%$  and its effect on the left-handed and right-handed transmission characteristics is studied. Refractive index sensitivity of the proposed DN-MSPC for various dielectric environments (corresponding refractive index of host matrix) is determined. Demonstration of resonance spectrum of DN-MSPC shows the potential of the proposed structure in the design and development of highly directional optical nano-antenna, miniature polarizer and filter devices.

In order to study the design and implement optical LHM, it is essential to study the basic constitute material including host semiconductor matrix and included metal behavior. In the analysis of designed structure: (i) we discuss the optical properties of used inverted semiconductor material and considered metals,

(ii) comparison of the dispersion properties of designed MSPC with different metallic nano-inclusion is presented with the conclusion that Ag and Al are the best suitable metals to form a isotropic LHM in blue region of visible light, (iii) the study of the proposed MSPC as a left-handed effective medium, where we calculate and compare the value of permittivity ( $\epsilon$ ) and permeability ( $\mu$ ) of the designed medium using coupled dipole approximation (CDA) [27] for both Al and Ag nano-inclusions, (iv) transmission spectrum is also demonstrated of the designed MSPC with different metallic nano-inclusion (Ag, Al, Ag and Cu), which shows a good agreement with numerical analysis. In this section effect of metal on transmission properties and left-handed transmission efficiency is also demonstrated, (v) nanophotonic device application potential of the designed MSPC is also discussed. Hence, designed structure is used to demonstrate AANR and its applications as a polarizer, wavelength filter and optical nano-antenna at nanoscale are also investigated, and (vi) fabrication tolerance analysis and refractive index sensitivity (RIS) of the proposed DN-MSPC are determined.

## 2. Design and analysis

### 2.1. Optical properties of the host semiconductor and included metal

We consider a hexagonal lattice of metallic nano-rods immersed in an inverted host semiconductor matrix GaAs [29–32]. Study and comparison of the effect of different plasmonic nanorod inclusions (Ag, Al, Au, Cu) on transmission and dispersion characteristics of designed structure is presented. The dielectric response of the host matrix (GaAs) is calculated by the Lorentz model,

$$\epsilon_h = \epsilon_\infty + \frac{A\omega_0^2}{\omega_0^2 - \omega^2 - i\omega\gamma}$$

where,  $\epsilon_\infty$ ,  $\omega_0$ ,  $\gamma$  and  $A$  is the permittivity at higher frequencies, the resonant frequency, the damping coefficient and macroscopic analog of Lorentz oscillator strength, respectively, that describe the concentration of quantum dots and the fraction of quantum dots in the excited state and ground state. Therefore, the parameter  $A$  resembles the gain and loss in the medium. Here medium can be classified into three categories based on  $A$  value: (i)  $A > 0$  corresponds to lossy medium, (ii)  $A = 0$  corresponds to number of quantum dots in excited state which are equal to the number of the quantum dots in ground state and (iii)  $A < 0$  corresponds to gain or inverted medium. Inverted medium can be achieved by external optical pumping or changing quantum dot doping and sample temperature [32–37]. For the proposed structure we have considered,  $A < 0$  ( $A = -0.03$ ), which gives inverse behavior for the host matrix. The permittivity behavior of the host matrix is shown in Fig. 2(b) and (c). Radius of nano-rods is  $r = 0.35a$ , (where,  $a = 125$  nm is the lattice constant), corresponds to filling fraction  $p$  and equals to 0.44.

The dielectric spectral response of four selected metals (Al, Ag, Au, and Cu) is observed using the Drude model [16] and is shown in Fig. 2(c) and (d). The Drude model of dielectric function is,

$$\epsilon = \epsilon_\infty - \frac{\omega_p^2}{\omega^2 + i\omega\omega_\tau}$$

where, real part represents,  $\epsilon_r = \epsilon_\infty - \frac{\omega_p^2}{\omega^2 + \omega_\tau^2}$ , and imaginary part is,  $\epsilon_{\text{Im}} = \frac{\omega_p^2\omega_\tau}{\omega^3 + \omega\omega_\tau^2}$ .

Here plasma frequency is expressed as,  $\omega_p = \frac{1}{2\pi\epsilon_0} \left[ \frac{4\pi Ne^2}{me_\infty} \right]$  and  $\omega_\tau$  is the damping frequency. The values of ( $\omega_p$ ,  $\omega_\tau$ ) for Al, Ag, Au and Cu are (3570, 19.4) THz, (2175, 4.35) THz, (2179, 6.5) THz and (2610, 8.34) THz respectively. Negative response of real  $\epsilon$  increases with increasing wavelength for various plasmonic

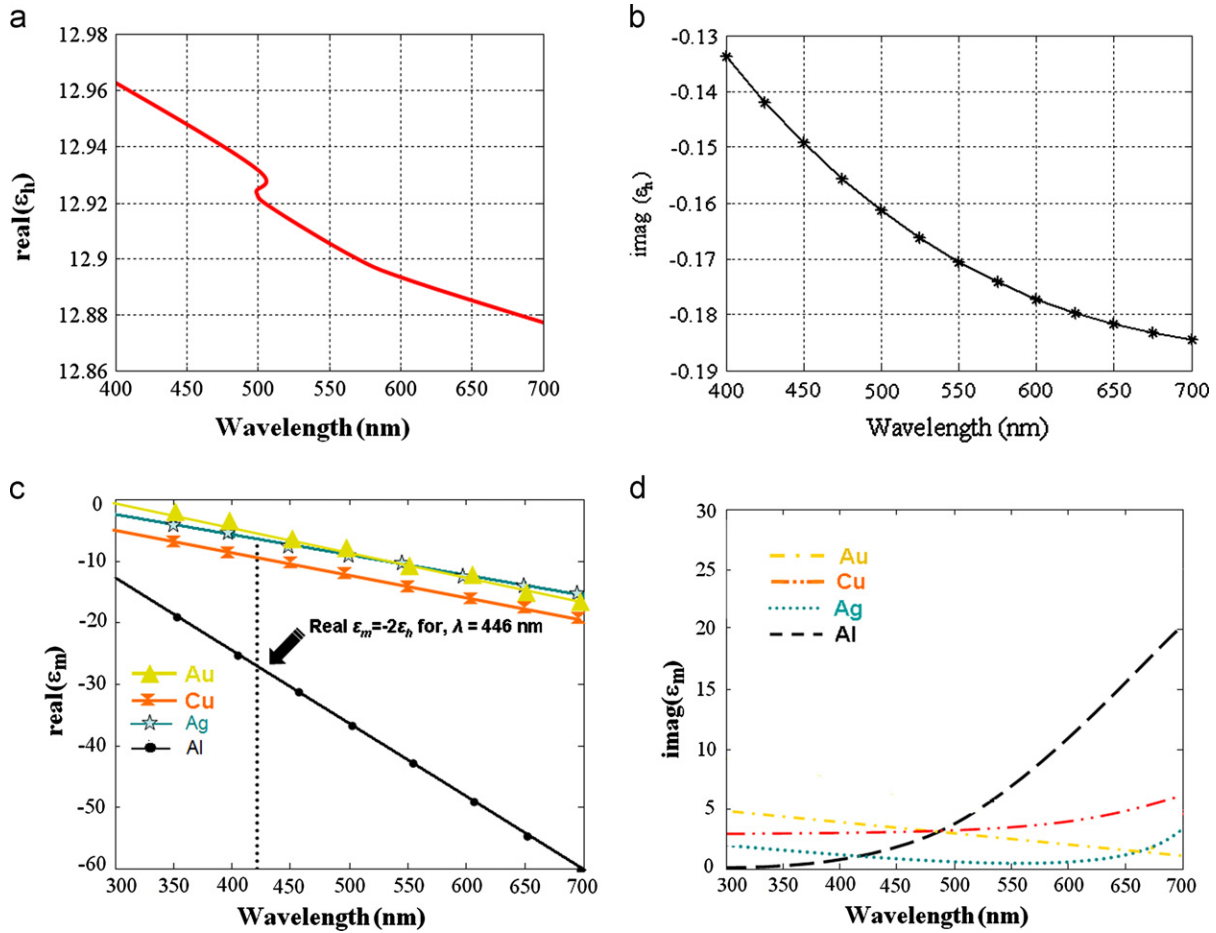


**Fig. 2.** Variation in (a) real and (b) imaginary parts of the dielectric permittivity with wavelength for inverted GaAs. Spectral response of (c) real  $\epsilon$  and (d) Im  $\epsilon$  for Al, Ag, Cu, Au.

metals. It is observed that Al shows plasmon excitation activity for the wavelength region from 200 to 750 nm with largest plasmonic behavior (i.e. largest negative real  $\epsilon$  values) for entire visible range than any other metal. From Fig. 2(d), the response of Im  $\epsilon$  with wavelength shows that absorption losses in ultraviolet and blue region of visible light are minimal for Al and Ag. However, Au and Cu are more suitable for infrared region and red region of visible light. The condition for surface plasmon polariton excitation (SPPE) is satisfied for different metals i.e., any interface between two media having electric permittivity ( $\epsilon$ ) with opposite signs of their real parts can support excitation of surface plasmon polariton. However, the condition for nano-particle polariton (NPP) ( $\epsilon_m \approx -2\epsilon_h$ ) is satisfied at  $\lambda = 446$  nm for the Al metal [39].

## 2.2. AANR and effect of different plasmonic nanocomposites

To study the refraction properties of light, band diagram and equi-frequency surface (EFS) curves for the proposed structure are obtained by employing plane wave expansion (PWE) method as shown in Fig. 3. The red curve in the band diagram corresponds to TE mode whereas blue curve stands for TM mode. It is observed that negative refraction can be achieved in the proposed structure with different metallic nano-inclusion but exhibiting different dispersion properties.

The salient features of dispersion diagrams of designed structure are: (i) band gap exist for TE polarization for the designed DN-MSPC, where the frequency bandwidth varies with different plasmonic nanorod inclusions. Normalized frequency ( $f$ ) band gap region for TE mode with different plasmonic nanocomposites decreases as: Ag ( $f = 0.215$  to  $0.41$ ) > Al ( $f = 0.22$  to  $0.33$ ) > Au ( $f = 0.215$  to  $0.26$ ) > Cu ( $f = 0.2$  to  $0.22$ ), (ii) in the second band of TM polarization for designed structure downward band folding (frequency decreases as magnitude of the wave vector increases) is shown. It indicates backward phase propagation and therefore wave vector  $\mathbf{k}$ , the electric field component  $\mathbf{E}$  and magnetic field component  $\mathbf{H}$  form a left-handed triplet, (iii) band diagram shows the interaction of light-line with downward moving band for designed DN-MSPC with all plasmonic nanocomposites (At  $f = 0.28$  with Al). This shows phase index ( $n_p$ ) is equal to 1.0 for designed structure and gives the ideal frequency range for negative refraction with index matching to the incident medium [16]. The light-line is represented by the gray line in band diagrams, (iv) light-line intersection with the corresponding eigen value curve indicates the maximum frequency for which free space EFS is included in EFS of designed crystal, which AANR. Here, EFS are circular for the top values of second band and the light shows isotropic behavior in this frequency range. Hence  $\mathbf{k}$  is anti-parallel to the poynting vector  $\mathbf{S}$  at all angles that shows negative effective index for all incident angles. It is observed that designed DN-MSPC shows more isotropic behavior with Ag and Al nanocomposites in comparison to Cu and Au nanocomposites,

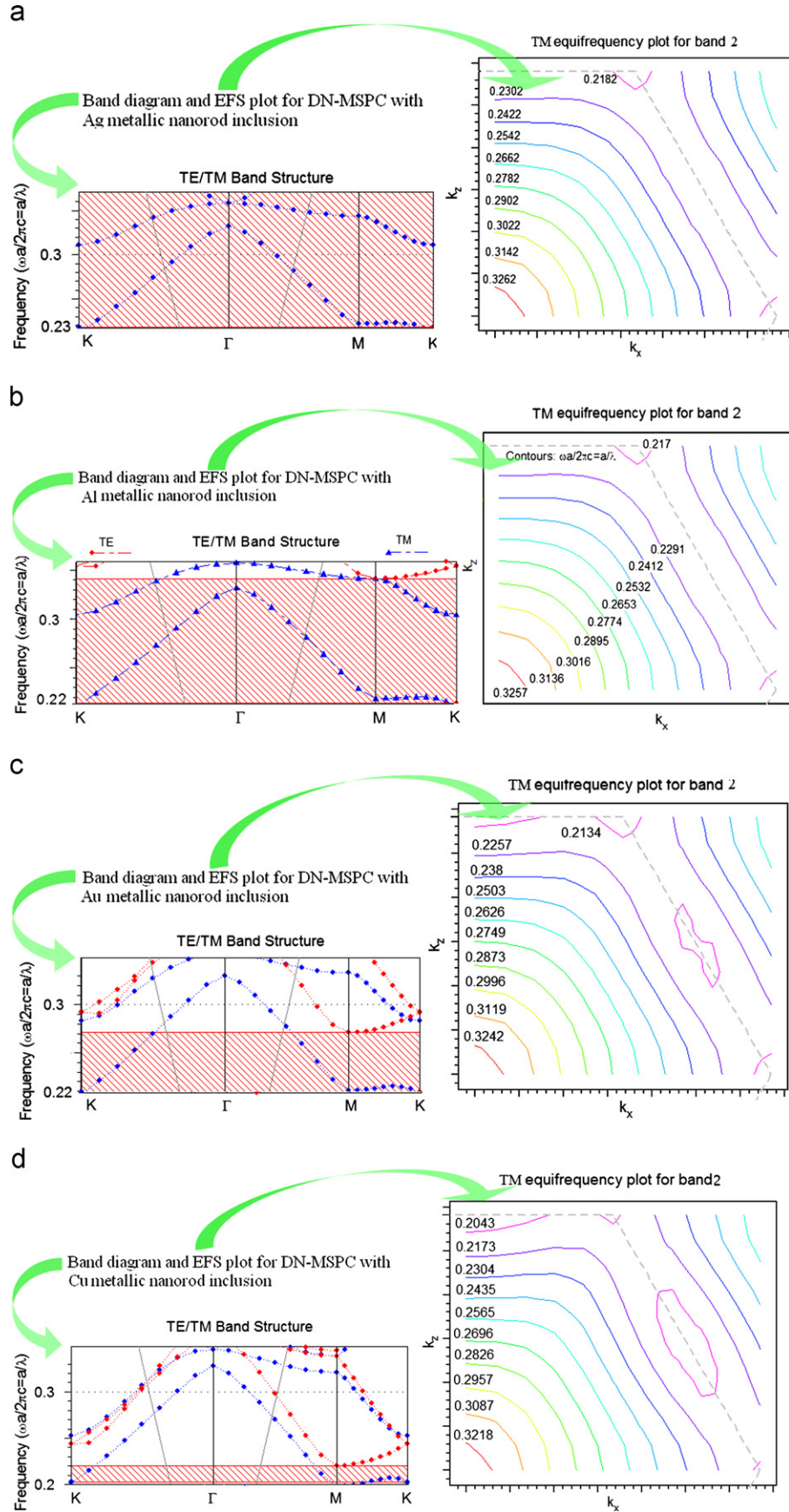


**Fig. 3.** Band structure and EFS of the designed DN-MSPC with (a) Ag, (b) Al, (c) Au, (d) Cu plasmonic metal inclusions, where 2nd band (shaded) and EFS for TM polarization shows negative refraction. Gray line represents light-line in the left-hand side part (band-diagram) of each figure. (For interpretation of the references to color in this figure, the reader is referred to the web version of this article.)

and (v) the EFS that move outwards from the center with increasing frequency corresponds to right-handed material (RHM) with  $\mathbf{v}_g \cdot \mathbf{k}_f > 0$  and inwards moving EFS corresponds to LHM with  $\mathbf{v}_g \cdot \mathbf{k}_f < 0$ . Unusual behavior ( $\mathbf{v}_g \cdot \mathbf{k}_f < 0$ ) of EFS for second band of designed structure with all four plasmonic metals confirmed the negative refractive index (Fig. 3(b)) [14,15].

Above comparison of dispersion properties for Al, Ag, Cu, and Au nanocomposites of a similar shape and geometry shows permittivity-dependent behavior. Hence, a left-handed isotropic structure exhibiting AANR with SPP wave excitation is proposed in this paper. From Fig. 3, it is observed that the isotropic behavior of EFS for TM mode and band-gap region for TE mode is varied for different plasmonic nanorod inclusions in the same host matrix. The curvature of the EFS is showing increasing convex behavior towards the center as we shift toward to Cu from Ag nanoinclusion. It is concluded that Al and Ag nanocomposites are more suitable to form isotropic left-handed structure in shorter wavelength region. The band-gap for TE polarization is the maximum for designed DN-MSPC with Ag nanocomposite and it is gradually decreasing with changing the metallic nanoinclusion from Ag to Cu.

### 2.3. Gain state in the DN-MSPC and negative parameters ( $\epsilon$ and $\mu$ )

The state (either gain or loss) of any material depends upon the  $\epsilon$  and  $\mu$  values of the medium and can be determined by the

sign of  $[\epsilon \text{Im}\mu + \mu \text{Im}\epsilon]$  as explained before. This given expression with positive sign represents loss state of the medium whereas with negative sign corresponds to the gain state of the medium [29]. Hence, variation of effective parameters ( $\epsilon$  and  $\mu$ ) with wavelength of the designed structure to explain its state, are also studied. As shown in Section 2, the condition for surface plasmon polariton wave excitation is already achieved around  $\lambda = 446$  nm, for designed structure (Fig. 2(d)) for different plasmonic metals. Excited SPP wave conserves its surface nature for a finite length nano-rod system and an efficient coupling with the plane wave occurs that is absent in infinite system. Therefore, coupling and resonant excitation between plane and Polariton wave is also responsible for the light amplification in the proposed DN-MSPC. The efficiency of SPP coupling is based upon the distance between two nano-rods, where the symmetric and anti-symmetric combination of two SPP waves correspond to electric and magnetic dipole moment in the system, respectively. To calculate electric and magnetic dipole moment, we consider a material, composed of pairs of nanorods parallel to each other. To evaluate the magnetic permeability and electric permittivity the composite medium is deduced by coupled dipole approximation, as mentioned in Reference [27]. Hence, variation of effective parameters ( $\epsilon$  and  $\mu$ ) of the paired plasmonic nano-rod composite is shown in Fig. 4, where the condition for LHMs or NIMs ( $\epsilon < 0$  and  $\mu < 0$ ) is satisfied. For the proposed structure, negative real parts of  $\epsilon$  and  $\mu$  with low values of their imaginary parts are achieved. Hence, NR

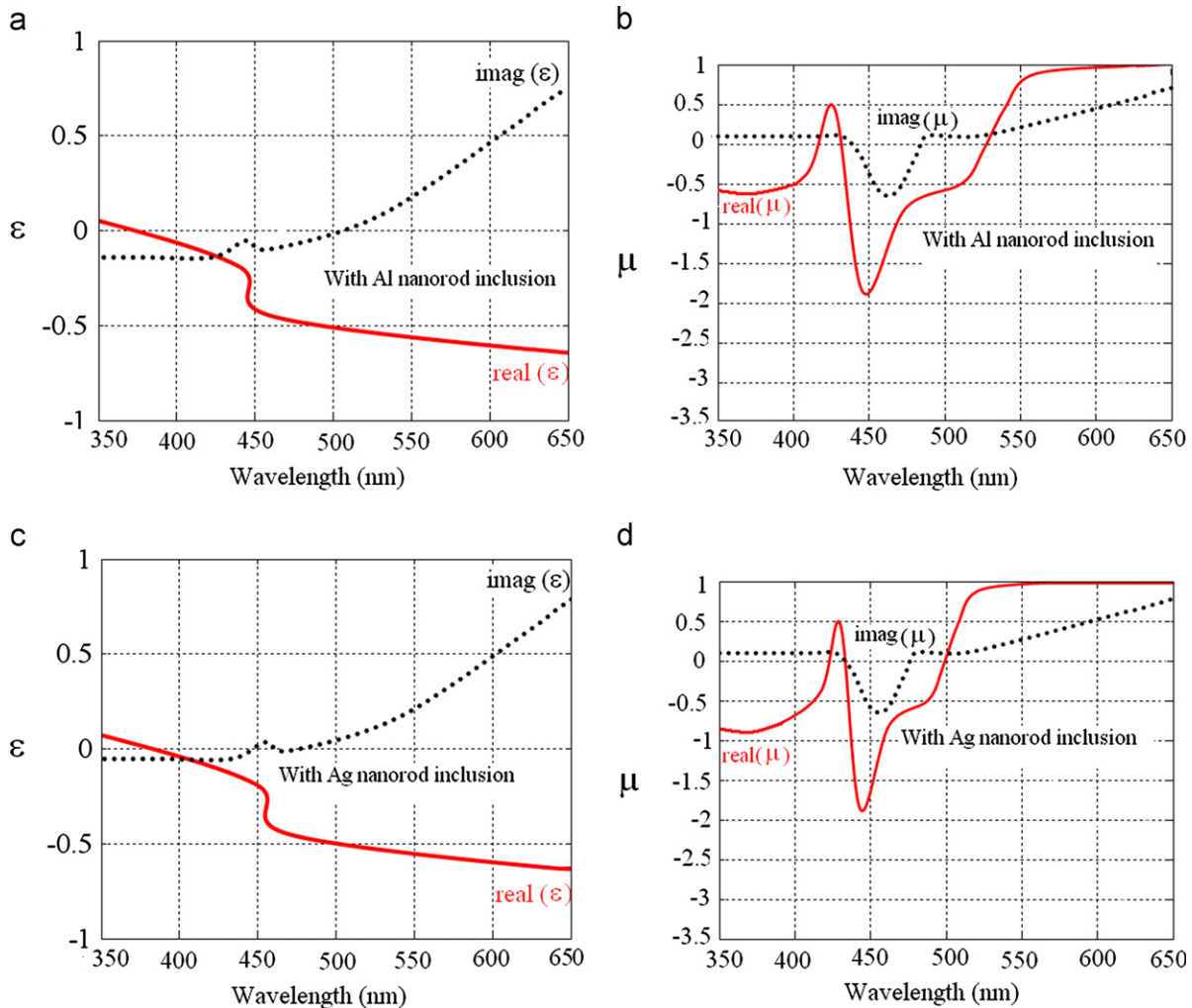


**Fig. 4.** Spectral variation of permittivity (a and c) and permeability (b and d) for paired nanorod designed structure having  $l = 445$  nm,  $r = 43.75$  nm and  $a = 125$  nm, for Al and Ag respectively. This confirms the negative refractive index in visible region with gain assistance for blue light.

having high transmission with minimum losses can be observed from the designed. Further, the vacuum wavelength of resonance can be determine as,  $\lambda_o = n_h \sqrt{(10\kappa(2\delta^2 + r^2)\ln\kappa)}$  here,  $n_h$  is the refractive index of the host matrix,  $\kappa = l/r$  is the aspect ratio and  $\delta = c/\omega_p$  is the skin depth of the metal. As explained earlier, the state (either gain or loss) of any material depends upon the sign of  $[\epsilon|\text{Im}\mu + |\mu|\text{Im}\epsilon]$  i.e. positive sign represents loss state of the medium whereas negative sign corresponds to the gain state of the medium [29]. From Fig. 4(a) and (c), it is observed that imaginary part of the permittivity corresponding to Al and Ag nanocomposites, has negative values from  $\lambda = 400$  to  $520$  nm and from  $\lambda = 400$  to  $460$  nm, respectively. This behavior fulfills the condition for the gain state of a medium [38] and provides the amplification of the blue light in the designed left-handed DN-MSPC over a broad wavelength range. Therefore, the proposed structure undergoes a transition from low-gain state to low-loss state due to variation of permittivity as shown in Fig. 4(a) and (c).

From Fig. 4, it is observed that the real values of both electric and magnetic dipole moments are comparable. Note that higher moments are vanished and highly directional emission with NR is achieved for the proposed DN-MSPC and shows potential to be used as a highly directional optical nano-antenna.

### 3. Optical and spectral analysis

#### 3.1. Transmission characteristics of the designed DN-MSPC with effect of different metallic inclusion on resonance properties

To get more insight about electromagnetic response of the designed DN-MSPC, the field map is shown in Fig. 5. The FDTD results show the NR for TM polarization (Fig. 5(a)) and complete reflection for TE polarization (Fig. 5(b)), demonstrating the polarization functionality of the proposed structure. Fig. 5(c) shows an amplified left-handed transmission spectrum for Ag, Al, Cu and Au nanorod arrays in inverse GaAs host environment with a similar shape and geometry. The resonance maxima for Ag, Al, Cu and Au nanocomposites are in decreasing order. The left-handed transmission wavelength maxima of Ag, Al, Cu and Au are  $4455$  nm,  $446$  nm,  $447$  nm, and  $4475$  nm, respectively. The approximate value of the full width at half maximum (FWHM) is maximum for Al and minimum for Ag. Comparison of the left-handed resonance for Cu, Ag, Au, and Al nanocomposites with similar shape and geometry shows that resonance maximum follows the order  $\text{Ag} > \text{Al} > \text{Cu} > \text{Au}$ , while the FWHM varies as  $\text{Al} > \text{Au} > \text{Cu} > \text{Ag}$ . Study of resonance behavior for Al, Cu, Ag, and Au concludes that the Ag nanocomposites display a most intense and sharper left-handed transmission compared to the other metals in the visible region.

#### 3.2. Left-handed transmission efficiency (LHTE)

In order to confirm the validity of the proposed structure as a LHM, its left-handed transmission efficiency (LHTE) is calculated, which is defined as,

$$\text{LHTE} = \left[ \frac{\{\text{Transmission in negative direction } (T_{NR})\} - \{\text{Transmission in positive direction } (T_{PR})\}}{\text{Transmission in negative direction } (T_{NR})} \right] \times 100\%$$

here, LHTE is calculated to be more than 99% with Al nanocomposites for designed DN-MSPC. Hence the proposed structure is highly efficient as a LHM and exhibits the property of directional optical nano-antenna. However, LHTE of designed DN-MSPC with different plasmonic nanocomposites has the order shown in Table 1.

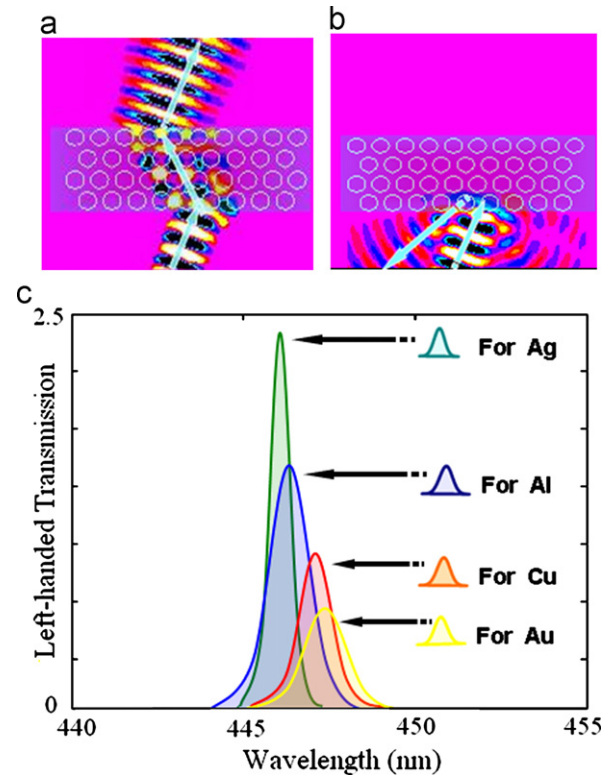


Fig. 5. Field map of (a) TM polarization exhibiting NR, (b) TE polarization exhibiting no propagation, from proposed design of DNM at  $\lambda = 446$  nm for incident angle of  $25^\circ$  and (c) comparison of the left-handed transmission of Ag, Al, Cu, and Au for a similar size and shape nanorod inclusions in proposed DN-MSPC.

Table 1

Variation of LHTE with different plasmonic nano-inclusion in designed LHM.

Plasmonic nanocomposites	Al (%)	Ag (%)	Au (%)	Cu (%)
LHTE	99	89	78	71

### 4. Tolerance analysis

We have carried out the tolerance analysis of the proposed DN-MSPC by considering: (i) a  $\pm 10\%$  variation in plasmonic (with Al and Ag) nanorod radius, and (ii) varying the refractive index of the host material.

#### 4.1. Effect of change in plasmonic nanorod radius

Change in transmission for  $\pm 10\%$  variation in plasmonic (with Al and Ag) nanorod radius is shown in Fig. 6.

The variation of left-handed and right-handed transmission is plotted on the both left and right hand y-axes, respectively and tolerance is shown on x-axis. The solid and dashed blue curves

represent the tolerance of left-handed transmission, while green solid and dotted curves correspond to the tolerance of right-handed transmission for Ag and Al nanocomposites, respectively. Tolerance analysis for Al and Ag nanocomposites is tabulated in Tables 1 and 2, respectively.

4.2. Refractive index sensitivity (RIS)

Study of variation in refractive index of the host matrix (different dielectric environments) and its impact on transmission and reflection characteristics of the designed DN-MSPC is demonstrated in Fig. 7.

Fig. 7(a) shows the transmission spectra for plasmonic Al nanocomposite in different refractive index environments. Effect of host dielectric environment on left-handed transmission, right-handed transmission and reflection is evaluated and is shown in Fig. 7. The variation in refractive index is chosen from  $n=3.5$  to 3.7. As shown in Fig. 7(a), the left-handed transmission increases,

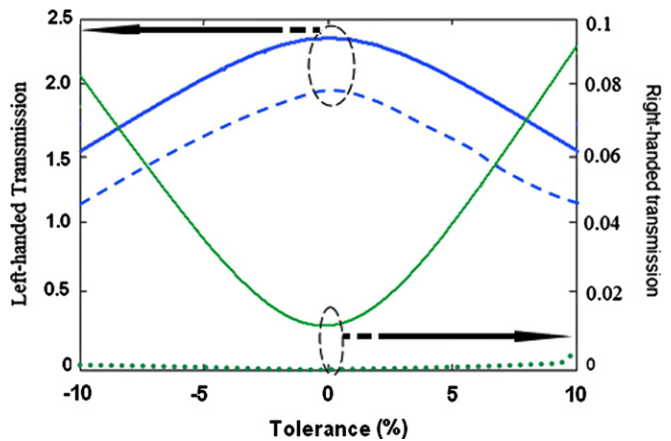


Fig. 6. Effect of tolerance in plasmonic (Al and Ag) nanorod radius on the left-handed and right-handed transmission of proposed DN-MSPC. (For interpretation of the references to color in this figure, the reader is referred to the web version of this article.)

Table 2  
Tolerance analysis of DN-MSPC for Al nanocomposites.

Variation in nanorod radius	Variation in intensity (a.u.) of left-handed transmission	Variation in intensity (a.u.) of right-handed transmission
0% to 10% (increase)	1.87 to 1.3 (decreases)	0.0004 to 0.00121 (increases)
0% to -10% (decrease)	1.87 to 1.3 (decreases)	0.0004 to 0.001 (increases)

when the RI of the medium increases and the slope of this plot yield a RI sensitivity of 1.2/Refractive index unit (RIU). The computed right-handed transmission and reflection values are minimum at  $n=3.6$ . The RIS for right-handed transmission and reflection are calculated as 0.2/RIU and 0.3/RIU, respectively. Fig. 7(b) represents the RIS of Ag nanocomposite. It is observed that RIS of Ag nanocomposite is much higher than the RIS of Al nanocomposite for the same dielectric environments. Left-handed transmission slope for Ag nanocomposite in Fig. 7(b) yields a RIS of  $\approx 5$ /RIU, which is much higher than that observed RIS for Al nanocomposites. Hence, designed DN-MSPC is more sensitive to the index change of the environment with Ag nanocomposites in comparison to Al nano-composites and shows bio-sensing application potential (Table 3).

5. Conclusion

We have studied and demonstrated the effect of different metallic (Al, Ag, Au and Cu) nanorod inclusion on the dispersion and transmission properties of the designed isotropic DN-MSPC. The AANR and index matching with incident medium for blue light region is also demonstrated by exploring their dispersion properties. It is also concluded that Al and Ag nanocomposites are more suitable to form isotropic left-handed structure in shorter wavelength region. The bang-gap for TE polarization is the maximum for designed DN-MSPC with Ag nanocomposite and it is gradually decreasing with changing metallic nanoinclusion from Al to Cu. Implementation of coupled dipole approximation provides negative real values for both permeability  $\mu$  and permittivity  $\epsilon$  with extremely low imaginary values in the visible region. The designed DN-MSPC exhibits gain assistance for blue light and therefore amplification of blue light is achieved in the structure. Comparison and calculation of their real and imaginary

Table 3  
Tolerance analysis of DN-MSPC for Ag nanocomposites.

Variation in nanorod radius	Variation in intensity (a.u.) of left-handed transmission	Variation in intensity (a.u.) of right-handed transmission
0% to 10% (increase)	2.31 to 1.55 (decreases)	0.012 to 0.091 (increases)
0% to -10% (decrease)	2.31 to 1.55 (decreases)	0.012 to 0.081 (increases)

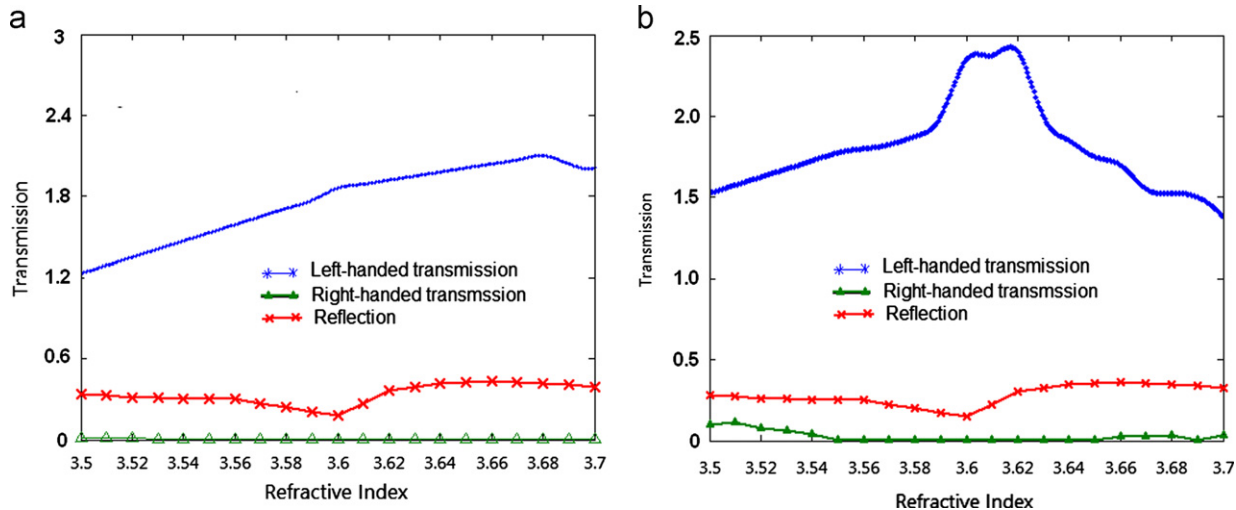


Fig. 7. Transmission (left-handed and right-handed) and reflection vs. variation in refractive index of the host matrix in proposed DN-MSPC for (a) Al and (b) Ag nanocomposites.

permeability and permittivity exhibit that the structure with Al nanocomposites has larger bandwidth for gain state for visible light in compare to Ag nanocomposites. A comparison of left-handed resonance for Al, Ag, Cu, and Au nanocomposites of a similar shape and geometry shows permittivity-dependent resonant behavior, where left-handed intensity maximum has the order  $\text{Ag} > \text{Al} > \text{Cu} > \text{Au}$ , while the FWHM satisfies the order  $\text{Al} > \text{Au} > \text{Cu} > \text{Ag}$  for blue light. Extremely high left-handed transmission efficiency is also calculated for the proposed DN-MSPC that is found to be in the order Al nanocomposites (99%) > Ag nanocomposites (89%) > Au nanocomposites (78%) > Cu nanocomposites (71%). Further, tolerance analysis was performed to check the effect on left-handed resonance characteristics for  $\pm 10\%$  variation in plasmonic nanorod radius of the proposed DN-MSPC that shows good fabrication skills. The refractive index sensitivity of plasmonic nanocomposites (for Al and Ag) for various dielectric environments is also determined that can be utilized for biosensing applications. It is observed that Al nanocomposites (1.2/RIU) have less refractive index sensitivity in comparison of Ag nanocomposites (5/RIU) with same structural parameters. Study of resonance spectra of proposed DN-MSPC display various functions e.g. polarization sensitivity, filtering over broad range of visible light, light ruling, and highly directional optical nano-antenna application.

## Acknowledgment

The authors gratefully acknowledge the initiatives and support towards establishment of “TIFAC Centre of Relevance and Excellence in Fiber Optics and Optical Communication at Delhi Technological University (formerly known as Delhi College of Engineering) Delhi” through “Mission REACH” program of Technology Vision-2020, Government of India.

## References

- [1] Veselago VG. Soviet Physics Uspekhi 1968;10:509–14.
- [2] Pendry JB, Holden AJ, Robbins DJ, Stewart WJ. IEEE Transactions on Microwave Theory and Techniques 1999;47:2075–84.
- [3] Pendry JB, Holden AJ, Stewart WJ, Youngs I. Physical Review Letters 1996;76:4773–6.
- [4] Shelby RA, Smith DR, Schultz S. Science 2001;292:77–9.
- [5] Parazzoli CG, Greger RB, Li K, Koltenbah BEC, Tanielian M. Physical Review Letters 2003;90:107401–4.
- [6] Houck A, Brock JB, Chuang IL. Physical Review Letters 2003;90:137401–4.
- [7] Notomi M. Physical Review B 2000;62:10696–705.
- [8] Luo C, Johnson SG, Joannopoulos JD. Physical Review B 2002;65:201104–01–201104–04.
- [9] Baba T, Matsumoto T. Applied Physics Letters 2002;81:2325–7.
- [10] Joannopoulos JD, Villeneuve P, Fan S. Nature (London) 1997;386:143–9.
- [11] Martinez A, Miguez H, Sanchez-Dehesa J, Marti J. Optics Express 2005;13:4160–74.
- [12] Cubukcu E, Aydin K, Ozbay E, Foteinopoulou S, Soukoulis CM. Nature (London) 2003;423:604–5.
- [13] Schonbrun E, Yamashita T, Park W, Summers CJ. Physical Review B 2006;73:195117–1–6.
- [14] Parimi PV, Lu WT, Vodo P, Sokoloff J, Derov JS, Sridhar S. Physical Review Letters 2004;92:127401–1–4.
- [15] Vodo P, Lu WT, Huang Y, Sridhar S. Applied Physics Letters 2006;89:084104–43.
- [16] El-kady I, Sigalas MM, Biswas R, Ho KM, Soukoulis C. Physical Review B 2000;62:15299–302.
- [17] Zhou J, Koschny T, Kafesaki M, Economou EN, Pendry JB, Soukoulis CM. Physical Review Letters 2005;95:223902.
- [18] Aydin K, Li Z, Sahin L, Ozbay E. Optics Express 2008;16:8835–44.
- [19] Yao J, Liu Z, Wang Y, Sun C, Bartal G, Stacy AM, et al. Science 2008;321:930.
- [20] Yan C, Wang Q, Zhuo S, Cui Y. Optics Express 2008;16:13818–23.
- [21] Ramakrishna SA, Martin OJF. Optics Letters 2005;30:2626–8.
- [22] Zhang S, Fan WJ, Panoiu PC, Malloy KJ, Osgood RM. Physical Review Letters 2005;95:137404.
- [23] Dolling G, Wegener M, Soukoulis CM, Linden S. Optics Letters 2007;32:53.
- [24] Kussow A-G, Akyurtlu A, Semichaevsky A, Angkawisittpan N. Physical Review B 2007;76:195123.
- [25] Nehmetallah G, Aylo R, Powers P, Sarangan A, Gao J, Li H, et al. Optics Express 2012;20:7095–100.
- [26] Rajput M, Sinha RK. Applied Physics B 2010;98:99–106.
- [27] Podolskiy VA, Sarychev AK, Shalaev VM. Optics Express 2003;11:735–45.
- [28] Liu Y, Bartal G, Zhang X. Optics Express 2008;16:15439–48.
- [29] Singh J, editor. Optical properties of condensed matter and applications. Wiley Series in Materials for Electronic and Optoelectronic Applications; 2006.
- [30] Grosso G, Parravicini GP. Solid state physics. Academic Press: London, UK; 2000.
- [31] Hu ZG, Rinzan MBM, Matsik SG, Perera AGU, Von Winckel G, Stintz A, et al. Journal of Applied Physics 2005;97:093529.
- [32] Ironside CN. IEEE Journal of Quantum Electronics 1992;28:842–7.
- [33] Klimov VI, Mikhailovsky AA, Xu S, Malko A, Hollingsworth JA, Leatherdale CA, et al. Science 2000;290:314–7.
- [34] Maier SA. Optics Communications 2006;258:295–9.
- [35] Noginov MA, Zhu G, Bahoura M, Adegoke J, Small CE, Ritzo BA, et al. Optics Letters 2006;31(20):3022–4.
- [36] Fang A, Koschny T, Wegener M, Soukoulis CM. Journal of Optics 2010;12:13.
- [37] Ramakrishna SA, Pendry JB. Physical Review B 2003;67:201101.
- [38] Govyadinov AA, Podolskiy VA. Applied Physics Letters 2007;91:191103–6.
- [39] Klar TA. Nanophotonics with surface plasmon. In: Shalaev VM, Kawata S, editors. Netherland: Elsevier; 2007 [chapter 8].

## Review Article

# Genetically Modified Plants: Public and Scientific Perceptions

**Smita Rastogi Verma**

*Department of Biotechnology, Delhi Technological University, Delhi 110042, India*

Correspondence should be addressed to Smita Rastogi Verma; [srsmitrastogi@gmail.com](mailto:srsmitrastogi@gmail.com)

Received 15 January 2013; Accepted 10 February 2013

Academic Editors: W. A. Kues, J. Sereikaite, and J. J. Valdes

Copyright © 2013 Smita Rastogi Verma. This is an open access article distributed under the Creative Commons Attribution License, which permits unrestricted use, distribution, and reproduction in any medium, provided the original work is properly cited.

The potential of genetically modified plants to meet the requirements of growing population is not being recognized at present. This is a consequence of concerns raised by the public and the critics about their applications and release into the environment. These include effect on human health and environment, biosafety, world trade monopolies, trustworthiness of public institutions, integrity of regulatory agencies, loss of individual choice, and ethics as well as skepticism about the real potential of the genetically modified plants, and so on. Such concerns are enormous and prevalent even today. However, it should be acknowledged that most of them are not specific for genetically modified plants, and the public should not forget that the conventionally bred plants consumed by them are also associated with similar risks where no information about the gene(s) transfer is available. Moreover, most of the concerns are hypothetical and lack scientific background. Though a few concerns are still to be disproved, it is viewed that, with proper management, these genetically modified plants have immense potential for the betterment of mankind. In the present paper, an overview of the raised concerns and wherever possible reasons assigned to explain their intensity or unsuitability are reviewed.

## 1. Introduction

Genetically modified (GM) plants, also called transgenic plants, are designed to acquire useful quality attributes such as insect resistance, herbicide tolerance, abiotic stress tolerance, disease resistance, high nutritional quality, high yield potential, delayed ripening, enhanced ornamental value, male sterility, and production of edible vaccines. Another major goal for raising the GM plants is their application as bioreactors for the production of nutraceuticals, therapeutic agents, antigens, monoclonal antibody fragments biopolymers, and so forth [1]. Thus, GM plants can potentially affect many aspects of modern society, including agricultural production and medical treatment. Despite these potential applications, the use of GM plants for human welfare has been restricted owing to various concerns raised by the public and the critics. These concerns are divided into different categories, namely, health, nutritional, environmental, ecological, socioeconomic, and ethical concerns [2–25]. These concerns include those arising due to properties of GM plants themselves, those resulting from the spread of the transgenes to other organisms, and also those resulting from their

release into the environment. Such concerns have led to the withdrawal of commercialization of *Bt* cotton and *Bt* brinjal in India. The campaign against GM plants was fueled by the instances of transgenic potatoes reported to be deleterious to rats, contamination of commercial corn products with unapproved StarLink and killing of monarch butterfly by *Bt* corn pollen [26–28]. Furthermore, the nongovernmental organizations (NGOs) such as Gene Campaign, Center for Sustainable Agriculture, Research Foundation for Science, Technology and Ecology, Greenpeace, and Friends of the Earth have also raised concerns related to genetic manipulation of plants [28, 29]. The regulators, activists, media personnel and scientific journals have been indiscriminating and overly tolerant of the misrepresentations and distortions of anti-GM activists [30, 31]. There are not even scientific explanations for some of the concerns, but today the amount of misinformation is such that it has become difficult to separate truth from public perception about the GM plants. The biotechnology scientists, however, believe that GM plants should be given public acceptance because most of the concerns are not specific for GM plants and can exist for non-GM plants as well. In the present paper, a review of public

perspectives regarding GM plants and their disapproval on the basis of scientific background is presented.

## 2. Concerns Related to Health and Nutritional Status

In case the products of GM plants are to be consumed by humans and animals, there is always a fear and risk in the society that these plants may create health problems or may lead to the development of newer microbial strains that may be pathogenic. Further, the plants themselves may be susceptible to such risks. Public and critics are also skeptical about the nutritional content and quality of the GM plants. Such health and nutrition related concerns and their negation by scientists are described in this section.

**2.1. Susceptibility to Allergens.** One of the major distressing problems with nontraditional proteins in GM foods is the risk of introducing allergens (usually glycoproteins) into the food supply of humans and animals. The public is concerned about the nature of these new food proteins as their allergenic or nonallergenic qualities are unknown [32]. Allergenicity has been demonstrated in transgenic soybeans due to the transfer of a major food allergen from Brazil nuts [33]. On the other hand, the scientists believe that the food allergens are found only in a few defined sources (peanut and other grain legumes, shellfish, tree nuts, etc.), and hence, only a dozen foods may produce allergic reactions. Moreover, allergenicity occurs when these food allergens are present in large proportions in the food and the individuals are sensitized to them over time to cause any adverse effects. Thus, it is highly unlikely for new allergens to be introduced into the food supply from GM plants.

**2.2. Transfer of Antibiotic Resistance Gene to Microbes and Reduced Efficacy of Antibiotic Therapy.** Public is also concerned about the potential risks associated with gene transfer from plants to microbes. It is speculated that the consumption of GM foods containing antibiotic resistance marker gene (e.g., *Npt II* gene encoding neomycin phosphotransferase for resistance to kanamycin and neomycin or *Amp<sup>r</sup>* gene encoding  $\beta$ -lactamase for resistance to ampicillin) by humans and animals may lead to transfer of these genes from GM food to microflora in the gut of humans and animals or to the pathogens in the environment transforming them into strains that are resistant to antibiotic therapy [32]. The transfer of antibiotic resistance gene to unrelated microorganisms such as *Aspergillus niger* has also been demonstrated [34]. Biotechnology scientists, however, are of the opinion that the *Npt II* gene used to develop GM plants currently in the market is safe for use because there is no evidence of allergenicity or toxicity related to it. Moreover, humans are also susceptible to consuming several kanamycin resistant bacteria that occur naturally in the environment. Human gut is reported to contain  $10^{12}$  kanamycin-resistant bacteria and by consuming a tomato harboring *Npt II* gene, the increase in frequency of kanamycin-resistant bacteria in the gut amounts only to  $10^{-6}\%$ . Furthermore, acid conditions prevalent in stomach or

rumen inactivate or degrade the encoded enzyme, neomycin phosphotransferase II. Also neomycin phosphotransferase II requires ATP for its activity, which is present in extremely low concentrations in the gut. Regarding the use of *Amp<sup>r</sup>* gene for selection of bacterial recombinants, it is not transferred to plants. Moreover, the *Amp<sup>r</sup>* gene is considered safe because it does not encode for any product in plants. The *Npt II* and *Amp<sup>r</sup>* genes have been declared safe to use in GM plants [35–37]. The public is, however, reluctant to accept this fact. Looking to the views of public, scientists have also developed nonresistance based selectable marker genes such as green fluorescent protein encoding gene (*Gfp*) and  $\beta$ -glucuronidase gene (*Uid A*) [38–40]. Besides, intron-containing *Npt II* gene has also been assessed as an efficient selectable marker in plant transformation [41]. Due to insertion of intron in the *Npt II* gene, the theoretical risk of gene flow from GM plants to enteric bacteria is eliminated. Strategies for the removal of antibiotic resistance genes have also been devised [42]. One such strategy is the cloning of selectable marker gene and the transgene on two separate transfer DNA (T-DNA) molecules in a single plasmid or on two separate plasmids that are contained in one or more *Agrobacterium tumefaciens* strains used for plant transformation. The transgene and selectable marker gene are, thus, inserted at the loci, which should recombine at reasonably high frequencies so that the transgene can be segregated from the selectable marker gene in the next generation [43, 44]. Second strategy to eliminate the selectable marker gene is to flank it with direct repeats of recognition sites for a site-specific recombinase so that the marker gene can be easily excised from the plant genome by recombinase-mediated site-specific recombination. Examples included in this category are the *Cre/lox* recombination system of bacteriophage P1, *Flp/frt* recombination system of yeast  $2\ \mu\text{m}$  plasmid and *R/Rs* system of *Zygosaccharomyces rouxii*. A common feature of these systems is that the first round of transformation produces transgenic plants with the selection marker between two directly oriented recognition sites for the respective recombinase. After expression of recombinase, either by crossing in plants expressing the enzyme, by transient expression via second transformation, or by the use of an inducible promoter, the recombinase reaction is initiated resulting in marker-free transgenic plants [45–50]. Marker gene may also be eliminated by placing it on a transposable element resulting in its loss after transposition [39, 51]. The transgene by itself may be mobile and the activation of transposase allows the relocation of the desired transgene to a new chromosomal position. Genetic crosses and/or segregation may dissociate the two transgenes [52]. Another novel strategy for the production of marker-free GM plants involves DNA deletion based on intrachromosomal homologous recombination between two homologous sequences, for example, by incorporating *att* sequence of  $\lambda$  bacteriophage [53].

**2.3. Development of New-Line Microbial Strains.** The third health risk is related to the ability of GM plants to create new toxic organisms. It is speculated that some nonpest microbial strains may acquire pathogenic trait by gene flow from GM

plants [32]. The risk can also be a new host being infected by a virus or recombining to form a more deadly virulent virus [54, 55]. Some plant pathologists also hypothesize that development of virus-resistant plants may allow viruses to infect new hosts through transencapsidation. Virus-resistant plants may also lead to the creation of new viruses through an exchange of genetic material or recombination between RNA virus genomes. Another matter of concern is that a small fraction of the DNA released from GM plants into soil may bind to the clay particles and hence protected from degradation. It is speculated that the soil bacteria may undergo transformation with the exogenous DNA of GM plant [56]. This is, however, a rare possibility as the amount of DNA derived from GM plants as a proportion of the total DNA in the soil is likely to be very small, even if such plants are grown on a commercial scale [57]. Moreover, the longevity of DNA in soil depends on various factors, including soil type and the presence of deoxyribonucleases in soil [11, 58–60]. Laboratory microcosm experiments have shown all but 0.1% of the target DNA from transgenic tobacco plants gets degraded within 40 days [56, 57].

**2.4. Skepticism about Nutritional Status.** Critics of GM crops have raised various concerns about the potential of golden rice to combat vitamin A deficiency (VAD). The primary concern amongst these is the presence of insufficient vitamin A in golden rice. There are still doubts about the speed of degradation of vitamin A after harvesting the plant and the amount of vitamin A left after cooking [61]. Vandana Shiva, an Indian anti-GMO activist, has criticized golden rice by saying “the golden rice is a hoax,” “golden rice is a blind approach for blindness control,” and “golden rice is just a recipe for creating hunger and malnutrition” [62–64]. She argues that the golden rice fails to pass the vitamin A need test and is incapable of removing VAD. It is calculated that one serving contains 30 g of rice on dry weight basis and golden rice can provide only 9.9  $\mu\text{g}$  of vitamin A, that is, only 1.32% of the required daily allowance (RDA) of 750  $\mu\text{g}$ . Even with the daily consumption of 100 g golden rice, only 4.4% of the required daily allowance will be met. Thus, an adult has to consume 2 kg 272 g of golden rice per day to complete his daily requirements of vitamin A. She is also of the view that, besides creating VAD, golden rice will also create deficiency in other micronutrients and nutrients. This is because the raw milled rice has a low content of fat (0.5 g/100 g), which is necessary for vitamin A uptake, low content of protein (6.8 g/100 g), which is required as a carrier molecule, and low content of iron (0.7 g/100 g), which is required for the conversion of  $\beta$ -carotene to vitamin A. Friends of the Earth, Greenpeace, and Vandana Shiva further emphasize that there is no need of golden rice to combat VAD as superior alternatives such as sweet potato, green leafy vegetables, coriander, amaranth, carrot, pumpkin, mango, jackfruit exist in nature [62–65]. It is reported that certain underutilized plants also exhibit far more nutritional value (vitamin A and other nutrients) than golden rice, for example, a combination of rice and leaves of *Moringa* (drumstick) tree, a native to India [62–64]. Similarly, in contrast to rice,

amaranth grain contains forty times more calcium, four times iron, and twice as much protein. The ragi millet, grown in India, has thirty five times more calcium than rice, twice as much iron, and five times more minerals [66]. It is opined that golden rice is not capable of increasing the production of  $\beta$ -carotene. Even if the target of 33.3  $\mu\text{g}$  of vitamin A in 100 g of rice is achieved, it will be only 2.8% of  $\beta$ -carotene that can be obtained from amaranth leaves, 2.4% as that obtained from coriander leaves, curry leaves, and drumstick leaves [62–64]. Thus, a far more efficient route to removing VAD is biodiversity conservation and propagation of naturally occurring vitamin A rich plants (wild-type or underutilized) in agriculture and diets. Even the World Bank has admitted that rediscovering and use of local plants and conservation of vitamin A rich green leafy vegetables and fruits have dramatically reduced VAD threatened children over the past 20 years in very cheap and efficient ways. It is also speculated that the cultivation of golden rice will lead to major water scarcity since it is a water intensive crop and displaces water prudent sources of vitamin A. The scientists, on the other hand, believe that the traditional breeding methods have been unsuccessful in producing crops containing a high vitamin A concentration and most national authorities rely on expensive and complicated supplementation programs to address the problem. They also believe that a varied diet is beyond the means of many of the poor and they have to rely on one or few foods to provide complete nutrition, for example, rice. Thus, golden rice may be a useful tool to help treat the problem of VAD in young children living in the tropics. They also emphasize that the critics are ignoring the fact that VAD disorders result from a deficiency of vitamin A and not its complete absence in the diet and the VAD individuals lack only 10%–50% of their daily requirements. Hence, any additional contribution toward daily requirements would be useful. In 2005, a team of researchers at Syngenta have produced a variety of golden rice, called “Golden rice 2,” which produces twenty-three times more carotenoids than golden rice (up to 37  $\mu\text{g/g}$ ) and preferentially accumulates  $\beta$ -carotene (up to 31  $\mu\text{g/g}$  of the 37  $\mu\text{g/g}$  of carotenoids) [67]. The Rockefeller Foundation emphasized that the new strains of golden rice contain substantially higher levels of  $\beta$ -carotene than the early versions on which the opponents based their calculations. In order to meet the RDA, 144 g of the most high-yielding golden rice strains would have to be eaten.

### 3. Environmental and Ecological Concerns

Large-scale cultivation of GM plants expressing viral and bacterial genes and their release into the environment is considered to be a threat and called as “genetic pollution” by the critics [68–76]. The risk of a transgene spreading in the environment is related to the likelihood for out-crossing, horizontal gene transfer, and the phenotype imparted by the gene [72]. Debates about the commercial introduction of GM plants in some parts of the world have led to questions about their potential impact on the environment unless necessary safeguards are taken into account [77]. Various concerns that

have arisen due to the application and release of GM plants into the environment are given in this section. It should, however, be acknowledged that agriculture inevitably has an impact on the environment and these concerns are not specific for GM plants.

**3.1. Transgene Escape to Wild-Type Plants.** There is a potential risk that the GM plants may hybridize (or cross-breed) with sexually compatible wild-type species [71, 78–82]. This genetic exchange is possible due to wind pollination, biotic pollination or seed dispersal. This may have an impact on the environment through the production of hybrids and their progeny. In an example, virus-resistant squash commercialized in 1994 was demonstrated to transfer its virus resistance gene to wild squash (*Cucurbita pepo*), an agricultural weed native to the southern United States, thereby decreasing its value to squash breeders [83, 84]. On the other hand, it is significant to note that for an effective pollen transfer to occur, the GM plants must be close enough to the wild species, should flower at same time, and must be genetically compatible [78–81, 85]. Further, the risk of any gene transfer to related weedy species through pollen has been eliminated by devising chloroplast transformation procedures [86, 87]. This is because, in many crop species, chloroplasts display only maternal inheritance.

**3.2. Selective Advantage to GM Plants in Natural Environments and Generation of Superweeds.** The concern of gene flow from GM plants to weedy relatives via pollination is quite intense [72, 88–91]. It is considered that the transfer of encoded characteristics to weed species could potentially give them a selective advantage, consequently leading to the generation of “superweeds.” Moreover, the newly introduced traits may make a plant, especially herbicide tolerant plant, more persistent or invasive (weedy) in agricultural habitats [92–101]. It is, however, pertinent to note that the risk of gene transfer to weeds is similar with both conventional and GM plants and is not contingent on how these genes have been introduced into plants. Such a risk of gene flow has always existed since the advent of modern plant breeding, even when there were no GM plants, and this can occur where possible. Several studies have demonstrated that tolerance to particular herbicide is often more likely to develop by evolution from within the weed gene pool rather than by gene flow from herbicide-tolerant plants [102, 103]. Nevertheless, the current scientific evidence indicates that the weediness arises from many different characters and that the addition of one gene is unlikely to cause a crop to become a weed. The transfer of novel genes from transgenics (or even conventionally bred plants) to weeds depends on the nature of the novel gene and the biology and ecology of the recipient weed species. The probability of successful out-crossing thus depends on sexual compatibility, physical proximity, distance of pollen movement both out of and into the GM plants, and ecology of recipient species [78–81]. Thus, only a few plants such as oilseed rape, barley, wheat, beans, and sugar beet can hybridize with weeds. For example, oilseed rape has been reported to hybridize with hoary mustard, wild radish, and

other wild *Brassica* species [80, 104–106]. Furthermore, the transfer of herbicide tolerance gene is unlikely to confer any competitive advantage to hybrids outside agricultural areas. It is also comforting to recognize that there is no proven evidence of enhanced persistence or invasiveness of GM plants and no major superweeds have developed so far.

**3.3. Effect on Nutritional Composition of Plants.** It is also speculated that the nutritional composition of GM products may be affected in GM plants. Another concern is that the transgenes from animals (obtained from fishes, mouse, human, and microbes) introduced into GM plant for molecular farming may pose a risk of changing the fundamental nature of vegetables. In a study, it was reported that as compared to non-GM soybean, GM plants exhibited lower levels of isoflavones [107]. This finding also raised a doubt on the regulatory system for the release of the GM plants. However, later it was found that the concentration of isoflavone in GM soybean was within the normal range [108].

**3.4. Mixing Genes from Unrelated Species (Interbreeding).** The public is worried about the risk that the GM plants can spread through nature and interbreed with natural organisms, thereby contaminating “non-GM” environments. This would in turn affect the future generations in an unforeseeable and uncontrollable way [72]. Such worries, however, ignore the history of plant breeding and the existing overwhelming sequence similarity of genes across kingdoms.

**3.5. Development of Tolerance to Target Herbicide.** It is viewed that the repeated use of the same herbicide in the same area to remove weeds amongst genetically modified herbicide-resistant crops (HRCs) (tolerant to single herbicide) will exacerbate the problem of herbicide-tolerant weeds [72]. Another matter of concern relates to the plants carrying different herbicide tolerance genes to become multiply tolerant to several herbicides by pollination between adjacent plants [109]. In several closely studied examples in Canada, farmers have detected oilseed rape plants tolerant to three different herbicides (note that two were acquired from GM plants and the third possibly from conventional breeding) [110]. The development of multiple tolerances in “volunteer” crop plants (from seeds remaining viable in agricultural soil) may also exert an impact on the environment by necessitating the use of less environment-friendly and possibly outdated herbicides by the farmers. On the other hand, the proponents believe that herbicide resistance develops due to excessive application of herbicide and is not exclusively associated with gene transfer from genetically modified HRCs. Thus, the pressure on weeds to evolve resistant biotypes has been reported to be pronounced with the excessive application of herbicides such as glyphosate, sulphonylureas, and imidazolinones.

**3.6. Sustainable Resistance in Insect Pests.** It is possible that the widespread use of disease-resistant GM plants may lead to the evolution of several insect pests that are resistant to

pesticides [111–115]. For example, *Bt* crops may develop resistance to *Bt* biopesticide, a permitted biopesticide successfully used by organic farmers in the integrated pest management (IPM) programs. There is to date no reported evidence of insect resistance to *Bt* crops under field conditions although *Bt* resistant insects (e.g., cotton budworm and bollworm) have been observed in areas where *Bt* biopesticides are sprayed on crops [116]. It has been a matter of concern that the development of such resistance may lead to the loss of the potential of the *Bt* biopesticide, which may in turn make it necessary for organic farmers to resort to less environmentally acceptable chemical pesticides. Therefore, proper resistance management strategies along with this comparatively newer technology are imperative. The most widely used is the ‘high-dose refuge’ strategy designed to prevent or delay the emergence of *Bt* toxin-resistant insects. Scientists are of the opinion that this strategy should be followed without fail, as the rate of noncompliance can increase the risk of plant resistance breakdown.

**3.7. Harm to Nontarget Organisms.** Nontarget effect, that is, undesirable effect of a novel gene (usually conferring pest or disease resistance) on “friendly” organisms in the environment, is another concern related to GM plants [117]. As many nontarget microbes harbor on plant surfaces or some insects harbor on flowers, it becomes quite challenging to target the insect resistance gene product to appropriate plant tissues and hence kill pests without exerting any adverse effect on friendly organisms such as pollinators and biological control agents. This is particularly difficult where the benign or beneficial organism is related and physiologically similar to the pest to be targeted. One of the most significant studies of nontarget impacts of GM plants has been the killing of monarch butterfly in the United States by *Bt* insecticidal proteins [9, 17, 27, 118–122]. It should, however, be noted that the pesticidal sprays used on *Bt* or non-*Bt* corn may be more harmful to the monarch butterfly as compared to *Bt* corn pollen [117]. Thus, in evaluating the use of *Bt* crops and the possible environmental damage caused, it is important to take into account the environmental damage caused by the use of pesticides in agriculture generally. It is argued that millions of birds and billions of insects, both harmful and beneficial, are killed each year due to excessive use of pesticides. It is, however, suggested that the scale and pattern of use may mitigate the effects of *Bt* on nontarget populations [123]. Furthermore, when toxins are produced within plant tissues, nontarget organisms are exposed to a much lesser extent than with spray applications because only those organisms which feed on the plant tissues come into contact with the toxin.

Harmful effect of *Bt* toxin residues in the soil after harvest of the GM crop on soil invertebrates has been another matter of concern. An investigation of the effect of *Cry1Ab* released from the roots and crop residues on soil organisms revealed the presence of toxin in the guts and casts of tested earthworms. There was, however, no significant difference in their mortality or weight. Moreover, no difference in the total number of other soil organisms (including nematodes, protozoa, bacteria, and fungi) between the soil rhizosphere of *Bt* and non-*Bt* crops was detected [124].

**3.8. Increased Use of Chemicals in Agriculture.** On one hand, the transgenes conferring herbicide resistance have been criticized because these would maintain, if not promote, the use of herbicides and their attendant problems [125, 126]. Similarly, there is a concern that the insect-resistant and disease-resistant GM plants will increase the application of insecticides and pesticides, respectively. On the contrary, reports demonstrate that there is no significant change in the overall amount of herbicide use in the United States since the introduction of GM soybeans [127]. An analysis by soybean growers at the United States has shown that \$7.2 millions of other herbicides were replaced by \$5.4 millions of glyphosate [19]. This substitution, thus, resulted in the replacement of highly toxic and more persistent herbicides with that of glyphosate. Furthermore, it has been reported that herbicide-tolerant oilseed rape eliminates the use of >6,000 tons of herbicide in the growing season [128].

**3.9. Loss of Biodiversity.** The public has long been worried about the loss of plant biodiversity due to global industrialization, urbanization, and the popularity of conventionally-bred high-yielding varieties. It is speculated that the biodiversity will be further threatened due to the encouraging use of GM plants. This is because development of GM plants may favor monocultures, that is, plants of a single kind, which are best suitable for one or other conditions or produce one product [72, 98, 129]. Further, the transformation of more natural ecosystems into agricultural lands for planting GM plants is adding to this ecological instability.

Another point of concern is the loss of weed diversity that may occur due to gene flow from HRCs to weeds [126]. It is argued that because the currently available HRCs confer tolerance to broad-spectrum herbicides such as glufosinate and glyphosate, their extensive use may shift the diversity of weeds in agricultural habitats. However, weeds exhibit considerable plasticity and adapt to a wide range of cultivation practices. Experience with conventional agriculture has shown that weed species composition varies within the same crop among different fields and at different times of year. Thus, weed population shifts are natural ecological phenomena in crop management and should not be viewed as exclusive to GM plants.

**3.10. Unpredictable Gene Expression.** It is speculated that the random gene insertion, transgene instability, and genomic disruption due to gene transfer may result in unpredictable gene expression. Such a risk is, however, unlikely to be unique to GM plants or of any significance considering our current knowledge of genomic flux in plants.

**3.11. Alteration in Evolutionary Pattern.** Plants adapt to the fluctuations in the environment through changing their genes and developing better races called “evolved races.” These mutations, however, occur at a very low frequency (i.e., one in about  $10^9$ /gene/generation). It is hypothesized that the cultivation of GM plants by the farmers at an increasing rate throughout the world may change the evolutionary pattern

drastically [72]. Another concern is the evolution of non-GM plants through hybridization with GM plants.

**3.12. Loss of Ecosystem in Marginal Lands.** As new plants are introduced mainly to marginal lands, loss of natural ecosystems in these areas has also been a matter of concern.

**3.13. Contamination of Soil and Water.** It is also sometimes argued that the widespread introduction of HRCs will increase the use of herbicides, which will in turn contribute to the contamination of soil and ground water. However, this is not the case. The cultivation of HRCs in the United States has been reported to facilitate zero-till agronomic system, which contributes to a reduction in soil erosion. The release of *Bt* toxin into the soil after harvest of *Bt* crops is also viewed as a risk factor associated with the cultivation of *Bt* crops [123, 124, 130]. It has been found that *Bt* toxins remain active in soil; however, it is not necessarily an environmental hazard because *Bt* toxins must be ingested and affect only selected groups of insects. Moreover, the potential leaching rate of *Bt* toxin is reduced due to its binding and adsorption on clay particles [131].

#### 4. Socioeconomic and Ethical Concerns

As the GM plants are likely to affect the society, their application is also related to certain social and ethical concerns. Besides, evaluation of their cost effectiveness (production cost versus potential benefits) is also a matter of concern. It is pertinent to note here that most of these concerns pertain to developing countries. A list of various socioeconomical and ethical concerns is presented below.

**4.1. Slow Progress Rate.** Critics are skeptical about the ability of genetic manipulation to increase food production and project that there will only be about slight increase in crop yield during the next decades [132]. Some persons further question why after so many years of research genetic engineers have not produced any high-yielding crop variety. The answer, according to plant scientists, is that plant breeders using traditional breeding techniques may have largely exploited the genetic potential for increasing the share of photosynthate that goes into the seed. Others feel lack of funds for pursuing research in the area of genetic manipulation of plants. Furthermore, the public ignorance about the GM technology is the prime factor for its slow progress rate.

**4.2. Prevalence of the Western Agriculture, Monopoly of Transnational Companies, and Exploitation of the Poor.** The public in developing countries were of the opinion that there is domination of majority of the biotechnology industry by transnational companies (TNCs) in the developed world the business of which is to generate profits [132]. One such example is that many HRCs raised by genetic manipulation belong to the group of key crops in Western agriculture. The “terminator gene technology” developed by TNCs was also criticized as the technology was considered as a step to build

monopoly over transgenic seed production [133, 134]. An apprehension related to the application of this technology was its accidental transfer to other varieties and related species of a specific crop through cross-pollination resulting in large-scale sterility. It has also been argued that pollen from crops carrying terminator trait would infect the fields of farmers who either rejected or could not afford this technology. Further, the imposition of heavy fees for use of seeds will lead to loss of control of cooperatives by local farmers. It is further argued that greater privatization will increase both legal and financial barriers to use of varieties. Activist groups view golden rice not as a boon for the world's hungry population but as a public relations campaign for the biotech industry. Charles Margulis of the Greenpeace Genetic Engineering Campaign viewed that the industry has shamelessly used golden rice in an attempt of the developed nations to quell growing distrust of its experimental foods. One social concern about the development of GM plants raised by the Third World countries is that TNCs may disadvantage poor farmers in developing countries, for example, for the packaging of GM seeds [132]. The situation is made even more complex because the majority of the genetic resources and thus biodiversity on which genetic manipulation depends are found in developing countries. Thus, in order to sustain the Third World, the targets should also include other plants, and these countries should be helped in bypassing expensive and high input crop production and in moving their traditional agriculture toward low input sustainable practices.

**4.3. Loss of Foreign Income and Employment.** Another apprehension regarding the application of GM plants is the loss of export market as their products get substituted by production of alternatives generated by genetic engineering in industrialized countries [132]. It is viewed that this will result in unemployment and loss of foreign income in the developing countries. Further, the large agricultural estates will be strengthened leading to dislocation of small-scale landholders and farmers. The requirement of labour for cultivation is also speculated to reduce. It is expected that the generation of genetically modified HRCs may reduce labour market in weeding and may also increase dependence on foreign imports of chemicals.

**4.4. Unaffordability by Poor.** Vandana Shiva also argued about the problems with poverty and loss of biodiversity in food crops, which are aggravated by the corporate control of agriculture based on GM foods [64]. She also argued that food security and nutritional security should be secured by some lower-cost, accessible, and safer alternative to GM rice, for example, amaranth, *Moringa*, sweet potato, green leafy vegetables, and so forth.

**4.5. Intellectual Property Rights and Patents Issue.** As genes extracted from ecosystems in developing nations are exploited for raising GM plants in the developed nations, it is quite possible for them to get the patents [132]. It has become a matter of concern because it will result in developing world

farmers paying for the products that originated from their nation's own resources.

**4.6. Ethical Issues.** Certain groups of public, including religious bodies, find it very unethical or inhumane to introduce human or animal genes into plants [135]. For example, the transfer of animal genes such as  $\alpha$ -interferon gene into plants is objectionable to the vegetarians. Such concern was one of the reasons due to which the concept of "edible vaccines" did not gain much impetus.

**4.7. Labeling and Segregation of GM Foods.** The public has always lived with food risks, but in the last few decades, they have become concerned about the contents in GM foods [135, 136]. Such concern was never there with the foods derived from classically bred plants. The proponents say that such a question is ridiculous because like GM plants the information regarding the contents has never been there with classically bred plants. Moreover, with GM plants, at least the source of new genetic material being introduced is known, and hence there is possibility of testing predictable and even many unpredictable effects. It is suggested that for GM foods to come in the market, a compromise among government, seed producers, farmers, and consumers may be practical. This involves the labeling of GM ingredients and segregation of GM plants and seeds from conventional ones.

## 5. Conclusion

Genetic Engineering Approval Committee (GEAC) granted permission to Maharashtra Hybrid Seed Company (Mahyco) in 2002 for commercial cultivation of three cotton hybrids, namely, MECH-12 *Bt*, MECH-162 *Bt*, and MECH-184 *Bt* after several years of field trials [1, 137, 138]. These were developed by introgression of insect resistance from *Bt*-containing Cocker-312 (Event MON 531) developed by Monsanto Corporation, USA, into parental lines of Mahyco propriety hybrids. These transgenic cotton plants (*Bt* cotton) harbored crystal protein gene (*CryIAc*) from the soil bacterium *Bacillus thuringiensis* and were resistant to infestation by Lepidopteran insects. Similarly, *Bt* brinjal (Event EE 1), harboring *CryIAc* gene obtained from Monsanto, was developed by Mahyco by introgression into various local varieties by University of Agricultural Sciences, Dharwad and Tamil Nadu Agricultural University, Coimbatore, through plant breeding [139, 140]. In 2006, an expert committee examined the biosafety data presented by Mahyco and concluded that *Bt* brinjal was safe and equivalent to its non-*Bt* counterpart according to the provided data; however, these findings should be reconfirmed by further field trials and the benefits of *Bt* brinjal with respect to existing methods for pest management and pesticide reduction should be ascertained. A second expert committee examined the data from these trials and approved its commercialization in India in 2009. However, for both *Bt* cotton and *Bt* brinjal, the government of India applied a moratorium on their release upon outcry by some scientists, farmers, and anti-GM activists due to biosafety reasons [1, 137–140].

Thus, public opinion regarding the application and development of genetic engineering is likely to be an important factor influencing the future development of the technology and its subsequent application within the commercial sector. It is, therefore, recommended that scientific research aimed at risk analysis, prediction, and prevention, combined with adequate monitoring and stewardship, must be done so that negative impact from GM products, if any, may be kept to a minimum. In this direction, a combination of demographic data from existing non-GM populations, simulation modeling of transgene dispersal, and monitoring field releases may guide in the assessment of risks related to the release of GM plants into the environment. Further, it is viewed that case-by-case studies can help in solving the raised concerns. Besides, public should be well informed that most of their concerns are skeptical and GM plants have tremendous potential in solving the present problems.

## References

- [1] S. Rastogi and N. Pathak, *Genetic Engineering*, Oxford University Press, New Delhi, India, 2009.
- [2] S. L. Huttner, C. Arntzen, R. Beachy et al., "Revising oversight of genetically modified plants," *Biotechnology*, vol. 10, no. 9, pp. 967–971, 1992.
- [3] R. P. Wrubel, S. Krimsky, and R. E. Wetzler, "Field testing transgenic plants," *BioScience*, vol. 42, no. 4, pp. 280–289, 1992.
- [4] H. I. Miller and D. Gunary, "Serious flaws in the horizontal approach to biotechnology risk," *Science*, vol. 262, no. 5139, pp. 1500–1501, 1993.
- [5] R. Stone, "Large plots are next test for transgenic crop safety," *Science*, vol. 266, no. 5190, pp. 1472–1473, 1994.
- [6] A. Saba, A. Moles, and L. J. Frewer, "Public concerns about general and specific applications of genetic engineering: a comparative study between the UK and Italy," *Nutrition & Food Science*, vol. 98, no. 1, pp. 19–29, 1998.
- [7] P. J. Dale, "Public reactions and scientific responses to transgenic crops," *Current Opinion in Biotechnology*, vol. 10, no. 2, pp. 203–208, 1999.
- [8] R. Lewis and B. A. Palevitz, "GM crops face heat of debate," *The Scientist*, vol. 13, no. 20, p. 9, 1999.
- [9] A. M. Shelton and R. T. Roush, "False reports and the ears of men," *Nature Biotechnology*, vol. 17, no. 9, p. 832, 1999.
- [10] J. E. Barton and M. Dracup, "Genetically modified crops and the environment," *Agronomy Journal*, vol. 92, no. 4, pp. 797–803, 2000.
- [11] A. Chiter, J. M. Forbes, and G. E. Blair, "DNA stability in plant tissues: implications for the possible transfer of genes from genetically modified food," *FEBS Letters*, vol. 481, no. 2, pp. 164–168, 2000.
- [12] N. G. Halford and P. R. Shewry, "Genetically modified crops: methodology, benefits, regulation and public concerns," *British Medical Bulletin*, vol. 56, no. 1, pp. 62–73, 2000.
- [13] W. Parrott, "Introduction: the GMO survival guide," *Agronomy Journal*, vol. 92, no. 4, p. 792, 2000.
- [14] S. G. Uzogara, "The impact of genetic modification of human foods in the 21st century: a review," *Biotechnology Advances*, vol. 18, no. 3, pp. 179–206, 2000.

- [15] L. L. Wolfenbarger and P. R. Phifer, "The ecological risks and benefits of genetically engineered plants," *Science*, vol. 290, no. 5499, pp. 2088–2093, 2000.
- [16] C. S. Prakash, "The genetically modified crop debate in the context of agricultural evolution," *Plant Physiology*, vol. 126, no. 1, pp. 8–15, 2001.
- [17] A. M. Shelton and M. K. Sears, "The monarch butterfly controversy: scientific interpretations of a phenomenon," *Plant Journal*, vol. 27, no. 6, pp. 483–488, 2001.
- [18] A. M. Shelton, J. Z. Zhao, and R. T. Roush, "Economic, ecological, food safety, and social consequences of the deployment of *Bt* transgenic plants," *Annual Review of Entomology*, vol. 47, pp. 845–881, 2002.
- [19] A. J. Trewavas and C. J. Leaver, "Is opposition to GM crops science or politics? An investigation into the arguments that GM crops pose a particular threat to the environment," *EMBO Reports*, vol. 2, no. 6, pp. 455–459, 2001.
- [20] K. Anderson and L. A. Jackson, "Some implications of GM food technology policies for Sub-Saharan Africa," *Journal of African Economies*, vol. 14, no. 3, pp. 385–410, 2005.
- [21] K. L. Heong, Y. H. Chen, D. E. Johnson et al., "Debate over a GM rice trill in China," *Science*, vol. 310, no. 5746, pp. 231–233, 2005.
- [22] M. Omura, *Seeds of Dispute: Crop Crusaders*, GRAIN, 2005, <http://www.grain.org/>.
- [23] O. V. Singh, S. Ghai, D. Paul, and R. K. Jain, "Genetically modified crops: success, safety assessment, and public concern," *Applied Microbiology and Biotechnology*, vol. 71, no. 5, pp. 598–607, 2006.
- [24] S. Key, J. K. C. Ma, and P. M. W. Drake, "Genetically modified plants and human health," *Journal of the Royal Society of Medicine*, vol. 101, no. 6, pp. 290–298, 2008.
- [25] Wikipedia, "Genetically modified food controversies," Wikipedia, 2013, <http://en.wikipedia.org/wiki>.
- [26] S. W. B. Ewen and A. Pusztai, "Effect of diets containing genetically modified potatoes expressing *Galanthus nivalis* lectin on rat small intestine," *Lancet*, vol. 354, no. 9187, pp. 1353–1354, 1999.
- [27] J. E. Losey, L. S. Rayor, and M. E. Carter, "Transgenic pollen harms monarch larvae," *Nature*, vol. 399, no. 6733, p. 214, 1999.
- [28] D. King and A. Gordon, "Contaminant found in taco bell taco shells," Friends of the Earth, 2001, <http://www.foe.org/>.
- [29] Greenpeace, "Genetically engineered food," Greenpeace, 1999, <http://www.greenpeace.org/>.
- [30] H. I. Miller, P. Morandini, and K. Ammann, "Is biotechnology a victim of anti-science bias in scientific journals?" *Trends in Biotechnology*, vol. 26, no. 3, pp. 122–125, 2008.
- [31] H. I. Miller, "A golden opportunity, squandered," *Trends in Biotechnology*, vol. 27, no. 3, pp. 129–130, 2009.
- [32] H. F. Kaeppler, "Food safety assessment of genetically modified crops," *Agronomy Journal*, vol. 92, no. 4, pp. 793–797, 2000.
- [33] J. A. Nordlee, S. L. Taylor, J. A. Townsend, L. A. Thomas, and R. K. Bush, "Identification of a Brazil-nut allergen in transgenic soybeans," *The New England Journal of Medicine*, vol. 334, no. 11, pp. 688–692, 1996.
- [34] T. Hoffmann, C. Golz, and O. Schieder, "Foreign DNA sequences are received by a wild-type strain of *Aspergillus niger* after co-culture with transgenic higher plants," *Current Genetics*, vol. 27, no. 1, pp. 70–76, 1994.
- [35] R. B. Flavell, E. Dart, R. L. Fuchs, and R. T. Fraley, "Selectable marker genes: safe for plants?" *Biotechnology*, vol. 10, no. 2, pp. 141–144, 1992.
- [36] World Health Organization, *Report of a WHO Workshop*, WHO, Geneva, Switzerland, 1993.
- [37] United States Food and Drug Administration, "Guidance for industry: use of antibiotic resistance marker genes in transgenic plants," USFDA, 1998, <http://www.fda.gov/food/guidancecomplianceregulatoryinformation/>.
- [38] R. A. Jefferson, "Assaying chimeric genes in plants: the GUS gene fusion system," *Plant Molecular Biology Reporter*, vol. 5, no. 4, pp. 387–405, 1987.
- [39] H. Ebinuma, K. Sugita, E. Matsunaga, and M. Yamakado, "Selection of marker-free transgenic plants using the isopen-tenyl transferase gene," *Proceedings of the National Academy of Sciences of the United States of America*, vol. 94, no. 6, pp. 2117–2121, 1997.
- [40] H. F. Kaeppler, G. K. Menon, R. W. Skadsen, A. M. Nuutila, and A. R. Carlson, "Transgenic oat plants via visual selection of cells expressing green fluorescent protein," *Plant Cell Reports*, vol. 19, no. 7, pp. 661–666, 2000.
- [41] G. Libiakova, B. Jørgensen, G. Palmgren, P. Ulvskov, and E. Johansen, "Efficacy of an intron-containing kanamycin resistance gene as a selectable marker in plant transformation," *Plant Cell Reports*, vol. 20, no. 7, pp. 610–615, 2001.
- [42] P. K. Jaiwal, L. Sahoo, N. D. Singh, and R. P. Singh, "Strategies to deal with the concern about marker genes in transgenic plants: some environment-friendly approaches," *Current Science*, vol. 83, no. 2, pp. 128–136, 2002.
- [43] M. De Block and D. Debrouwer, "Two T-DNA's co-transformed into *Brassica napus* by a double *Agrobacterium tumefaciens* infection are mainly integrated at the same locus," *Theoretical and Applied Genetics*, vol. 82, no. 3, pp. 257–263, 1991.
- [44] M. Daley, V. C. Knauf, K. R. Summerfelt, and J. C. Turner, "Co-transformation with one *Agrobacterium tumefaciens* strain containing two binary plasmids as a method for producing marker-free transgenic plants," *Plant Cell Reports*, vol. 17, no. 6–7, pp. 489–496, 1998.
- [45] E. C. Dale and D. W. Ow, "Gene transfer with subsequent removal of the selection gene from the host genome," *Proceedings of the National Academy of Sciences of the United States of America*, vol. 88, no. 23, pp. 10558–10562, 1991.
- [46] S. H. Russell, J. L. Hoopes, and J. T. Odell, "Directed excision of a transgene from the plant genome," *Molecular and General Genetics*, vol. 234, no. 1, pp. 49–59, 1992.
- [47] N. J. Kilby, G. J. Davies, M. R. Snaith, and J. A. Murray, "FLP recombinase in transgenic plants: constitutive activity in stably transformed tobacco and generation of marked cell clones in *Arabidopsis*," *Plant Journal*, vol. 8, no. 5, pp. 637–652, 1995.
- [48] H. Onouchi, R. Nishihama, M. Kudo, Y. Machida, and C. Machida, "Visualization of site-specific recombination catalyzed by a recombinase from *Zygosaccharomyces rouxii* in *Arabidopsis thaliana*," *Molecular and General Genetics*, vol. 247, no. 6, pp. 653–660, 1995.
- [49] L. A. Lyznik, K. V. Rao, and T. K. Hodges, "FLP-mediated recombination of FRT sites in the maize genome," *Nucleic Acids Research*, vol. 24, no. 19, pp. 3784–3789, 1996.
- [50] A. C. Vergunst, L. E. T. Jansen, and P. J. J. Hooykaas, "Site-specific integration of *Agrobacterium* T-DNA in *Arabidopsis thaliana* mediated by Cre recombinase," *Nucleic Acids Research*, vol. 26, no. 11, pp. 2729–2734, 1998.

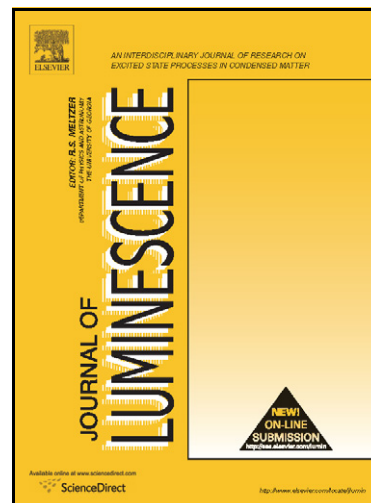
- [51] J. I. Yoder and A. P. Goldsbrough, "Transformation systems for generating marker-free transgenic plants," *Biotechnology*, vol. 12, no. 3, pp. 263–267, 1994.
- [52] A. P. Goldsbrough, C. N. Lastrella, and J. I. Yoder, "Transposition mediated re-positioning and subsequent elimination of marker genes from transgenic tomato," *Biotechnology*, vol. 11, no. 11, pp. 1286–1292, 1993.
- [53] E. Zubko, C. Scutt, and P. Meyer, "Intrachromosomal recombination between *attP* regions as a tool to remove selectable marker genes from tobacco transgenes," *Nature Biotechnology*, vol. 18, no. 4, pp. 442–445, 2000.
- [54] B. W. Falk and G. Bruening, "Will transgenic crops generate new viruses and new diseases?" *Science*, vol. 263, no. 5152, pp. 1395–1396, 1994.
- [55] D. Gonsalves, "Control of papaya ringspot virus in papaya: a case study," *Annual Review of Phytopathology*, vol. 36, pp. 415–437, 1998.
- [56] F. Widmer, R. J. Seidler, and L. S. Watrud, "Sensitive detection of transgenic plant marker gene persistence in soil microcosms," *Molecular Ecology*, vol. 5, no. 5, pp. 603–613, 1996.
- [57] F. Widmer, R. J. Seidler, K. K. Donegan, and G. L. Reed, "Quantification of transgenic plant marker gene persistence in the field," *Molecular Ecology*, vol. 6, no. 1, pp. 1–7, 1997.
- [58] E. Paget, M. Lebrun, G. Freyssinet, and P. Simonet, "The fate of recombinant plant DNA in soil," *European Journal of Soil Biology*, vol. 34, no. 2, pp. 81–88, 1998.
- [59] P. S. Duggan, P. A. Chambers, J. Heritage, and J. M. Forbes, "Survival of free DNA encoding antibiotic resistance from transgenic maize and the transformation activity of DNA in ovine saliva, ovine rumen fluid and silage effluent," *FEMS Microbiology Letters*, vol. 191, no. 1, pp. 71–77, 2000.
- [60] G. Head, J. B. Surber, J. A. Watson, J. W. Martin, and J. J. Duan, "No detection of CryI<sub>Ac</sub> protein in soil after multiple years of transgenic *Bt* cotton (Bollgard) use," *Environmental Entomology*, vol. 31, no. 1, pp. 30–36, 2002.
- [61] C. Then, "The campaign for genetically modified rice is at the crossroads: a critical look at golden rice after nearly 10 years of development," Foodwatch in Germany, 2009, <http://www.foodwatch.de/>.
- [62] V. Shiva, *Stolen Harvest: The Hijacking of the Global Food Supply*, South End Press, 2000.
- [63] V. Shiva, "Vitamin A rice: a blind approach to blindness control," Genet News, 2000, <http://www.gene.ch/genet/>.
- [64] V. Shiva, "Genetically engineered vitamin A rice," in *Redesigning Life? The Worldwide Challenge to Genetic Engineering*, B. Tokar, Ed., Zed Books Ltd, London, UK, 2001.
- [65] Greenpeace, "All that glitters is not gold: the false hope of golden rice," Greenpeace, 2005, <http://www.greenpeace.org/>.
- [66] Rural Advancement Foundation International, RAFI, 2000, <http://www.rafi.org/>.
- [67] J. A. Paine, C. A. Shipton, S. Chaggar et al., "Improving the nutritional value of Golden Rice through increased pro-vitamin A content," *Nature Biotechnology*, vol. 23, no. 4, pp. 482–487, 2005.
- [68] H. J. Rogers and H. C. Parkes, "Transgenic plants and the environment," *Journal of Experimental Botany*, vol. 46, no. 286, pp. 467–488, 1995.
- [69] T. R. Mikkelsen, B. Andersen, and R. B. Jørgensen, "The risk of crop transgene spread," *Nature*, vol. 380, no. 6569, p. 31, 1996.
- [70] M. G. Paoletti and D. Pimentel, "Genetic engineering in agriculture and the environment," *BioScience*, vol. 46, no. 9, pp. 665–673, 1996.
- [71] A. A. Snow and P. M. Palma, "Commercialization of transgenic plants: potential ecological risks," *BioScience*, vol. 47, pp. 86–96, 1996.
- [72] R. R. James, S. P. Difazio, A. M. Brunner, and S. H. Strauss, "Environmental effects of genetically engineered woody biomass crops," *Biomass and Bioenergy*, vol. 14, no. 4, pp. 403–414, 1998.
- [73] M. A. Altieri, "The ecological impacts of transgenic crops on agroecosystem health," *Ecosystem Health*, vol. 6, no. 1, pp. 13–23, 2000.
- [74] A. Latifah, "Potential risks of genetically modified organisms release into the environment," in *Proceedings of the Regional Symposium on Environment and Natural Resources*, vol. 1, pp. 205–214, 2002.
- [75] A. J. Conner, T. R. Glare, and J. P. Nap, "The release of genetically modified crops into the environment—part II: overview of ecological risk assessment," *Plant Journal*, vol. 33, no. 1, pp. 19–46, 2003.
- [76] M. Mellon, "Environmental effects of genetically modified food crops—recent experiences," Union of Concerned Scientists, Cambridge, Mass, USA, 2012, <http://www.ucsusa.org/>.
- [77] P. J. Dale, B. Clarke, and E. M. G. Fontes, "Potential for the environmental impact of transgenic crops," *Nature Biotechnology*, vol. 20, no. 6, pp. 567–574, 2002.
- [78] P. F. Umbeck, K. A. Barton, E. V. Nordheim, J. C. McCarty, W. L. Parrott, and J. N. Jenkins, "Degree of pollen dispersal by insects from a field test of genetically engineered cotton," *Journal of Economic Entomology*, vol. 84, pp. 1943–1950, 1991.
- [79] A. J. A. M. Kapteijns, "Risk assessment of genetically modified crops. Potential of four arable crops to hybridize with the wild flora," *Euphytica*, vol. 66, no. 1-2, pp. 145–149, 1993.
- [80] A. F. Raybould and A. J. Gray, "Genetically modified crops and hybridization with wild relatives: a UK perspective," *Journal of Applied Ecology*, vol. 30, no. 2, pp. 199–219, 1993.
- [81] T. Klinger and N. C. Ellstrand, "Engineered genes in wild populations: fitness of weed-crop hybrids of *Raphanus sativus*," *Ecological Applications*, vol. 4, no. 1, pp. 117–120, 1994.
- [82] G. Giddings, "Modelling the spread of pollen from *Lolium perenne*. The implications for the release of wind-pollinated transgenics," *Theoretical and Applied Genetics*, vol. 100, no. 6, pp. 971–974, 2000.
- [83] L. J. Spencer and A. A. Snow, "Fecundity of transgenic wild-crop hybrids of *Cucurbita pepo* (Cucurbitaceae): implications for crop-to-wild gene flow," *Heredity*, vol. 86, no. 6, pp. 694–702, 2001.
- [84] M. Fuchs, E. M. Chirco, and D. Gonsalves, "Movement of coat protein genes from a commercial virus-resistant transgenic squash into a wild relative," *Environmental Biosafety Research*, vol. 3, no. 1, pp. 5–16, 2004.
- [85] S. E. Scott and M. J. Wilkinson, "Transgene risk is low," *Nature*, vol. 393, no. 6683, p. 320, 1998.
- [86] P. Maliga, "Plastid transformation in higher plants," *Annual Review of Plant Biology*, vol. 55, pp. 289–313, 2004.
- [87] H. Daniell, S. Kumar, and N. Dufourmantel, "Breakthrough in chloroplast genetic engineering of agronomically important crops," *Trends in Biotechnology*, vol. 23, no. 5, pp. 238–245, 2005.
- [88] L. Landbo and R. B. Jørgensen, "Seed germination in weedy *Brassica campestris* and its hybrids with *B. napus*: implications for risk assessment of transgenic oilseed rape," *Euphytica*, vol. 97, no. 2, pp. 209–216, 1997.

- [89] H. Daniell, R. Datta, S. Varma, S. Gray, and S. B. Lee, "Containment of herbicide resistance through genetic engineering of the chloroplast genome," *Nature Biotechnology*, vol. 16, no. 4, pp. 345–348, 1998.
- [90] R. B. Jorgensen, B. Andersen, T. P. Hauser, L. Landbo, T. Mikkelsen, and H. Ostergard, "Introgression of crop genes from oilseed rape (*Brassica napus*) to related wild species—an avenue for the escape of engineered genes," *Acta Horticulturae*, vol. 459, pp. 211–217, 1998.
- [91] L. B. Hansen, H. R. Siegmund, and R. B. Jørgensen, "Introgression between oilseed rape (*Brassica napus* L.) and its weedy relative *B. rapa* L. in a natural population," *Genetic Resources and Crop Evolution*, vol. 48, no. 6, pp. 621–627, 2001.
- [92] R. Manasse and P. Kareiva, "Quantifying the spread of recombinant genes and organisms," in *Assessing Ecological Risks of Biotechnology*, L. R. Ginzburg, Ed., pp. 215–231, Butterworth-Heinemann, Boston, Mass, USA, 1991.
- [93] K. H. Keeler, "Can genetically engineered crops become weeds?" *Biotechnology*, vol. 7, pp. 1134–1139, 1992.
- [94] M. J. Crawley, R. S. Hails, M. Rees, D. Kohn, and J. Buxton, "Ecology of transgenic oilseed rape in natural habitats," *Nature*, vol. 363, no. 6430, pp. 620–623, 1993.
- [95] M. J. Crawley, S. L. Brown, R. S. Hails, D. D. Kohn, and M. Rees, "Transgenic crops in natural habitats," *Nature*, vol. 409, no. 6821, pp. 682–683, 2001.
- [96] M. Williamson, "Invaders, weeds and the risk from genetically manipulated organisms," *Experientia*, vol. 49, no. 3, pp. 219–224, 1993.
- [97] J. F. Hancock, R. Grumet, and S. C. Hokanson, "The opportunity for escape of engineered genes from transgenic crops," *HortScience*, vol. 31, no. 7, pp. 1080–1085, 1996.
- [98] J. B. Sweet and R. Shepperson, "The impact of genetically modified herbicide tolerant oilseed rape in UK," *Acta Horticulturae*, vol. 459, pp. 225–234, 1997.
- [99] M. A. Rieger, C. Preston, and S. B. Powles, "Risks of gene flow from transgenic herbicide-resistant canola (*Brassica napus*) to weedy relatives in southern Australian cropping systems," *Australian Journal of Agricultural Research*, vol. 50, no. 2, pp. 115–128, 1999.
- [100] A. A. Snow, B. Andersen, and R. B. Jorgensen, "Costs of transgenic herbicide resistance introgressed from *Brassica napus* into weedy *B. rapa*," *Molecular Ecology*, vol. 8, no. 4, pp. 605–615, 1999.
- [101] K. Ammann, Y. Jacot, and R. Al Mazyad, "Weediness in the light of new transgenic crops and their potential hybrids," *Journal of Plant Diseases*, vol. 17, pp. 19–29, 2000.
- [102] C. L. Moyes, J. M. Lilley, C. A. Casais, S. G. Cole, P. D. Haeger, and P. J. Dale, "Barriers to gene flow from oilseed rape (*Brassica napus*) into populations of *Sinapis arvensis*," *Molecular Ecology*, vol. 11, no. 1, pp. 103–112, 2002.
- [103] I. J. Senior and P. J. Dale, "Herbicide-tolerant crops in agriculture: oilseed rape as a case study," *Plant Breeding*, vol. 121, no. 2, pp. 97–107, 2002.
- [104] J. A. Scheffler and P. J. Dale, "Opportunities for gene transfer from transgenic oilseed rape (*Brassica napus*) to related species," *Transgenic Research*, vol. 3, no. 5, pp. 263–278, 1994.
- [105] J. A. Sheffler, A. Parkinson, and P. J. Dale, "Evaluating the effectiveness of isolation distances for field plots of oilseed rape (*Brassica napus*) using a herbicide-resistance transgene as a selectable marker," *Plant Breeding*, vol. 14, pp. 317–321, 1995.
- [106] National Research Council, *Genetically Modified Pest Protected Plants: Science and Regulation*, National Academy Press, Washington, DC, USA, 2000.
- [107] M. A. Lappe, E. B. Bailey, C. Childress, and K. D. R. Setcheil, "Alterations in clinically important phytoestrogens in genetically modified herbicide-tolerant soybeans," *Journal of Medicinal Food*, vol. 1, no. 4, pp. 241–245, 1998.
- [108] American Soybean Association, "ASA confirms the natural variability in isoflavones in soybean," American Soybean Association, 1999, <http://www.soygrowers.com/>.
- [109] J. H. Westwood and P. L. Traynor, *Ecological Effects of Pest Resistance Genes in Managed Ecosystems*, Information Systems for Biotechnology, Blacksburg, Va, USA, 1999.
- [110] J. Orson, *Gene Stacking in Herbicide Tolerant Oilseed Rape: Lessons from the North American Experience*, vol. 1 of *English Nature Research Reports*, no. 443, English Nature, 2002.
- [111] K. F. Raffa, "Genetic engineering of trees to enhance resistance to insects," *BioScience*, vol. 39, no. 8, pp. 524–534, 1989.
- [112] B. E. Tabashnik, "Evolution of resistance to *Bacillus thuringiensis*," *Annual Review of Entomology*, vol. 39, pp. 47–79, 1994.
- [113] L. S. Bauer, "Resistance: a threat to the insecticidal crystal proteins of *Bacillus thuringiensis*," *Florida Entomologist*, vol. 87, pp. 414–443, 1995.
- [114] S. B. Powles, C. Preston, I. B. Bryan, and A. R. Jutsum, "Herbicide resistance: impact and management," *Advances in Agronomy*, vol. 58, pp. 57–93, 1996.
- [115] A. Dove, "Survey raises concerns about *Bt* resistance management," *Nature Biotechnology*, vol. 19, no. 4, pp. 293–294, 2001.
- [116] D. N. Alstad and D. A. Andow, "Managing the evolution of insect resistance to transgenic plants," *Science*, vol. 268, no. 5219, pp. 1894–1896, 1995.
- [117] D. S. Pimentel and P. H. Raven, "*Bt* corn pollen impacts on nontarget Lepidoptera: assessment of effects in nature," *Proceedings of the National Academy of Sciences of the United States of America*, vol. 97, no. 15, pp. 8198–8199, 2000.
- [118] R. L. Hellmich, B. D. Siegfried, M. K. Sears et al., "Monarch larvae sensitivity to *Bacillus thuringiensis*-purified proteins and pollen," *Proceedings of the National Academy of Sciences of the United States of America*, vol. 98, no. 21, pp. 11925–11930, 2001.
- [119] K. S. Oberhauser, M. D. Prysby, H. R. Mattila et al., "Temporal and spatial overlap between monarch larvae and corn pollen," *Proceedings of the National Academy of Sciences of the United States of America*, vol. 98, no. 21, pp. 11913–11918, 2001.
- [120] D. E. Stanley-Horn, G. P. Dively, R. L. Hellmich et al., "Assessing the impact of Cry1Ab-expressing corn pollen on monarch butterfly larvae in field studies," *Proceedings of the National Academy of Sciences of the United States of America*, vol. 98, no. 21, pp. 11931–11936, 2001.
- [121] M. K. Sears, R. L. Hellmich, D. E. Stanley-Horn et al., "Impact of *Bt* corn pollen on monarch butterfly populations: a risk assessment," *Proceedings of the National Academy of Sciences of the United States of America*, vol. 98, no. 21, pp. 11937–11942, 2001.
- [122] A. R. Zangerl, D. McKenna, C. L. Wraight et al., "Effects of exposure to event 176 *Bacillus thuringiensis* corn pollen on monarch and black swallowtail caterpillars under field conditions," *Proceedings of the National Academy of Sciences of the United States of America*, vol. 98, no. 21, pp. 11908–11912, 2001.
- [123] P. C. Jepson, B. A. Croft, and G. E. Pratt, "Test systems to determine the ecological risks posed by toxin release from

- Bacillus thuringiensis* genes in crop plants,” *Molecular Ecology*, vol. 3, pp. 81–99, 1994.
- [124] D. Saxena and G. Stotzky, “Insecticidal toxin from *Bacillus thuringiensis* is released from roots of transgenic *Bt* corn *in vitro* and *in situ*,” *FEMS Microbiology Ecology*, vol. 33, no. 1, pp. 35–39, 2000.
- [125] R. J. Goldberg, “Environmental concerns with the development of herbicide-tolerant plants,” *Weed Technology*, vol. 6, no. 3, pp. 647–652, 1992.
- [126] S. R. Radosevich, C. M. Ghersa, and G. Comstock, “Concerns a weed scientist might have about herbicide-resistant crops,” *Weed Technology*, vol. 6, no. 3, p. 635, 1992.
- [127] United States Department of Agriculture, “Genetically engineered crops: has adoption reduced pesticide use?” USDA, 2000, <http://www.ers.usda.gov>.
- [128] Canola Council of Canada, “An agronomic and economic assessment of transgenic canola,” Canola Council of Canada, 2001, <http://www.canolacouncil.org/>.
- [129] V. Shiva, *Monocultures of the Mind*, Zed Books Ltd, London, UK, 1993.
- [130] H. Tapp and G. Stotzky, “Insecticidal activity of the toxins from *Bacillus thuringiensis* subspecies *kurstaki* and *tenebrionis* adsorbed and bound on pure and soil clays,” *Applied and Environmental Microbiology*, vol. 61, no. 5, pp. 1786–1790, 1995.
- [131] G. Stotzky, “Persistence and biological activity in soil of insecticidal proteins from *Bacillus thuringiensis* and of bacterial DNA bound on clays and humic acids,” *Journal of Environmental Quality*, vol. 29, no. 3, pp. 691–705, 2000.
- [132] M. C. Jordan, “The privatization of food: corporate control of biotechnology,” *Agronomy Journal*, vol. 92, no. 4, pp. 803–806, 2000.
- [133] P. K. Gupta, “The terminator technology for seed production and protection: why and how?” *Current Science*, vol. 75, no. 12, pp. 1319–1323, 1998.
- [134] S. Rakshit, “Terminator technology: science and politics,” *Current Science*, vol. 75, pp. 747–749, 1998.
- [135] D. B. Whitman, “Genetically modified foods: harmful or helpful?” CSA, 2000, <http://www.csa.com/>.
- [136] B. R. Glick and J. J. Pasternak, *Molecular Biotechnology: Principles and Applications of Recombinant DNA*, ASM Press, Washington, DC, USA, 2003.
- [137] Asia-Pacific Consortium on Agricultural Biotechnology (APCoAB), *Bt Cotton in India—A Status Report*, New Delhi, India, 2006.
- [138] Asia-Pacific Association of Agricultural Research Institutions (APAARI), “Expert Consultation on Agricultural Biotechnology, Biosafety and Biosecurity: Proceedings and Recommendations,” APAARI, 2012, <http://www.apaari.org/>.
- [139] M/s Maharashtra Hybrid Seeds Company Ltd. (Mahyco), Mumbai University of Agricultural Sciences (UAS), Dharwad, and Tamil Nadu Agricultural University (TNAU), *Report of the Expert Committee (EC-II) on Bt Brinjal Event EE-1*, Genetic Engineering Approval Committee, Ministry of Environment and Forests, Government of India, New Delhi, India, 2009.
- [140] J. Samuels, “Genetically engineered *Bt* brinjal and the implications for plant biodiversity—revisited,” Greenpeace, 2012, <http://www.greenpeace.org/india/>.

Optical Absorption and Luminescent Characteristics of Dy<sup>3+</sup> doped Zinc Alumino Bismuth Borate Glasses for Lasing materials and White LEDs

K. Swapna, Sk. Mahamuda, A. Srinivasa Rao, M. Jayasimhadri, T. Sasikala, L. Rama Moorthy



[www.elsevier.com/locate/jlumin](http://www.elsevier.com/locate/jlumin)

PII: S0022-2313(13)00091-4  
DOI: <http://dx.doi.org/10.1016/j.jlumin.2013.02.035>  
Reference: LUMIN11753

To appear in: *Journal of Luminescence*

Received date: 1 October 2012  
Revised date: 14 January 2013  
Accepted date: 14 February 2013

Cite this article as: K. Swapna, Sk. Mahamuda, A. Srinivasa Rao, M. Jayasimhadri, T. Sasikala and L. Rama Moorthy, Optical Absorption and Luminescent Characteristics of Dy<sup>3+</sup> doped Zinc Alumino Bismuth Borate Glasses for Lasing materials and White LEDs, *Journal of Luminescence*, <http://dx.doi.org/10.1016/j.jlumin.2013.02.035>

This is a PDF file of an unedited manuscript that has been accepted for publication. As a service to our customers we are providing this early version of the manuscript. The manuscript will undergo copyediting, typesetting, and review of the resulting galley proof before it is published in its final citable form. Please note that during the production process errors may be discovered which could affect the content, and all legal disclaimers that apply to the journal pertain.

## Optical Absorption and Luminescent Characteristics of Dy<sup>3+</sup> doped Zinc Alumino Bismuth Borate Glasses for Lasing materials and White LEDs

K.Swapna<sup>1</sup>, Sk.Mahamuda<sup>1</sup>, A. Srinivasa Rao<sup>\*1,2</sup>, M.Jayasimhadri<sup>2</sup>, T.Sasikala<sup>3</sup> and  
L. Rama Moorthy<sup>3</sup>

<sup>1</sup>Department of Physics, K. L. University, Green Fields, Vaddeswaram- 522 502, A.P., India

<sup>2</sup>Department of Applied Physics, Delhi Technological University, Delhi-110 042 India

<sup>3</sup>Department of Physics, S.V. University, Tirupathi 517 502, A P, India

### Abstract

Good optical quality Dy<sup>3+</sup> doped Zinc Alumino Bismuth Borate (ZnAlBiB) glasses were prepared by the conventional melt quenching technique and characterized by optical absorption and luminescence studies. The glassy nature of these materials has been confirmed through XRD measurements. From the absorption spectra, the three phenomenological JO parameters  $\Omega_\lambda$  ( $\lambda=2,4$  and  $6$ ) have been determined from the absorption spectral intensities by using the JO theory. Luminescence spectra measured for different concentrations of Dy<sup>3+</sup> ions doped glasses by exciting the glasses at 387 nm. The intensity of Dy<sup>3+</sup> emission spectra increases from 0.5 mol% to 1 mol % and beyond 1 mol % the concentration quenching is observed. The suitable concentration of Dy<sup>3+</sup> ions for ZnAlBiB glassy material to act as good lasing material has been discussed by measuring the branching ratios and emission cross-sections for two strong emission transitions such as  $^4F_{9/2} \rightarrow ^6H_{15/2}$  and  $^4F_{9/2} \rightarrow ^6H_{13/2}$  observed in visible region. By exciting these glassy materials at various excitation wavelengths in n-UV region, the CIE Chromaticity coordinates were evaluated for the two sharp emissions observed in blue ( $^4F_{9/2} \rightarrow ^6H_{15/2}$ ) and yellow ( $^4F_{9/2} \rightarrow ^6H_{13/2}$ ) regions to understand suitability of these materials for White Light Generation.

### Keywords:

Glasses, Rare-earths, Judd-Ofelt theory, Luminescence properties, White light generation

### \*Corresponding author:

E-mail: drsrallam@yahoo.co.in, Tel: +918586039007

## 1. Introduction

Recently, research on rare earth doped materials is of significant importance due to their potential applications in the fields of optoelectronic devices, laser technology, fiber optic amplifiers, infra-red to visible up converters and phosphors [1-3]. The design and development of optical devices suitable for the above applications requires in detailed characterization of optical absorption and luminescent properties. These properties mostly depend on the nature and type of local environment around the rare earth ion and on the phonon energies of the host glass. Therefore luminescent properties of RE doped different glass hosts are being prepared and investigated with an aim to know their utility for the above mentioned luminescent applications. Several glassy materials such as fluorides, phosphates, fluorophosphates, borates, fluoborates and tellurites have been widely investigated to understand the effect of host glass on the lasing properties of rare earth ions [4-8]. In general a host glass with low phonon energies decreases non-radiative relaxation rates and gives high quantum efficiencies, which are useful to design lasers and optical fiber amplifiers [9]. Boric acid ( $B_2O_3$ ) is one of the best glass formers known and can form glass alone at lower melting point with good transparency, high chemical durability, thermal stability and good rare earth ion solubility [10]. Normally, glass with  $B_2O_3$  alone possesses high phonon energies ( $\sim 1300\text{ cm}^{-1}$ ) and cannot suppress non radiative decay process and hence rare earth ion emissions are strongly reduced. Hence, heavy metal oxide ( $Bi_2O_3$ ) has been added to  $B_2O_3$  to suppress the phonon energies. Moreover, Bismuth containing glasses become the subject of extensive research nowadays as they can exhibit broad band luminescence in the near-infrared (NIR) region, which receives considerable attention for potential applications in the fields of telecommunications, tunable fiber lasers and spectral converters [11,12].

On the other hand, solid state lighting (SSL) technology is emerging as a highly competent and viable alternative to the existing technology in the back drop of the growing importance for energy saving and environmental friendliness. SSL is becoming an interesting field for researchers especially to produce white light sources having wide applications in the fields of LCD displays, colored displays, traffic signals, automotive displays and cellular phone illumination and so on. White light emitting diodes are having certain advantages such as high brightness, low power consumption, longevity, reliability and excellent low temperature performance.  $\text{Dy}^{3+}$  is capable of emitting several interesting wavelengths between its f-f transitions, which are having potential applications in diversified fields. Among the rare earth ions,  $\text{Dy}^{3+}$  is one of the important rare-earth ions for the preparation of phosphor materials which is playing a major role in the preparation of white light emitting phosphors. The  $\text{Dy}^{3+}$  ions has two characteristic intense emission bands in the visible region corresponding to the transitions  $^4\text{F}_{9/2} \rightarrow ^6\text{H}_{13/2}$  (Yellow) and  $^4\text{F}_{9/2} \rightarrow ^6\text{H}_{15/2}$  (Blue) [13]. The optimization of local environment is an important task to obtain white light from  $\text{Dy}^{3+}$  doped glasses at suitable yellow to blue (Y/B) intensity ratio [14, 15]. The modulation of Y/B intensity ratio of  $\text{Dy}^{3+}$  ions to emit white light in a glassy material can be achieved by varying the composition of the glass and excitation wavelengths [16,17].

In the present work, Zinc Alumino Bismuth Borate glasses were prepared by varying  $\text{Dy}^{3+}$  concentration to study and enhance the optical and luminescent properties with the aim to ascertain their utility for solid state laser devices and also for n-UV based white light emitting sources.

## 2. Experimental

$\text{Dy}^{3+}$  doped Zinc Alumino Bismuth Borate (ZnAlBiB) glasses were prepared using melt quenching technique with the following chemical compositions:  $20 \text{ ZnO} + 8 \text{ Al}_2\text{O}_3 + (12-x) \text{ Bi}_2\text{O}_3 + 60 \text{ B}_2\text{O}_3 + x \text{ Dy}_2\text{O}_3$  ( $x=0.5, 1, 1.5, 2$  and  $2.5$  mol %). For convenience, the samples were designated as glass A to E in accordance with the 'x' value. The raw materials were thoroughly mixed in an agate mortar and melted in an electric furnace at the temperature  $1200^\circ\text{C}$  for 1h. The melt was then poured on to a preheated brass plate and pressed by an identical brass plate to obtain transparent glasses. The synthesized glass samples were subsequently annealed at  $400^\circ\text{C}$  to remove thermal strains and then polished to do spectral measurements. The densities were measured by using Archimedes method using water as an immersion liquid. The refractive indices of these glasses are measured by the Brewster angle method using He-Ne laser (650 nm line) as the source. The optical absorption spectra of the samples were recorded at room temperature in the spectral wavelength range covering 300-1800 nm with a spectral resolution of 0.1nm using JASCO model V-670 UV-VIS-NIR spectrophotometer. The luminescence spectra for all these glasses were recorded at room temperature using JOBIN YVON Fluorolog-3 spectrofluorimeter with Xenon arc lamp as radiation source and photomultiplier tube (R928 P PMT) is used as a detector.

## 3. Result and Discussions

### 3.1 XRD Spectral Measurements

In order to check the non-crystallinity nature of the ZnAlBiB glass, XRD measurements were taken for an undoped ZnAlBiB glass and is shown in figure 1. The XRD spectrum exhibits broad

hump, which is the characteristic feature of the amorphous material. Hence, the prepared ZnAlBiB glass confirms the amorphous nature.

### 3.2 Physical properties

From the estimated values of both density ( $d$ ) and refractive index( $n_d$ ), other related physical parameters, such as average molecular weight( $M$ ), molar volume( $V$ ), molar refractivity( $R_M$ ), molecular electronic polarizability ( $\alpha_e$ ), rare-earth ion concentration( $N$ ), interionic distance( $r_i$ ), polaran radius( $r_p$ ) and field strength ( $F$ ) of the glasses have been computed by using the relevant expressions available in the literature [18] and are given Table 1. From Table 1 it can be observed that the mol % of  $Dy^{3+}$  is proportional to the  $Dy^{3+}$  ion concentration. The molar refractivity ( $R_M$ ), molecular electronic polarizability ( $\alpha_e$ ), interionic distance ( $r_i$ ), and polaran radius ( $r_p$ ), were found to be decreasing with the increasing the  $Dy^{3+}$  ion concentration.

### 3.3 Absorption Spectral measurements

Fig. 2 shows the absorption spectrum of 1 mol%  $Dy^{3+}$  doped ZnAlBiB glass, which has been recorded at room temperature in the wavelength range 300-1800 nm. The absorption spectra for the remaining glasses are also quite similar with slight variation in intensities. Each spectrum consist of ten absorption bands corresponding to the transitions  ${}^6H_{15/2} \rightarrow {}^4F_{7/2}$ ,  ${}^4I_{15/2}$ ,  ${}^4F_{9/2}$ ,  ${}^6F_{1/2}$ ,  ${}^6F_{3/2}$ ,  ${}^6F_{5/2}$ ,  ${}^6F_{7/2}$ ,  ${}^6F_{9/2}$ ,  ${}^6F_{11/2}$ ,  ${}^6H_{11/2}$  and the identification of bands has been shown in Fig. 2. The bands identified at 387nm ( ${}^6H_{15/2} \rightarrow {}^4F_{7/2}$ ) and 447nm ( ${}^6H_{15/2} \rightarrow {}^4I_{15/2}$ ) are very weak due to strong absorption of the host glass in UV region. The intensities of absorption bands are expresses by measuring oscillator strengths experimentally ( $f_{exp}$ ) using the expression given in reference [19] and such oscillator strengths for all the glasses are given in Table 2. Among the all the absorption transitions, the transition  ${}^4I_{9/2} \rightarrow {}^6F_{11/2}$  centered at 1267nm approximately, shows high intensity when compared with other transitions in all the glasses. For

this transition the observed oscillator strengths ( $f_{\text{exp}}$ ) are very large when compared with other transitions as shown in Table 2. Such transitions are called as hypersensitive transitions which obeys the selection rule  $\Delta J = \pm 2$  and  $\Delta L = \pm 2$  and are very sensitive to the host environment [20].

The Judd Ofelt theory has been applied to the experimentally evaluated oscillator strengths to find the JO intensity parameters ( $\Omega_2$ ,  $\Omega_4$  and  $\Omega_6$ ), by least square fit analysis. The utilization of JO theory to evaluate the JO intensity parameters was discussed in detailed in our previous paper [19]. The JO parameters thus evaluated are used to calculate oscillator strengths ( $f_{\text{cal}}$ ) and such calculated oscillator strengths are also given in Table 2 along with  $f_{\text{exp}}$ . The small rms deviation value obtained between the experimental and calculated oscillator strengths indicate good fit between the two values and also the validity of JO theory. The JO intensity parameters obtained for the present glasses are also given in Table 2 along with the spectroscopic quality factor ( $\chi$ ). The  $\Omega_\lambda$  follows the trend  $\Omega_2 > \Omega_6 > \Omega_4$  in all the glasses. The JO parameters are important to investigate the local structure and bonding vicinity of RE ions. According to Jorgensen and Reisfield [21], the magnitude of  $\Omega_2$  parameter depends on the covalency of metal ligand bond and also on the asymmetry of ion sites in the neighborhood of RE ion. The magnitudes of  $\Omega_4$  and  $\Omega_6$  parameters are related to the bulk properties such as viscosity and rigidity of the medium in which the ions are situated. The  $\Omega_2$  parameter is also most sensitive to the local structure and composition of glass. The largest magnitude of  $\Omega_2$  observed for all ZnAlBiB glasses suggests that, the bonding of  $\text{Dy}^{3+}$  ions with the ligands is of covalent nature and the rare earth ion sites are having lower asymmetry in these host glasses. The value of spectroscopic quality factor ( $\Omega_4 / \Omega_6$ ) which allows to predict the channels by which the rare-earth ions from the meta stable state  $^4\text{F}_{9/2}$  can relax through luminescence [22]. Reasonably high value of spectroscopic quality factor ( $\Omega_4 / \Omega_6$ ) observed for the present glasses predicts efficient stimulated emission from these glasses.

### 3.4 Visible luminescence analysis

To analyze the luminescence spectra for the prepared glasses, it is necessary to know the excitation wavelengths of  $\text{Dy}^{3+}$  ions. For this purpose, we have recorded an excitation spectra of 1 mol % of  $\text{Dy}^{3+}$  ions in ZnAlBiB glasses by fixing the emission at 484 nm as shown in Fig. 3. The excitation spectra recorded from 340 - 440 nm gives four excitation bands at wavelengths approximately 351, 357, 387 and 426 nm corresponding to the transitions  $^4\text{H}_{15/2} \rightarrow ^6\text{P}_{7/2}$ ,  $^4\text{P}_{3/2}$ ,  $^4\text{I}_{13/2}$  and  $^4\text{G}_{11/2}$ , respectively. It is well known that the wavelength corresponding to the intense excitation band can give intense emissions. Among all excitation bands, a band corresponding to

the transition  ${}^6\text{H}_{15/2} \rightarrow {}^4\text{I}_{13/2}$  (387 nm) is more intense and is used as an excitation wavelength to record the emission spectra for all the glasses under investigation. Fig. 4 shows the emission spectra of ZnAlBiB glasses doped with different concentrations of  $\text{Dy}^{3+}$  at room temperature. The emission spectra consisting of three peaks centered at around 484, 577 and 665 nm, which are assigned to the transitions  ${}^4\text{F}_{9/2} \rightarrow {}^6\text{H}_{15/2}$ ,  ${}^6\text{H}_{13/2}$  and  ${}^6\text{H}_{11/2}$ , respectively. Among the three transitions, two transitions such as  ${}^4\text{F}_{9/2} \rightarrow {}^6\text{H}_{15/2}$  and  ${}^4\text{F}_{9/2} \rightarrow {}^6\text{H}_{13/2}$  are intense than the third transition  ${}^4\text{F}_{9/2} \rightarrow {}^6\text{H}_{11/2}$ . Among the two intense transitions, a transition corresponding  ${}^4\text{F}_{9/2} \rightarrow {}^6\text{H}_{13/2}$  is in yellow region and hypersensitive obeying the selection rules  $\Delta J = \pm 2$  and  $\Delta L = \pm 2$  [23]. From Figure 4, it can be seen that the fluorescence intensity of  ${}^4\text{F}_{9/2} \rightarrow {}^6\text{H}_{15/2}$  transition is slightly higher than  ${}^4\text{F}_{9/2} \rightarrow {}^6\text{H}_{13/2}$  transition and this may be due to the addition of  $\text{Al}_2\text{O}_3$ , that improves the optical quantity and decreases the phonon energy of the host [24,25]. When the  $\text{Dy}^{3+}$  ions are excited with 387 nm to the  ${}^4\text{I}_{13/2}$ , due to small energy gap between all energy states lying above  $21000 \text{ cm}^{-1}$ , the  ${}^4\text{F}_{9/2}$  state is rapidly populated by non-radiative relaxation and as a result blue and yellow luminescence originating from the  ${}^4\text{F}_{9/2}$  state is observed. The  ${}^4\text{F}_{9/2}$  level possesses purely radiative relaxation rates since this level has sufficient energy gap  $\sim 8000 \text{ cm}^{-1}$  with respect to the next lower level of  ${}^6\text{F}_{5/2}$ . The variation of intensity of  ${}^4\text{F}_{9/2} \rightarrow {}^6\text{H}_{13/2}$  and  ${}^6\text{H}_{15/2}$  transitions with  $\text{Dy}^{3+}$  ion concentrations in ZnAlBiB glass is shown in the inset of Fig. 4. It is found that the intensity of emission bands increases with increase in concentration of  $\text{Dy}^{3+}$  ion from 0.5 to 1 mol % and beyond 1 mol % the concentration quenching is observed.

To understand the  $\text{Dy}^{3+}$  luminescence in the glasses under study, the JO theory [26,27] has been applied to determine radiative properties such as transition probability (A), total transition probability ( $A_T$ ), luminescence branching ratio ( $\beta_{\text{cal}}$ ), radiative lifetime ( $\tau_R$ ) and stimulated

emission cross-section( $\sigma_e$ ) for the intense emission transitions  ${}^4F_{9/2} \rightarrow {}^6H_{15/2}$  and  ${}^6H_{13/2}$  using the relevant expressions given our previous paper [19] and are presented in Table 3. The luminescence branching ratio which characterizes and makes the transition as potential for laser emission, if its value  $\beta_{cal} \geq 0.5$ . In the present work, the emission transition  ${}^4F_{9/2} \rightarrow {}^6H_{13/2}$  has higher  $\beta_{cal}$  than the other transition  ${}^4F_{9/2} \rightarrow {}^6H_{15/2}$  and are comparable to the values reported in literature [28,29]. The experimental branching ratios ( $\beta_{exp}$ ) are obtained by using the relative intensities of individual peaks to that of the total intensity of emission peaks and are given in Table 3. The variation in calculated and experimental branching ratios may be attributed to the non radiative contributions from the  ${}^4F_{9/2}$  level of  $Dy^{3+}$  ions in these ZnAlBiB glasses.

The value of stimulated emission cross-section has been used to identify the potential laser transition of rare earth ions in glasses. A good laser transition can have a large stimulated emission cross-section. The stimulated emission cross-sections obtained for  ${}^4F_{9/2} \rightarrow {}^6H_{13/2}$  transition in ZnAlBiB glasses are in good agreement with the values reported for the other glass hosts [28,29]. The relatively larger  $\beta_{cal}$  values and stimulated emission cross-sections observed for ZnAlBiB glasses makes them as promising materials for lasing action through the emission channel  ${}^4F_{9/2} \rightarrow {}^6H_{13/2}$  with its wavelength around 578 nm. From Table 3, it is clear that among all the ZnAlBiB glasses, for  ${}^4F_{9/2} \rightarrow {}^6H_{13/2}$  transition the glass A possesses more  $\beta_{cal}$  and  $\sigma_{se}$  values when compared with other glasses. Hence glass A can be recommended as a good host for lasing emission at 578 nm. A glassy material doped with rare earth can act as a good optical fiber if the gain band width ( $\sigma_e \times \Delta\lambda_p$ ) and optical gain ( $\sigma_e \times 1/A_T$ ) parameters are having higher values. The relatively higher values of ( $\sigma_e \times \Delta\lambda_p$ ) and ( $\sigma_e \times 1/A_T$ ) obtained for ZnAlBiB glasses suggests that they are the suitable candidates for optical amplification.

### 3.5 CIE chromaticity Coordinates

As we have discussed in the previous sections,  $\text{Dy}^{3+}$  ion is well known for light emission in visible range and offers an excellent possibility for the development of white light emitting devices, because it has many excitation bands falling in n-UV region. The excitation spectrum recorded for 1 mol %  $\text{Dy}^{3+}$  doped  $\text{ZnAlBiB}$  glass gives four excitation bands as shown in Fig. 3. So it is possible to use the present glasses as white light emitting devices excited by n-UV to blue light as per the optical requirements. We have recorded the emission spectra for all the glasses by exciting them with wavelength values 357, 365, 387, 397, 405 nm and the CIE color coordinates are evaluated for  $\text{ZnAlBiB}$  glasses doped with  $\text{Dy}^{3+}$  ions and are given in Table 4 along with Y/B ratio for glass A. From Table 4, it can be observed that among different excited wavelengths,  $\text{ZnAlBiB}$  glasses are giving average color coordinates ( $x = 0.309$ ,  $y = 0.312$ ) under 357 nm excitation as shown in Fig. 5, which are very close to the perfect white light CIE coordinates ( $x = 0.33$ ,  $y = 0.33$ ). Hence it is concluded that the  $\text{ZnAlBiB}$  glasses could act as white light emitters effectively, when excited at 357 nm. Also among all  $\text{ZnAlBiB}$  glasses, the glass C with 1.5 mol % of  $\text{Dy}^{3+}$  concentration can act as good white light emitter at 357 nm.

#### 4. Conclusions

Zinc Alumino Bismuth Borate ( $\text{ZnAlBiB}$ ) Glasses were prepared with good optical quality by doping them with different concentrations of  $\text{Dy}^{3+}$  ions. The room temperature absorption and luminescence spectra of  $\text{Dy}^{3+}$  ions doped  $\text{ZnAlBiB}$  glasses were recorded and analyzed using JO theory. The reasonably small r.m.s deviations observed between the measured and calculated oscillator strengths indicates the accuracy of JO parameters. The room temperature luminescence spectra recorded at different concentrations of  $\text{Dy}^{3+}$  ions show two strong emissions one at blue region ( ${}^4\text{F}_{9/2} \rightarrow {}^6\text{H}_{15/2}$ ) and other one is at yellow region ( ${}^4\text{F}_{9/2} \rightarrow {}^6\text{H}_{13/2}$ ). It is well known that a

good material for laser emission must have large stimulated emission cross-section and high branching ratio. Based on the visible emission spectra, the large stimulated emission cross-section and high branching ratios ( $\beta_{cal}$ ) observed for  $^4F_{9/2} \rightarrow ^6H_{13/2}$  transition for all these glasses suggest the utility of these materials as lasing material. Among all the ZnAlBiB glasses studied, the glass-A may be used as a luminescence material for the development of laser and photonic devices operating in visible region. The CIE chromaticity coordinates also evaluated from the emission spectra under the excitation of different n-UV wavelengths confirmed the possibility of generating white light emission in principle from these ZnAlBiB glasses. Among all the excitation wavelengths, ZnAlBiB glasses are quite useful under 357 nm excitation for n-UV based white light emitting diodes.

### Acknowledgements

One of the authors Swapna Koneru is very much thankful to Department of Science and Technology (DST), Govt. of India, New Delhi, for awarding her with a Women Scientist's scheme under DST - WOS (A) programme. Dr. M. Jayasimhadri is grateful to DAE-BRNS, Govt. of India, for the sanction of research project (No. 2011/34/2/BRNS/130, dt. 21/04/2011).

### References:

- [1] Feng Zhang, Yuhua Wang, Ye Tao, J. Lumin. 136 (2013) 51-56

- [2] Xinghua Zhang, Zunming Lu, Fanbin Meng, Long Hu, Xuewen Xu, Jing Lin, Chengchun Tang Mater. Lett. 79 (2012) 292-295.
- [3] B. Vengala Rao, M. Jayasimhadri, Junho Jeong, Kiwan Jang, Ho Sueb Lee, Soung-Soo Yi, Jung-Hyun Jeong, J. Phys. D: Appl. Phys. 43 (2010) 395103
- [4] L. Xiao, Q. Xiao, Y. Liu, P. Ai, Y. Li, H. Wang, J. Alloys Compd. 495 (2010) 72-75.
- [5] J. Pisarska, R. Lisecki, W. Ryba-Romanowski, T. Goryczka, W.A. Pisarski, Chem. Phys. Lett. 489 (2010) 198-201.
- [6] J. Suresh Kumar, K. Pavani, A. Mohan Babu, N.K. Giri, S.B. Rai, L. Rama Moorthy, J. Lumin. 130 (2010) 1916-1923.
- [7] W.A. Pisarski, J. Pisarska, G. Dominiak-Dzik, W. Ryba-Romanowski, J. Alloys Compd. 484 (2009) 45-49.
- [8] G. Lakshminarayana, J. Qiu, J. Alloys Compd. 476 (2009) 470-476.
- [9] Y.G. Choi, J. Heo, J. Non-Cryst. Solids 217 (1997) 199-207.
- [10] A. H. Varshnaya, Fundamentals of Inorganic Glasses, Academic press, San Diego, 1994.
- [11] M. Peng, C. Zollfrank and L. Wondraczek, J. Phys.: Condens. Matter 21 (2009) 285106 (6 pp)
- [12] M. Peng, L. Wondraczek, Optics Lett. 35 (2010) 2544-46.
- [13] B.V. Ratnam, M. Jayasimhadri, Kiwan Jang, Ho Sueb Lee, Soung-Soo Yi, Jung-Hyun Jeong, J. Amer. ceramic Soc. 93 (2010) 3857-3861.
- [14] S. Liu, G. Zhao, H. Ying, J. Wang, and G. Han, Opt. Mater. 31 (2008) 47.
- [15] X. Liang, Y. Yang, C. Zhu, S. Yuan, and G. Chen, Appl. Phys. Lett. 91 (2007) 091104.
- [16] B. Liu, C. Shi, Z. Qi, Appl. Phys. Lett. 86 (2005) 191111-191113.
- [17] J. Kuang, Y. Liu, J. Zhang, J. Solid State Chem. 179 (2006) 266-269.

- [18] A.S. Rao, Y.N. Ahammed, R.R. Reddy, T.V.R. Rao, Opt. Mater. 10 (1998) 245-252.
- [19] A. Srinivasa RAo , B Rupa Venkateswara rao, MVVK Prasad, JV Shanmukha Kumar, M. Jayasimhadri, JL RAo, and RPS Chakradhar, Physica B, 404 (2009) 3717-3721.
- [20] C.K. Jorgenson, B. R. Judd, Mol. Phys. 8 (1964) 281-290.
- [21] C.K. Jorgensen, R. Reisfeld, J. Less. Commn. Mat 93 (1983) 107-112.
- [22] D. K. Sardar, W. M. Bradley, R.M Yow, J.B Gruber, B. Zandi, J. Lumin. 106 (2004) 195-203.
- [23] A. Mohan Babu, B.C. Jamalaiah, J. Suresh Kumar, T. Sasikala, L. Rama Moorthy, J. Alloys Compd. 509 (2011) 457-462.
- [24] Sindey, J.L. Ribeiro, Ph. Goldner, Francois Auzel, J. Non-Cryst. Solids 219 (1997) 176-181.
- [25] L. Zhang, L. Wen, H. Sun, J. Zang, L. Hu., J. Alloys. Compounds. 391 (2005) 156-161.
- [26] B. R. Judd, Phys. Rev 127 (1962) 750-761.
- [27] G.S. Ofelt, J. Chem. Phys. 37 (1962) 511-520.
- [28] M. Jayasimhadri, L. R. Moorthy, K. Kojima, K. Yamamoto, Wada Noriko, Wada Noriyuki, J. Phys. D: Appl. Phys. 39 (2006) 635-641.
- [29] Joanna pisarska, J. Phys. Condense. Matter, 21 (2009) 285101.

**Table 1: Various physical properties of Dy<sup>3+</sup> - doped Zinc Alumino Bismuth Borate (ZnAlBiB) glasses**

S.No	Physical Property	Glass A	Glass B	Glass C	Glass D	Glass E
1.	Refractive index ( $n_d$ )	1.80	1.80	1.80	1.80	1.80
2.	Density, d (gm/cm <sup>3</sup> )	4.03	4.02	4.02	4.01	4.01
3.	Average molecular weight, $\bar{M}^G$ (g)	121.6	121.1	120.7	119.7	120.2
4.	Dy <sup>3+</sup> ion concentration N(x10 <sup>22</sup> ions/cm <sup>3</sup> )	0.997	1.999	3.007	4.029	5.025
5.	Mean atomic volume (g/cm <sup>3</sup> /atom)	6.86	6.84	6.83	6.79	6.81
6.	Optical dielectric constant ( $p\partial t / \partial p$ )	2.24	2.23	2.23	2.23	2.23
7.	Dielectric constant ( $\epsilon$ )	3.24	3.23	3.23	3.23	3.23
8.	Reflection losses (R %)	8.163	8.148	8.148	8.148	8.148
9.	Molar refraction (R <sub>m</sub> )(cm <sup>-3</sup> )	12.90	12.86	12.82	12.76	12.79
10.	Polaron radius (r <sub>p</sub> ) (Å)	1.904	1.51	1.32	1.2	1.11
11.	Interatomic distance (r <sub>i</sub> ) (°Å)	4.725	3.75	3.27	2.97	2.76
12.	Molecular electronic polarizability, $\alpha$ (x10 <sup>-23</sup> cm <sup>3</sup> )	1.024	0.51	0.3390	0.253	0.203
13.	Field strength ,F (x 10 <sup>16</sup> cm <sup>-2</sup> )	0.827	1.31	1.731	2.17	2.43
14.	Optical basicity ,(□ <sub>Th</sub> )	0.437	0.438	0.441	0.443	0.445

**Table 2:** Experimental ( $f_{\text{exp}} \times 10^{-6}$ ) and calculated ( $f_{\text{cal}} \times 10^{-6}$ ) oscillator strengths, rms deviation ( $\delta_{\text{rms}}$ ), J-O parameters ( $\Omega_2$ ,  $\Omega_4$  and  $\Omega_6$ ) and spectroscopic quality factor ( $\Omega_4 / \Omega_6$ ) for  $\text{Dy}^{3+}$  ions doped ZnAlBiB glasses

Transitions from $^4\text{I}_{9/2}$	Glass A		Glass B		Glass C		Glass D		Glass E	
	$f_{\text{exp}}$	$f_{\text{cal}}$	$f_{\text{exp}}$	$f_{\text{cal}}$	$f_{\text{exp}}$	$f_{\text{cal}}$	$f_{\text{exp}}$	$f_{\text{cal}}$	$f_{\text{exp}}$	$f_{\text{cal}}$
$^6\text{H}_{11/2}$	1.51	1.75	1.18	1.51	1.35	1.58	0.97	0.70	1.6	1.58
$^6\text{F}_{11/2}$	8.72	8.68	5.74	5.69	6.09	6.05	2.63	2.66	5.2	5.2
$^6\text{F}_{9/2}$	3.59	3.66	2.88	3.03	2.78	2.82	1.61	1.49	2.5	5.00
$^6\text{F}_{7/2}$	3.38	2.99	3.43	2.74	2.93	2.73	0.97	1.30	2.69	2.71
$^6\text{F}_{5/2}$	1.74	1.39	1.55	1.34	2.09	1.39	1.04	6.22	1.49	1.42
$^6\text{F}_{3/2}$	0.00	0.26	0.00	0.25	0.00	0.25	0.00	0.11	0.00	0.26
$^6\text{F}_{1/2}$	0.0	0.00	0.00	0.00	0.00	0.00	0.00	0.00	0.00	0.00
$^4\text{F}_{9/2}$	0.82	0.22	0.59	0.21	0.38	0.21	0.14	0.09	0.27	0.2
$^4\text{I}_{15/2}$	0.00	0.61	0.00	0.53	0.00	0.55	0.00	0.24	0.00	0.56
$^4\text{F}_{7/2}$	0.00	0.80	0.00	0.57	0.00	0.49	0.00	0.30	0.00	0.34
$\delta_{\text{rms}} (\times 10^{-6})$	0.421		0.385		0.352		1.652		0.229	
$\Omega_2$	7.321		4.659		5.491		2.064		5.017	
$\Omega_4$	2.567		1.614		1.118		0.898		0.515	
$\Omega_6$	2.807		2.710		2.776		1.261		2.865	
$\chi = \Omega_4 / \Omega_6$	0.915		0.596		0.403		0.712		0.180	
<b>Trend</b>	$\Omega_2 > \Omega_6 > \Omega_4$		$\Omega_2 > \Omega_6 > \Omega_4$		$\Omega_2 > \Omega_6 > \Omega_4$		$\Omega_2 > \Omega_6 > \Omega_4$		$\Omega_2 > \Omega_6 > \Omega_4$	

**Table-3: Emission peak wavelength ( $\lambda_p$ )(nm), effective band widths( $\Delta\lambda_p$ )(nm), radiative properties such as Transition probability (A)( $S^{-1}$ ), total radiative transition probabilities( $A_T$ ) ( $S^{-1}$ ), radiative life time ( $\tau_R$ ) ( $\mu s$ ), branching ratio ( $\beta_{cal}$  and  $\beta_{mea}$ ) and stimulated emission cross-sections ( $\sigma_e$ )( $cm^2$ ) for sharp emission transitions of  $Dy^{3+}$  ions doped ZnAlBiB glasses.**

Transition $^4F_{9/2}$ $\rightarrow$	Parameters	Glass A	Glass B	Glass C	Glass D	Glass E
$^6H_{15/2}$	$\lambda_p$	483	485	485	485	485
	$\Delta\lambda_p$	17.39	17.39	18.18	17.39	17.39
	A	359.9	327.1	326.7	328.6	155.8
	$A_T$	1957	1490	1580	1515	757.9
	$\beta_{mea}$	0.527	0.532	0.444	0.59	0.59
	$\beta_{cal}$	0.183	0.219	0.206	0.216	0.205
	$\tau_R$	510	670	632	659	1319
	$\sigma_e (x 10^{-22})$	4.61	4.27	4.08	4.29	2.03
$^4H_{13/2}$	$\lambda_p$	577	577	577	577	577
	$\Delta\lambda_p$	15.21	15.21	15.90	17.39	17.39
	A	1225	875	956.6	906.5	404.7
	$A_T$	1957	1490	1580	1515	757.9
	$\beta_{mea}$	0.473	0.468	0.556	0.41	0.41
	$\beta_{cal}$	0.625	0.586	0.605	0.120	0.534
	$\tau_R$	510	670	632	659	1319
	$\sigma_e (x 10^{-22})$	36.5	26.2	27.3	23.7	10.6

**Table 4: Chromaticity color co-ordinates and yellow ( $^4F_{9/2} \rightarrow ^6H_{13/2}$ ) to blue ( $^4F_{9/2} \rightarrow ^6H_{15/2}$ ) intensity ratios (Y/B) for the visible**

**emission spectra of  $Dy^{3+}$  ions doped ZnAlBiB glasses.**

Excitation wavelength(n m)	Chromaticity Coordinates						
	Glass A	Glass B	Glass C	Glass D	Glass E	Average	Y/B ratio (glas s A)
357	(0.312,0.27 6)	(0.373,0.39 4)	(0.302,0.30 4)	(0.283,0.29 9)	(0.278,0.29 1)	(0.309,0.31 2)	1.18
365	(0.308,0.33 2)	(0.309,0.33 1)	(0.292,0.32 0)	(0.275,0.31 9)	(0.283,0.30 0)	(0.293,0.32 0)	1.18
387	(0.330,0.30 0)	(0.300,0.28 0)	(0.300,0.28 0)	(0.280,0.30 0)	(0.320,0.32 0)	(0.306,0.29 6)	1.19
397	(0.314,0.36 2)	(0.300,0.37 0)	(0.300,0.30 7)	(0.279,0.35 9)	(0.285,0.35 5)	(0.295,0.35 0)	1.18
405	(0.290,0.33 4)	(0.318,0.35 1)	(0.452,0.50 7)	(0.257,0.35 2)	(0.641,0.35 9)	(0.391,0.38 0)	1.19

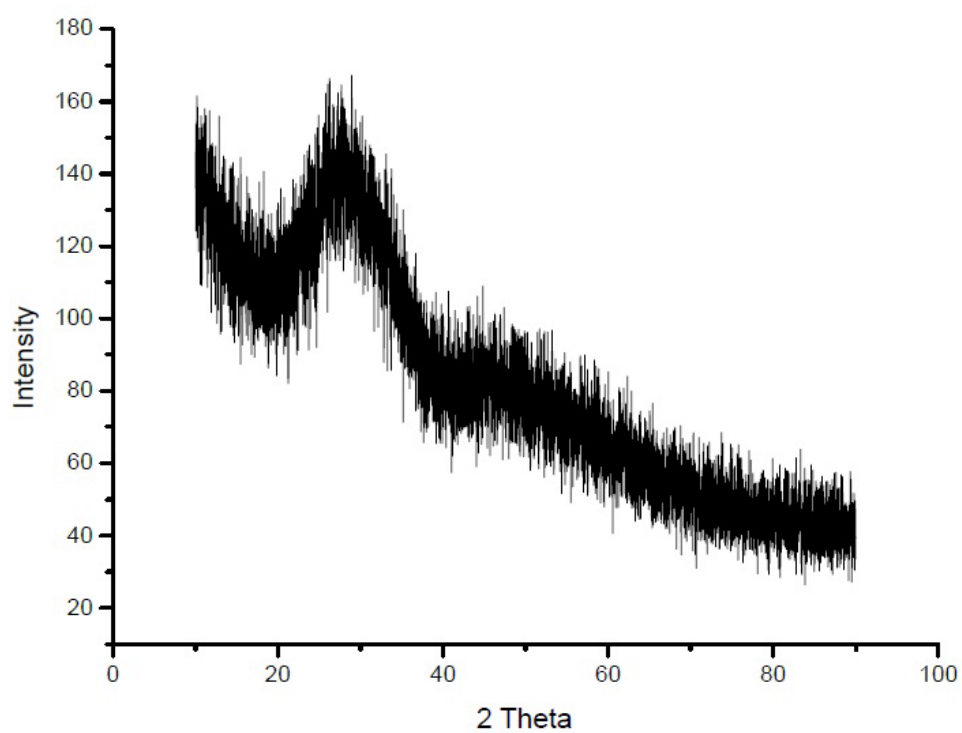


**Fig.1.** XRD spectrum for undoped ZnAlBiB glass

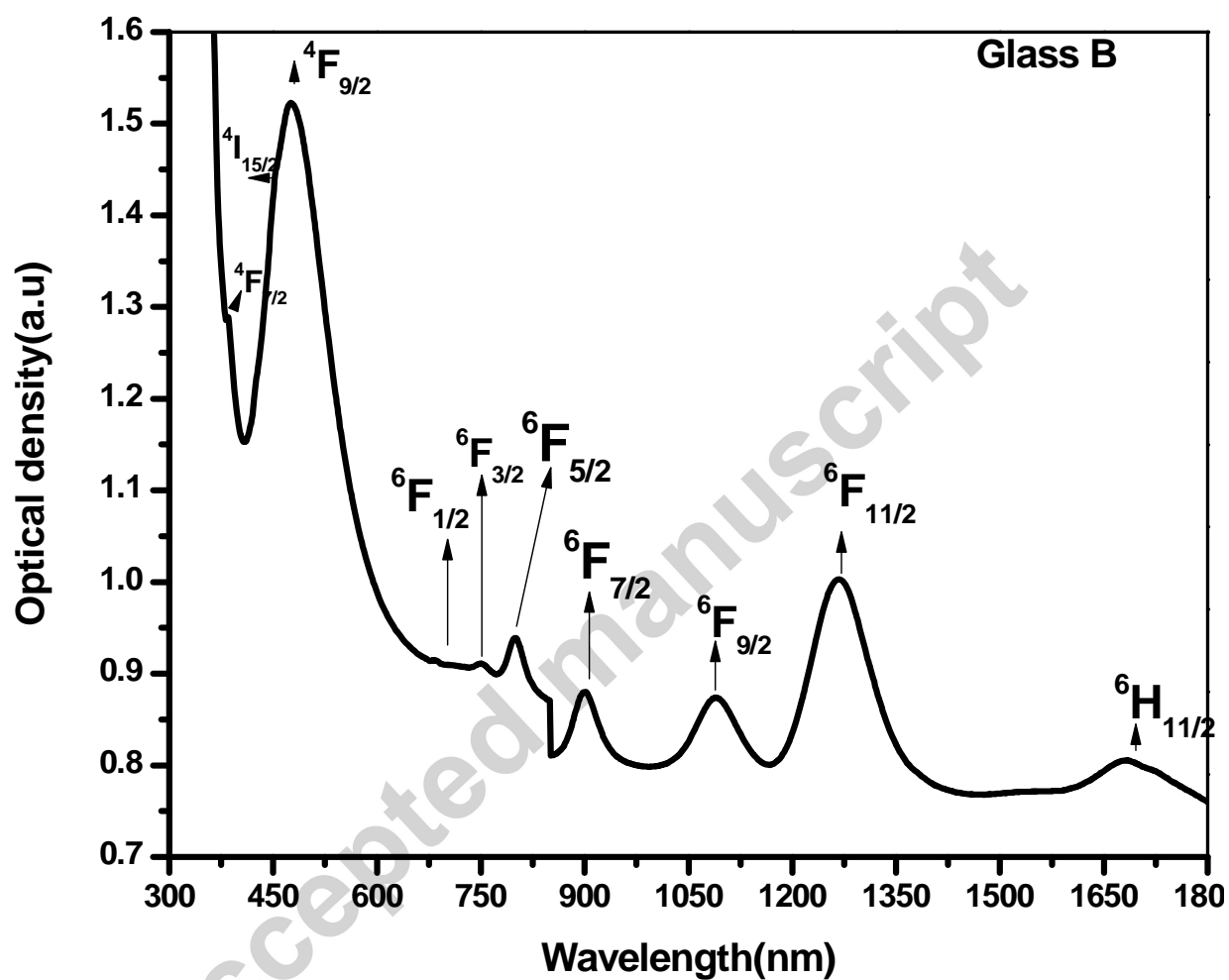
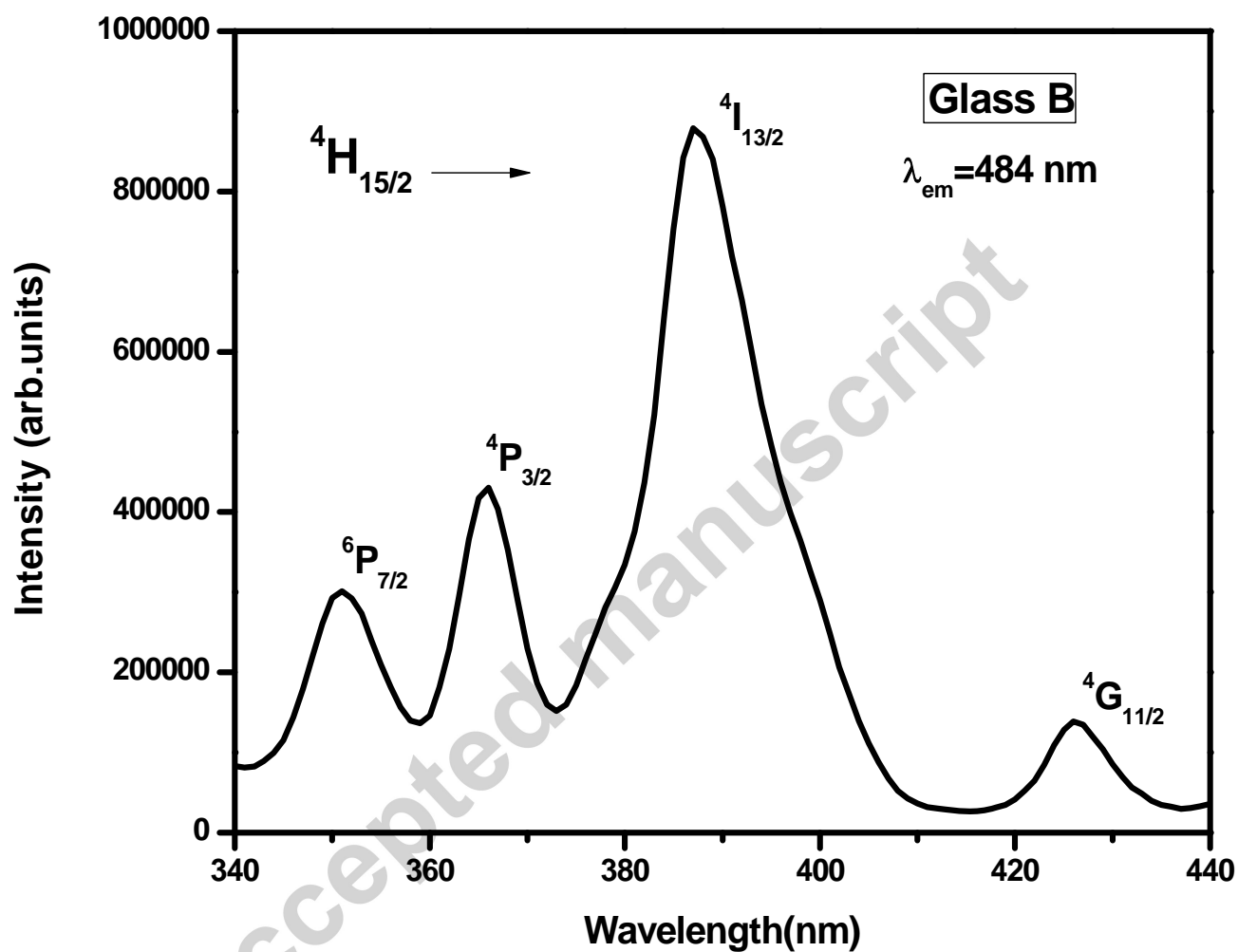
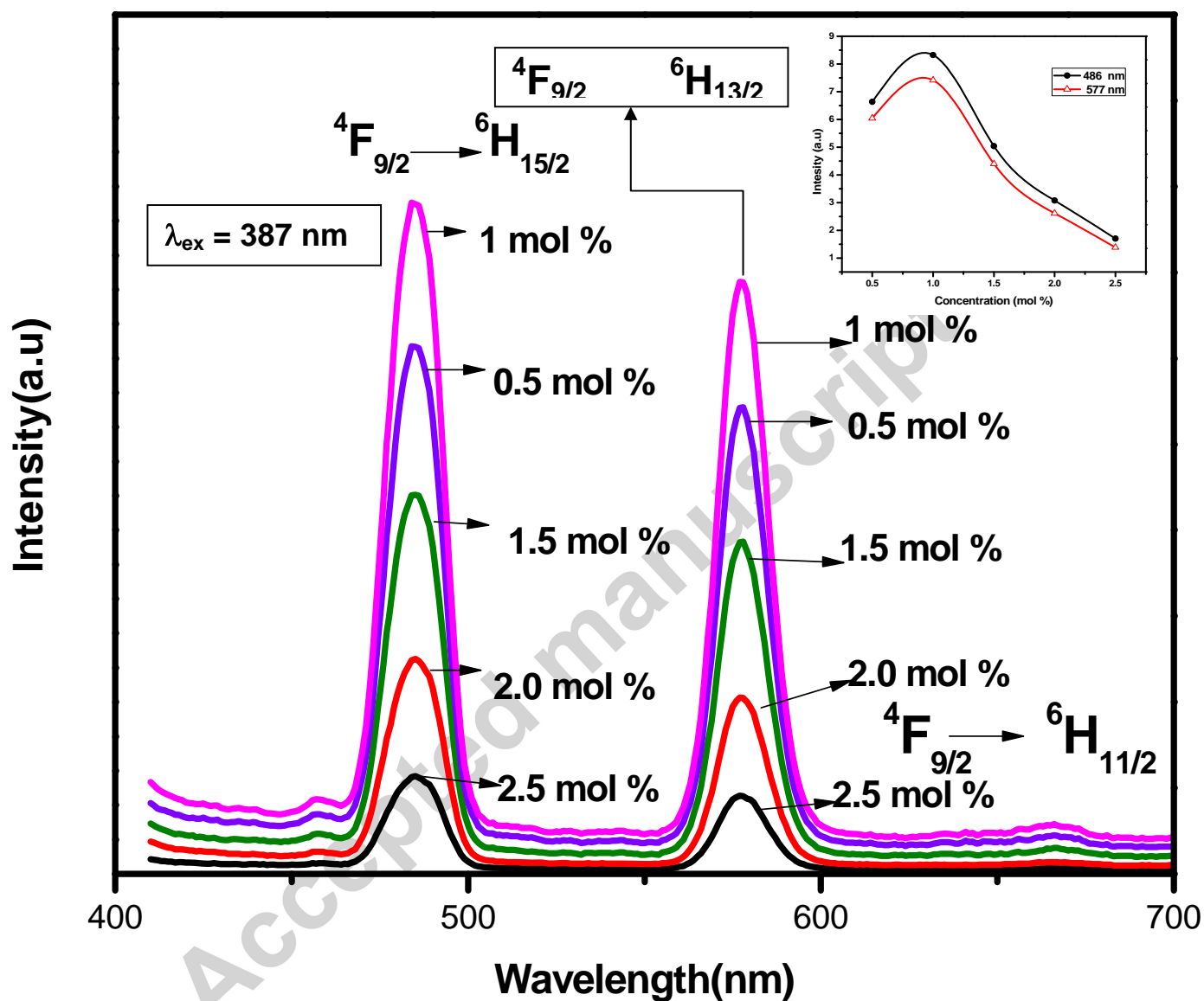


Fig. 2. Absorption spectrum of 1 mol% Dy<sup>3+</sup> ions doped ZnAlBiB glass



**Fig. 3.** Excitation spectrum of 1.0 mol %  $\text{Dy}^{3+}$  ions doped ZnAlBiB glass.



**Fig. 4.** Fluorescence spectra of  $\text{Dy}^{3+}$  ions doped in  $\text{ZnAlBiB}$  glasses.

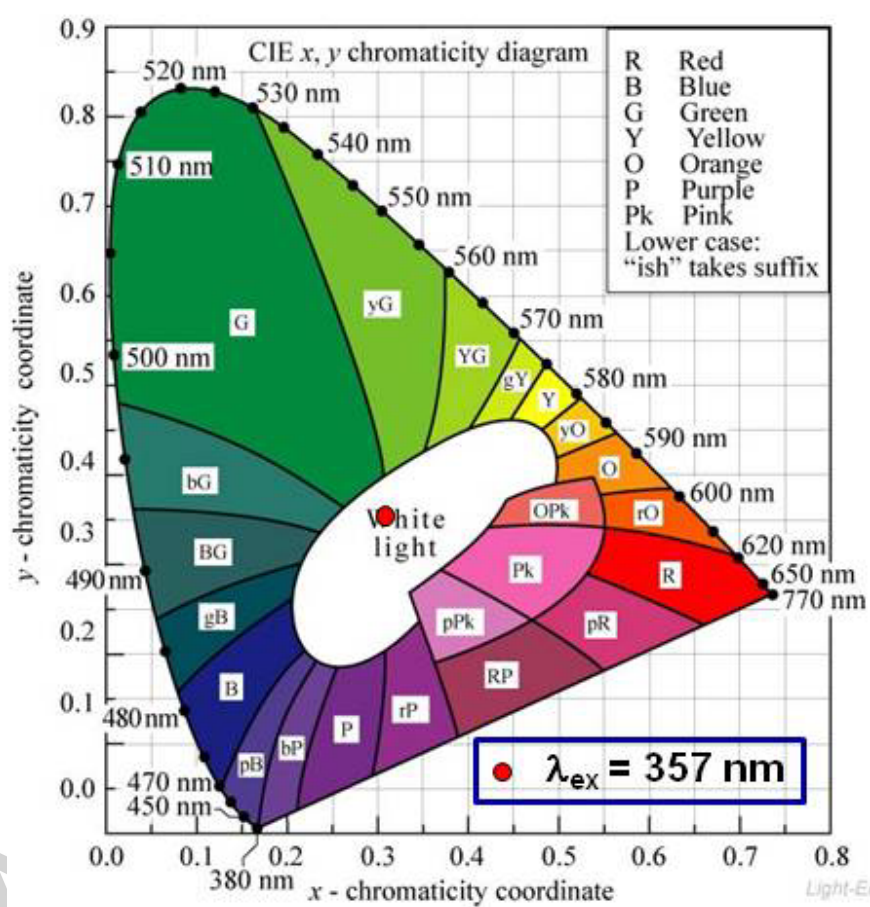


**Fig. 5.** CIE chromaticity coordinates of  $\text{Dy}^{3+}$  ions in  $\text{ZnAlBiB}$  glasses under 357 nm excitation.

**Highlights:**

- Successfully synthesized the transparent Zinc Alumino Bismuth Borate Glasses
- Measured the Absorption and Luminescence properties
- Discussed the spectroscopic properties by using Judd- Ofelt analysis for ZnAlBiB Glasses.
- Finally, suitability of these glasses for Lasers and white LEDs has been discussed

# Performance Analysis of MIMO Network Coding with SISO Physical-Layer Network Coding

Alpana Sahu<sup>1</sup>, Rajveer Mittal<sup>2</sup>

<sup>1,2</sup>Electronics and Communication Engg. Department, Maharaja Agrasen Institute Of Technology, PSP Area, Plot No.1, Sector-22, Rohini Delhi-110086, India.

## ABSTRACT

*In this paper, a two-step communication protocol combined with MIMO (Multiple Input Multiple Output) and network coding is proposed. A three nodes network with two transceiver antennas on relay node is taken. In transmitting phase ZF (Zero-forcing) and MMSE (Minimum Mean Square) detecting techniques are used. In relay node forwarding network coding and Alamouti scheme are exploited together. Theoretical and simulative analyses prove that BER (Bit Error Rate) MMSE in transmitting phase is better than ZF and in relay forwarding MIMO alamouti outperforms the PNC (Physical-layer-network coding).*

**Keywords:** MIMO (Multiple Input Multiple Output), ZF (Zero Forcing), MMSE (Minimum Mean Square) BER (Bit Error Rate) PNC (Physical-layer-network coding), SISO (Single Input Single Output).

## 1. INTRODUCTION

Network coding helps conveying more information by broadcasting mixed information from an intermediate network node to the receiver nodes, where interference can be canceled by appropriately altering the transmit information as in [1]. In MIMO transmission, multiple antennas are put at both the transmitter and the receiver to improve communication performance. MIMO technology has attracted attention in wireless communication, because it offer significant increase in data throughput and link range without additional bandwidth or transmit power. It achieves this by higher spectral efficiency (more bits per second per hertz of bandwidth) and link reliability or diversity (reduced fading). Because of these properties, MIMO is an important part of modern wireless communication standards. A technique known as Alamouti STC (Space Time Coding) is employed at the transmitter with two antennas. STC allows the transmitter to transmit signals (information) both in time and space, meaning the information is transmitted by two antennas at two different times consecutively. By combining network coding and MIMO technology into relay network, system can benefit throughput improvement from network doing as well as spatial multiplexing, and more reliable transmission from spatial diversity [2-5]. In this paper, a two-way relay network with combined MIMO and network coding is presented. The paper is organized as follows: Section II describes the system model of a three nodes relay network with two transceiver antenna at the relay. Section III is devoted to source node transmission. Section IV presented relay node forwarding. Finally, in sections V and VI simulation results and conclusion are presented.

## 2. SYSTEM MODEL

Our system model is based on the canonical two-way network shown in Fig.1. Source nodes,  $N_1$  and  $N_2$ , out of eachother's communication range, have messages to exchange. They communicate through a relay node R that is within the range of both  $N_1$  and  $N_2$ . We assume that the transmission is organized in consecutive time slots enumerated by  $i$ . The source nodes use a single transceiver antenna each. The difference of our system compared to the classical model is that relay node R has two transceiver antennas instead of one. Since the signals originating at  $N_1$  and  $N_2$  are mutually independent from each other and are locally displaced, and since R has two transceiver antennas, the system can be seen as a  $2 \times 2$  virtual MIMO system with spatial diversity scheme.

## 3. SOURCE NODE TRANSMISSION

Let us denote the signal transmitted by the source node  $N_1$  in the  $i^{\text{th}}$  time slot by  $s_i^{(1)}(t)$  and the signal transmitted by the source node  $N_1$  in the  $(i+1)^{\text{th}}$  time slot by  $s_{(i+1)}^{(1)}(t)$ . Similarly, the signals transmitted by the source node  $N_2$  in the  $i^{\text{th}}$  and the  $(i+1)^{\text{th}}$  time slots shall be denoted by  $s_i^{(2)}(t)$  and  $s_{(i+1)}^{(2)}(t)$ , respectively. Let us assume that the transmit signals

$s_i^{(1)}(t)$ ,  $s_{(i+1)}^{(1)}(t)$ ,  $s_i^{(2)}(t)$  and  $s_{(i+1)}^{(2)}(t)$  are Binary phase shift keying (BPSK) modulated signals, each comprising single bit. Let  $E_b$  denote the bit energy and  $T_b$  shall be the bit duration. Now, let  $b_i^{(1)}$  be the data vector, representing the data, transmitted by the source node  $N_1$  in the time slot  $i$  using  $b_i^{(1)} \in \{-1, +1\}$  and correspondingly, let  $b_i^{(2)}$  denote the data vector at source node  $N_2$  in the same time.[7-10]

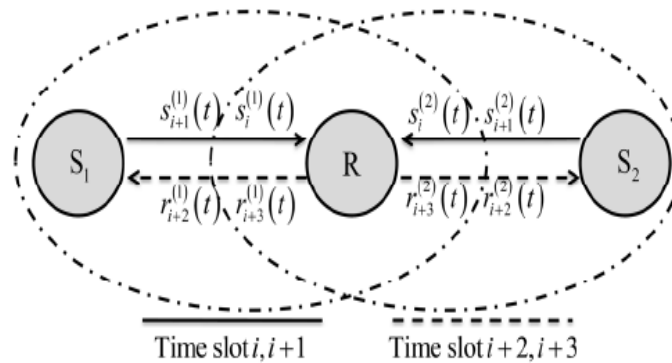


**Figure 1:** Three Nodes Relay Network with Two-Step transmission

Slot  $i$ . The transmit signals hence given by

$$S_i^{(1)}(t) = b_i^{(1)}p(t) \quad (1)$$

and

$$S_i^{(2)}(t) = b_i^{(2)}p(t) \quad (2)$$

in the time slot  $i$  when using the BPSK impulse

$$p(t) = \sqrt{\frac{2E_b}{T_b}} \begin{cases} 1 & \text{for } 0 \leq t < T_b \\ 0 & \text{else} \end{cases} \quad (3)$$

The relay node  $R$  receives these signals via its two transceiver antennas. Let  $h_i^{(1,1)}(t)$  denote the channel impulse response between the first source node  $N_1$  and the first antenna of the relay node  $R$  in the time slot  $i$ . Furthermore, let  $h_i^{(1,2)}(t)$  denote the channel impulse response between the first source node and the second antenna of the relay node  $R$  in the time slot  $i$ . Similarly,  $h_i^{(2,1)}(t)$  and  $h_i^{(2,2)}(t)$  represent the channel impulse responses between the second source node  $N_2$  and the first as well as the second antenna of the relay node  $R$ . In this case, the channel impulse responses approximately represent single path channels with negligible time variance; rather, inter-time slot time variations can occur. Hence, the general complex-valued numbers  $h_i^{(1,1)}(t)$ ,  $h_i^{(1,2)}(t)$ ,  $h_i^{(2,1)}(t)$  and  $h_i^{(2,2)}(t)$  can be used to represent the channel impulse responses. We will take into account that  $h_i^{(1,1)}(t)$ ,  $h_i^{(1,2)}(t)$ ,  $h_i^{(2,1)}(t)$  and  $h_i^{(2,2)}(t)$  represent Rayleigh-flat-fading channels with variance  $\sigma^2$  equal to 1 with the additive white Gaussian noise signals  $n_i^{(1)}(t)$  and  $n_i^{(2)}(t)$  at the first and the second antenna of  $R$  in the time slot  $i$  and each having double-sided spectral noise power density  $N_0/2$ .

### 3.1 Numerical Analysis

Let us assume that  $e_{R,i}^{(1)}(t)$  and  $e_{R,i}^{(2)}(t)$  being the received signals at the first and the second antenna of  $R$  in the time slot  $i$ , the communication system is given by

$$e_{R,i}^{(1)}(t) = h_i^{(1,1)} S_i^{(1)}(t) + h_i^{(2,1)} S_i^{(2)}(t) + n_i^{(1)}(t) \quad (4)$$

$$e_{R,i}^{(2)}(t) = h_i^{(1,2)} S_i^{(1)}(t) + h_i^{(2,2)} S_i^{(2)}(t) + n_i^{(2)}(t) \quad (5)$$

Equations (4) and (5) can be represented in matrix form as

$$\begin{bmatrix} e_{R,i}^{(1)}(t) \\ e_{R,i}^{(2)}(t) \end{bmatrix} = \begin{bmatrix} h_i^{(1,1)} & h_i^{(2,1)} \\ h_i^{(1,2)} & h_i^{(2,2)} \end{bmatrix} \begin{bmatrix} S_i^{(1)}(t) \\ S_i^{(2)}(t) \end{bmatrix} + \begin{bmatrix} n_i^{(1)}(t) \\ n_i^{(2)}(t) \end{bmatrix} \quad (6)$$

Similarly,  $e_{R,(i+1)}^{(1)}(t)$  and  $e_{R,(i+1)}^{(2)}(t)$  being the received signals at the first and the second antenna of  $R$  in the time slot  $i+1$ . The relay node  $R$  determines the information contained in the received signals, yielding the detected versions  $b_i^{(1)}$  and  $b_i^{(2)}$  of  $b_i^{(1)}$  and  $b_i^{(2)}$ . Different detection techniques, for example Zero-forcing (ZF) based V-BLAST as in [4] or its Minimum mean square error (MMSE) as explained in [5] could be used.

### 3.2 MIMO ZF receiver

In this section, we will try to improve the bit error rate performance by trying out Successive Interference Cancellation (SIC). We will assume that channel is a flat fading Rayleigh multipath channel and the modulation is BPSK. Equations (4) and (5) can be represented in matrix form as shown in equation (6).

Equivalently,

$$e = hs + n \quad (7)$$

where

$\mathbf{s} = \mathbf{b} \cdot \mathbf{p}$  in this  $\mathbf{b} \in \{1, -1\}$  and  $p = 1$  = BPSK impulse power. Now, equation (7) can also be written as

$$\mathbf{e} = \mathbf{h}\mathbf{b} + \mathbf{n} \quad (8)$$

To solve for  $\mathbf{b}$ , the Zero-Forcing (ZF) in [4] linear detector for meeting the constraint is given by

$$\mathbf{W} = (\mathbf{h}^H \mathbf{h})^{-1} \mathbf{h}^H \quad (9)$$

Where  $\mathbf{H}$  = Hermitian Transpose. To do the Successive Interference Cancellation (SIC), the receiver needs to perform the following:

Using the ZF equalization approach described above, the receiver can obtain an estimate of the two transmitted symbols  $\mathbf{b}^{(1)}$  and  $\mathbf{b}^{(2)}$

$$\begin{bmatrix} \tilde{\mathbf{b}}^{(1)} \\ \tilde{\mathbf{b}}^{(2)} \end{bmatrix} = (\mathbf{h}^H \mathbf{h})^{-1} \mathbf{h}^H \begin{bmatrix} \mathbf{e}^{(1)} \\ \mathbf{e}^{(2)} \end{bmatrix} \quad (10)$$

### 3.3 BER for ZF receiver

Till now we have seen that  $h$  is used to represent the channel impulse response and is called Rayleigh Random Variable. It is a identical distributed Gaussian random variable with mean 0 and variance  $\sigma^2$ . The magnitude  $|h|$  has a probability density function

$$p(h) = \frac{h}{\sigma^2} e^{-\frac{h^2}{2\sigma^2}} \quad (11)$$

$$\mathbf{e} = \mathbf{h}\mathbf{b} + \mathbf{n} \quad (12)$$

where  $\mathbf{e}$  is the received symbol,  $h$  is complex scaling factor corresponding to Rayleigh multipath channel  $\mathbf{b}$  is the transmitted symbol (taking values +1's and -1's) and  $\mathbf{n}$  is the Additive White Gaussian Noise (AWGN)

#### Assumptions:

1. The channel is flat fading; In simple terms, it means that the multipath channel has only one tap. So, the convolution operation reduces to a simple multiplication.
2. The channel is randomly varying in time; meaning each transmitted symbol gets multiplied by a randomly varying complex number. Since modeling is a Rayleigh channel, the real and imaginary parts are Gaussian distributed having mean 0 and variance 1/2.
3. The noise has the Gaussian probability density function with

$$p(n) = \frac{h}{2\pi\sigma^2} e^{-\frac{(n-\mu)^2}{2\sigma^2}} \quad (13)$$

with  $\mu=0$  and  $\sigma^2=N_0/2$ .

4. The channel  $h$  is known at the receiver. Equalization is performed at the receiver by dividing the received symbol  $\mathbf{e}$  by the apriori known as  $\mathbf{h}$  i.e.

$$\tilde{\mathbf{e}} = \frac{\mathbf{e}}{h} = \frac{h\mathbf{b} + \mathbf{n}}{h} = \mathbf{b} + \tilde{\mathbf{n}} \quad (14)$$

Where,  $\tilde{\mathbf{n}} = \mathbf{n}/h$

In the BER computation in AWGN, the probability of error for transmission of either +1 or -1 is computed by integrating the tail of the Gaussian probability density function for a given value of bit energy to noise ratio  $E_b/N_0$ . The bit error rate is,

$$p_b = \frac{1}{2} \text{erfc}\left(\sqrt{\frac{E_b}{N_0}}\right) \quad (15)$$

However, in the presence of channel  $h$ , the effective bit energy to noise ratio is  $|h|^2 E_b/N_0$ . So, the bit error probability for a given value of  $h$  is,

$$p_b = \frac{1}{2} \text{erfc}\left(\sqrt{\frac{|h|^2 E_b}{N_0}}\right) = \frac{1}{2} \text{erfc}(\sqrt{\gamma}) \quad (16)$$

Where,  $\gamma = |h|^2 E_b/N_0$ . To find the error probability over all random values of  $|h|^2$ , one must evaluate the conditional probability density function  $P_{(b|h)}$  over the probability density function of  $\gamma$ .

#### Probability density functions of $\gamma$ :

From chi-square random variable, we know that if  $|h|$  is a Rayleigh distributed random variable, then  $|h|^2$  is chi-square distributed with two degrees of freedom. Since  $|h|^2$  is chi square distributed,  $\gamma$  is also chi square distributed. The probability density function of is,

$$P_{\gamma} = \left( \frac{1}{E_b / N_o} \right) e^{-\frac{\gamma}{E_b / N_o}} \quad (17)$$

Error probability: the error probability is,

$$P_b = \int_0^{\infty} \frac{1}{2} \operatorname{erfc}(\sqrt{\gamma}) p(\gamma) d\gamma \quad (18)$$

This equation reduces to

$$P_b = 1 - \left( \frac{E_b / N_o}{1 + E_b / N_o} \right)^{1/4} \quad (19)$$

or

$$P_b = 1 - \left( \frac{\gamma_b}{1 + \gamma_b} \right)^{1/4} \quad (20)$$

### 3.4 MIMO MMSE receiver

In this section, we extend the concept of successive interference cancellation to the MMSE equalization in [5] and simulate the performance. We will assume that the channel is a flat fading Rayleigh multipath channel and the modulation is BPSK. In the first time slot i.e. i, the received signal on the first receive antenna is shown in equation (4) and the received signal on the second receive antenna is given in equation (5). For convenience, the equations (4) and (5) can be represented in matrix notation as given by equation (6).

Equivalently,

$$\mathbf{e} = \mathbf{h}\mathbf{s} + \mathbf{n} \quad (21)$$

where,

$\mathbf{s} = \mathbf{b} \cdot \mathbf{p}$  in this  $\mathbf{b} \in \{-1, +1\}$  and  $p=1$ =BPSK impulse power. Now, equation (21) can also be written as

$$\mathbf{e} = \mathbf{h}\mathbf{b} + \mathbf{n} \quad (22)$$

The Minimum Mean Square Error (MMSE) approach tries to find a coefficient which minimizes the criterion,

$$E = \{[\mathbf{W}\mathbf{e} - \mathbf{b}][\mathbf{W}\mathbf{e} - \mathbf{b}]^H\} \quad (23)$$

Solving,

$$\mathbf{W} = [\mathbf{h}^H \mathbf{h} + N_o \mathbf{I}]^{-1} \quad (24)$$

Using the Minimum Mean Square Error (MMSE) equalization, the receiver can obtain an estimate of the two transmitted symbols  $\mathbf{b}^{(1)}$  and  $\mathbf{b}^{(2)}$  i.e.

$$\begin{bmatrix} \tilde{\mathbf{b}}^{(1)} \\ \tilde{\mathbf{b}}^{(2)} \end{bmatrix} = (\mathbf{h}^H \mathbf{h} + N_o \mathbf{I})^{-1} \mathbf{h}^H \begin{bmatrix} \mathbf{e}^{(1)} \\ \mathbf{e}^{(2)} \end{bmatrix} \quad (25)$$

### 3.5 RELAY NODE FORWARDING

The decode-and-forward (DF) forwarding scheme is deployed in the second step i.e in relay node forwarding. The relay node R re-encodes and re-modulates the received signals  $\tilde{\mathbf{b}}_i^{(1)}$  and  $\tilde{\mathbf{b}}_i^{(2)}$ , the detected version of  $\mathbf{b}_i^{(1)}$  and  $\mathbf{b}_i^{(2)}$  forwards them to source nodes. In this section, network coding and space-time block coding (STBC), like e.g. the Alamouti scheme [3] and [6] are exploited together to get coding multiplexing and spatial diversity gain. Network coding will improve network throughput, and STBC will help overcome channel fading [11-15]. In order to validate this paradigm, a simple network coding scheme will be applied, first. Let  $\mathbf{r}_{i+2}^{(1)}(t)$  and  $\mathbf{r}_{i+2}^{(2)}(t)$  represent the signals transmitted over the first and the second antenna of the relay node R, respectively, in the time slot (i+2) to both the source nodes  $N_1$  and  $N_2$ . The network coding scheme is given by the bit-wise multiplication of the signals received in the  $i^{\text{th}}$  and the  $(i+1)^{\text{th}}$  time slots according to the following rule:

$$\mathbf{r}_{i+2}^{(1)}(t) = \tilde{\mathbf{b}}_i^{(1)} \tilde{\mathbf{b}}_i^{(2)} \cdot P(t) \quad (26)$$

$$\mathbf{r}_{i+2}^{(2)}(t) = \tilde{\mathbf{b}}_{(i+1)}^{(1)} \tilde{\mathbf{b}}_{(i+1)}^{(2)} \cdot P(t) \quad (27)$$

Similarly, Let  $\mathbf{r}_{i+3}^{(1)}(t)$  and  $\mathbf{r}_{i+3}^{(2)}(t)$  represent the signals transmitted over the first and the second antenna of the relay node R, respectively, in the time slot (i + 3) to both the source nodes  $N_1$  and  $N_2$  and are given by

$$\mathbf{r}_{i+3}^{(1)}(t) = \tilde{\mathbf{b}}_{(i+1)}^{(1)} \tilde{\mathbf{b}}_{i+1}^{(2)} \cdot P(t) \quad (28)$$

$$r_{i+3}^{(2)}(t) = \tilde{b}_i^{(1)} \tilde{b}_i^{(2)} P(t) \quad (29)$$

After network coding, the Alamouti scheme is applied with the formats

$$r_{i+2}^{(2)}(t) = -(r_{i+3}^{(1)}(t))^* \quad (30)$$

$$r_{i+2}^{(2)}(t) = (r_{i+2}^{(1)}(t))^* \quad (31)$$

The signal received at the source node  $N_1$  in the time slot  $(i+2)$  and  $(i+3)$  is given by

$$e^{(1)}_{N,(i+2)}(t) = h_{(i+2)}^{(1,1)} r_{(i+2)}^{(1)}(t) + h_{(i+2)}^{(1,2)} r_{(i+2)}^{(2)}(t) + n_{(i+2)}^{(1)}(t) \quad (32)$$

$$e^{(1)}_{N,(i+3)}(t) = h_{(i+3)}^{(1,1)} r_{(i+3)}^{(1)}(t) + h_{(i+3)}^{(1,2)} r_{(i+3)}^{(2)}(t) + n_{(i+3)}^{(1)}(t) \quad (33)$$

On applying Alamouti scheme in equation (33) from equations (30) and (31) we get

$$e^{(1)}_{N,(i+3)}(t) = -h_{(i+3)}^{(1,1)} (r_{(i+2)}^{(1)}(t))^* + h_{(i+3)}^{(1,2)} (r_{(i+3)}^{(2)}(t))^* + n_{(i+3)}^{(1)}(t) \quad (34)$$

On rearranging the terms we get

$$e^{(1)}_{N,(i+3)}(t) = h_{(i+3)}^{(1,2)} (r_{(i+3)}^{(2)}(t))^* - h_{(i+3)}^{(1,1)} (r_{(i+2)}^{(1)}(t))^* + n_{(i+3)}^{(1)}(t) \quad (35)$$

Now, equations (32) and (35) can be represented in matrix form as

$$\begin{bmatrix} e^{(1)}_{N,(i+2)}(t) \\ e^{(1)}_{N,(i+3)}(t) \end{bmatrix} = \begin{bmatrix} h_{(i+2)}^{(1,1)} & h_{(i+2)}^{(1,2)} \\ (h_{(i+3)}^{(1,2)})^* & -(h_{(i+3)}^{(1,1)})^* \end{bmatrix} \begin{bmatrix} r_{(i+2)}^{(1)}(t) \\ r_{(i+2)}^{(2)}(t) \end{bmatrix} + \begin{bmatrix} n_{(i+2)}^{(1)}(t) \\ n_{(i+3)}^{(1)}(t) \end{bmatrix} \quad (36)$$

Similarly, the signals received at the source node  $N_2$  in the time slots  $(i+2)$  and  $(i+3)$  can be represented in matrix form as

$$\begin{bmatrix} e^{(2)}_{N,(i+2)}(t) \\ e^{(2)}_{N,(i+3)}(t) \end{bmatrix} = \begin{bmatrix} h_{(i+2)}^{(2,1)} & h_{(i+2)}^{(2,2)} \\ (h_{(i+3)}^{(2,2)})^* & -(h_{(i+3)}^{(2,1)})^* \end{bmatrix} \begin{bmatrix} r_{(i+2)}^{(1)}(t) \\ r_{(i+2)}^{(2)}(t) \end{bmatrix} + \begin{bmatrix} n_{(i+2)}^{(2)}(t) \\ n_{(i+3)}^{(2)}(t) \end{bmatrix} \quad (37)$$

Now the source nodes  $N_1$  and  $N_2$  detect  $\tilde{b}_{(i+2)}^{(1)}$  and  $\tilde{b}_{(i+3)}^{(1)}$ , then estimate the combined signal using Maximum likelihood (ML) decision rule. The corresponding bit error probability of this  $2 \times 1$  MISO system [7], is given by

$$P_{e, \text{Alam}} = \frac{1}{2} \left( 1 - \frac{1}{2} \sqrt{\frac{\gamma_b}{2 + \gamma_b}} \left( 3 - \frac{\gamma_b}{2 + \gamma_b} \right) \right) \quad (38)$$

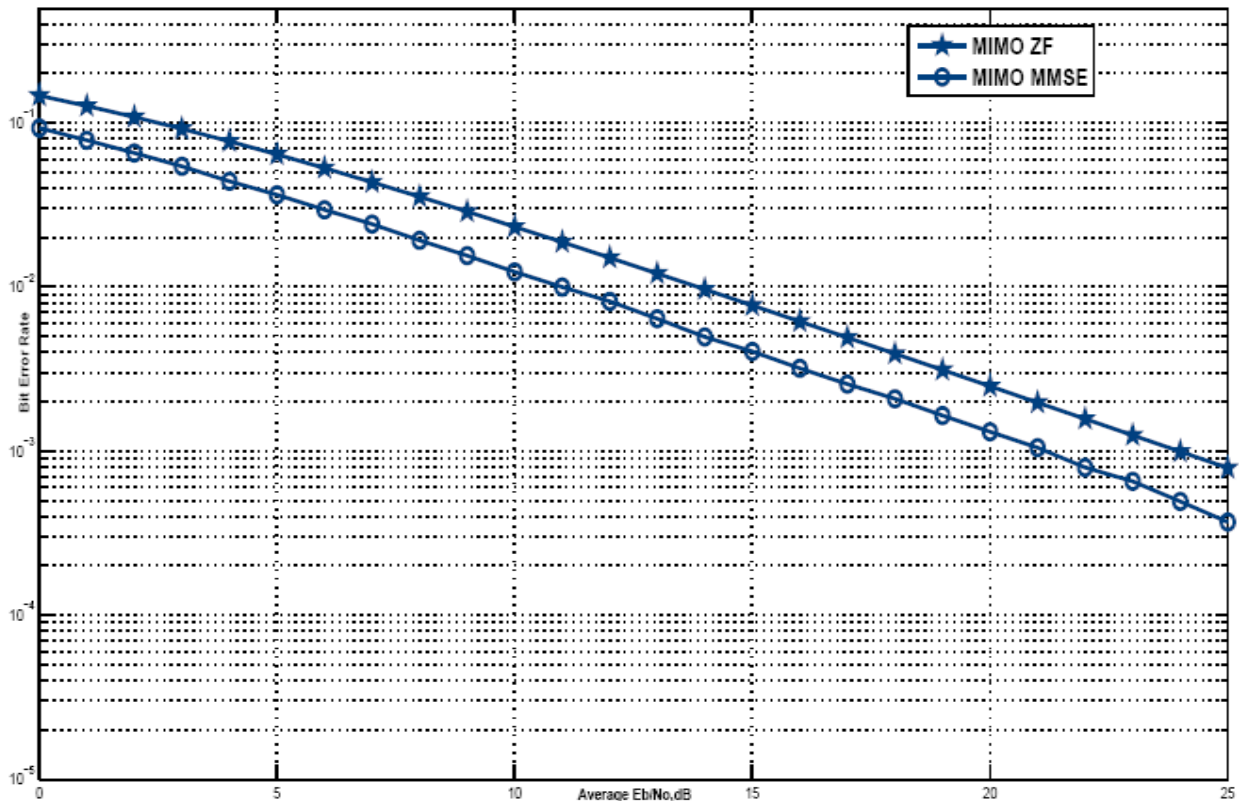
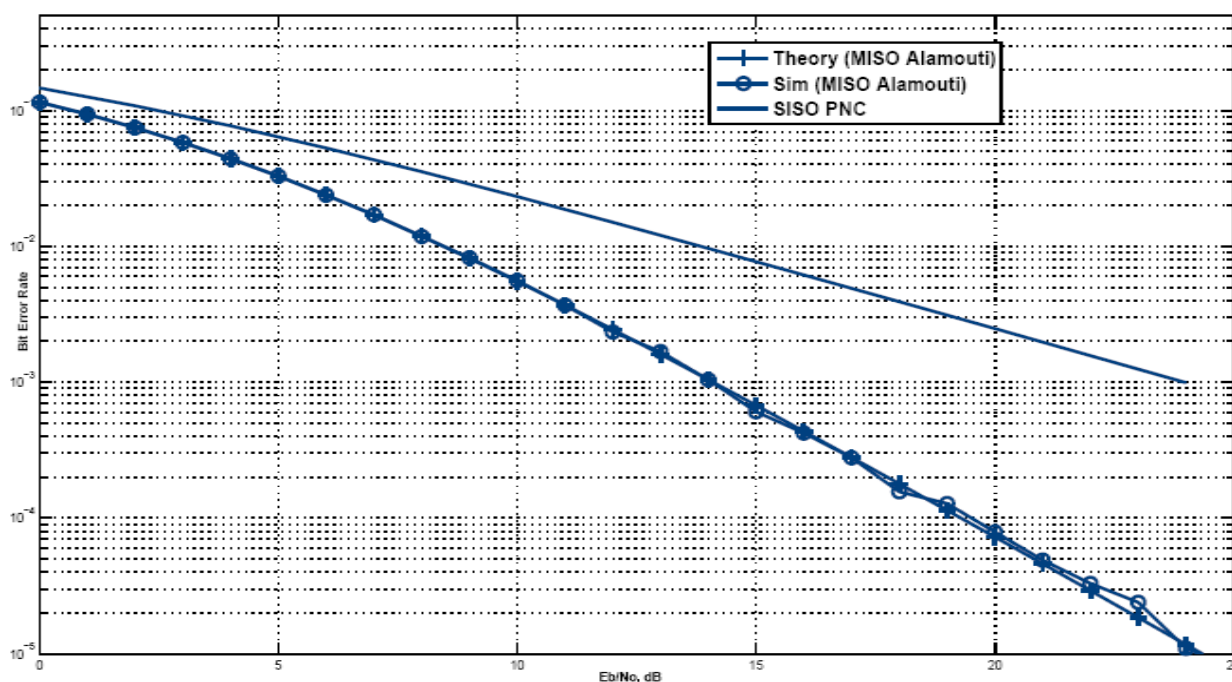


Figure 2: Overall BER Comparison of ZF and MMSE in transmitting phase.

## 5. SIMULATION RESULTS

In this paper, we compare the performance of the physical layer network coding (PNC) with the newly proposed Multiple Input Multiple Output Network Coding Scheme. Both schemes use BPSK, Rayleigh-flat-fading channel model is assumed between each antenna pair in the system. Fig.2 and Fig.3 provides a comparison of the overall bit error performance obtained in the three nodes relay network. In the source node transmission of the MIMO network coding scheme, two different spatial multiplexing receivers, ZF and MMSE are deployed at the relay node R. The BER comparison of both is shown in Fig.2. In the relay node forwarding of MIMO network coding scheme (BER comparison with PNC shown in Fig.3), the source node  $N_1$  or  $N_2$  applies Maximum Likelihood (ML) symbol detector followed by a binary exclusive or (XOR) operation to extract BPSK signals from the other. At last we found that MIMO network coding outperforms the PNC.



**Figure 3:** BER for BPSK modulation with 2×1 MISO Alamouti and PNC (Rayleigh Channel)

## 6. CONCLUSION

In this paper, a new two-way protocol with combination of MIMO and network coding has been proposed. The benefits of MIMO network coding come from two transceiver antennas at the relay node R, where both code multiplexing and spatial diversity gains can be jointly exploited. Theoretical and simulative performance analyses show that MIMO network coding protocol with MMSE detection at the transmitting phase outperforms PNC schemes and provides more robust and efficient transmission.

## REFERENCES

- [1] S. Zhang, S.C. Liew, and P.P. Lam, "Physical layer network coding", IEEE Trans. On Networking.
- [2] S.M. Alamouti, "A Simple transmit diversity technique for wireless communication", IEEE J. Sel. Areas Commun., vol. 16, pp.1451-1458, October 1998.
- [3] E. Fasolo, F. Rossetto, and M. Zorzi, "Network Coding meets MIMO", Network Coding, Theory and Applications, 2008. Fourth Workshop on (NetCod 2008), pp. 1-6, January 2008.
- [4] M. Kiessling, and J. Speidel, "Analytical performance of MIMO zeroforcing receivers in correlated Rayleigh fading environments", Signal Processing Advances in Wireless Communications, 2003. SPAWC 2003. 4th IEEE Workshop on., pp. 383-387, June 2003.
- [5] M. Kiessling, and J. Speidel, "Analytical performance of MIMO MMSE receivers in correlated Rayleigh Fading Environment", Vehicular Technology Conference, 2003. VTC 2003-Fall., vol. 3, pp. 1738-1742, October 2003.
- [6] D. Gesbert, M. Shafi, D. Shiue, P.J. Smith and A. Nagueb, "From theory to practice: An overview MIMO Space Time Coded Wireless Systems", IEEE J-SEC, vol. 21, no.3, pp. 281-302, March 2003.
- [7] H. Zhang, and T.A. Gulliver, "Capacity and error probability analysis for orthogonal space-time block codes over fading channels", IEEE Trans. Wireless Commun., vol. 4, pp. 808-819, March 2005.

- [8] Y. Wu, P.A. Chou, S.Y. Kung, "Information exchange in wireless networks with network coding and physical-layer broadcast", in Proc. 39th Annual Conf. Inform. Sci. and Systems (CISS), 2005.
- [9] S. Zhang, and S.C. Liew, "Capacity of Two-Way Relay Channel", the 3rd Beijing-Hong Kong Doctoral Forum, 2008.
- [10] A. Vardy, and Y. Be'ery, "Maximum likelihood soft-decision decoding of BCH codes." IEEE Trans. Inform. theory, Vol.40, pp. 546-554, Mar. 1994.
- [11] N. shulman and M.feder, "Random Coding Techniques for non-random codes," IEEE Trans. Inform. theory, Vol.45, no.6, pp. 2101-2104, september 1999.
- [12] C. Schnurr, T.J. Oechtering, and S. Stanczak, "On Coding for the broadcast phase in the two way relay channel", in Proc. Conference on Information Sciences and Systems (CISS'07), March 2007.
- [13] L. Ekroot and S. Dolinar, "A decoding of block codes", IEEE Trans. Commun., vol. 50, No.9, pp. 1052-1056, Sep. 1996.
- [14] M.O. Hasna and M.S. Alouini, "Enc-to-end performance of transmission systems with relay over Rayleigh-fading channels", IEEE Trans. Wireless Commun., Vol.2, No.6, pp. 1126-1131, Nov. 2003.
- [15] P. Larsson, N. Johansson, and K. E. Sunell, "Coded bi-directional relaying", in Proc. IEEE Int. Veh. Tech. Conf. (VTC), Melbourne, Australia, May 2006, pp.851-855.

#### **AUTHOR**



**Alpana Sahu** received her B.Tech degree in Electronics and communication engineering from Vira college of Engineering, UP.Technical University, India in 2004, M.Tech. degree in Signal Processing from, Netaji Subhas Institute of Technology, Delhi University, Delhi, India in 2011. Currently, she is working as an Assistant professor in Electronics and communication Engineering Department with the Maharaja Agrasen Institute of Technology, Rohini, Delhi under GGSIP University, Delhi, India. Her research interests include power quality, network coding in physical layer and signal processing.



**Rajveer Mittal** received his B.E degree in Electrical Engineering from R.E.C, Kurukshetra, Haryana, India in 1987, the M.E degree in Electrical Engineering (Instrumentation & Control) from Delhi College of Engineering, Delhi University, Delhi, India in 2003, and is currently pursuing the Ph.D. degree in the research area of "Power Quality Studies of Wind Energy Systems" of Electrical Engineering from N.I.T, Kurukshetra, Haryana, India. Currently, he is working as HOD (EEE) Department with the Maharaja Agrasen Institute of Technology, Rohini, Delhi under GGSIP University, Delhi, India. His research interests include power quality, motor drives, and Renewable energy.

# **PROTECTION OF FLOOD EMBANKMENTS BY SPURS WITH REFERENCE TO KOSI RIVER**

**S.K. MAZUMDER**

Individual Consultant, New Delhi

(Former AICTE Emeritus Professor of Civil Engg. Delhi College of Engineering)

e-mail:somendrak64@rediffmail.com, web: www.profskmazumder.com

## **SYNOPSIS**

Flood embankments are constructed to train a river and protect the flood prone areas due to spill of the river. Embankments are to be protected in all such reaches vulnerable to river attack by providing revetments/pitching/stone crates/gabions. Spurs are usually provided to deflect the river away from the bank when the river flows hugging the embankment. Long impermeable spurs cause flow restriction, afflux and deep scour near the spur heads. Permeable spurs are cheaper and flexible since they cause partial obstruction to flow. In spite of providing 378 impermeable spurs on left and right flood embankments in Kosi river, the embankments breached on several occasions due to failure of the spurs. The breach that occurred at Kusaha in the left flood embankment of Kosi in 2008 was triggered by the failure of two long spurs upstream of the breach site. It caused avulsion of Kosi river flow bringing devastation of five districts in north Bihar. An effort has been made to analyse the cause of the 2008 breach which is likely due to choking of flow and flow instability resulting in wash out of the spurs and subsequent breaching of the flood embankment.

## **INTRODUCTION**

Flood embankments are constructed along river banks to protect the countryside from flood damages due to spilling of river banks. In India, we have constructed about 34,000 km of flood embankments (at central and state level) - a large percentage of which are in north and north east India where the rivers are shallow and wide due to meandering/braiding of river course. Flood embankments are constructed with earth made of clay, silt and sand locally available from river bed and banks. Guidelines for planning and design of flood embankments are available in IS (12094:2000, 11532:1995) and IRC (89: 1997) codes.

Flood embankments often breach (Mazumder, 2011 ) due to a number of reasons, resulting in damage to standing crops, loss of human and animal life, destruction of properties, dislocation of communication and unimaginable sufferings of people which can not be measured in terms of money. Spurs are often constructed along the river banks for protection of embankments against direct attack by the river. 378 numbers of spurs of different lengths were constructed on the eastern and western marginal flood embankments on either side of river Kosi to save the embankments from the fury of the river. Yet, the embankments breached on several occasions. About 2.2 km long breach of the left flood embankment occurred in 2008 due to failure of spurs near Kusaha about 12 km upstream of Kosi barrage. It caused flow avulsion of the river Kosi resulting in devastation in the five districts of north Bihar (Pun-2009, Mishra-2008, Sinha-2009a &b).

One of the primary objectives of writing this paper is to critically examine the effectiveness of impervious spurs-especially long ones- provided in the left flood embankment near Kusaha used for the protection of Kosi flood embankments (Mazumder,1985).

## PURPOSE AND CLASSIFICATION OF SPURS

Spurs (earthen spurs are also called groins) are constructed transverse to the river flow and extend from the bank into the river. Impervious earthen spurs/groins are made of locally available materials like clay, silt, sand and gravels etc. Rocks, rock filled crates or gabions, sand filled geo-bags and geo-tubes are also used to construct spurs where the river is steep with high flow velocity. Nose and adjacent shank portion of spurs are protected by heavy materials like stones or stone filled crates or cement concrete blocks. Main objectives of constructing spurs are

- Training of a river along a desired course
- Reduction of flow concentration at the point of attack by altering flow direction
- Protection of the bank by keeping the flow away from it
- Creation of slack flow with the object of silting up the area in the vicinity of river bank
- Dampening the flow and reduce the velocity due to energy dissipation in the eddies
- Increasing the depth of flow for navigation purpose by reducing width and aligning a wide and poorly defined channel into well defined channel
- Controlling wild meandering and migration of a stream to a defined course.

Fig.1 illustrates a typical spur field used to train a river along a desired course

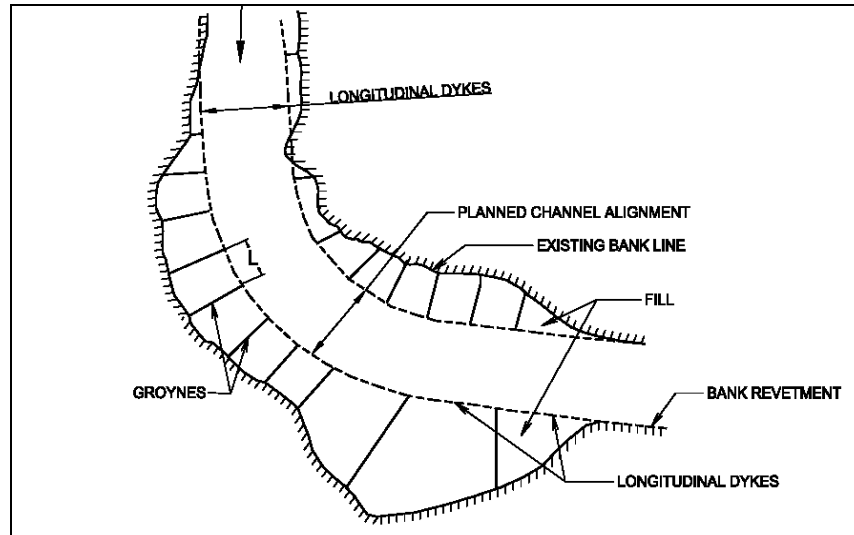


Fig. 1 Typical Spur field for training a river along a desired course

Different types of spurs used for protection of embankments may be classified according to:

- a) Methods and materials of construction: namely, permeable, impermeable, slotted etc.
- b) Height of spurs with respect to HFL: namely, submerged, unsubmerged, sloping etc.
- c) Mode of action: namely, deflecting, attracting, repelling etc.
- d) Special shapes: namely, T-headed, hockey type, kinked type, dagger type etc.

In case of deep and narrow rivers or rivers carrying considerable suspended sediments, permeable spurs are preferred. These spurs are comparatively cheaper and offer flexibility in construction, maintenance and any alteration required at a later stage. Unlike impermeable earthen spurs, they cause partial obstruction to flow by allowing water to flow through their bodies and promote deposition of sediments due to flow dampening through production of micro-turbulence. In long impermeable spurs, there is high afflux and flow concentration near the head resulting in deep scour and failure of spur heads. Common types of permeable spurs generally in use are pile spurs, tree spurs, porcupines, cribs etc. Plan and elevation of a typical pile spur are shown in fig.2.

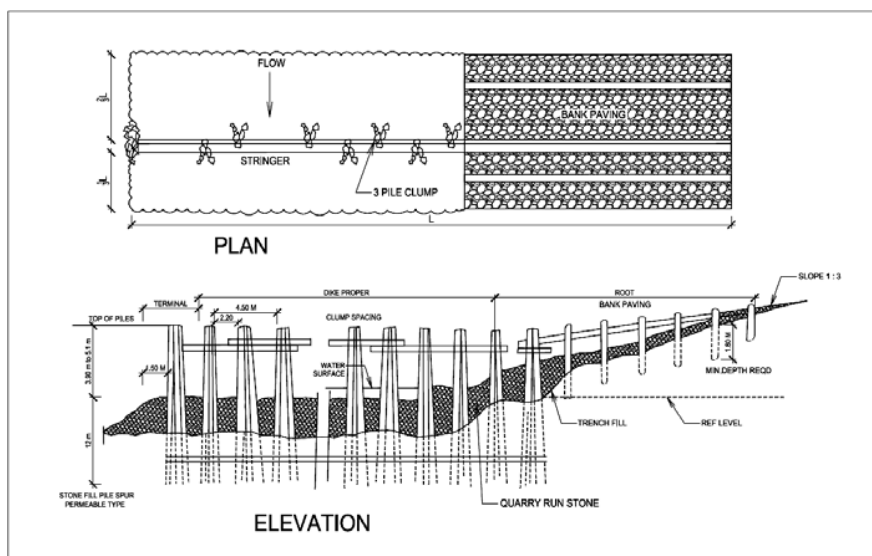


Fig.2 Plan and Elevation of a Typical Pile Spurs

## PLANNING AND DESIGN OF SPURS

Spurs can be used singly or in groups (Spur Field) in case the reach to be protected is long as shown in Fig 1. They can be used in combination with other training measures also. Length, spacing and orientation of spurs in a group are usually decided by the desired river course and determined by physical model tests. Spurs are designed for a flood discharge of 50 year return period. As per IS : 8408 (1994), length of spur measured from top of bank should not be less than  $2.5 (d_s + y_o)$ , where  $d_s$  is the scour depth below river bed and  $y_o$  is the mean depth of flow. This provision is made to ensure that the scour hole formed at the nose of spur is kept away from the toe of scoured bank. Restriction of normal waterway by long spurs cause sharp rise in Froude's number of flow at the head resulting in deep scour in the vicinity of head. Hydraulic model study was conducted at CWPRS, Pune (CW & PRS, 1991-92) to find maximum scour depth at nose of solid spurs of length (L) in a channel of width (B) as illustrated in fig.3.

As per IS code (IS:8408,1994), the effective length of spurs should not exceed  $1/5^{\text{th}}$  of width of the flow in the case of a single channel. In case of wide, shallow and braided channels, the protrusion of the spurs in the channel adjacent to bank should not usually exceed  $1/5^{\text{th}}$  of the width of that channel on which the spur is proposed. The spacing of spurs is normally 2 to 3 times its effective length. Lagasse (1995) made exhaustive study of spurs and his recommendations for planning and design of spur field are summarized in table-1

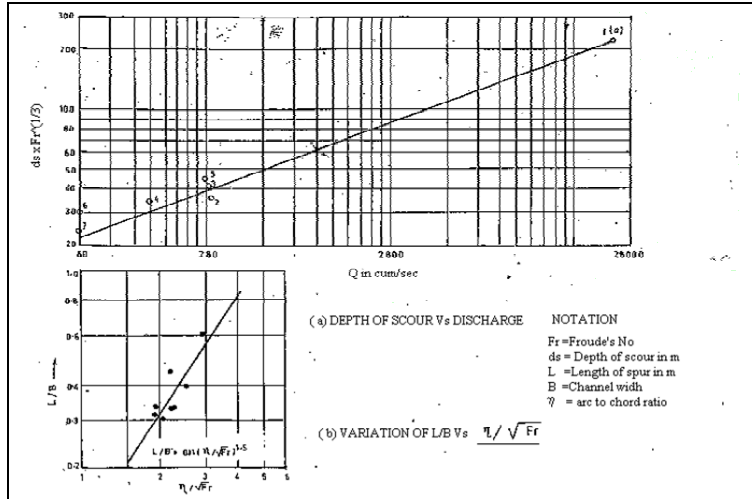


Fig.3 Determination of Depth of Scour(  $ds$ ) and Length of spur( $L$ )

Table-1 PRINCIPLES GOVERNING DESIGN OF SPUR FIELD  
( AFTER LAGASSE 1995)

Factor	Design criteria
Longitudinal extent of spur field.	Field and aerial surveys of the extent of scour are a good basis for determination of the necessary extent of the spur field. Protection downstream of a bend is especially important because meander bends propagate downstream.
Spur length	Where the bank is irregular,spur length should b adjusted to provide even curvature of the thawleg. Generally $L_g < 0.15 W$ ( $W$ =channel width ) for impermeablespurs. $L_g < 0.25W$ for permeable spurs.
Spur orientation	Orientation effects spurs spacing,scour depth at the tip of the spur and the degree of flow control achieved. spurs oriented normal to the flow are most economic because they provide maximum protrusion for a given spur length.The first (upstream) should be angled downstream.
Spur spacing, $S_g$	$S_g = L_{ge} \cot \theta$ , where $L_{ge}$ is effective length = distance between arcs describing the toe of the spur field and the desired bank line; $\theta$ is flow expansion angle downstream of the spur tips = $17^\circ$ for impermeable spurs
Spur height	Impermeable spurs generally do not exceed bank height. Permeable spurs should allow floating debris to pass over, unless the design requires trapping of light debris.
Spur plan shape	Straight spurs are preferred.Top width of the impermeable spurs should be atleast 1m.
Spur side slopes	Side slopes should be 2:1 (H:V) or flatter.

Permeability of spur	Permeability upto 35% does not effect the length of the channel bank protected. Impermeable Spurs give better flow control, but induce greater end scour, and if submerged, can cause bank erosion. High permeability spurs are preferred for mild bends and small flow velocity reduction applications.
Bed and Bank contact	Adequate bed contact is necessary to avoid undermining of the spur, especially at the toe, where a launching apron is advantageous. Adequate bank contact is necessary to avoid outflanking of the spur.
Erosion protection	Riprap protection to the upstream and downstream faces and at the end of the spur is recommended.

### **BRIEF HISTORY OF BREACHES IN KOSI MARGINAL FLOOD EMBANKMENTS**

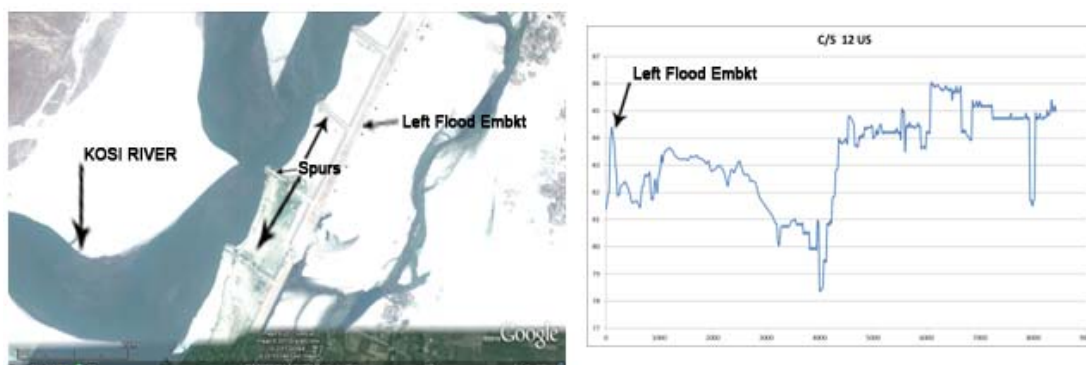
River Kosi originating from the Himalayas travels a distance of 468 km through Tibet, Nepal and India before joining river Ganga at a place called Kursela in Bihar. Before the construction of marginal flood embankments, river Kosi used to devastate both Nepal and north Bihar due to periodic change in its course. With its apex at Chatra in Nepal where Kosi comes out of the mountains in Nepal, it has shifted its course - sometimes in the east and sometimes in the west - by a distance of about 150 km over a period of 202 years from 1731 to 1933. A barrage of 1150m length and 1.53 m crest height was built at a place called Hanuman Nagar (near Indo-Nepal border) with marginal flood embankments on either side of the river (144 km in the east and 125 km on the west) in the year 1961 with a view to confine its course within the embankments with spacing of embankment varying from 4 km to 6 km.

Kosi flood embankments breached on several occasions resulting in devastating floods, loss of life and properties and unimaginable sufferings of the people in north Bihar. Details of spurs and the history of the breaches that occurred after the construction of flood embankments are given in tables-2(a) and 2(b) respectively. Most of these breaches were triggered due to failure of spurs. A total of 378 numbers of impermeable spurs of different lengths were constructed on either side of Kosi river over the years to save the flood embankments from the fury of the River. The latest breach of 2.2 km length at Kushaha occurred in left marginal embankment about 12 km upstream of the barrage as illustrated the Google Picture-1. Fig.4 shows river section near the breach site.

Unlike earlier breaches which had occurred during high floods, 2008 breach occurred at a discharge of only about 4081 cumec (1.44 lakh cusec) which is even less than one sixth of the design flood discharge of 26,922 cumec (9.5 lakh cusec). At this low flow, river Kosi is reported to flow in two different channels near the breach site of left embankment due to bifurcation of the river (anabranching) at about ch.14 km upstream of the barrage. Two spurs of 200 m and 269 m length at km.12.1 and 12.9 respectively caused obstruction to the flow, flow choking and consequent instability of flow resulting in wash out of the spurs and subsequent breach of flood embankment at such a low flow.

### **EFFECTIVENESS OF LONG SPURS IN PROTECTING FLOOD EMBANKMENT**

While designing a spur or spur field, the maximum length of spurs are usually fixed by an amount of  $1/5$  Lacey's regime waterway. In other words, the length of spurs should not cause restriction (or fluming) more than  $4/5$ th of Lacey's waterway. Spurs are usually spaced at an interval of 2 to 3 times their lengths. With a design flood of 26,922 cumec, Lacey's regime waterway is 788 m and the maximum permissible length of spurs at design flood is 158m as per IS:8408.



Picture-1 Spurs Prior to Breach at Kusaha Fig.4 Cross Section of Kosi at Kusaha

**Table-2 (a): Detail of Spurs**

<u>Embankment</u>	<u>Location</u>	<u>NumberofSpurs</u>
Eastern afflux bund	Nepal (Upstream of Barrage)	60 nos.
Western afflux bund	Nepal (upstream of barrage)	21 nos.
Eastern Embankment	India (Downstream of Barrage)	204nos.
Western embankment	Nepal (downstream of barrage)	29 nos.
Western embankment	India (Downstream of Barrage)	64 nos.

**Table- 2(b)Summary of Past Breaches in Kosi Flood Embankments**

<u>Year</u>	<u>Location of Breach</u>	<u>Embankment Breached</u>
1963	Dalwa, Nepal	West Embankment
1968	Jamalpur, Bihar	West Embankment
1971	Matniyabandha, Bihar	East Embankment
1980	Barharawa, Bihar	East Embankment
1984	Hempur, Bihar	East Embankment
1987	Gandaul and Samani In Bihar	West Embankment
1991	Joginiyan, Nepal	West Embankment
2008	Kusaha, Nepal	East Embankment

Length of the spur at km12.9 (upstream of the barrage) near Kusaha is 269 m. It is too long - more than 1.7 times the permissible length as per IS: 8408. The wash out of two spurs at ch.12.1 and 12.9 (measured u/s of barrage axis) took place at a low flood of 4081 cumec only. At this flow, Lacey's waterway is 306 m and 1/5 of waterway is 54m as against 269 m length of the spur near the left channel of about 800m width (See Fig.4) adjacent to the left embankment. Thus the spurs are too long - far exceeding a maximum permissible restriction of one fifth of Lacey's waterway- resulting in flow choking and flow instability as explained in the following paragraph.

One of the important factors responsible for wash out of the spurs and subsequent breaching of left flood embankment is formation of multiple channels upstream of barrage due to sediment deposition in the submerged area of the barrage deigned with a high afflux of 3.21m. It is reported that nearly 85% incoming flow (4081 cumec) was flowing through the left channel hugging the left embankment just before the breach. As seen in Fig.4, the difference in bed levels between left and right bank channels is nearly 4m. Such a situation which occurred due to silt deposition upstream of the barrage was, perhaps, never envisaged by the designer of spurs at the planning stage. With high flow concentration near left embankment, the spurs failed due to flow choking and consequent wash out of the spurs and subsequent breaching of the left embankment.

### HYDRAULIC ANALYSIS OF BREACH

Assuming the left channel adjacent to the left embankment to be rectangular having apperoximate bed width ( $B_1$ ) of 800m and a depth ( $y_1$ ) equal to 2.3 m (Fig.4), its sectional area ( $A_1$ ) of the channel is

$$A_1 = B_1 \cdot y_1 = 1840 \text{ m}^2 \text{ and the mean velocity of approach flow } (V_1) \text{ in the channel is}$$

$$V_1 = 0.85 \cdot 4081 / 1840 = 1.895 \text{ m/s. Hence the Froude's number of incoming Flow } (F_1)$$

$$F_1 = V_1 / \sqrt{(gy_1)} = 0.4$$

Using principles of continuity of flow and assuming no loss in energy in the transition in a rectangular channel, Mazumder (1978) proved that the fluming ratio,  $r = B_0/B_1$  can be expressed as

$$r = B_0/B_1 = (F_1/F_0)[(2+F_0^2)/(2+F_1^2)]^{3/2}$$

Where  $F_1 = V_1 / \sqrt{(gy_1)}$  is the Froude's number of incoming flow in the normal channel section and  $F_0$  is the Froude's number at throat (or flumed) section. For Choked flow,  $F_0 = 1$  and hence the critical fluming ratio  $r_{cr} = (B_0/B_1)_{cr}$  in this case is given by

$$r_{cr} = (0.4/1) [(2+1)/(2+0.16)]^{3/2} = 0.66$$

Since the length of spur in the Left Channel is 269 m, therefore, width of flow at the flumed section is

$$B_0 = 800 - 269 = 531 \text{ m and the actual fluming ratio}$$

$$B_0/B_1 = 531 / 800 = 0.66 = r_{cr}$$

Thus the flow in the left channel was just choked. In fact, due to non-uniform distribution of velocity, the flow at throat gets choked even at a value of  $F_0 = 0.7$ . Corresponding value of  $r_{cr} = 0.71$  and hence the flow at a fluming ratio of 0.66 is definitely choked. Less the fluming ratio (i.e. more is the restriction), higher is the flow choking.

In a choked flow, there is high afflux associated with hydraulic jump formation downstream. Flow becomes supercritical downstream of the throat section. Since the flow is highly asymmetric after the flumed throat (downstream of the spur head), the jump is skewed type and the flow downstream is highly asymmetric and unstable (Mazumder, 2000) in the expanding zone downstream of the spur. This may have resulted in direct attack on the spurs resulting in their washout.

### ACKNOWLEDGEMENT

The support received from Shri K.N. Keshri , Chief Engineer, CWC, S.A. Kabir, Flood Management Specialist, Bihar, Kosi Flood Recovery Project, Government of Bihar and Sh.

M.N.Singh of CWPRS in getting various information for preparation of this paper is gratefully acknowledged

## REFERENCES

- Dixit,A. "Kosi Embankment Breach in Nepal –Need for a Paradigm Shift in Responding to Floods", Economic and Political Weekly
- IRC:89 (1997), "Guidelines for Design and Construction of River Training Works for Road Bridges" The Indian Roads Congress, Kama Kothi Marg, R. K. Puram, New Delhi-28
- IS:8408-1994, Planning and design of groynes in alluvial river-Guidelines (first revision) Bureau of Indian Standards, Manak Bhawan, New Delhi-3
- IS 12094:2000 "Guidelines for Planning and Design of River Embankments (Levees)-First Edition" by Bureau of Indian Standards, Manak Bhawan, New Delhi-3
- IS 11532:1995 "Construction and Maintenance of River Embankments (Levees)- First Edition" by Bureau of Indian Standards, Manak Bhawan, New Delhi-3
- Lagasse,P.F.,Shall,J.D.,Richardson, E.V. and Chang,F.(1995) "Stream Stability at Highway Structures",hydraulic Engg. Circular no.20 (HEC-20), Report No.FHWA-IP-90-014, Federal Highway Admn. USDOT, Washington,D.C., U.S.A.
- Mazumder, S.K. and Ahuja, K.C(1978). "Optimum length of contracting transition in open channel sub critical flow" J1. Of CE Div., Inst of Engr. (1), Vol. 58, pt CI-5, March 78.
- Mazumder,S.K.(1985),"Effectiveness of Impermeable type Groins in River Training with Particular reference to River Kosi in India"Proc.2<sup>nd</sup> Int. Conf. on Hydraulics of Floods and Flood Control' Cambridge, UK, 24-26<sup>th</sup> Sept.1985
- Mazumder, S. K.(2000) "Stability of Flow Downstream of an Expansion"-Research Report (F.No.1/CD/EF(10)/97-98 dt.20.01.98) submitted to AICTE, Deptt. of CE, DCE (Now DTU).
- Mazumder, S.K.(2011) "Breaching of flood embankments with particular reference to Kosi and Farakka Barrages in India" paper published in the Journal 'Water and Energy International'by CBIP, Vol.68,No.3, March,2011
- Mishra, D."Bihar is Destined to Die-Nobody Counts us" photographs of Flood Affected Areas available in Internet, dated Sept.8,2008
- Pun,S.B.(2009)"Kosi Pralaya-Could the Catastrophe Have Been Averted and What Next?"Hydro Nepal, Issue No.4, Jan.2009
- Sinha,R.(2009a) "Dynamics of a River System-The Case of Kosi River in North Bihar", J. of Earth Sciences India, Vol.2(1), Jan.2009,pp.33-45
- 1Sinha,R.(2009b)"Kosi Rising Waters, Dynamic Channels and Human Disaster", Economic and Political Weekly, Nov.15<sup>th</sup>, 2009.



Contents lists available at SciVerse ScienceDirect

Optics Communications

journal homepage: [www.elsevier.com/locate/optcom](http://www.elsevier.com/locate/optcom)

# Realization of AND gate in Y shaped photonic crystal waveguide

Q1 Preeti Rani, Yogita Kalra, R.K. Sinha \*

TIFAC-Centre of Relevance and Excellence in Fiber Optics and Optical Communication, Department of Applied Physics, Delhi Technological University (Formerly) Delhi College of Engineering, Bawana Road, Delhi 110042, India

## ARTICLE INFO

### Article history:

Received 17 December 2012

Received in revised form

31 January 2013

Accepted 1 February 2013

### Keywords:

Photonic logic integrated circuit

Y shaped waveguide

Photonic crystal

AND gate

## ABSTRACT

We report the design of an AND optical logic gate based on two dimensional triangular lattice of air holes in Si. The proposed structure consists of Y-branch waveguide without nonlinear materials and optical amplifiers. The simulation results show that the proposed all optical structure could really function as an AND logic gate. This structure is favorable for large scale optical integration and can potentially be used in on-chip photonic logic integrated circuits.

© 2013 Elsevier B.V. All rights reserved.

## 1. Introduction

Photonic crystal (PhC) is a versatile platform to construct devices with dimensions of a few wavelengths of light being confined and have emerged as one of the most significant topic in the field of optical communication. They have some unique properties such as compactness, high speed, low power consumption and better confinement.

Recently all optical logic gates have received much attention for their applications in real time optical processing and information communications [1–12], because all optical signal processing can handle large bandwidth signals, large information flows and have no need of electrical to optical conversion. In recent years different schemes have been demonstrated for the designing of all optical logic gates using nonlinear effects in optical fibers [13–15] and in waveguides [16–18], but most of these works suffer from certain limitations such as big size, low speed and difficult to perform chip-scale integration. As logic gates are capable of performing many logic functions and have many applications in optical communication, photonic microprocessors, optical signal processors and optical instrumentation. Thus photonic crystal based all optical logic gates are considered as key elements in future photonic integrated circuits and such optical devices have attracted significant research in recent years. Most of the recent research work is based on material rods assembled in air with air cladding on both sides [19–22] i.e. the PhC structures are freely

suspended in air. These air-bridge structures having air cladding on both sides are mechanically unstable from practical perspective as well as not suitable for future integrated circuits [23–24] and large scale integration. Structures with solid support are more realistic and suitable. To the best of our knowledge, no optical logic gates have been proposed in two dimensional photonic crystal structures (2D PhC) composed of air holes in silicon (Si). In this paper, we have proposed the design of AND logic gate based on two dimensional triangular lattice photonic crystals composed of air holes in Si with Y-shaped PhC waveguide. Optical AND gate has many applications, such as, AND logic gate is used to perform address recognition, packet-header modification, and data-integrity verification. AND gate also serves as a sampling gate in optical sampling oscilloscopes owing to their ultrafast operation compared to the traditional electrical methods. The structure proposed for the realization of AND logic gate is a line defect induced symmetric Y-branch waveguide. Earlier many applications have been realized on Y-shaped waveguide, such as, demultiplexer [25–26] and XOR logic gate [27]. The simulation results show that all the proposed optical photonic crystal waveguide structure could really function as AND logic gate. By appropriately choosing the size of the holes at the center of the Y shaped waveguide the optimal performance for the proposed AND logic gate has been achieved.

## 2. Model and operating principle of AND logic gate

Fig. 1 shows the design of an all optical AND logic gate on the platform of 2D PhC. In the schematic indicated in Fig. 1 symmetric Y-shaped waveguide is formed and a hole is introduced at the

\* Corresponding author. Tel.: +91 995 305 1499.

E-mail addresses: [preeti1703.soni@yahoo.in](mailto:preeti1703.soni@yahoo.in) (P. Rani),

[dryogitakalra@gmail.com](mailto:dryogitakalra@gmail.com) (Y. Kalra), [dr\\_rk\\_sinha@yahoo.com](mailto:dr_rk_sinha@yahoo.com),

[rk\\_sinha@dce.edu](mailto:rk_sinha@dce.edu) (R.K. Sinha).

center of the three waveguides. The proposed two dimensional photonic crystal structures consist of  $15a \times 15a$  two dimensional triangular lattices. The refractive index of silicon (Si) is equal to  $n=3.5$ . The radius of air holes is ( $r=0.4a$ ), where “ $a$ ” is the lattice constant. According to the band diagram (shown in Fig. 2) of our proposed structure as calculated by the plane wave expansion (PWE) method, light with wavelengths between  $1.166 \mu\text{m}$  and  $1.926 \mu\text{m}$  for TE modes cannot pass through the uniform PhC structure and thus is completely reflected. In Fig. 1 the input signals are coming from the left lower and upper waveguides indicated as input port A and input port B. Output signals are obtained from the right port of the horizontal waveguide. AND gate encompasses of two input signals and an output signal. The output is logically “1” if and only if both of the input values are 1. For AND gate the radius of the central hole is optimized in such a way that for a single input as well as for both the inputs maximum power is obtained at the output port. Optimization of the structure is also carried out for increasing transmittance from output waveguide with wavelength. Transmittance ( $T$ ) is defined as the ratio of output intensity obtained from the output waveguide to the incident intensity at the input waveguides, i.e.  $T = I_{out}/I_{in}$ . Fig. 3 shows the spectral response of proposed AND gate for TE like polarization of incident light from single input port and Fig. 4 for both the input ports. In Fig. 3, transmittance

has been shown with respect to the wavelength when incident light is launched at one of the two input ports. Similarly Fig. 4 represents transmittance with respect to the wavelength of incident light launched at both the input ports. The contrast ratio

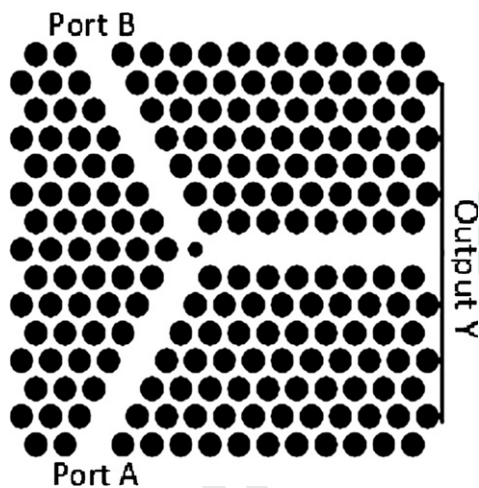


Fig. 1. Schematic of all-optical “AND” logic gate.

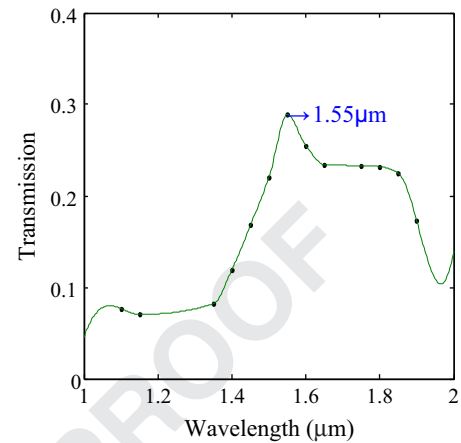


Fig. 3. Variation of transmittance with wavelength from the output waveguide for the single input signal for TE like polarization of incident light.

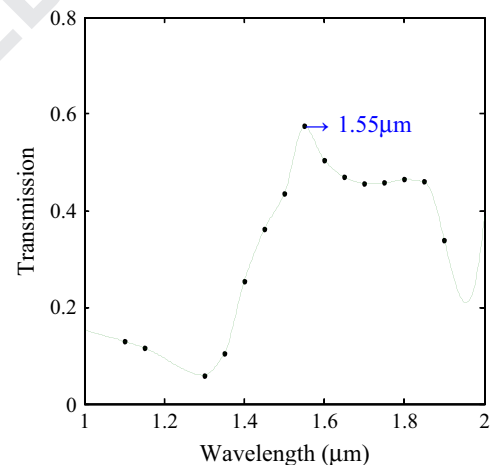


Fig. 4. Variation of transmittance with wavelength from the output waveguide for both the input signals for TE like polarization of incident light.

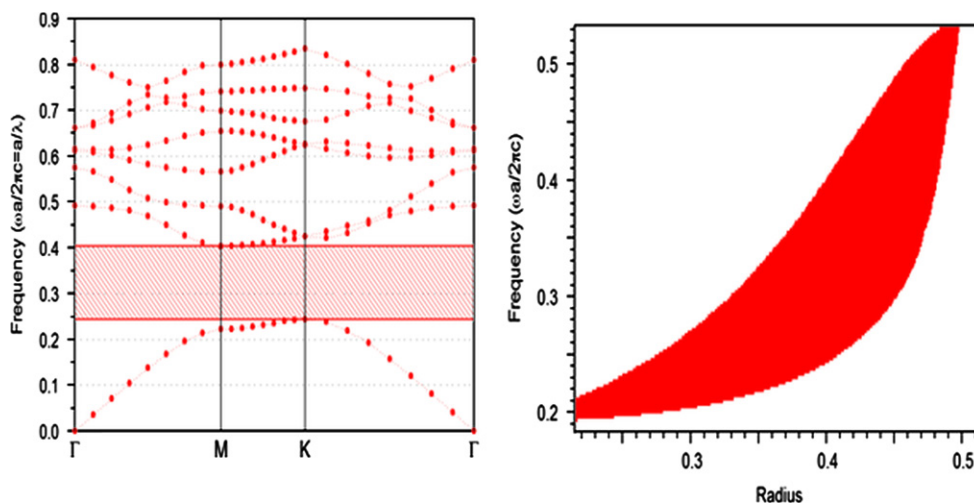


Fig. 2. Band gap structure of the photonic crystal layout.

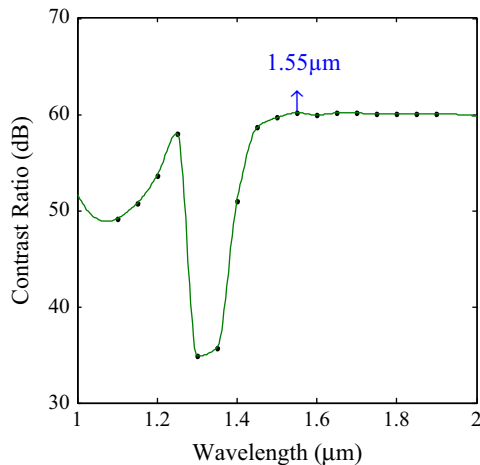


Fig. 5. Contrast ratio versus the normalized operating wavelength.

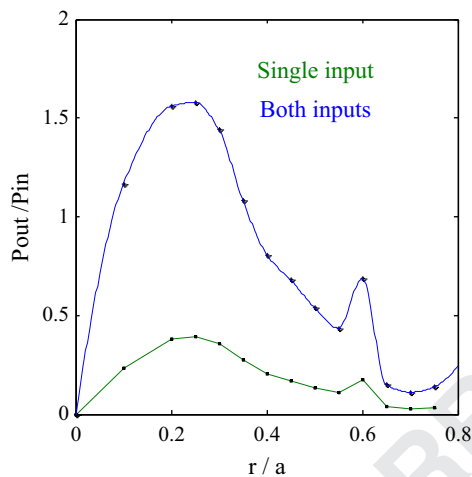


Fig. 6. Power transmittance versus the normalized radius of the central hole in the cavity.

Table 1

Truth table for AND logic gates where output Y is in terms of input power  $P_a$

Input A	Input B	Logic output	Output Y
<i>AND gate</i>			
0	0	0	0
0	1	0	0.395 $P_a$
1	0	0	0.395 $P_a$
1	1	1	1.580 $P_a$

has also been calculated, i.e. Contrast ratio =  $10 \log(P_1/P_0)$  dB, where  $P_1$  represents power for logic-1 and  $P_0$  represents power for logic-0. Fig. 5 shows the variation of contrast ratio with respect to the wavelength. Figs. 3–5 clearly show that the optimized structure can be best worked out at the normalized operating wavelength  $1.55 \mu\text{m}$  which lies in optical communication range. The response time [28,29] for the proposed logic gate structure has also been calculated.

### 3. Optimization of the radius of the hole at the center of the three waveguides

To obtain the reasonable initial value of the radius of the hole at the center of waveguides, the radius of all the other holes

except for the central hole has been taken as  $r = 0.4a$ . The radius of central hole has been scanned when one of the input signals as well as both the input signals are 1. Fig. 6 indicates that, as radius of central hole increases, the output power increases to a maximum value for both the input signals as well as for the single input signal. From Fig. 6 it is evident that as the value of radius is increased beyond  $0.25a$  power at the output port goes on decreasing. Hence the radius of hole at the center is to be taken as  $r_c = 0.25a$ .

### 4. Results and discussion for AND gate

The proposed optimized structure ( $r_c = 0.25a$  and  $r = 0.4a$ ) has been simulated using the finite difference time domain (FDTD) method and the input ports have been excited by continuous wave sources with power  $P_a$ . For simulation and optimization of the structure shown in Fig. 1, the finite difference time domain method with perfectly matched boundary conditions has been employed to absorb waves and avoid reflections at the boundaries. The magnetic field polarization of the wave has been chosen to be parallel to the y-axis, which is the axis of air holes in Si and the wave propagates in the (x, z) plane. Convergence of the simulations has been done according to the given rule, i.e.  $\Delta x < \lambda/10$  and  $\Delta z < \lambda/10$  where x and z axes are the horizontal and vertical direction coordinates and the axis of holes is along y direction. The space grid and the time grid has been chosen such that the structure meets the requirement of courant condition which is given by the equation  $c\Delta t < 1/\sqrt{\Delta x^{-2} + \Delta z^{-2}}$ , where c is the speed of light in medium. We first apply continuous wave signal at ports A and B separately and then simultaneously at both the input ports A and B with power  $P_a$ . It has been found out that output power is  $0.395P_a$  for separate excitation with power  $P_a$  at input port A as well as for separate excitation at input port B. For simultaneous excitation with power  $P_a$  at both input ports A and B the output power obtained is  $1.580P_a$ . Thus the system performs as an AND gate as summarized in Table 1. Table 1 shows the truth table for the proposed optical AND logic gate.

From Fig. 5 it has been found out that the contrast ratio between logic-1 output power and that for logic-0 is 60.17 dB at the normalized operating wavelength ( $\lambda = 1.55 \mu\text{m}$ ) which lies in the optical communication range. The field distribution at steady state for all combinations has been shown in Fig. 7 which exhibits the operation of the proposed structure of an AND gate.

The response time of the proposed optimized optical AND logic gate has been determined using the time evolving curve of the output power similar to [29] and shown in Fig. 8.

From Fig. 8, it has been concluded that the time for the output power to reach from 0% to 90% of the average output power  $P_{av}$  in the final steady state is  $ct = 54.1 \mu\text{m}$  or  $t = 0.63$  ps. The time “t” consists of two parts one of which is time due to transmission delay i.e.  $t_1 = 0.330$  ps and another is the time for the output power to climb from 0.1%  $P_{av}$  to 90%  $P_{av}$  is found to be  $t_2 = 0.301$  ps. As the system operates on linear material, hence it is expected that the falling time from average output power  $P_{av}$  to 10%  $P_{av}$  is approximately equal to  $t_2$ . Thus a narrow pulse with a width of  $2t_2 = 0.602$  ps can be produced. Hence, the response period of the signal is obtained to be 1.204 ps, i.e. the proposed AND logic gate can operate at a bit rate of 0.830 Tbits/s.

### 5. Conclusion

In this paper we have proposed the design for all optical AND logic gate based on Y-shaped photonic crystal architecture. The device performance has been analyzed by PWE method and

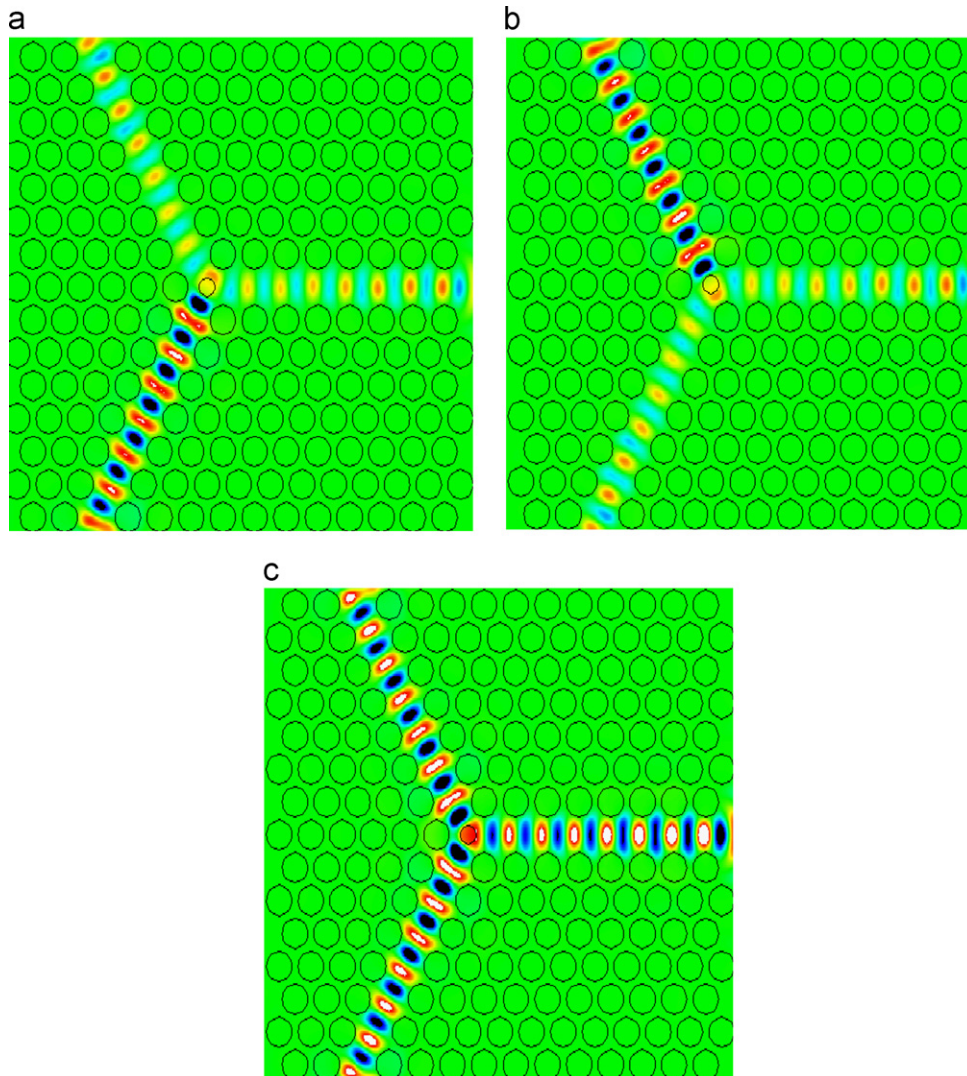


Fig. 7. Field distributions at steady state of the "AND" logic gate for (a)  $A=1, B=0$ ; (b)  $A=0, B=1$  and (c)  $A=1, B=1$ .

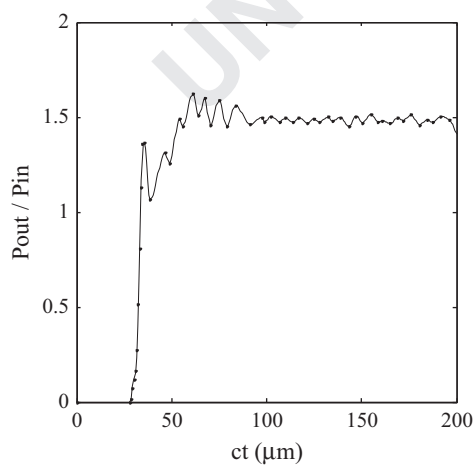


Fig. 8. Time evolving curve of the output power.

characteristics of the material and hence it can operate at very low powers. It is expected that such a design will help in realizing devices and components for broadband optical communication systems and networks. The proposed structure could be the strong candidate for future photonic crystal based all optical logic gates.

#### Acknowledgments

The authors gratefully acknowledge the initiatives and support towards the establishment of "TIFAC CENTRE of Relevance and Excellence in Fiber Optics and Optical Communication at Delhi Technological University, formerly Delhi College of Engineering" through "Mission REACH" Program of Technology Vision-2020, Government of India.

#### References

- [1] W.B. Fraga, J.W.M. Menezes, M.G. da Silva, C.S. Sobrinho, A.S.B. Sombra, Optics Communications 262 (2006) 32.
- [2] A. Rostami, G. Rostami, Optics Communications 228 (2003) 39.
- [3] K. Igarashi, K. Kikuchi, IEEE Journal of Selected Topics in Quantum Electronics 14 (2008) 551.
- [4] Y.-D. Wu, T.-T. Shih, M.-H. Chen, Optical Express 16 (2008) 248.

simulated using the FDTD method. The method of determining the operating parameters has been explained and the optimized parameters are obtained for achieving high contrast ratio. In this paper, the design of the AND logic gate is based on linear

- [5] S. Pereira, P. Chak, J.E. Sipe, Optics Letters 28 (2003) 444.
- [6] Z. Li, Z. Chen, B. Li, Optical Express 13 (2005) 1033.
- [7] M. Lipson, Optical Materials 27 (2005) 731.
- [8] Y. Dumeige, L. Ghisa, P. Féron, Y. Dumeige, Optics Letters 31 (2006) 2187.
- [9] T.A. Ibrahim, K. Amarnath, L.C. Kuo, R. Grover, V. Van, P.-T. Ho, Optics Letters 29 (2004) 2779.
- [10] C.A. Barrios, Electronics Letters 40 (2004) 862.
- [11] C. Lixue, D. Xiaoxu, D. Weiqiang, C. Liangcai, L. Shutian, Optics Communications 209 (2002) 491.
- [12] T. Fujisawa, M. Koshiba, Journal of the Optical Society of America B 23 (2006) 684.
- [13] K.H. Ahn, X.D. Cao, Y. Liang, B.C. Barnett, S. Chaikamnerd, M.N. Islam, Journal of the Optical Society of America B 14 (1997) 1228.
- [14] A. Bogoni, L. Poti, R. Progetti, G. Meloni, F. Ponzini, P. Ghelfi, Electronics Letters 41 (2005) 435.
- [15] J.W.M. Menezes, W.B. Fraga, A.C. Ferreira, K.D.A. Saboia, A.F.G.F. Filho, G.F. Guimaraes, J.R.R. Sousa, H.H.B. Rocha, A.S.B. Sombra, Optical and Quantum Electronics 39 (2007) 1191.
- [16] Y. Tetsuro, G. Masahiro, K. Toshiaki, N. Kazuhiro, S. Shinnosuke, IEEE Journal of Quantum Electronics 38 (2002) 37.
- [17] W. Yaw-Dong, IEEE Journal of Selected Topics in Quantum Electronics 11 (2005) 307.
- [18] W. Yaw-Dong, S. Tien-Tsornng, C. Mao-Hsiung, Optics Express 16 (2008) 248.
- [19] Q. Liu, Z. Ouyang, C.J. Wu, C.P. Liu, J.C. Wang, Optics Express 16 (2008) 18992.
- [20] P. Andalib, N. Granpayeh, Journal of the Optical Society of America B 26 (2009) 10.
- [21] Zhi-Hong Zhu, Wei-Min Ye, Jia-Rong Ji, Xiao-Dong Yuan, Chun Zen, Optics Express 14 (2006) 1783.
- [22] J. Bai, J. Wang, J. Jiang, X. Chen, H. Li, Y. Qiu, Z. Qiang, Applied Optics 48 (2009) 6923.
- [23] N. Kawai, K. Inoue, N. Carlsson, N. Ikeda, Y. Sugimoto, K. Asakawa, T. Takemori, Physical Review Letters 86 (2001) 2289.
- [24] R.K. Sinha, Y. Kalra, Optics Express 14 (2006) 10790.
- [25] R.K. Sinha, S. Rawal, Optical and Quantum Electronics 40 (2008) 603.
- [26] S. Rawal, R.K. Sinha, Optics Communications 282 (2009) 3889.
- [27] Kun-Yi Lee, Jhe-Min Lin, Yi-Cheng Yang, Yi-Bin Yang, Jia-Sing Wu, Yen-Juei Lin, Wei-Yu Lee, Proceedings of SPIE 7135 (2008) 71353Y-1.
- [28] Z. Zang, Optics Communications 285 (2012) 521.
- [29] C.J. Wu, C.P. Liu, Z. Ouyang, Applied Optics 51 (2012) 680.

## Accepted Manuscript

Synthesis and Luminescent Features of  $\text{NaCaPO}_4$ :  $\text{Tb}^{3+}$  Green Phosphor for near UV-based LEDs

B.V. Ratnam, M. Jayasimhadri, G. Bhaskar Kumar, Kiwan Jang, S.S. Kim, Y.I. Lee, J.M. Lim, D.S. Shin, T.K. Song

PII: S0925-8388(13)00290-9

DOI: <http://dx.doi.org/10.1016/j.jallcom.2013.01.203>

Reference: JALCOM 27825



To appear in:

Received Date: 24 December 2012

Revised Date: 20 January 2013

Accepted Date: 26 January 2013

Please cite this article as: B.V. Ratnam, M. Jayasimhadri, G. Bhaskar Kumar, K. Jang, S.S. Kim, Y.I. Lee, J.M. Lim, D.S. Shin, T.K. Song, Synthesis and Luminescent Features of  $\text{NaCaPO}_4$ :  $\text{Tb}^{3+}$  Green Phosphor for near UV-based LEDs, (2013), doi: <http://dx.doi.org/10.1016/j.jallcom.2013.01.203>

This is a PDF file of an unedited manuscript that has been accepted for publication. As a service to our customers we are providing this early version of the manuscript. The manuscript will undergo copyediting, typesetting, and review of the resulting proof before it is published in its final form. Please note that during the production process errors may be discovered which could affect the content, and all legal disclaimers that apply to the journal pertain.

## Synthesis and Luminescent Features of NaCaPO<sub>4</sub>: Tb<sup>3+</sup> Green Phosphor for near UV-based LEDs

B. V. Ratnam<sup>1</sup>, M. Jayasimhadri<sup>2</sup>, G. Bhaskar Kumar<sup>1</sup>, Kiwan Jang<sup>1,\*</sup>, S. S. Kim<sup>1</sup>, Y. I. Lee<sup>3</sup>, J. M. Lim<sup>3</sup>, D. S. Shin<sup>3</sup> and T. K. Song<sup>4</sup>

<sup>1</sup>Department of Physics, Changwon National University, Changwon, Korea 641-773

<sup>2</sup>Department of Applied Physics, Delhi Technological University, Delhi-110 042, INDIA

<sup>3</sup>Department of Chemistry, Changwon National University, Changwon, Korea 641-773

<sup>4</sup>School of Nano and Advanced Materials Engineering, Changwon National University, Changwon, Korea 641-773

### ABSTRACT

An efficient green emitting Tb<sup>3+</sup> doped NaCaPO<sub>4</sub> (NCP) phosphor was synthesized by using conventional solid-state reaction for solid-state lighting applications. X-ray diffraction (XRD), field emission scanning electron microscope (FE-SEM), FT-IR, emission and excitation properties were extensively investigated for NCP phosphors. X-ray diffraction analysis confirmed the formation of NaCaPO<sub>4</sub> with orthorhombic structure. The excitation spectrum consists of strong 4f-4f transition at around 370 nm, which has higher intensity than the f-d transition. Emission spectra indicated that this phosphor can be efficiently excited by UV light in the range from 250 to 400 nm, and shows strong emission band centered at 547 nm. Analysis of the emission spectra with different Tb<sup>3+</sup> concentrations revealed that the optimum dopant concentration for these NCP phosphors is about 5 mol% of Tb<sup>3+</sup>. Diminishing of <sup>5</sup>D<sub>3</sub> level and increasing of <sup>5</sup>D<sub>4</sub> level emission intensity with the Tb<sup>3+</sup> concentration explained successfully. The emission color was analyzed and confirmed with the help of chromaticity coordinates and color temperature. The excellent luminescent properties of NaCaPO<sub>4</sub>: Tb<sup>3+</sup> phosphor makes it as a potential green phosphor upon near-UV LED excitation.

**Keywords:** Luminescence, Green emitting phosphor, phosphor converted White LEDs

\* Corresponding author: Tel.: +82-55-213-3425; fax: +82-55-267-0263

E-mail: kwjang@changwon.ac.kr (K. Jang), jayaphysics@yahoo.com

## 1. Introduction

With rapid progress in material design and device fabrication, light-emitting diode (LED) is one of the most efficient potential light sources for applications in solid-state lighting [1-3]. White light-emitting diode (W-LED) is an emerging solid-state light source that stands a real chance of replacing the traditional light sources such as tungsten light bulbs and fluorescent lamps [4-6]. W-LEDs are widely used due to their many advantages, such as power efficiency, energy saving, long lifetime and safety [7, 8]. Nowadays, the combination of yellow phosphors (YAG: Ce<sup>3+</sup>) and a blue LED is the most popular and conventional method to generate white light due to simple fabrication and mature processing. However, this type of white LED has at least two drawbacks. Firstly, the overall efficiency decreases rapidly when the correlated color temperature of the device is decreasing. Secondly, low colour rendering index, which is not very suitable for solid-state lighting. This problem could be solved by mixing green and red phosphors instead of YAG:Ce<sup>3+</sup> phosphor. This type of white light is generated by mixing green and red phosphors with blue light emitted from a blue LED. However the green emission is one of the important components of the tricolor luminescence. So far, green phosphors reported in the patents and the research literature have some disadvantages, including low stability for sulfide phosphors and low temperature quenching for silicate phosphors [9]. In recent years, the studies on red/green/blue tricolor phosphors excited by near UV InGAN-based LED chips ( $\lambda_{em}$  = 350-410) for solid state lighting applications have attracted more attentions [10-12]. Therefore, it is necessary to explore novel green phosphors, which exhibit intense green emission upon strong near-UV excitation. Considering the rare earth ions, trivalent terbium is an important activator ion for luminescent materials due to its intense  $^5D_4 \rightarrow ^7F_5$  emission in the green region. Terbium activated green phosphors (Ce,Gd)MgB<sub>5</sub>O<sub>10</sub>: Tb<sup>3+</sup> have been used in three band fluorescent lamps and Gd<sub>2</sub>O<sub>2</sub>S: Tb<sup>3+</sup> for X-ray intensifying screens [13].

In the tricolor white LEDs, inorganic phosphors would be the best candidates for RGB phosphors in terms of both chemical stability and luminescence efficiency. Among them, phosphate is one of the best promising phosphor materials for lamps, CRT and plasma display panels (PDPs) due to its excellent thermal and hydrolytic stability, high index of refraction and inexpensive cost [14, 15]. Recently, Chuanxiang Qin et al. [16] reported that  $\text{NaCaPO}_4$  host consists of higher thermal luminescence stability and it is well known that  $\text{NaCaPO}_4$  has a wide range of technological applications. There were few reports recently on rare earth activated phosphate based phosphors for white light emitting diodes [15,17-19]. But there was no detailed report on the structural and luminescent properties of  $\text{Tb}^{3+}$  doped  $\text{NaCaPO}_4$  phosphor.

Present work is essentially motivated by the quest to acquire a deeper insight into the optimization of doping concentration and energy transfer process based on the emission and excitation for  $\text{NaCaPO}_4:\text{Tb}^{3+}$  phosphors. For this purpose, orthorhombic  $\text{NaCaPO}_4:\text{Tb}^{3+}$  phosphors were synthesized by a solid state reaction method. The luminescent properties were investigated by varying the doping concentration of  $\text{Tb}^{3+}$  ions in the host and determined the optimum doping concentration with the highest emission intensity.

## 2. Experimental details

Green emitting phosphors with general composition  $\text{NaCa}_{(1-x)}\text{PO}_4: x \text{ Tb}^{3+}$  ( $x = 1, 2, 3, 5$  and  $7 \text{ mol } \%$ ) were prepared by solid state reaction using  $\text{Na}_2\text{CO}_3$ ,  $\text{CaCO}_3$ ,  $\text{NH}_4\text{H}_2\text{PO}_4$  and  $\text{TbCl}_3 \cdot 6\text{H}_2\text{O}$  as starting materials. The stoichiometric amounts of these materials were weighed and then thoroughly wet mixed in an agate mortar with methyl alcohol as the wetting medium. The mixture was calcined by three step heating process (i.e Firstly at  $185^\circ\text{C}$  for 2 h, then  $714^\circ\text{C}$  for 1 h and finally at  $950^\circ\text{C}$  for 3 h).

The crystal structure and the phase purity of the calcined samples were identified by recording the powder X-ray diffraction (XRD) using a Cu K radiation (Xpert MPD, Philips).

The data were recorded over the  $2\theta$  range of  $20^\circ$ - $80^\circ$ . The morphology analysis of the samples was performed by a JEOL-5600 field emission scanning electron microscope (FE-SEM). The structural properties were measured by using JASCO, FT/IR-6300 spectrometer. The emission and excitation spectra were measured with a Shimadzu, RF-5301PC spectrofluorophotometer. The lifetime measurement was also carried out by exciting the sample with Nd-YAG laser upon 355 nm excitation.

### 3. Results and Discussion

#### 3.1. Crystalline structure and morphology

The X-ray diffraction patterns of the 1 mol %  $\text{Tb}^{3+}$  doped  $\text{NaCaPO}_4$  phosphor is shown in Fig. 1 and has a good match with the standard patterns reported by the Joint Committee on Powder Diffraction Standards (JCPDS) number: 76-1456. A pure orthorhombic phase of  $\text{NaCaPO}_4$  synthesized belongs to the  $\text{Pn}2_1\text{a}$  space group with lattice parameters  $a = 20.39 \text{ \AA}$ ,  $b = 5.412 \text{ \AA}$ ,  $c = 9.161 \text{ \AA}$  (JCPDS No: 76-1456). It is found that there is no change in the position of the peaks with different concentration. The ionic radius of the  $\text{Tb}^{3+}$  ion (92 pm) is smaller than that of  $\text{Ca}^{2+}$  ion (99 pm). Hence, it is expected that  $\text{Tb}^{3+}$  ions may substitute in the  $\text{Ca}^{2+}$  site.

Fig. 2 shows the FE-SEM image for the 5 mol%  $\text{Tb}^{3+}$  doped  $\text{NaCaPO}_4$  phosphor. The powder particles appear to be highly crystalline with slight agglomeration. The particles are in the  $\mu\text{m}$  range with an inhomogeneous nature. The microstructure of the phosphor consists of irregular fine grains with an average size of about 4–8  $\mu\text{m}$ .

Fig. 3 presents FT-IR spectra of the 5 mol%  $\text{Tb}^{3+}$  doped  $\text{NaCaPO}_4$  phosphor. The intense absorption bands at around 570 and 1051  $\text{cm}^{-1}$  are due to stretching vibrations of phosphate groups [20]. The band around 2374  $\text{cm}^{-1}$  originates from asymmetrical stretching of  $\text{CO}_2$ . The peak at 3465  $\text{cm}^{-1}$  is ascribed to the  $\text{OH}^-$  stretching vibration mode and 1983  $\text{cm}^{-1}$

<sup>1</sup> is assigned to the H-O-H bending vibration mode of the H<sub>2</sub>O molecule, respectively. The characteristic vibrations of water molecule may arise from absorbed moisture at sample surface during the measurement.

### 3.2. Luminescent properties

The excitation spectrum of 5 mol % Tb<sup>3+</sup> doped NaCaPO<sub>4</sub> phosphor by monitoring the green emission (<sup>5</sup>D<sub>4</sub>→<sup>7</sup>F<sub>5</sub>) at around 547 nm is shown in Fig. 4. For comparison, the overall excitation spectrum can be divided into two parts: one broader excitation band at the shorter wavelength in the range from 250 to 290 nm represents the transition 4f<sup>8</sup>→4f<sup>7</sup>5d<sup>1</sup> and the other at the longer wavelength region in the range from 290 to 400 nm represents the 4f-4f transitions of Tb<sup>3+</sup>. This is important to note that the transition <sup>7</sup>F<sub>6</sub>→<sup>5</sup>G<sub>6</sub> at 370 nm has the highest intensity than 4f-5d/4f-4f transitions of Tb<sup>3+</sup>, which was not observed in many hosts and indicating that this NaCaPO<sub>4</sub>: Tb<sup>3+</sup> phosphor can be much suitable to excite well with the UV based LED chips.

Luminescent properties of Tb<sup>3+</sup> doped NaCaPO<sub>4</sub> phosphors exhibit characteristic emission bands of Tb<sup>3+</sup> due to <sup>5</sup>D<sub>3</sub>→<sup>7</sup>F<sub>J</sub> and <sup>5</sup>D<sub>4</sub>→<sup>7</sup>F<sub>J</sub> transitions upon near UV light excitation at 370 nm as illustrated in Fig. 5. The blue emission lines centered at 416 and 438 nm are corresponding to <sup>5</sup>D<sub>3</sub>→<sup>7</sup>F<sub>J</sub> (J = 5 and 4) transitions and the emission lines 493, 547, 586 and 624 nm are from <sup>5</sup>D<sub>4</sub>→<sup>7</sup>F<sub>J</sub> (J=6, 5, 4 and 3) transitions, respectively. Among these peaks, the green emission at 547 nm corresponding to the <sup>5</sup>D<sub>4</sub>→<sup>7</sup>F<sub>5</sub> transition has the strongest intensity and this transition has the largest probability for electric-dipole transition as this transition is most intensive. The <sup>5</sup>D<sub>4</sub>→<sup>7</sup>F<sub>6</sub> (J=2) transition is a forced electric dipole allowed transition. The intensities of blue emission peaks (<sup>5</sup>D<sub>3</sub>→<sup>7</sup>F<sub>J</sub>) were much weaker than those of the green emission peaks (<sup>5</sup>D<sub>4</sub>→<sup>7</sup>F<sub>J</sub>). In order to verify the optimum Tb<sup>3+</sup> doping concentration, the emission spectra measured with increasing the Tb<sup>3+</sup> concentration (1 -7 mol%) by exciting the samples at 370 nm excitation (Fig. 5). The observed emission

intensities corresponding to the  $^5D_3 \rightarrow ^7F_J$  and  $^5D_4 \rightarrow ^7F_J$  bands have been considerably varying with the  $Tb^{3+}$  concentration. The decrease in emission intensity with increasing activator concentration may be due to the well established concept of concentration quenching. In the present work, the emission intensities from  $^5D_4$  excited states increased with increasing terbium concentration, they reach maximum at 5 mol% of  $Tb^{3+}$  and then decreasing due to the concentration quenching process. On the other hand, emission peaks from  $^5D_3$  level decrease with increasing of terbium concentration. The inset of Fig. 5 shows the relative intensity of  $^5D_4 \rightarrow ^7F_5$  transition of  $Tb^{3+}$ : NaCaPO<sub>4</sub> as a function of  $Tb^{3+}$  concentration. This graph clearly shows that the optimum doping concentration for  $Tb^{3+}$  is about 5 mol% in the NaCaPO<sub>4</sub>: $Tb^{3+}$  phosphors, which exhibits maximum emission intensity. Fig. 6 shows the emission spectra of NaCaPO<sub>4</sub>:  $Tb^{3+}$  with different  $Tb^{3+}$  concentrations, where the intensities are normalized to the green emission ( $^5D_4 \rightarrow ^7F_5$ ). When the concentration of  $Tb^{3+}$  was increased from 1 to 7 mol % the emission intensities from  $^5D_3$  level decreased and almost vanished at 7 mol%  $Tb^{3+}$  concentration. From Figs. 5 and 6, the decrement in emission intensities for  $^5D_3$  excited level transitions and the enhancement in emission intensities for  $^5D_4$  excited level transitions are due to cross relaxation effect of  $Tb^{3+}$  ions. This non-radiative cross relaxation is induced by the resonance between the excited and the ground states of two  $Tb^{3+}$  ions, which can be described as  $(^5D_3 + ^7F_6) \rightarrow (^5D_4 + ^7F_0)$  [21]. High  $Tb^{3+}$  concentrations make the distance of  $Tb^{3+}$ - $Tb^{3+}$  shorten and thus a fast cross relaxation from  $^5D_3$  to  $^5D_4$  energy level. As a result, the emission peaks originating from  $^5D_3$  level were almost vanished and the green emission becomes increased up to a critical concentration has reached.

In addition, critical distance corresponding to the critical quenching concentration is defined as the average shortest distance between the nearest  $Tb^{3+}$  ions between which energy

transfer occurs. Blasse [22] has suggested that the critical distance of energy transfer can be estimated by the equation:

$$R_c = 2 \left[ \frac{3V}{4\pi x_c N} \right]^{\frac{1}{3}} \quad (1)$$

where  $x_c$  is the critical concentration,  $N$  is the number of cations in the unit cell, and  $V$  is the volume of the unit cell. By taking the experimental and analytical values of  $V$ ,  $N$  and  $x_c$  (1010.9 Å<sup>3</sup>, 4 and 0.05, respectively). The critical transfer distance in NaCaPO<sub>4</sub>:Tb<sup>3+</sup> is calculated to be about 2.1 nm, which is in accordance with other reported values for different hosts [23, 24]

The emission spectra of optimized 5 mol % Tb<sup>3+</sup> doped NaCaPO<sub>4</sub> phosphors upon different excitations are measured and shown in Fig. 7. The inset of Fig. 7 shows the relative intensity as a function of excitation wavelength. From this figure, it can be revealed that these phosphors emit maximum intensity upon 370 nm excitation. The emission color was analyzed and confirmed with the help of CIE chromaticity coordinates. The CIE chromaticity coordinates for the 5 mol % Tb<sup>3+</sup>-doped NaCaPO<sub>4</sub> phosphors at different excitations (274, 319, 353, 370 and 378 nm) are nearly ( $x = 0.27, 0.58$ ) with correlated color temperature 6660 K, which are indicated in the CIE diagram as shown in Fig. 8. It is obvious that these coordinates are in good agreement with the well known green phosphors (Zn,Cd)S:Ag (0.26, 0.60) and ZnS:Au<sub>0.05</sub>, Cu<sub>0.01</sub> (0.267, 0.582) [25] and exhibit green light emission in the chromaticity diagram. So, the Tb<sup>3+</sup> can be used as activator ion and doped in to NaCaPO<sub>4</sub> host to obtain white light phosphor and this phosphor can be strongly excited by 352, 367 and 389 nm, which one of the wavelengths is matching well with the UV LED emission (350-410 nm). Hence it is suggested that Tb<sup>3+</sup>-doped NaCaPO<sub>4</sub> phosphor is suitable for phosphor-converted LEDs.

Fig. 9 shows the mean decay time for the  $^5D_4$  level measured for 5 mol%  $Tb^{3+}$  doped  $NaCaPO_4$  phosphors by monitoring at 547 nm emission, which is found to be 2.69 ms. The measured lifetime is found to be shorter than those published elsewhere, which is suitable for PDP application [26, 27].

#### 4. Conclusions

Orthorhombic  $NaCaPO_4:Tb^{3+}$  phosphors were prepared by using conventional solid state reaction technique. A single-phase phosphor powder was obtained by means of XRD analysis. A series of  $NaCaPO_4:Tb^{3+}$  phosphors with various  $Tb^{3+}$  concentrations prepared and effect of the  $Tb^{3+}$  concentration on the emission intensity was investigated. These phosphors exhibit strong green emission at around 547 nm due to the  $^5D_4 \rightarrow ^7F_5$  transition of  $Tb^{3+}$  and the highest emission intensity was observed for 5 mol% of  $Tb^{3+}$  doping concentration. The critical energy transfer distance of  $Tb^{3+}:NaCaPO_4$  is about 2.1 nm. This phosphor can be efficiently excited by light with wavelength of 370 nm to emit green emission with high correlated color temperature (CCT=6660 K). Therefore, the phosphor  $NaCaPO_4:Tb^{3+}$  is a potential candidate to utilize as a green phosphor for white light emitting diodes upon near UV-LED excitation.

#### Acknowledgements

This work has been supported by Priority Research Centers Program through the National Research Foundation of Korea (NRF) funded by the Ministry of Education, Science and Technology (2010-0029634). One of the authors (M. Jayasimhadri) is grateful to DAE-BRNS, Govt. of India for the sanction of research project (No. 2011/34/2/BRNS/130, dt. 21/04/2011).

**References:**

- [1] S. Pimputkar, J. S. Speck, S. P. Den Baars, S. Nakamura, Prospectus for LED lighting, Nat. Photonics 3 (4) (2009) 180-182. S. Pimputkar, J. S. Speck, S. P. Den Baars & S. Nakamura, Nat. Photonics 3 (2009) 180
- [2] H.S. Jang, H. S., H.Y. Kim, Y.S. Kim, H.M. Lee, D.Y. Jeon, Opt. Express 20 (2012) 2761.
- [3] E. Fred Schubert, K. Kyu Kim, H. Luo, J-Q. Xi, Rep. Prog. Phys. 69 (2006) 3069
- [4] Y. Shuanglong, C. Xianlin, Z. Chaofeng, Y. Yunxia, C. Guorong, Opt. Mater. 30 (2007) 192
- [5] H. Jing, C. Guo, G. Zhang, X. Su, Z. Yang, J.H. Jeong, J. Mater. Chem. 22 (2012) 13612.
- [6] X. Zhang, H. Chen, W. Ding, H. Wu, J. Kim, J. Am. Ceram. Soc. 92 (2009) 429.
- [7] M. Bredol, U. Kynast, C. Ronda, Adv. Mater. 3 (1991) 361.
- [8] X. Zhang, J. Zhnag, J. Huang, X. Tang, M. Gong, J. Lumin. 130 (2010) 554
- [9] Y. Liu, J. Hao, W. Zhuang and Y. Hu, J. Phys. D: Appl. Phys. 42 (2009) 245102
- [10] X. Wang, Y. Xian, G. Wang, J. Shi, Q. Su, M. Gong, Opt. Mater. 30 (2007) 521.
- [11] M. Jayasimhadri, Kiwan Jang, H.S. Lee, B. Chen, S.S. Yi and J.-H. Jeong, J. Appl. Phys. 106 (2009) 013105
- [12] S. Choi, Y.-M. Moon, K. Kim, H.-K. Jung, S. Nahm, J. Lumin. 129 (2009) 988-990
- [13] Y.S. Chang, H. J. Lin, Y.C. Li, Y. L. Chai, Y. Y. Tsai, J. Solid State Chem. 180 (2007) 3076
- [14] Z. C. Wu, J. X. Shi, J. Wang, M. L. Gong, Q. Su, J. Solid State Chem. 179 (2006) 2356
- [15] C.C. Lin, Y.S. Tang, S.F. Hu, R.S. Liu, J. Lumin. 129 (2009) 1682
- [16] C. Qin, Y. Huang, L. Shi, G. Chen, X. Qiao, H. J. Seo, J. Phys. D: Appl. Phys. 42 (2009) 185105

- [17] F. Ren, D. Chen, Opt. Laser Technol. 42 (2010) 110
- [18] J. Wang, Z. Zhang, M. Zhang, Q. Zhang, Q. Su, J. Tang, J. Alloys Comp. 488 (2009) 582.
- [19] K.N. Shinde, S. J. Dhoble, Adv. Mater. Lett. 1 (2010) 254
- [20] Y. Tanaka, Y. Hirata, R. Yoshinaka, J. Ceram. Process. Res. 4 (2003) 197.
- [21] J. Liao, B. Qiu, H. Wen and W. You, Opt. Mater. 31 (2009) 1513
- [22] G. Blasse, Philips Res. Rep. 24 (1969) 131.
- [23] S.H.M. Poort, W.P. Blokpoel, G. Blasse, Chem. Mater. 7 (1995) 1547
- [24] K.S. Sohn, B. Cho, H.D. Park, Mater. Lett. 41 (1999) 303
- [25] W. M. Yen, S. Shionoya and H. Yamamoto, Phosphor Handbook, Second edition, CRC Press, NY, 2006, Ch. 6.
- [26] U. Caldino, A. Speghini, M. Bettinelli, J. Phys.: Condens. Matter 18 (2006) 3499.
- [27] J. Zhong, H. Liang, B. Han, Q. Su, Y. Tao, Chem. Phys. Lett. 453 (2008) 192.

**Figure Captions:**

**Fig. 1.** XRD patterns of the 1 mol % Tb<sup>3+</sup> doped NaCaPO<sub>4</sub> phosphor

**Fig. 2.** FE-SEM image for 5 mol% Tb<sup>3+</sup> doped NaCaPO<sub>4</sub>

**Fig. 3.** FT-IR spectrum for  $\text{Tb}^{3+}:\text{NaCaPO}_4$  phosphors

**Fig. 4.** Excitation spectrum of  $\text{NaCaPO}_4:\text{Tb}^{3+}$  phosphor

**Fig. 5.** Emission spectra of  $\text{NaCaPO}_4:\text{Tb}^{3+}$  phosphor with different  $\text{Tb}^{3+}$  concentrations.  
Inset shows the dependence of  $^5\text{D}_4 \rightarrow ^7\text{F}_5$  peak intensity with  $\text{Tb}^{3+}$  concentration.

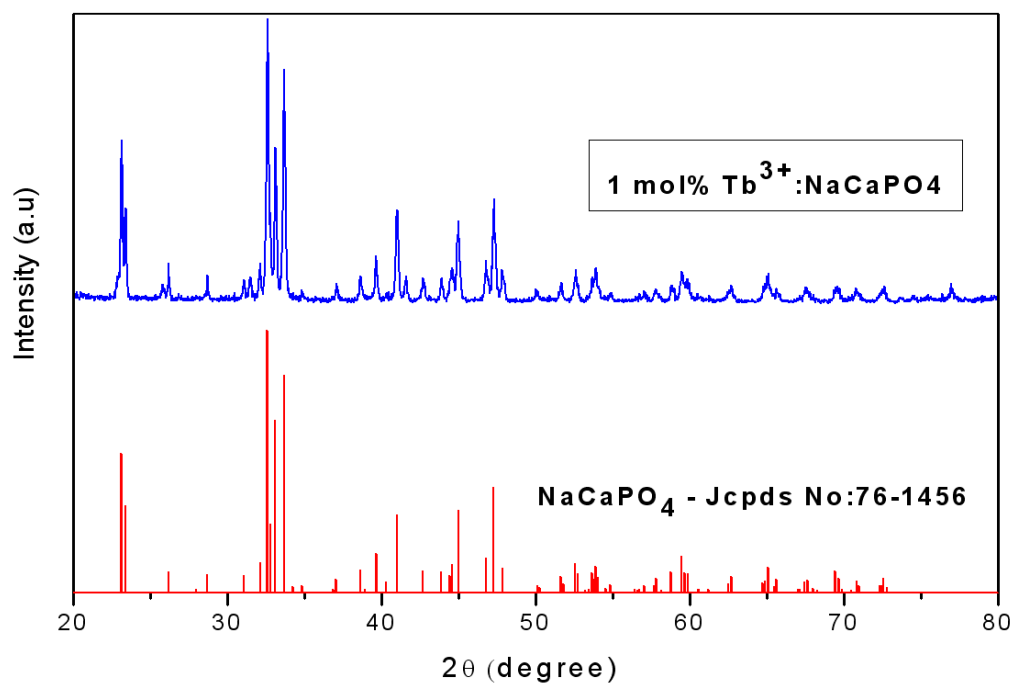
**Fig. 6.** Emission spectra of  $\text{Tb}^{3+}$  doped  $\text{NaCaPO}_4$  phosphor with different concentrations, where the intensities of the green emission ( $^5\text{D}_4 \rightarrow ^7\text{F}_5$ ) are normalized.

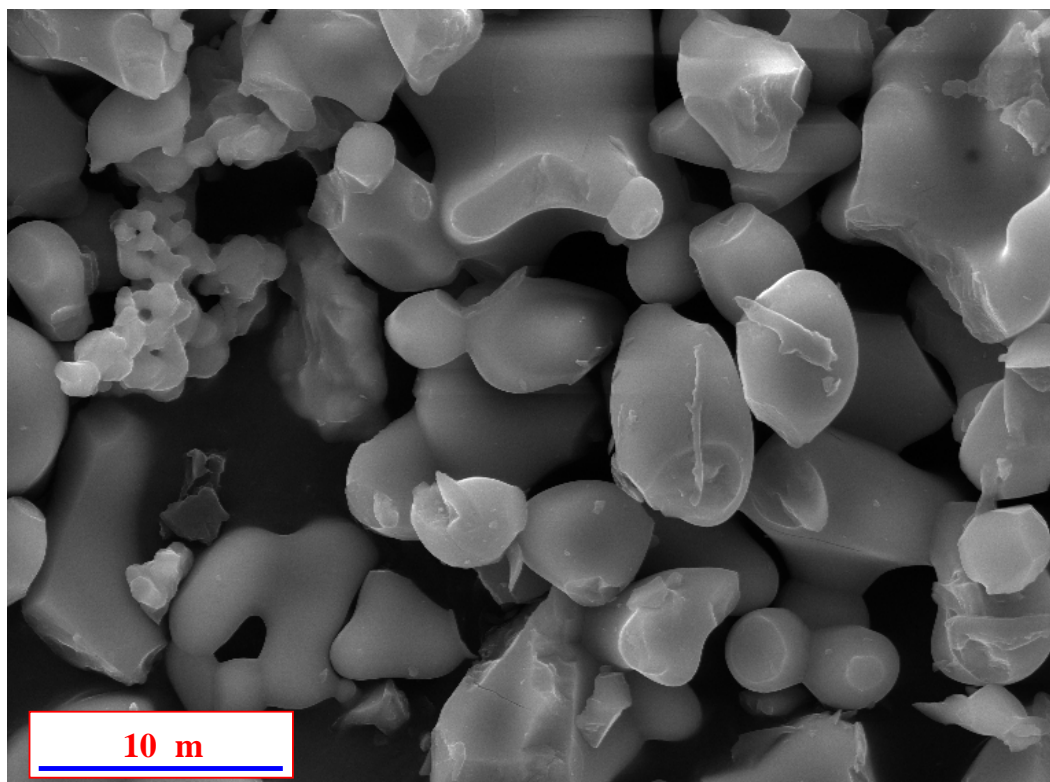
**Fig. 7.** Emission spectra of 5 mol %  $\text{Tb}^{3+}$  doped  $\text{NaCaPO}_4$  phosphor upon different excitations.

**Fig. 8.** The CIE color coordinates for 5 mol %  $\text{Tb}^{3+}:\text{NaCaPO}_4$  phosphor upon different excitations

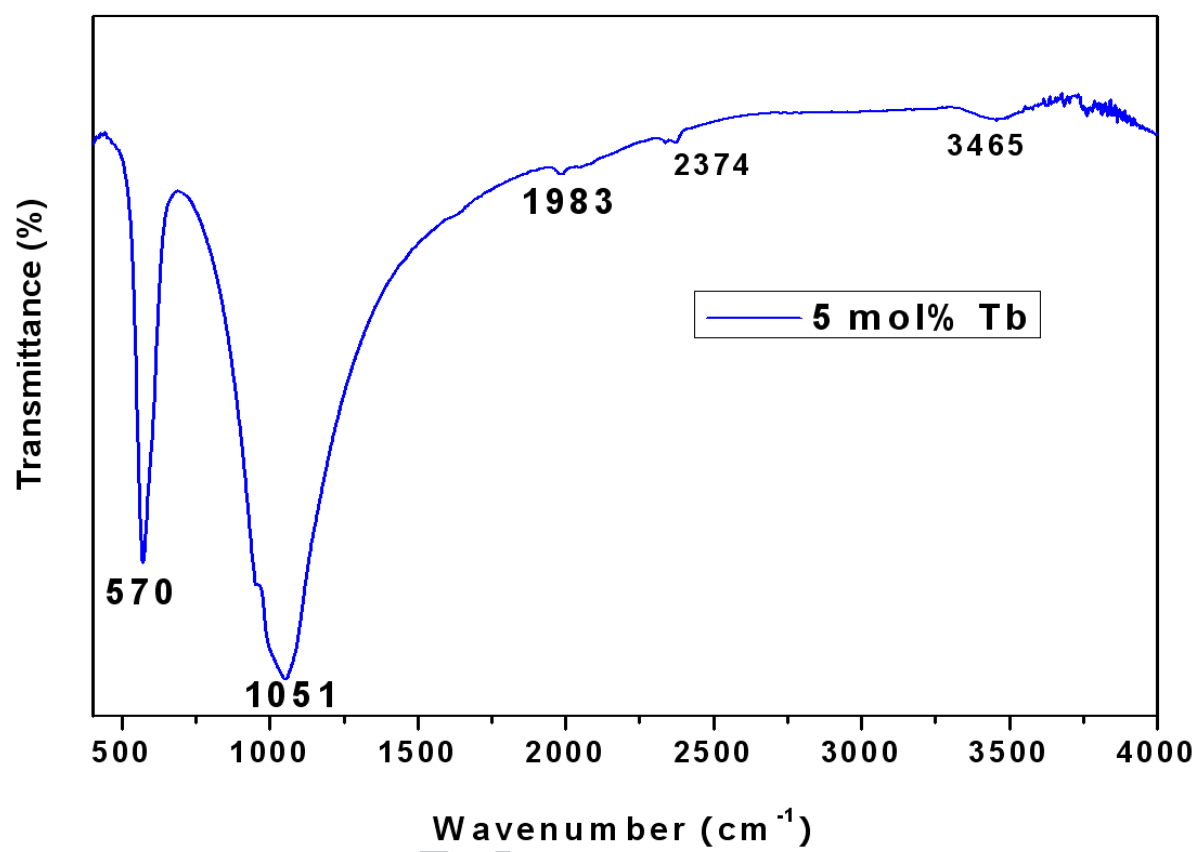
**Fig. 9.** The decay curves for the  $^5\text{D}_4$  level of  $\text{Tb}^{3+}$  at 547 nm under the third harmonic (355 nm) of a Nd: YAG laser excitation

**Fig. 1.**

**Fig. 2.**



**Fig. 3.**

**Fig. 4.**

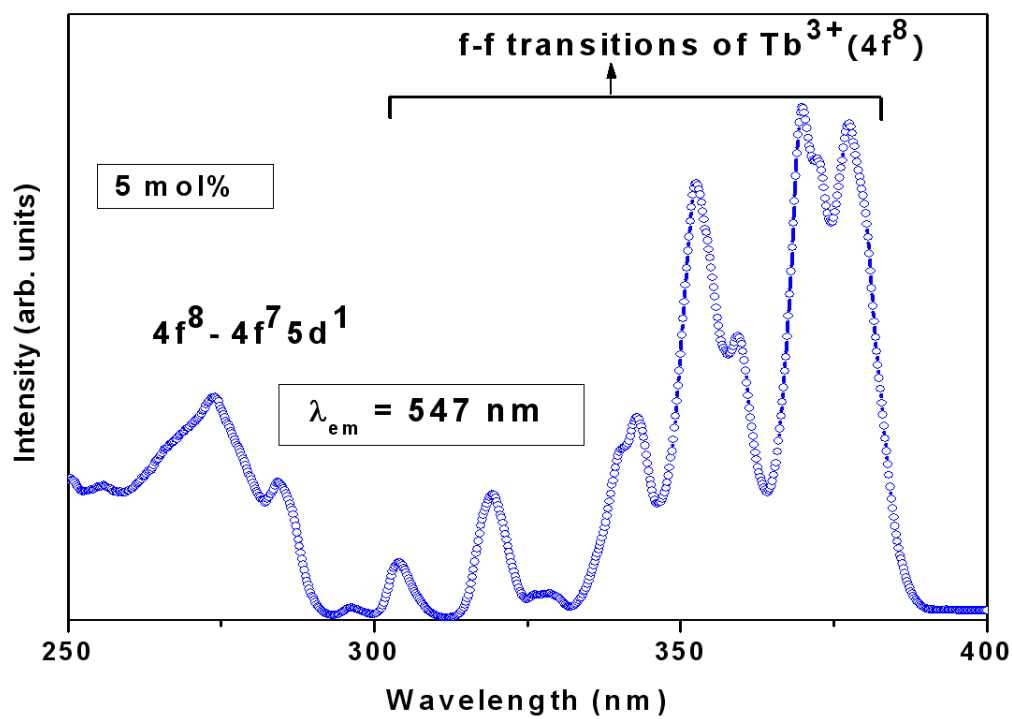


Fig. 5.

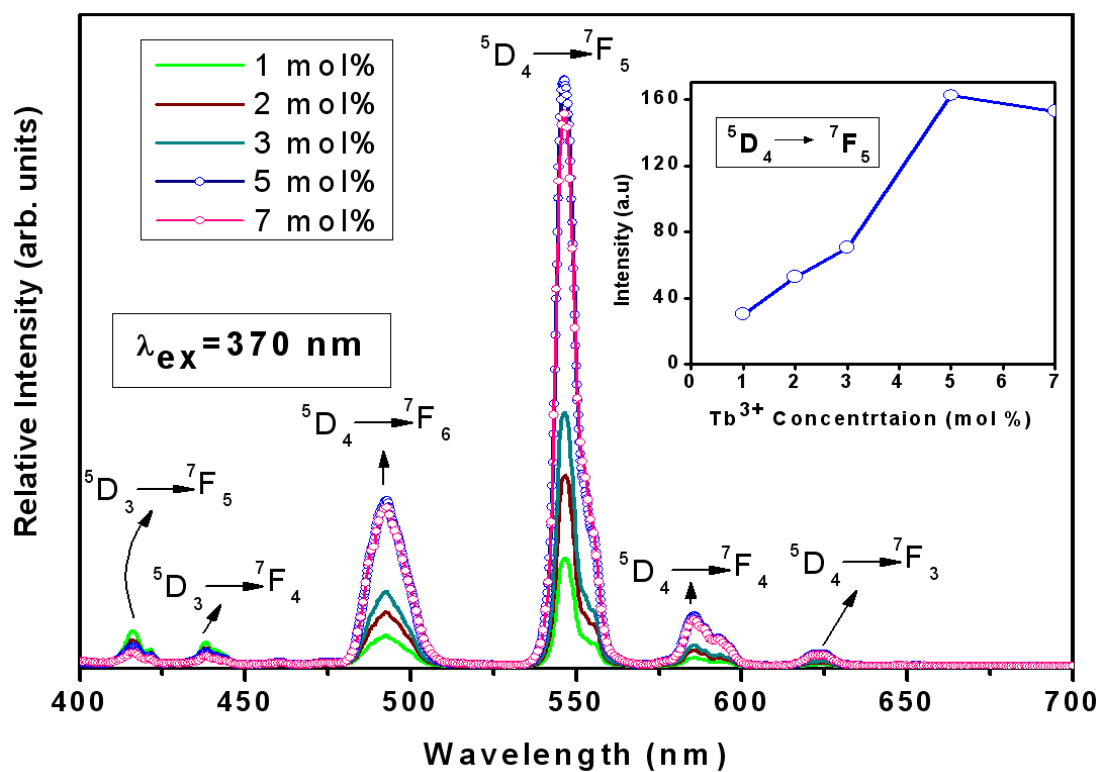


Fig. 6.

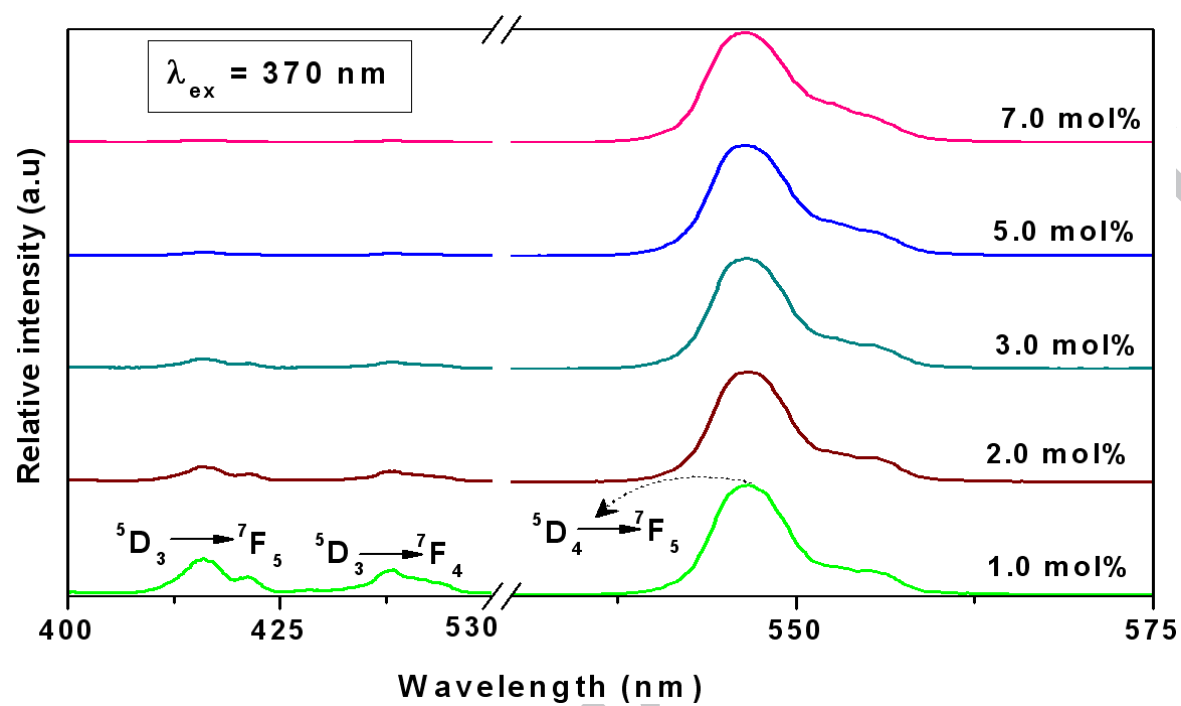
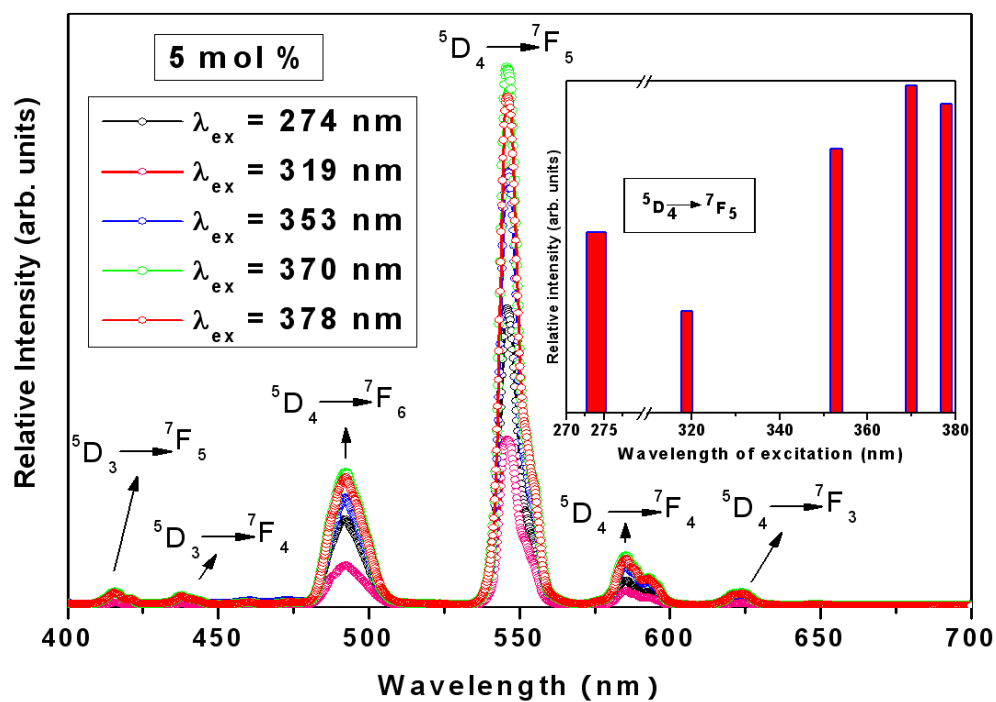


Fig. 7.



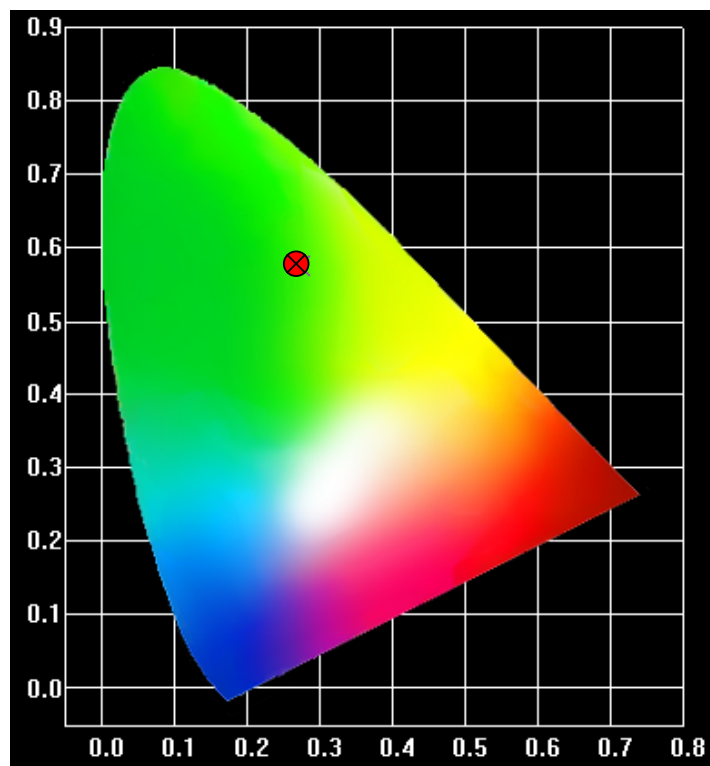
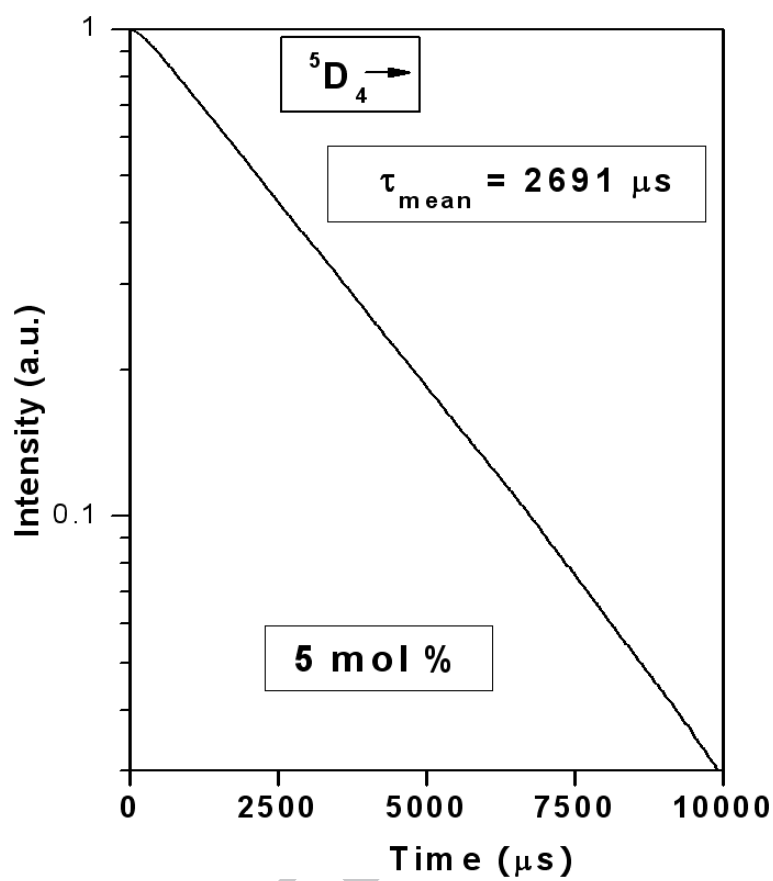
**Fig. 8.**

Fig. 9.



**Highlights**

- Successfully synthesized orthorhombic phase of NaCaPO<sub>4</sub> (NCP) phosphors
- Structural and Luminescent properties have been investigated.
- In the excitation spectrum,  $^7F_6 \rightarrow ^5G_6$  transition at 370 nm exhibit highest intensity.
- CIE coordinates of Tb<sup>3+</sup>: NCP phosphor indicate green light emission in CIE diagram
- Hence, Tb<sup>3+</sup> doped NaCaPO<sub>4</sub> is suitable for UV based pc-LEDs